NAG1-1648

IN-24-CR

NASA/CR- -97- 208345 306710

ANALYSIS OF SMART COMPOSITE STRUCTURES INCLUDING DEBONDING

NASA LaRC Technical Monitor: Anna McGowan
Principle Investigator: Aditi Chattopadhyay
Graduate Research Associate: Charles E. Seeley
Department of Mechanical and Aerospace Enginerring
Arizona State Univeristy
Tempe, AZ 85287-6106
August, 1997

ABSTRACT

Smart composite structures with distributed sensors and actuators have the capability to actively respond to a changing environment while offering significant weight savings and additional passive controllability through ply tailoring. Piezoelectric sensing and actuation of composite laminates is the most promising concept due to the static and dynamic control capabilities. Essential to the implementation of these smart composites are the development of accurate and efficient modeling techniques and experimental validation. This research addresses each of these important topics.

A refined higher order theory is developed to model composite structures with surface bonded or embedded piezoelectric transducers. These transducers are used as both sensors and actuators for closed loop control. The theory accurately captures the transverse shear deformation through the thickness of the smart composite laminate while satisfying stress free boundary conditions on the free surfaces. The theory is extended to include the effect of debonding at the actuator-laminate interface. The developed analytical model is implemented using the finite element method utilizing an induced strain approach for computational efficiency. This allows general laminate geometries and boundary conditions to be analyzed. The state space control equations are developed to allow flexibility in the design of the control system. Circuit concepts are also discussed.

Static and dynamic results of smart composite structures, obtained using the higher order theory, are correlated with available analytical data. Comparisons, including debonded laminates, are also made with a general purpose finite element code and available experimental data. Overall, very good agreement is observed. Convergence of the finite element implementation of the higher order theory is shown with exact solutions. Additional results demonstrate the utility of the developed theory to study piezoelectric actuation of composite laminates with pre-existing debonding. Significant changes in the modes shapes and reductions in the control authority result due to partially debonded actuators.

An experimental investigation addresses practical issues, such as circuit design and implementation, associated with piezoelectric sensing and actuation of composite laminates. Composite specimens with piezoelectric transducers were designed, constructed and tested to validate the higher order theory. These specimens were tested with various stacking sequences, debonding lengths and gains for both open and closed loop cases. Frequency changes of 15% and damping on the order of more than 20% of critical damping, via closed loop control, was achieved. Correlation with the higher order theory is very good. Debonding is shown to adversely affect the open and closed loop frequencies, damping ratios, settling time and control authority.

ACKNOWLEDGMENTS

I would first like to thank my advisor, Dr. Aditi Chattopadhyay, for guidance and support throughout the completion of this research. I would also like to thank the other members of my advisory committee, Dr. Barzin Mobasher, Dr. David H. Laananen, Dr. Marc P. Mignolet, and Dr. Robert L. Rankin for their helpful suggestions and insightful discussions. I indebted to all of my fellow graduate students, past and present, including Brian Biswell, Tracy Blake, Haozhong Gu, Ratan Jha, Jarek Knap, Jeff Lyon, Thomas R. Mccarthy, Narayanan S. Pagaldipti, and Tom Warren. Special thanks to Bruce Tachoir whose depth of computer knowledge never ceases to amaze me, Larry Goss who helped with the circuit design, Ed Robinson for network administration, as well as the boys in the A.S.U machine shop. Tony Cook of Simula Inc. was very helpful in constructing the smart composite laminates.

Finally I wish to thank the aeroelasticity branch at NASA Langley Research Center for supporting this research through grant number NAG-1-1648, branch head Dr. Tom Noll and technical monitors Jennifer Heeg and Anna McGowan.

TABLE OF CONTENTS

Page

Page

LIST OF TABLES

Page

LIST OF FIGURES

Figure Page

Figure Page

NOMENCLATURE

$\mathbf{A}$	plant matrix
$A_{ij},B_{ij},D_{ij},E_{ij},F_{ij},H_{ij}$	laminate stiffness matrices
a^r, b^r	lower and upper surfaces of r-th region
$\mathbf{B}$	control matrix
$\mathbf{B}^c$	matrix of elemental shape functions
$\mathbf{C}$	damping matrix
$\mathbf{C}$	observer matrix
c	midplane
c_{ijkl}	elastic coefficient tensor
C_k	capacitance of k-th ply
c^r, d^r	midplane and thickness of r-th region
$\mathbf{d}$	piezoelectric strain coefficient matrix
D_i	charge
d_{ijk}	piezoelectric strain coefficient tensor
$\mathbf{E}$	disturbance matrix
E_i	electric field
e_{ijk}	piezoelectric stress coefficient tensor
$\mathbf{F}$	forcing vector
f	frequency (Hz)
$\mathbf{G}$	matrix of z-dependence
g_j	constraint function vector
H	electric enthalpy density function
$\mathbf{H}$	sensor matrix
h	laminate thickness

i_k	current of k-th ply
$\mathbf{K}$	Stiffness matrix
k_{ij}	dielectric coefficient tensor
$\mathbf{L}$	derivative operator matrix
L	plate length
$\mathbf{M}$	mass matrix
NPLY	number of plies
N^e	elemental shape function
N_i, M_i, P_i	inplane forces, moments and higher order moments
$\mathbf{P}$	penalty matrix
P	average power
q	distributed load
$\mathbf{q}$	vector of modal participation factors
Q_{ij}	constitutive matrix
q_k	charge of k-th ply
$\tilde{\mathbf{R}}$,$\mathbf{R}_{ii}$,$\mathbf{R}_{ij}$,$\mathbf{R}_{jj}$,	matrix of geometric parameters
S	interface between nondebonded and debonded region
$\mathbf{T}$	coordinate transformation matrix
T	kinetic energy
t	time
U	strain energy
$\mathbf{u}$	vector of control outputs
U, V, W	displacement functions
U_o	strain energy density
V_k	applied voltage to k-th ply

$\mathbf{w}$	vector of displacements
x, y, z	global coordinate system
$\mathbf{y}$	vector of sensor inputs
$\mathbf{Z}$	modal damping matrix
Greek	
α^r, β^r, γ^r	geometric parameters for r-th region
δ	variational operator
ε_{ij}	strain tensor
Φ	modal matrix
Λ	modal frequency matrix
θ	ply angle
σ_{ij}	stress tensor
ω	frequency (radians/second)
Ω^r	r-th region
superscripts	
A	nonpiezoelectric term
div	divergence
flut	flutter
P	piezoelectric term
r	region (u,d1,d2,etc.)
subscripts	
B	bending/extension term
cp	cut-off frequency
e	element
k	k-th ply

T	transverse term
G	gust

1. Introduction

Structures by nature are subjected to static and dynamic forces which cause deformation. In the past, designers have compensated for undesirable deformation and vibration by adding stiffeners and passive devices which often introduce a significant weight penalty. The concept of smart structures has received a great deal of attention recently as an alternative to conventional techniques. These advanced structures can be designed to actively react to disturbance forces to maintain structural integrity while maintaining, or even improving, the level of performance. Although smart structures have enormous potential for an abundance of applications ranging from reducing helicopter noise (Anonymous; 1994), precision antenna positioning (Stevens; 1991), improving aeroelastic stability of fixed (Heeg; 1992) and rotory wing (Chandra and Chopra; 1993) aircraft, a number of basic issues still require further investigation. These issues include development of accurate, yet efficient, mathematical modeling techniques and experimental investigations. The primary focus of this dissertation is to address these key issues related to smart composite structures.

The exact definition of a smart structure is rather ambiguous and deserves some discussion. A smart structure does not necessarily posses any inherent "intelligence". For instance, the mechanical governor for a gasoline engine, which serves to automatically limit the speed of the engine, could be termed a smart structure. Although this device actively controls the operation of the engine, it is not really smart. Other useful devices have been invented in the past, such as the bimorph thermostat or the modern elevator, which could be termed smart structures. These structures actively respond to their surroundings, but do not posses any real intelligence. The term smart structures is a more generic term which is simply being used to describe the next generation of these devices aimed at enhancing functionality while reducing weight (Sirkis; 1996). A more precise definition has been suggested to characterize smart structures as load bearing structures with the ability to actively sense and react to its environment via onboard sensors, actuators and computational/control capabilities (Rogers; 1989). It must be noted that in the current literature, the terms smart, active, adaptive, metamorphic and intelligent are used interchangeably.

Integral components of these structures are smart materials. This class of materials can change their mechanical properties in response to an external stimuli. They can be used in sensing and/or actuation modes either independently, or as part of a larger system. Several different types of these materials exist, each with its own set of unique properties, and are described in the next section. Key issues associated with the development of smart structures, including mathematical modeling techniques, are discussed.

1.1 Smart Materials

Magnetostrictive and electrostrictive materials change shape when subjected to magnetic and electric fields, respectively. The most common magnetostrictive material is Terfenol-D which is capable of inducing strains up to 0.2%. It is named after its components terbium (TER), iron (FE), dysprosium (-D) and the place it was discovered, the Naval Ordinance Lab (NOL). Metglas is another magnetostrictive material. Although the maximum induced strain is much less, it can be manufactured as a foil for easy embedding in composites. An integrated actuation system for individual control of helicopter rotor blades using Terfenol-D actuators has been investigated by several researchers (Ghorayeb and Straub; 1995: Freidmann et al.; 1995). This class of smart materials have the advantage that wires connecting to the material directly are not necessary. However, the metal components used in these actuators result in a significant weight penalty. Other potential applications include torpedo control surfaces, gimballing cockpit simulators and vibration damping of optical benches (Card; 1992). Electrostrictive transducers have been used in a number of applications including adaptive optic systems, scanning tunneling microscopes and precision micropositioners. (Newnham and Ruschau; 1991). Both magnetostrictive and electrostrictive materials change shape in one direction only regardless of the polarity of the applied field. Therefore, a return mechanism needs to be implemented along with the materials themselves. This introduces additional complexities and restrictions on their potential for use as simple and light weight actuators.

Another class of smart materials is electrorheological (ER) fluids which are characterized by a considerable variation of their rheological properties when an electric field is applied (Winslow; 1949). In the absence of an electric field, the strain rate of ER fluids is directly proportional to the applied stress, much like typical Newtonian flow characteristics. When exposed to an electric field, the viscosity, damping capability and shear strength of these materials increase significantly. These properties can also be rapidly altered with the application or removal of an electric field. This makes ER fluids attractive for providing a rapid response interface in controlled mechanical devices (Carlson et al.; 1990). An active engine mount system has been proposed utilizing ER fluids (Card; 1992). In this application, the viscosity of the ER fluid is adjusted to change the natural frequency of the system away from the dominant frequency band during service. Advanced helicopter rotor systems, such as soft hingeless and bearingless rotors, are mechanically less complex than traditional articulated rotors. However, aeroelastic instabilities, such as air and ground resonance, have emerged as major problems in these rotor systems. ER fluid based dampers are a viable candidate for active damping and stability augmentation (Kamath and Wereley; 1995). Cable-stayed highway bridges must be flexible enough to avoid damage due to seismic activity, but not so flexible as to allow an adverse buffet response to a wind loading. Traffic loading which generates small deck vibrations is also a consideration. An ER fluid damper suitable for vibration and seismic protection of civil structures which addresses these considerations has been designed and tested (Makris et al.; 1995)

Shape memory alloys (SMA) are another type of smart material. SMAs such as Nitinol recover their previously undeformed shape upon heating (Funakubo; 1987). This is due to a change in the crystalline structure known as a reversible austenite to martensite phase transformation at a specific temperature. Large induced strains are possible and the Young's modulus increases by almost a factor of three. SMAs have been used in spacecraft antenna. A wire hemisphere of the material is crumpled into a tight ball. When heated above 77°C, the ball opens into its original shape of a fully formed antenna (Schetky; 1979). In another application, the fundamental frequency of a solid rectangular composite beam was altered by as much as 35% using a 1.3% volume fraction of SMA wires (Chandra; 1993). This concept was also exploited to design a variable speed helicopter rotor (Chopra; 1993). Solar collectors that are focused on a central receiver are designed with a mechanism for defocusing the collector or deactivating it by turning it out of the path of the sun's rays. This is required to avoid damaging the receiver during periods of inoperability. SMAs have been shown to exceed design specifications to actuate these solar arrays (Lobitz; 1995). Smart dental braces could also be made using SMAs (Newnham and Ruschau; 1991). Since SMAs are actuated by heat, the response time is quite slow. While electrical heating sources allow the material to respond within seconds, cooling often takes on the order of minutes. Although positioning and stiffening applications appear promising, SMAs are impractical as actuators for vibration control due to their slow response time.

Currently, piezoelectric materials are the most versatile smart materials. When a piezoelectric material is stressed mechanically by a force, it generates and electric charge. If the electrodes are not short circuited, a voltage associated with the charge appears. This is the direct effect discovered by Jacques and Pierre Curie in 1880. A year later, Gabriel Lippman predicted the converse effect which was verified by the Curies. The converse effect occurs when a piezoelectric material is stressed electrically by a voltage which results in a change in the material's dimensions (Encyclopedia Britannica; 1994). A piezoelectric element is therefore capable of being used as either a sensor or as an actuator when it is coupled to a composite substructure via surface bonding or embedding. The nature of the electric charge and the dimension change (positive or negative) depends on the polarity of the mechanical stress and the applied electric field, respectively. Consequently, bidirectional actuation and sensing are possible and no external return mechanism is necessary. This property of piezoelectric materials makes them distinct from electrostrictive materials which can only be actuated in one direction. Natural crystals, such as quartz, Rochelle salts, troumaline and lithium sulfate, were the first piezoelectric materials to be used. A quartz transmitter used for sonar applications appeared in 1916 (Mason; 1950). Early phonograph pickups were made from Rochelle salts. In the 1940s it was discovered that the ceramic material barium titanate could be induced to exhibit piezoelectric properties by exposing it to a high temperature and an electric field. Currently, most piezoelectric devices utilize a similar piezoceramic material, lead zirconate titanate (PZT), which was first used in the 1950s. The desirable properties of PZT include a high level of piezoelectric activity and a wide frequency range. Active flight control using PZT actuators has been explored by several researchers for both fixed wing aircraft (Lin and Crawley; 1995: Leeks and Weisshaar; 1995) and rotorcraft (Spangler and Hall; 1990: Ben-Zeev and Chopra; 1995). Active flutter suppression using PZTs has also been investigated (Heeg; 1992). Vibration control using PZTs has been studied extensively (Crawley and de Luis; 1987: Hanagud et al; 1992: Chandrashekhara and Agarwal; 1993). PZTs have also been used in the emerging field of MicroElectroMechanical Systems (MEMS) for building microactuators (Ikuta; 1992). A video tape head positioner has been developed based on a bimorph PZT actuator. The nonlinear properties of some materials allows for the creation of tunable transducers using bias fields or forces. For instance, rubber is a highly nonlinear elastic medium since the material stiffens noticeably under stress. A transducer can be constructed which consists of alternating layers of rubber and PZT. Under low stress bias, the piezoelectric layers dominate at the resonant frequency of the transducer. Under a high stress bias, the rubber stiffens and dominates at a different resonant frequency. Therefore, the transducer is tunable to a specific resonant frequency using a stress bias (Xu; 1990). Piezoceramic materials can also be used for sensing applications. Accelerometers are often constructed using PZTs. A PZT sensor has been proposed to monitor the rate of rain fall and adjusts automobile windshield wipers to the optimal speed (Taguchi; 1987). PZT sensors and actuators have also been investigated for use in smart automobile suspensions which improve drivability while enhancing passenger comfort (Tsuka and Nakomo; 1990: Thirupathi and Naganathan; 1992).

In 1969, it was discovered that the polymer Polyvinylidene Fluoride (PVDF) can also develop piezoelectric properties (Kawai; 1969). The polymeric piezoelectric material PVDF has a variety of actuation applications including vibration control (Bailey and Hubbard; 1985), artificial hands (Brei; 1994) and trailing edge flap actuation for rotorcraft (Seeley et al.; 1996). Although the compliant nature of PVDF often has certain advantages, it is not stiff enough to develop the force needed for most applications. Therefore, PVDF materials are more commonly used in sensing applications such as accelerometers (Andre et al.; 1992) and microphones (Garner; 1977: Sullivan and Powers; 1978). PZT actuation is more common than PVDF due to the larger forces that can be generated resulting from the higher stiffness.

1.2 Key Issues in Smart Structures

Induced strain actuation and sensing using piezoelectric materials offers significant advantages, such as weight savings, over other possible actuation and sensing mechanisms. Therefore, piezoelectric materials are used in this dissertation. Composite structures, which are becoming increasingly popular due to their light weight and innovative design possibilities offered by ply tailoring, can be very effective as elements of smart structures. Many of the smart structure applications for piezoelectric materials, including positioning, vibration control and aeroelastic response, involve the surface bonding or embedding of these materials in the primary composite substructure. Several key issues must be addressed for the efficient implementation of these smart composite structures. Perhaps the most important issue is the development of accurate mathematical tools for the analysis of surface bonded/embedded induced strain actuators in composite laminates (Chopra; 1996). The mathematical analysis technique must be general in nature, computationally efficient and be able to include debonding between the piezoelectric elements and the composite substructure. Experimental investigation is also necessary to validate the developed model. All of these issues are addressed in this dissertation.

1.2.1 Mathematical modeling and analysis: A key issue in the efficient implementation of these smart composite laminates is the development of practical mathematical modeling tools. There is a need for a general theory which is both accurate and computationally efficient and accounts for debonding at the piezoelectric actuator-composite substructure interface. A detailed review of the existing literature, including both analytical and finite element approaches, is described next.

Bernoulli-Euler beam analysis was used by Bailey and Hubbard (1985) to derive a distributed parameter control theory for active control of a cantilever beam. An uniform strain model was proposed by Crawley and deLuis (1987). They showed that a bonding layer between the piezoelectric actuator and the beam which is sufficiently thin and stiff becomes negligible. In a later work, Crawley and Anderson (1989) proved that the simple uniform strain model, which assumes a constant state of strain in the piezoelectric layers, is not accurate when the beam to actuator thickness ratio is less than five. They also discussed the nonlinear nature of piezoelectric materials at higher electric fields. The ability of piezoelectric actuators to produce bending and twist in a composite plate, both independently and simultaneously, was first investigated by Lee (1990) using classical laminate theory (CLT). His derivation of the governing equations for piezoelectric sensors and actuators, based on classical laminate theory, has been referred to in the literature by many different researchers. Wang and Rogers (1991) used Heaviside functions to model spatially discrete actuators embedded in composite laminates. Crawley and Lazarus (1991) presented an exact solution for a free isotropic plate. They also presented a Ritz solution for anisotropic plates with bonded actuators and more complex boundary conditions. Their mathematical model was based on classical laminate theory (CLT) and was verified experimentally. Classical approaches have also been extended to included transverse shear effects in anisotropic sandwich plates (Koconis et al.; 1994). All of the above analyses were based on the classical laminate theory which does not include transverse shear deformation and is therefore restricted to thin beam/plate applications. First order theory, also known as the Timoshenko theory for beams and the Midlin theory for plates, has been used to model composite structures with embedded piezoelectric actuators and sensors (Richard and Cudney; 1993: Tzou and Zhong; 1993). Although an improvement over classical theory, the first order shear deformation theory accounts for transverse shear deformation only in an average sense. Mitchell and Reddy (1995) recently presented a hybrid theory which more accurately accounts for the transverse shear strain. In their work, they also discuss the influence of the electric potential on a Navier type solution and show that it is important only in certain cases. The induced strain actuation problem for a beam was solved in closed form by Lin and Rogers (1993) by using approximations for the stress fields. The exact solution for a simply supported rectangular laminated composite plate, including piezoelectric actuation, has also been presented (Ray et al.; 1993). This work was based on an earlier elasticity solution of Pagano (1970). A power series solution was presented for composite cylinders with piezoelectric layers (Mitchell and Reddy; 1995). Other analytical investigations include the optimal design of embedded piezoelectric actuators (Kim and Jones; 1990) and increasing the authority of actuators through discrete attachment techniques (Chaudhry and Rogers; 1993). The aforementioned research using analytical approaches provides essential physical insight into problems involving piezoelectric sensing and actuation. However, it is very difficult to generalize these analytical solutions to practical problems with realistic shapes and boundary conditions.

The finite element method offers the flexibility to model many different types of structures with integrated piezoelectric materials and various boundary conditions. The majority of research using this approach has focused on using one and two dimensional beam and plate type approaches. Hanagud et al. (1992) and Hwang et al. (1993) developed finite element models using classical beam and plate theories, respectively. Viscoelastic effects have also been incorporated into a finite element model based on classical laminate theory (Shieh; 1993). These models are the least complex, but they do not account for transverse shear effects which are known to be important in the analysis of anisotropic composite laminates. They are also restricted to thin beams and plates. Finite element approaches based on first order shear deformation theory do account for transverse shear deformation, but only in an average sense. These approaches have been used by several researchers to model piezoelectric actuation of composite laminates (Shah et al; 1993: Detwiler et al.; 1995) and have been extended to investigate vibration control (Chandrashekhara and Agarwal; 1993). The crude approximation of the transverse shear strains in the theory requires the use of shear correction factors. Furthermore, the finite element implementation of the first order theory is susceptible to unwarranted complexity and/or large inaccuracies due to spurious stiffness effects depending on the choice of interpolation. A very accurate approach is the layerwise theory of Reddy (Robbins and Reddy; 1991) which has been used to model piezoelectrically actuated beams (Chandrashekhara and Donthireddy; 1996) and has also been extended to included thermoelastic effects (Lee and Saravanos; 1995). However, the computational effort depends on the number of plies and can become prohibitively expensive for thick laminates. A global/local approach, proposed by Robbins and Reddy (1993), uses the concept of finite element mesh superposition in which an independent overlay mesh is superimposed on a global mesh to provide localized refinement in regions of interest for a more economical analysis. Mitchell and Reddy (1995) have developed a refined hybrid theory to model piezoelectric actuation and sensing in composite laminates which would be appropriate to implement using the finite element method. A three dimensional approach has also been investigated (Ha et al; 1992). An important distinction in the above analyses must be made regarding the electric potential. Some approaches include the electric potential in the total energy potential (Detwiler et al; 1995: Ha et al. 1992). The not so typical case of a nonuniform electric field can be modeled using this approach at the expense of additional degrees of freedom which are required at each of the nodes leading to increased CPU time. By neglecting the electric potential (Hwang et al; 1993: Chandrashekhara and Agarwal; 1993; Seeley and Chattopadhyay, 1996), the extra degrees of freedom can be neglected resulting in significant computational savings while retaining the ability to accurately model most practical actuator/sensor configurations.

Relatively little attention in the literature has been paid to detailed modeling issues associated with adaptive composite structures, with surface bonded/embedded piezoelectric actuators and sensors, which include debonding. The global control capabilities of composite structures with piezoelectric sensing and actuation are a result of local stresses introduced by the piezoelectric actuators. However, the introduction of piezoelectric materials creates discontinuities which complicates the analysis of these smart composites. Debonding may also occur during the lifetime of the structure. In most of the existing work mentioned earlier, the actuators are assumed to be perfectly embedded or bonded to the primary structure . Therefore, issues associated with debonding of actuators is avoided. However, it has recently been shown by Seeley and Chattopadhyay (Seeley and Chattopadhyay; 1996) that the control authority of smart structures can be significantly mispredicted in the presence of debonding. The effects of these problems must be investigated. Although three dimensional approaches for modeling debonding in composite structures (Yang and He; 1994: Whitcomb; 1989) are more accurate than two dimensional theories (Pavier and Clarke; 1996: Whitcomb; 1981: Kardomateas and Schmueser; 1988: Gummadi and Hanagud; 1995), their implementation can be very expensive for practical applications. The layer-wise approach (Barbero and Reddy; 1991) is an alternative since it is capable of modeling displacement discontinuities. However, the computational effort increases with the number of plies. Recently, a refined higher order theory, developed by Chattopadhyay and Gu (1994), was shown to be both accurate and efficient for modeling delamination in composite plates and shells of moderately thick construction.. This theory has also been shown to agree well with both elasticity solutions (Chattopadhyay and Gu; 1996) and experimental results (Chattopadhyay and Gu; 1996).

For the analysis of arbitrarily thick composites with surface bonded or embedded piezoelectric actuators and sensors, it is important to have a more effective general theory than is currently available. It has long been recognized that higher order laminate theories provide an effective solution tool for accurately and efficiently predicting the deformation behavior of composites laminates subjected to bending loads. However, it is difficult to provide a consistent displacement field which accurately satisfies the stress free boundary conditions at the free surfaces while maintaining continuity of strains through the thickness. Modeling the debonding of the piezoelectric materials has not been adequately addressed in the literature. To investigate this issue, a general theory is developed for the analysis of smart composites including the presence of debonding. The developed theory is based on the general higher order theory of Reddy (1990) which was implemented using the finite element method by Bhimaraddi and Stevens (1984) and Ren and Hinton (1986). In this dissertation, the higher order theory is extended to model composites with arbitrary thicknesses including surface bonded or embedded piezoelectric actuators and sensors.

The current formulation also allows for both separation and slipping which are a result of debonding. The theory developed here, which is implemented using the finite element method, is expected to more effectively model the complex stress distributions found in smart composite laminates with a reasonable amount of computational effort.

1.2.2 Experimental research: Experiments are essential for validating mathematical models and for understanding practical aspects associated with the actual implementation of such structures. However, experimental studies of smart structures are reported less frequently in the literature than mathematical models. Bailey and Hubbard (1985) performed an experimental investigation to provide increased vibration damping of a flexible beam using a piezoelectric film (PVDF). Chopra et al. (1993: 1995: 1996) has performed several experiments involving piezoelectric actuation with application to rotorcraft. Crawley and Lazarus (1991) presented an experimental investigation of a cantilever composite plate utilizing piezoelectric actuation for static shape control. Torsion and bending of piezopolymer plates were experimentally demonstrated by Lee and Moon (1989). Experimental optimal control has been studied for a cantilever beam using piezoelectric sensors and actuators (Hanagud; 1992). Moiré interferometry was used to study the induced strains on a plate resulting from piezoelectric actuation (Mollenhauer and Griffen; 1994). This study concluded that numerical approaches can be used to accurately predict induced strains. Heeg (1992) experimentally investigated the improvement of aeroelastic stability for fixed wing aircraft using piezoelectric actuation. Debonding of smart composite laminates using piezoelectric actuation is an important issue. Yet, no experimental testing of composite laminates utilizing piezoelectric actuation with debonding has been reported in the literature. Therefore, this important topic is investigated in the current research.

2. Objectives

The objective of this research is to address important issues related to smart structures. First, a general theory is developed to model composite structures with surface bonded or embedded piezoelectric transducers used as both sensors and actuators for closed loop control. The theory accounts for the presence of debonding. Experiments are then performed to validate the developed theory.

The developed theory, which utilizes a refined higher order displacement field, accurately captures the transverse shear deformation through the thickness of the smart composite laminate while satisfying stress free boundary conditions on the free surfaces. The model is implemented using the finite element method to allow general laminate geometries and boundary conditions to be analyzed. The state space equations of motion are developed to allow insight into the design of the controls. The model is extended to incorporate the presence of debonding in the composite laminate at the interface between the piezoelectric actuators and the underlying substructure. The developed model is accurate, computationally efficient and is applicable to practical geometries.

Extensive correlation studies are presented to demonstrate the utility of the higher order theory to model smart composite laminates. Comparisons, including debonded laminates, are made with a general purpose finite element code and available experimental and analytical data. An experimental investigation addresses practical issues, such as circuit design and implementation, associated with piezoelectric sensing and actuation of composite laminates. Composite specimens with piezoelectric transducers were designed, constructed and tested to validate the higher order theory. The composite specimens were tested at various stacking sequences, debonding lengths and gains for both open and closed loop cases.

Following are the principal objectives of the proposed research.

1. Develop a new mathematical analysis technique using the higher order theory for modeling smart composite laminates with embedded/surface bonded piezoelectric actuators and sensors. The model is accurate, general in nature and computationally efficient. The equations of motion include piezoelectric sensing and actuation for controls design.

2. Extend the capabilities of the developed model to include debonded actuators.

3. Correlate the developed mathematical model with published analytical and experimental data and results using a general purpose finite element code.

4. Perform an experimental investigation to address practical issues such as smart composite laminate construction, implementation of the developed control law and vibration testing. Correlate the experimental results with the higher order theory.

3. Mathematical Model Development

A general theory is formulated to analyze composite laminates with piezoelectric sensing and actuation in this chapter. The theory is extended to account for debonding. When a piezoelectric element is stressed mechanically, it generates an electric charge. If the electrodes are not short circuited, a voltage associated with the charge appears. Conversely, when a piezoelectric element is stressed electrically by applying a voltage, its dimensions change. By incorporating piezoelectric materials into structures, they can be used as sensors and actuators to alter the static and dynamic response of the structure. The basis of the mathematical theory presented in this dissertation to investigate these "smart structures" is developed through the constitutive laws which govern piezoelectric materials and composite laminates. The constitutive laws are then implemented using the higher order laminate theory which is extended to account for debonding. The state space control equations are used to develop the control systems and the finite element method is used to implement the developed theory so that practical structures can be analyzed.

3.1 Piezoelectric and Laminate Constitutive Relations

The objective is to utilize the macroscopic properties of piezoelectric materials by integrating them as elements of smart composite structures for both sensing and actuation. To achieve this, it is first necessary to present the electro-mechanical constitutive relationships. These equations relate stress, strain, charge and electric field of a piezoelectric material. They are derived from the electric enthalpy density function as follows and were first formalized by Voigt (1928).

$$H(\varepsilon_{ij}, E_i) = \frac{1}{2} c_{ijkl}\varepsilon_{ij}\varepsilon_{kl} - e_{ijk}E_i\varepsilon_{jk} - \frac{1}{2} k_{ij}E_iE_j \qquad i,j,k,l = 1,2,3 \qquad (3.1.1)$$

where ε_{ij} and E_i are components of the strain tensor and electric field vector, respectively and c_{ijkl}, e_{ijk} and k_{ij} are the elastic, piezoelectric and dielectric permittivity constants, respectively. All material constants are assumed to be isagric (measured at constant electric field). It must be noted that repeated indices indicate summation. The charge and stress are determined as follows.

$$D_i = -\frac{\partial H}{\partial E_i} \tag{3.1.2}$$

$$\sigma_{ij} = \frac{\partial H}{\partial \varepsilon_{ij}} \tag{3.1.3}$$

It must be noted that there are only six unique values of the stress and strain tensors due to symmetry. Therefore, the following notation is used to define these quantities.

$$\begin{Bmatrix} \sigma_1 \\ \sigma_2 \\ \sigma_3 \\ \sigma_4 \\ \sigma_5 \\ \sigma_6 \end{Bmatrix} = \begin{Bmatrix} \sigma_{xx} \\ \sigma_{yy} \\ \sigma_{zz} \\ \sigma_{yz} \\ \sigma_{xz} \\ \sigma_{xy} \end{Bmatrix}, \quad \begin{Bmatrix} \varepsilon_1 \\ \varepsilon_2 \\ \varepsilon_3 \\ \varepsilon_4 \\ \varepsilon_5 \\ \varepsilon_6 \end{Bmatrix} = \begin{Bmatrix} \varepsilon_{xx} \\ \varepsilon_{yy} \\ \varepsilon_{zz} \\ 2\varepsilon_{yz} \\ 2\varepsilon_{xz} \\ 2\varepsilon_{xy} \end{Bmatrix} \tag{3.1.4}$$

where x, y and z correspond to the 1, 2 and 3 directions in the tensor relationships. Further details of the piezoelectric constitutive relationships are found in the following sections and in Appendix A.

3.1.1 Composite laminates: Consider a composite laminate which is constructed from layers of both orthotropic (transversely isotropic) and piezoelectric materials as shown in Fig 1.1. The piezoelectric coupling coefficients and the electric terms are set to zero for the nonpiezoelectric layers. Equation 3.1.2 is discarded and Eqn. 3.1.3 reduces to the familiar Hooke's law.

$$\hat{\sigma}_{i_k} = \mathbf{Q}_{ij_k}\hat{\varepsilon}_{j_k} \quad (i,j = 1,2,\cdots,6) \tag{3.1.5}$$

where $\hat{\sigma}_{i_k}$ are the stresses, $\hat{\varepsilon}_{j_k}$ are the strains and $\mathbf{Q}_{ij_k}$ are the elastic stiffness coefficients defined in the material coordinate system for the k-th layer. Stresses and strains in the global coordinate system for the k-th layer (σ_{i_k} and ε_{j_k}) are related as follows.

$$\sigma_{i_k} = \overline{\mathbf{Q}}_{ij_k} \varepsilon_{j_k} \quad (i, j = 1, 2, \cdots, 6) \tag{3.1.6}$$

where, in matrix form,

$$\overline{\mathbf{Q}}_k = \mathbf{T}_k^{-1} \mathbf{Q}_k \mathbf{T}_k \tag{3.1.7}$$

and

$$\mathbf{T}_k = \begin{bmatrix} m^2 & n^2 & 0 & 0 & 0 & 2mn \\ n^2 & m^2 & 0 & 0 & 0 & -2mn \\ 0 & 0 & 1 & 0 & 0 & 0 \\ 0 & 0 & 0 & m & -n & 0 \\ 0 & 0 & 0 & n & m & 0 \\ -mn & -mn & 0 & 0 & 0 & m^2 - n^2 \end{bmatrix} \tag{3.1.8}$$

where $m = \cos\theta_k$, $n = \sin\theta_k$ and θ_k is the angle of rotation about the Z axis between the global and material coordinate system for the k-th layer (Fig. 3.1). Furthermore, for orthotropic (transversely isotropic) plies, only five independent elastic coefficients remain and the transformed elastic stiffness matrix is as follows. The exact formulation of the elements of $\overline{\mathbf{Q}}_k$ are readily found in texts on composite materials (Vinson and Sierakowski; 1987: Agarwal and Broutman; 1990).

$$\overline{\mathbf{Q}}_k = \begin{bmatrix} \overline{Q}_{11} & \overline{Q}_{12} & 0 & 0 & 0 & \overline{Q}_{16} \\ \overline{Q}_{12} & \overline{Q}_{22} & 0 & 0 & 0 & \overline{Q}_{26} \\ 0 & 0 & 0 & 0 & 0 & 0 \\ 0 & 0 & 0 & \overline{Q}_{44} & \overline{Q}_{45} & 0 \\ 0 & 0 & 0 & \overline{Q}_{45} & \overline{Q}_{55} & 0 \\ \overline{Q}_{16} & \overline{Q}_{26} & 0 & 0 & 0 & \overline{Q}_{66} \end{bmatrix}_k \tag{3.1.9}$$

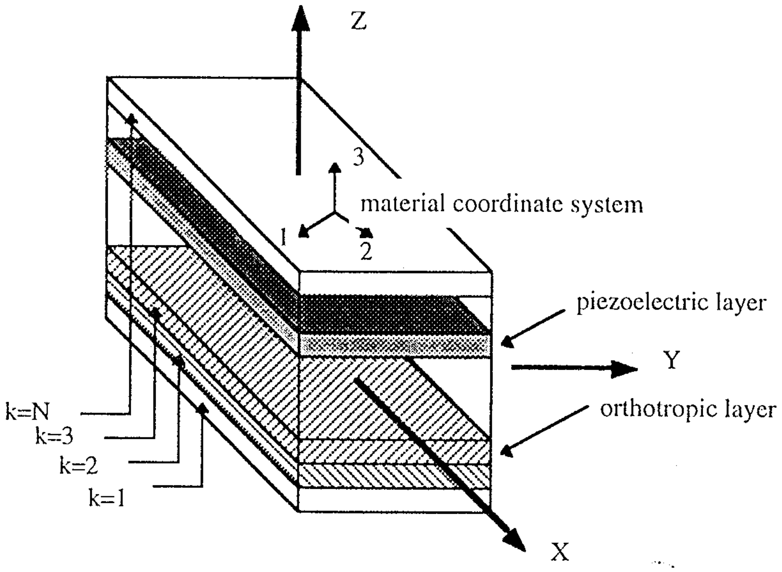

Fig. 3.1 Composite laminate with piezoelectric layer.

3.1.2 Piezoelectric materials': Now consider the plies introduced in to the composite laminate which posses piezoelectric properties. Differentiating Eqns. 3.1.2 and 3.1.3 and utilizing the symmetry of the stress and strain tensors as before yields the following expressions.

$$D_i = e_{ij}\varepsilon_j + k_{ik}E_k \quad i = 1,2,3 \tag{3.1.10}$$

$$\sigma_i = c_{ij}\varepsilon_j - e_{ki}E_k \quad i = 1,2,\cdots,6 \tag{3.1.11}$$

Using the relationship

$$e_{ij} = d_{ik}c_{kj} \quad i = 1,2,3 \quad j = 1,2,\cdots,6 \tag{3.1.12}$$

the above relationships are represented as follows.

$$D_i = d_{ij}c_{jk}\varepsilon_k + k_{im}E_m \quad i = 1,2,3 \tag{3.1.13}$$

$$\sigma_i = c_{ij}\varepsilon_j - c_{ik}d_{km}E_m \quad i = 1,2,\cdots,6 \tag{3.1.14}$$

The piezoelectric materials used in this work are assumed to be either PZT (piezoceramic) or PVDF (piezopolymeric). Both of these materials display orthorhombic mm2 symmetry for which the piezoelectric coefficients contained in d_{ij} (in matrix form) are as follows.

$$\mathbf{d} = \begin{bmatrix} 0 & 0 & 0 & 0 & d_{15} & 0 \\ 0 & 0 & 0 & d_{24} & 0 & 0 \\ d_{31} & d_{32} & d_{33} & 0 & 0 & d_{36} \end{bmatrix} \tag{3.1.15}$$

These piezoelectric materials are also isotropic in the context of laminate theory and are therefore independent of material orientation. Therefore, converting to matrix notation, Eqns.3.1.13 and 3.1.14 are written as follows.

$$\begin{bmatrix} D_1 \\ D_2 \\ D_3 \end{bmatrix}_k = \begin{bmatrix} 0 & 0 & d_{31} \\ 0 & 0 & d_{32} \\ 0 & 0 & d_{33} \\ 0 & d_{24} & 0 \\ d_{15} & 0 & 0 \\ 0 & 0 & d_{36} \end{bmatrix}^T \begin{bmatrix} \overline{Q}_{11} & \overline{Q}_{12} & 0 & 0 & 0 & 0 \\ \overline{Q}_{12} & \overline{Q}_{22} & 0 & 0 & 0 & 0 \\ 0 & 0 & 0 & 0 & 0 & 0 \\ 0 & 0 & 0 & \overline{Q}_{44} & 0 & 0 \\ 0 & 0 & 0 & 0 & \overline{Q}_{55} & 0 \\ 0 & 0 & 0 & 0 & 0 & \overline{Q}_{66} \end{bmatrix}_k \begin{bmatrix} \varepsilon_1 \\ \varepsilon_2 \\ \varepsilon_3 \\ \varepsilon_4 \\ \varepsilon_5 \\ \varepsilon_6 \end{bmatrix}_k + \begin{bmatrix} k_{11} & 0 & 0 \\ 0 & k_{22} & 0 \\ 0 & 0 & k_{33} \end{bmatrix}_k \begin{bmatrix} E_1 \\ E_2 \\ E_3 \end{bmatrix}_k \tag{3.1.16}$$

$$\begin{bmatrix} \sigma_1 \\ \sigma_2 \\ \sigma_3 \\ \sigma_4 \\ \sigma_5 \\ \sigma_6 \end{bmatrix}_k = \begin{bmatrix} \overline{Q}_{11} & \overline{Q}_{12} & 0 & 0 & 0 & 0 \\ \overline{Q}_{12} & \overline{Q}_{22} & 0 & 0 & 0 & 0 \\ 0 & 0 & 0 & 0 & 0 & 0 \\ 0 & 0 & 0 & \overline{Q}_{44} & 0 & 0 \\ 0 & 0 & 0 & 0 & \overline{Q}_{55} & 0 \\ 0 & 0 & 0 & 0 & 0 & \overline{Q}_{66} \end{bmatrix}_k \begin{bmatrix} \varepsilon_1 \\ \varepsilon_2 \\ \varepsilon_3 \\ \varepsilon_4 \\ \varepsilon_5 \\ \varepsilon_6 \end{bmatrix}_k - \begin{bmatrix} 0 & 0 & d_{31} \\ 0 & 0 & d_{32} \\ 0 & 0 & d_{33} \\ 0 & d_{24} & 0 \\ d_{15} & 0 & 0 \\ 0 & 0 & d_{36} \end{bmatrix}_k \begin{bmatrix} E_1 \\ E_2 \\ E_3 \end{bmatrix}_k \tag{3.1.17}$$

The above constitutive relationships are quite cumbersome in their general form. It is appropriate to simplify them in the context of the current research as follows. When a piezoelectric layer is used as a sensor, no electric field is applied (E_m=0). Furthermore, the charge of interest (D_3) is normally collected on electrodes located on the upper and lower surfaces of the piezoelectric layer while the charge in the in-plane directions are ignored due to the geometry of the piezoelectric layer as shown in Fig. 1.2. This charge (D_3), which is determined for the k-th ply from Eqn. 3.1.16, is now reduced to the following form.

$$D_{3_k} = \begin{bmatrix} d_{31} & d_{32} & 0 & 0 & 0 & d_{36} \end{bmatrix}_k \begin{bmatrix} \overline{Q}_{11} & \overline{Q}_{12} & 0 & 0 & 0 & 0 \\ \overline{Q}_{12} & \overline{Q}_{22} & 0 & 0 & 0 & 0 \\ 0 & 0 & 0 & 0 & 0 & 0 \\ 0 & 0 & 0 & \overline{Q}_{44} & 0 & 0 \\ 0 & 0 & 0 & 0 & \overline{Q}_{55} & 0 \\ 0 & 0 & 0 & 0 & 0 & \overline{Q}_{66} \end{bmatrix}_k \begin{bmatrix} \varepsilon_1 \\ \varepsilon_2 \\ \varepsilon_3 \\ \varepsilon_4 \\ \varepsilon_5 \\ \varepsilon_6 \end{bmatrix}_k \qquad (3.1.18)$$

The above equation represents the charge resulting from an applied force to the piezoelectric material and is referred to as the direct effect. A piezoelectric layer can also be used as an actuator. That is, an induced strain results from an applied electric field. Normally, the electric field is applied through the thickness of the piezoelectric layer used as an actuator and the constitutive relationship (Eqn. 3.1.18) is simplified as follows.

$$\begin{bmatrix} \sigma_1 \\ \sigma_2 \\ \sigma_3 \\ \sigma_4 \\ \sigma_5 \\ \sigma_6 \end{bmatrix}_k = \begin{bmatrix} \overline{Q}_{11} & \overline{Q}_{12} & 0 & 0 & 0 & 0 \\ \overline{Q}_{12} & \overline{Q}_{22} & 0 & 0 & 0 & 0 \\ 0 & 0 & 0 & 0 & 0 & 0 \\ 0 & 0 & 0 & \overline{Q}_{44} & 0 & 0 \\ 0 & 0 & 0 & 0 & \overline{Q}_{55} & 0 \\ 0 & 0 & 0 & 0 & 0 & \overline{Q}_{66} \end{bmatrix}_k \begin{bmatrix} \varepsilon_1 \\ \varepsilon_2 \\ \varepsilon_3 \\ \varepsilon_4 \\ \varepsilon_5 \\ \varepsilon_6 \end{bmatrix}_k - \begin{bmatrix} d_{31} \\ d_{32} \\ 0 \\ 0 \\ 0 \\ d_{36} \end{bmatrix}_k E_{3_k} \qquad (3.1.19)$$

This is known as the converse effect.

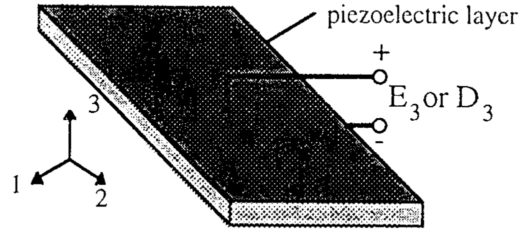

Fig. 3.2 Piezoelectric layer

3.2 Analytical Development

3.2.1 Higher order displacement field: The general higher order displacement field which describes deformation in the composite laminate is defined as follows.

$$\begin{aligned}
U(x,y,z) &= u(x,y) + (z-c)\left(-\frac{\partial}{\partial x}w(x,y) + \phi_x(x,y)\right) \\
&\quad + (z-c)^2 u_2(x,y) + (z-c)^3 u_3(x,y) \\
V(x,y,z) &= v(x,y) + (z-c)\left(-\frac{\partial}{\partial y}w(x,y) + \phi_y(x,y)\right) \\
&\quad + (z-c)^2 v_2(x,y) + (z-c)^3 v_3(x,y) \\
W(x,y,z) &= w(x,y)
\end{aligned} \tag{3.2.1}$$

where U, V and W are the total displacements (Fig 3.3), u, v and w denote the midplane displacements of a point (x,y), the partial derivatives of w represent the rotations of normals to the midplane corresponding to the slope of the laminate and ϕ_x and ϕ_y represent the additional rotations due to shear deformation about the y and x axes, respectively. The quantities u_2, u_3, v_2 and v_3 represent higher order functions. The thickness coordinate, z, is measured from the global midplane of the laminate and c is the local midplane where c = 0 for a laminate with no debonding present. This displacement field has the advantage of easily reducing to the well known classical theory if the higher order terms are eliminated. This particular form of the displacement field has desirable properties for the finite element implementation as discussed in Appendix B. In the current work, assuming that displacements and rotations are small, a linear relationship for the kinematic equations is used.

$$\begin{aligned}
&\varepsilon_1 = \frac{\partial U}{\partial x}, \quad \varepsilon_2 = \frac{\partial V}{\partial y}, \quad \varepsilon_3 = 0 \\
&\varepsilon_4 = \frac{\partial V}{\partial z} + \frac{\partial W}{\partial y}, \quad \varepsilon_5 = \frac{\partial U}{\partial z} + \frac{\partial W}{\partial x}, \quad \varepsilon_6 = \frac{\partial U}{\partial y} + \frac{\partial V}{\partial x}
\end{aligned} \tag{3.2.2}$$

where ε_1-ε_6 represent the linear strains as before.

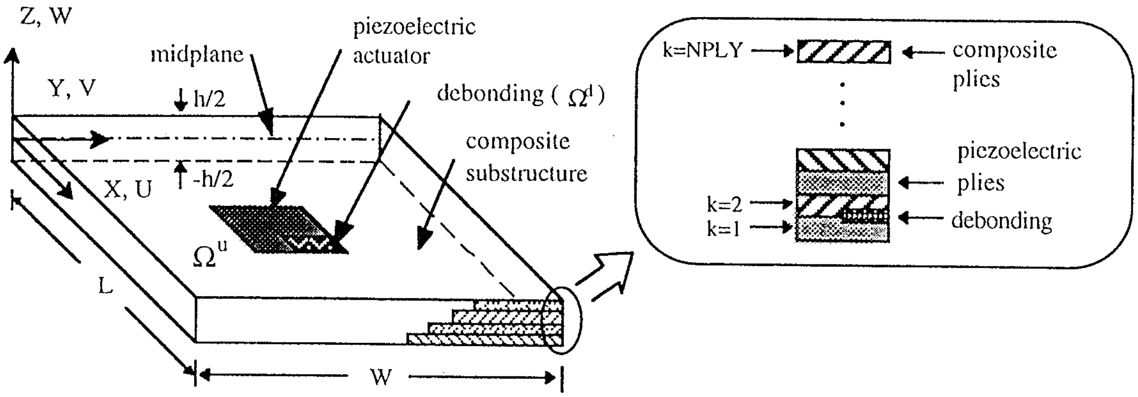

Fig. 3.3 Smart composite plate incorporating piezoelectric layers.

In the general form presented above, the higher order displacement field does not necessarily satisfy the requirement that the transverse shear stresses vanish on the free surfaces of the laminate. In addition, the displacements in the portion of the laminate where a debonding is assumed to be pre-existing must be independent to account for the slipping and separation which occurs at the debonding. These concepts are addressed in the next section.

3.2.2 Refined displacement fields to incorporate debonding: Consider the cross section of a debonded smart composite shown in Fig. 3.4. The entire structure is divided into three regions (Fig. 3.4b) including the nondebonded region $\left(\Omega^u\right)$, the region above the debonding $\left(\Omega^{d1}\right)$ and the region below the debonding $\left(\Omega^{d2}\right)$. An interface region (S) is also defined where the nondebonded region $\left(\Omega^u\right)$ and the debonded regions $\left(\Omega^{d1},\Omega^{d2}\right)$ are joined. The presence of debonding requires that the transverse shear stresses, σ_4 and σ_5, vanish not only on the plate top and bottom surfaces, but on the debonded surfaces in the debonded region as well. That is,

$$\begin{aligned} &\sigma_4\left(x,y,a^r\right)=0, \quad \sigma_4\left(x,y,b^r\right)=0 \qquad (x,y)\in\Omega^r \quad (r=u,d1,d2) \\ &\sigma_5\left(x,y,a^r\right)=0, \quad \sigma_5\left(x,y,b^r\right)=0 \qquad (x,y)\in\Omega^r \quad (r=u,d1,d2) \end{aligned} \tag{3.2.3}$$

where

$$\begin{Bmatrix} a^r \\ b^r \end{Bmatrix} = \begin{Bmatrix} h/2 \\ -h/2 \end{Bmatrix}, \quad (x,y) \in \Omega^r, \quad r = u \text{ (nondebonded region)}$$

$$\begin{Bmatrix} a^r \\ b^r \end{Bmatrix} = \begin{Bmatrix} h/2 \\ h_1 \end{Bmatrix}, \quad (x,y) \in \Omega^r \quad r = d1 \text{ (above debonding)} \qquad (3.2.4\text{ a-c})$$

$$\begin{Bmatrix} a^r \\ b^r \end{Bmatrix} = \begin{Bmatrix} h_1 \\ -h/2 \end{Bmatrix}, \quad (x,y) \in \Omega^r \quad r = d2 \text{ (below debonding)}$$

For orthotropic plates, these conditions are equivalent to the requirement that the corresponding strains be zero on these surfaces. Therefore,

$$\begin{aligned} &\varepsilon_4(x,y,a^r) = 0, \quad \varepsilon_4(x,y,b^r) = 0 \quad (x,y) \in \Omega^r \quad (r = u, d1, d2) \\ &\varepsilon_5(x,y,a^r) = 0, \quad \varepsilon_5(x,y,b^r) = 0 \quad (x,y) \in \Omega^r \quad (r = u, d1, d2) \end{aligned} \qquad (3.2.5)$$

Three independent refined displacement fields are obtained by applying these boundary conditions for each region $(\Omega^r, \quad r = u, d1, d2)$ which allows several of the higher order functions to be identified in terms of the lower order functions as follows.

$$\begin{aligned} U^r &= u^r + (z - c^r)\left(-\frac{\partial w^r}{\partial x} + \phi_x^r\right) - (z - c^r)^3 \frac{4}{3(d^r)^2}\phi_x^r \\ V^r &= v^r + (z - c^r)\left(-\frac{\partial w^r}{\partial y} + \phi_y^r\right) - (z - c^r)^3 \frac{4}{3(d^r)^2}\phi_y^r \qquad (r = u, d1, d2) \qquad (3.2.6) \\ W^r &= w^r \end{aligned}$$

where $c^r = \frac{(a^r + b^r)}{2}$ is the local midplane and $d^r = b^r - a^r$ is the thickness of the region as shown in Fig. 3.5.

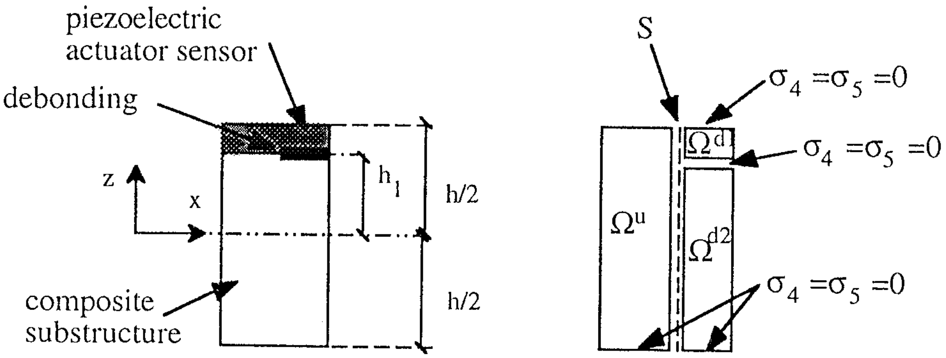

(a) (b)

Fig. 3.4 Smart composite cross section including debonding.

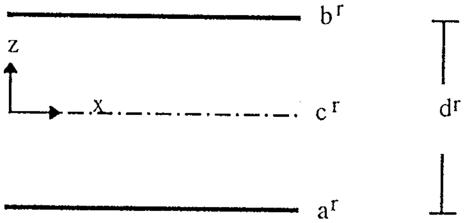

Fig. 3.5 Local region plate geometry.

<u>3.2.3 Continuity conditions</u>: Additional boundary conditions must be imposed to ensure continuity of displacements at the interface of the nondebonded and debonded regions (S) shown in Fig. 3.6. A vector of the displacements is constructed to simplify formulation of the boundary conditions as follows.

$$\mathbf{U}^r = \begin{bmatrix} U^r \\ V^r \\ W^r \end{bmatrix} \qquad (r = u, d1, d2) \tag{3.2.7}$$

The continuity conditions at the interface of the nondebonded and debonded regions (S), are imposed as follows.

$$\mathbf{U}^u = \mathbf{U}^{d1} \quad a^{d1} < z \leq \min\left(b^u, b^{d1}\right) \qquad (x, y) \in S \tag{3.2.8}$$

$$\mathbf{U}^u = \mathbf{U}^{d2} \quad \max\left(a^u, a^{d2}\right) < z \leq b^{d2} \qquad (x, y) \in S \tag{3.2.9}$$

The above equations can be satisfied exactly for the classical theory since the displacement distribution through the thickness is linear. However, the displacement distribution using the refined theory is nonlinear and must be satisfied in an average sense as follows. An error function vector for the first of the above equations is formulated as follows.

$$\mathbf{e} = \mathbf{U}^{u} - \mathbf{U}^{d1} \quad a^{d1} < z \leq \min\left(b^{d1}, b^{d2}\right) \qquad (x,y) \in S \tag{3.2.10}$$

where a and b are the limits of the interval given in Eqn. 3.2.4 a-c. It is desired to minimize the difference between $\mathbf{U}^{u}$ and $\mathbf{U}^{d1}$ at each point through the thickness in S. This can be accomplished by first integrating the square of the error through the thickness as follows.

$$E = \frac{1}{2}\int_{a}^{b}\left(\mathbf{e}^{T}\mathbf{e}\right)dz \tag{3.2.11}$$

where a and b define the limits of integration through the thickness as indicated in the interval given in Eqn. 3.2.4 (b). These integration limits must be considered carefully since the presence of surface bonded actuators/sensors may change the dimensions of the laminate in any of the regions. It is desired to find a relationship between the independent displacement functions in Ω^{d1} and Ω^{d2} which minimizes the error in terms of the displacement functions in the nondebonded region to satisfy the continuity conditions. Therefore, derivatives of E are taken with respect to the independent functions in Ω^{d1} and are set to zero as follows.

$$\frac{\partial E}{\partial u^{d1}} = \frac{\partial E}{\partial v^{d1}} = \frac{\partial E}{\partial w^{d1}} = 0$$

$$\frac{\partial E}{\partial\left(\frac{\partial w^{d1}}{\partial x}\right)} = \frac{\partial E}{\partial\left(\frac{\partial w^{d1}}{\partial y}\right)} = 0 \tag{3.2.12}$$

$$\frac{\partial E}{\partial \phi_x^{d1}} = \frac{\partial E}{\partial \phi_y^{d1}} = 0$$

Taking derivatives and rearranging the above equations lead to the following relationships which satisfy the continuity conditions.

$$\begin{gathered}
u^r = u^u + \left(c^u - c^r\right)\frac{\partial w^u}{\partial x} + \alpha^r \phi_x^u \\
v^r = v^u + \left(c^u - c^r\right)\frac{\partial w^u}{\partial y} + \alpha^r \phi_y^u \\
w^r = w^u \\
\frac{\partial w^r}{\partial x} = \frac{\partial w^u}{\partial x} + \beta^r \phi_x^u \\
\frac{\partial w^r}{\partial y} = \frac{\partial w^u}{\partial y} + \beta^r \phi_y^u \\
\phi_x^r = \gamma^r \phi_x^u \\
\phi_y^r = \gamma^r \phi_y^u
\end{gathered} \tag{3.2.13 a-g}$$

where r=d1 and the above relationships correspond to regions Ω^u and Ω^{d1}. The constants α^r, β^r and γ^r are as follows.

$$\alpha^r = (- 4a^4 - 36a^3b - 60a^2b^2 - 36ab^3 - 4b^4 + 36a^2(c^u)^2 + 68ab(c^u)^2 + 36b^2(c^u)^2 + 52a^3c^r + 228a^2bc^r + 228ab^2c^r + 52b^3c^r - 72a^2c^uc^r - 136abc^uc^r - 72b^2c^uc^r - 140a(c^u)^2c^r - 140b(c^u)^2c^r - 156a^2(c^r)^2 - 388ab(c^r)^2 - 156b^2(c^r)^2 + 280ac^u(c^r)^2 + 280bc^u(c^r)^2 + 140(c^u)^2(c^r)^2 + 140a(c^r)^3 + 140b(c^r)^3 - 280c^u(c^r)^3 - 27a^2(d^u)^2 - 51ab(d^u)^2 - 27b^2(d^u)^2 + 105ac^r(d^u)^2 + 105bc^r(d^u)^2 - 105(c^r)^2(d^u)^2)/(3(9a^2 + 17ab + 9b^2 - 35ac^r - 35bc^r + 35(c^r)^2)(d^u)^2)$$

$$\beta^r = (18a^2 + 34ab + 18b^2 - 35ac^u - 35bc^u - 35ac^r - 35bc^r + 70c^uc^r)(d^r)^2/(2(9a^2 + 17ab + 9b^2 - 35ac^r - 35bc^r + 35(c^r)^2)(d^u)^2)$$

$$\gamma^r = (- 30a^3c^u - 110a^2bc^u - 110ab^2c^u - 30b^3c^u + 72a^2c^{u2} + 136ab(c^u)^2 + 72b^2(c^u)^2 + 30a^3c^r + 110a^2bc^r + 110ab^2c^r + 30b^3c^r + 56a^2c^uc^r + 168abc^uc^r + 56b^2c^uc^r - 280a(c^u)^2c^r - 280b(c^u)^2c^r - 128a^2(c^r)^2 - 304ab(c^r)^2 - 128b^2(c^r)^2 + 140ac^u(c^r)^2 + 140bc^u(c^r)^2 + 280(c^u)^2(c^r)^2 + 140a(c^r)^3 + 140b(c^r)^3 - 280c^u(c^r)^3 - 18a^2(d^u)^2 - 34ab(d^u)^2 - 18b^2(d^u)^2 + 70ac^r(d^u)^2 + 70bc^r(d^u)^2 - 70c^{r2}(d^u)^2 + 18a^2(d^r)^2 + 34ab(d^r)^2 +$$

$$18b^2(d^r)^2 - 35ac^u(d^r)^2 - 35bc^u(d^r)^2 - 35ac^r(d^r)^2 - 35bc^r(d^r)^2 + 70c^uc^r(d^r)^2)/(2(9a^2 + 17ab + 9b^2 - 35ac^r - 35bc^r + 35(c^r)^2)(d^u)^2) \quad \text{(3.2.14 a-c)}$$

where r=d1. Identical expressions corresponding to regions Ω^u and Ω^{d2} are similarly formulated by setting r = d2 in Eqns. 3.2.13(a-g) It is also required that continuity of velocities be maintained between Ω^u and Ω^{d2}. These conditions are obtained by simply differentiating Eqns 3.2.13 (a-g) with respect to time. Since the formulation for the geometric parameters is independent of time, they remain unchanged. Multiple debondings can be easily be incorporated into the developed theory by defining additional regions of debonding at arbitrary locations in the laminate.

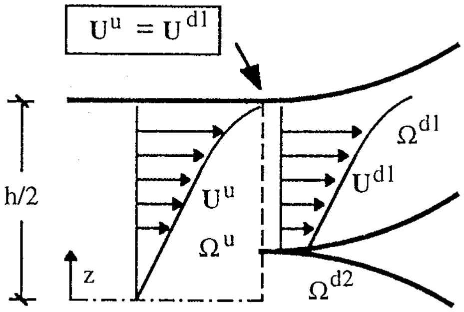

Fig. 3.6 Displacement distribution in cross section.

3.3 Laminate Stress Resultants

The laminate stress resultants, which include effects due to piezoelectric actuation, are formulated by integrating the stresses through the thickness as follows.

$$N_i = \int_{-h/2}^{h/2} \sigma_i dz, \quad M_i = \int_{-h/2}^{h/2} z\sigma_i dz, \quad P_i = \int_{-h/2}^{h/2} z^3\sigma_i dz \qquad (i = 1,2,6) \qquad (3.3.1)$$

$$(Q_1, Q_2) = \int_{-h/2}^{h/2} (\sigma_5, \sigma_4) dz, \qquad (R_1, R_2) = \int_{-h/2}^{h/2} (\sigma_5, \sigma_4) z^2 dz \qquad (3.3.2)$$

The first three of the above terms (N_i, M_i and P_i) are the in-plane terms which are decomposed into two components as follows.

$$N_i = N_i^A - N_i^P$$

$$M_i = M_i^A - M_i^P \quad (i = 1,2,6) \qquad (3.3.3\text{ a-c})$$

$$P_i = P_i^A - P_i^P$$

The first terms on the right hand sides of the above equations (superscript "A") represent the resultants from the actual strain field while the second terms (superscript "P") represent the resultants from the piezoelectric actuation. These in-plane terms, as well as the transverse shear terms (Q_i, R_i i=1,2) are the laminate stress resultants and are discussed in the following sections.

3.3.1 Non-piezoelectric stress resultants: It is worthwhile to write the terms from the actual strain field in terms of the elastic constants and strains as follows.

$$\left(N_i^A, M_i^A, P_i^A,\right) = \int_{-h/2}^{h/2} \left(1, z, z^3\right) \overline{Q}_{ij} \varepsilon_j dz \quad (i, j = 1,2,6) \qquad (3.3.4)$$

where $\overline{Q}_{ij}$ contains the elastic constants and the strains, ε_j, are defined in Eqn. 3.2.2. Since the material properties may differ between plies, it is necessary to replace the continuous integrals in the above equation by the summation of integrals representing the contribution of each layer as follows.

$$\left(N_i^A, M_i^A, P_i^A,\right) = \sum_{k=1}^{N} \left\{ \int_{h_{k-1}}^{h_k} \left(1, z, z^3\right) \overline{Q}_{ij_k} \varepsilon_j dz \right\} \quad (i, j = 1,2,6) \qquad (3.3.5)$$

It is convenient to write the in-plane strains in terms of their respective midplane strains and curvatures as follows.

$$\varepsilon_1 = \varepsilon_1^0 + z\kappa_1^0 + z^3\kappa_1^2$$

$$\varepsilon_2 = \varepsilon_2^0 + z\kappa_2^0 + z^3\kappa_2^2 \qquad (3.3.6\text{ a-c})$$

$$\varepsilon_6 = \varepsilon_6^0 + z\kappa_6^0 + z^3\kappa_6^2$$

where

$$\varepsilon_1^0 = \frac{\partial u}{\partial x}, \quad \kappa_1^0 = \frac{\partial \phi_x}{\partial x} - \frac{\partial^2 w}{\partial x^2}, \quad \kappa_1^2 = -\frac{4}{3h^2}\frac{\partial \phi_x}{\partial x}$$

$$\varepsilon_2^0 = \frac{\partial v}{\partial y}, \quad \kappa_2^0 = \frac{\partial \phi_y}{\partial y} - \frac{\partial^2 w}{\partial y^2}, \quad \kappa_2^2 = -\frac{4}{3h^2}\frac{\partial \phi_y}{\partial y} \tag{3.3.7}$$

$$\varepsilon_6^0 = \frac{\partial u}{\partial y} + \frac{\partial v}{\partial x}, \quad \kappa_6^0 = \frac{\partial \phi_x}{\partial y} + \frac{\partial \phi_y}{\partial x} - 2\frac{\partial^2 w}{\partial x \partial y}, \quad \kappa_6^2 = \frac{4}{3h^2}\left(\frac{\partial \phi_x}{\partial y} + \frac{\partial \phi_y}{\partial x}\right)$$

The summation and integration in Eqn. 3.3.5 can now be carried out, allowing it to be written in matrix form as follows.

$$\mathbf{N}_B = \mathbf{A}_B \varepsilon_B \tag{3.3.8}$$

where

$$\mathbf{N}_B = \begin{bmatrix} N_i^A & M_i^A & P_i^A \end{bmatrix}^T \qquad (i = 1,2,6) \tag{3.3.9}$$

The quantity $\mathbf{A}_B$ is the laminate stiffness matrix and ε_B is the generalized strain vector. The laminate stiffness matrix is obtained by integrating the elastic constants through the thickness of the laminate, ply by ply and summing the result as follows.

$$\mathbf{A}_B = \begin{bmatrix} [A_{ij}] & [B_{ij}] & [E_{ij}] \\ & [D_{ij}] & [F_{ij}] \\ \text{sym} & & [H_{ij}] \end{bmatrix} \quad (i,j = 1,2,6) \tag{3.3.10}$$

where

$$(A_{ij}, B_{ij}, D_{ij}, E_{ij}, F_{ij}, H_{ij},) = \sum_{k=1}^{N} \left\{ \int_{h_{k-1}}^{h_k} \overline{Q}_{ij}(1, z, z^2, z^3, z^4, z^6) dz \right\} \quad (i,j = 1,2,6) \tag{3.3.11}$$

The generalized strain vector, ε_B, is formulated using the definitions in Eqns. 3.3.7 as follows

$$\varepsilon_B = \left[\varepsilon_i^o \quad \kappa_i^o \quad \kappa_i^2\right]^T \qquad (i = 1,2,6) \tag{3.3.12}$$

Notice that the z-dependence is eliminated from the generalized strains by shifting this dependence to the formulation of the laminate stiffness matrix.

The quantities Q_i and R_i (i=1,2) arise due to transverse shear which is present in the laminate and are accounted for by using the higher order laminate theory. As before, these stress resultants are written in terms of the elastic constants and strains as follows.

$$(Q_1, R_1) = \int_{-h/2}^{h/2} \left(1, z^2\right)\left\{\overline{Q}_{54}\varepsilon_4 + \overline{Q}_{55}\varepsilon_5\right\}dz \tag{3.3.13}$$

$$(Q_2, R_2) = \int_{-h/2}^{h/2} \left(1, z^2\right)\left\{\overline{Q}_{44}\varepsilon_4 + \overline{Q}_{45}\varepsilon_5\right\}dz \tag{3.3.14}$$

where $\overline{Q}_{ij}$ contains the elastic constants and the transverse shear strains, $\varepsilon_{4,5}$, are defined in Eqn. 3.2.2. Since the material properties may differ between plies, it is again necessary to replace the continuous integrals in the above equation by the summation of integrals representing the contribution of each layer as follows.

$$(Q_1, R_1) = \sum_{k=1}^{N} \left\{ \int_{h_{k-1}}^{h_k} \left(1, z^2\right)\left\{\overline{Q}_{54}\varepsilon_4 + \overline{Q}_{55}\varepsilon_5\right\}dz \right\} \tag{3.3.15}$$

$$(Q_2, R_2) = \sum_{k=1}^{N} \left\{ \int_{h_{k-1}}^{h_k} \left(1, z^2\right)\left\{\overline{Q}_{44}\varepsilon_4 + \overline{Q}_{45}\varepsilon_5\right\}dz \right\} \tag{3.3.16}$$

The transverse strains are also represented by their respective midplane strains and curvatures.

$$\varepsilon_4 = \varepsilon_4^0 + z^2\kappa_4^2$$

$$\varepsilon_5 = \varepsilon_5^0 + z^2\kappa_5^2 \qquad (3.3.17\text{ a-b})$$

and

$$\varepsilon_4^0 = u_{21}, \quad \varepsilon_5^0 = u_{11}, \quad \kappa_4^2 = -\frac{4}{h^2}u_{21}, \quad \kappa_5^2 = -\frac{4}{h^2}u_{11} \qquad (3.3.18)$$

This allows the transverse stress resultants to be written in matrix form as follows.

$$\mathbf{N}_T = \mathbf{A}_T\varepsilon_T \qquad (3.3.19)$$

where

$$\mathbf{N}_T = [Q_i \quad R_i]^T \qquad (i = 1,2) \qquad (3.3.20)$$

The laminate stiffness matrix $\mathbf{A}_T$ is written as follows.

$$\mathbf{A}_T = \begin{bmatrix} [A_{ij}] & [D_{ij}] \\ \text{sym} & [F_{ij}] \end{bmatrix} \qquad (i,j = 4,5) \qquad (3.3.21)$$

where

$$(A_{ij}, D_{ij}, F_{ij}) = \sum_{k=1}^{N} \left\{ \int_{h_{k-1}}^{h_k} \overline{Q}_{ij}(1, z^2, z^4)dz \right\} \qquad (i,j = 4,5) \qquad (3.3.22)$$

The generalized transverse strain vector is written as follows.

$$\varepsilon_T = [\varepsilon_i^0 \quad \kappa_i^2]^T \qquad (i = 4,5) \qquad (3.3.23)$$

where the definitions for the midplane strains and curvatures are given in Eqns. 3.3.18.

3.3.2 Piezoelectric stress resultants: The second terms in Eqns. 3.3.3 a-c represent the resultant forces due to piezoelectric actuation and are discussed next. First, these resultants are represented in terms of the elastic constants, piezoelectric constants and applied electric field as follows.

$$\left(N_i^P, M_i^P, P_i^P,\right) = \int_{-h/2}^{h/2} \left(1, z, z^3\right) \overline{Q}_{ij} \Lambda_j dz \quad (i, j = 1, 2, 6) \tag{3.3.24}$$

where $\overline{Q}_{ij}$ contains the elastic constants and Λ_j are the induced strains due to piezoelectric actuation. Since the material, piezoelectric and electric properties may differ from ply to ply, it is necessary to integrate ply by ply and sum the contributions of each ply as before.

$$\left(N_i^P, M_i^P, P_i^P,\right) = \sum_{k=1}^{N} \left\{ \int_{h_{k-1}}^{h_k} \left(1, z, z^3\right) \overline{Q}_{ij_k} d_{j_k} E_{3_k} dz \right\} \quad (i, j = 1, 2, 6) \tag{3.3.25}$$

where the piezoelectric constants in the k-th layer are nonzero only for the piezoelectric plies energized with electric field E_{3_k} and expressed as follows.

$$d_{j_k} = \left[d_{31} \quad d_{32} \quad 0 \quad 0 \quad 0 \quad d_{36}\right]_k^T \tag{3.3.26}$$

It is convenient to express Eqn. 3.3.25 in terms of the applied voltage rather than the electric field using the following relationship.

$$E_{3_k} = \frac{V_k}{\left(h_k - h_{k-1}\right)} \tag{3.3.27}$$

Substituting the above expression for the electric field, Eqn. 3.3.25, can be written in matrix form as follows.

$$N^P = \begin{bmatrix} N_i^P \\ M_i^P \\ P_i^P \end{bmatrix} = \begin{bmatrix} \sum_{k=1}^{N} \left\{ \int_{h_{k-1}}^{h_k} \frac{V_k}{\left(h_k - h_{k-1}\right)} \overline{Q}_{ij_k} d_{j_k} dz \right\} \\ \sum_{k=1}^{N} \left\{ \int_{h_{k-1}}^{h_k} z \frac{V_k}{\left(h_k - h_{k-1}\right)} \overline{Q}_{ij_k} d_{j_k} dz \right\} \\ \sum_{k=1}^{N} \left\{ \int_{h_{k-1}}^{h_k} z^3 \frac{V_k}{\left(h_k - h_{k-1}\right)} \overline{Q}_{ij_k} d_{j_k} dz \right\} \end{bmatrix} \quad (i, j = 1, 2, 6) \tag{3.3.28}$$

It is not practical to present Eqn. 3.3.29 in a compact matrix form for the general case. It must also be noted that the terms in Eqn. 3.3.28 are nonzero only for energized piezoelectric layers.

In realistic applications, piezoelectric layers are often implemented in symmetric pairs (Fig. 3.7). Simplification of Eqn. 3.29 is possible if the magnitude of the electric field applied to each piezoelectric layer is the same. Consider the common case where a symmetric pair of piezoelectric actuators are implemented and both the magnitude and the sign of the applied electric field (E_3) is the same for each actuator (Fig. 3.7a). This is known as a unimorph configuration and results in an in-plane force in symmetric laminates. Eqn. 3.3.28 is then simplified as follows.

$$\mathbf{N}^P = \begin{bmatrix} \left[N_i^P\right] \\ \left[M_i^P\right] \\ \left[P_i^P\right] \end{bmatrix} = \begin{bmatrix} \left[A_{ij}^P\right] & 0 & 0 \\ 0 & 0 & 0 \\ 0 & 0 & 0 \end{bmatrix} \Lambda \quad (i,j=1,2,6) \tag{3.3.29}$$

where

$$A_{ij}^P = \sum_{k=1}^{N} \left\{ \int_{h_{k-1}}^{h_k} \overline{Q}_{ij} dz \right\} \quad (i,j=1,2,6) \tag{3.3.30}$$

The integration in the above equation is carried out only over the piezoelectric layers. The induced strain due to the piezoelectric actuation is as follows.

$$\Lambda = \begin{bmatrix} d_{31} & d_{31} & 0 & 0 & 0 & 0 & 0 & 0 & 0 \end{bmatrix}^T E_3 \tag{3.3.31}$$

Bending moments are produced if one of the symmetric pair of actuators is energized with an equal, but opposite, electric field from the other (Fig. 3.7b). This case is termed a bimorph configuration and Eqn. 3.3.28 simplifies to the following.

$$\mathbf{N}^P = \begin{bmatrix} \left[N_i^P\right] \\ \left[M_i^P\right] \\ \left[P_i^P\right] \end{bmatrix} = \begin{bmatrix} 0 & 0 & 0 \\ \left[D_{ij}^P\right] & & 0 \\ \left[H_{ij}^P\right] & 0 & \end{bmatrix} \Lambda \quad (i,j=1,2,6) \tag{3.3.32}$$

where

$$\left(D^{P}_{ij}, H^{P}_{ij}\right) = \sum_{k=1}^{N} \left\{ \int_{h_{k-1}}^{h_k} \left(z, z^3\right)\overline{Q}_{ij}\,dz \right\} \quad (i,j = 1,2,6) \tag{3.3.33}$$

Again, the integration is carried out only through the piezoelectric layers and Λ is identical to Eqn. 3.3.31. It is helpful to note that the voltage, which must be applied to a piezoelectric layer to obtain a specified electric field, is calculated as follows

$$V = E_3 t \tag{3.3.34}$$

where V is the voltage and t is the thickness of the piezoelectric layer.

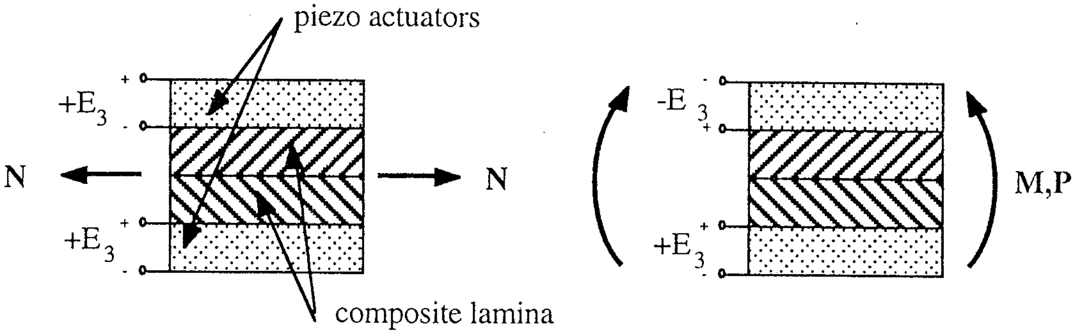

(a) (b)

Fig.3.7 Piezoelectric actuator configuration; (a) unimorph and (b) bimorph.

3.4 Piezoelectric Sensors

Piezoelectric layers are also used as sensors in the current research to detect the strain and rate of strain in the host structure. The procedure used to develop the piezoelectric sensor equations is based on work presented by Lee (1990) and used by Chandrashekhara and Agarwal (1993). It is extended here for use with the higher order laminate theory.

3.4.1 Sensor relations: When a piezoelectric layer is used as a sensor, a charge appears in response to the mechanical load. Only the charge in the thickness, or 3, direction (Fig.

3.2) is of interest. The relationship for this direct effect was obtained in section 3.1 and is repeated here for convenience.

$$D_{3_k} = \mathbf{d}_k^T \overline{\mathbf{Q}}_k \varepsilon_k \tag{3.4.1}$$

where

$$\mathbf{d}_k^T = \begin{bmatrix} d_{31} & d_{32} & 0 & 0 & 0 & d_{36} \end{bmatrix}_k \tag{3.4.2}$$

$$\overline{\mathbf{Q}}_k = \begin{bmatrix} \overline{Q}_{11} & \overline{Q}_{12} & 0 & 0 & 0 & 0 \\ \overline{Q}_{12} & \overline{Q}_{22} & 0 & 0 & 0 & 0 \\ 0 & 0 & 0 & 0 & 0 & 0 \\ 0 & 0 & 0 & \overline{Q}_{44} & 0 & 0 \\ 0 & 0 & 0 & 0 & \overline{Q}_{55} & 0 \\ 0 & 0 & 0 & 0 & 0 & \overline{Q}_{66} \end{bmatrix}_k \tag{3.4.3}$$

and

$$\varepsilon_k^T = \begin{bmatrix} \varepsilon_1 & \varepsilon_2 & \varepsilon_3 & \varepsilon_4 & \varepsilon_5 & \varepsilon_6 \end{bmatrix}_k \tag{3.4.4}$$

The charge enclosed by the surface $\overline{S}$ is calculated from Gauss' Law (Lee; 1990) as follows

$$q = \int_S \mathbf{D} \bullet ds \tag{3.4.5}$$

where q is the charge, **D** is the electric displacement vector and ds is the differential area normal vector of $\overline{S}$. However, this equation cannot be used directly since the results will be identically zero due to the fact that the charge within a dielectric is neutral. Since charge is built up on the surface of a piezoelectric lamina while it is under the action of an external force field, an equivalent circuit model is used to relate the closed-circuit charge signal measured from the surface electrode to the force field (Fig. 3.8). The charge built up on the surface due to the mechanical action is equivalent to the charge stored inside the capacitor of the equivalent circuit. In order for the charge to be measured, the electric loop must be closed. That is, electrodes must exist on both the top and bottom surfaces of the piezoelectric layer so that the induced charge can move in the 3 direction. It is assumed that these electrodes cover the entire upper and lower surfaces, respectively, as shown in Fig. 3.8 and are short circuited to measure the charge built up. Neglecting edge effects and assuming that the sensor layers are thin, the charge built up corresponding to a sensor in the k-th layer is approximated as follows.

$$q_k = \frac{1}{2}\left\{\left.\left(\int_S D_{3_{k-1}} dS\right)\right|_{z=z_{k-1}} + \left.\left(\int_S D_{3_k} dS\right)\right|_{z=z_k}\right\} \tag{3.4.6}$$

where S is the area of the sensor electrodes which is assumed to be the same on the top and bottom of the sensor layer and equal to the area of the sensor patch. Substituting the expression for D_{3_k} into the above equation yields the following.

$$q_k = \frac{1}{2}\left\{\mathbf{d}_k^T \overline{\mathbf{Q}}_k \int_S [\varepsilon_{k-1} + \varepsilon_k] dS\right\} \tag{3.4.7}$$

The strains are written in terms of the derivative operator matrix, $\mathbf{H}_k$ and the vector of the unknown displacement functions, **u** as follows.

$$q_k = \mathbf{d}_k^T \mathbf{Q}_k \int_A \mathbf{H}_k \mathbf{u} dA \tag{3.4.8}$$

where

$$\mathbf{H}_k = \begin{bmatrix} d_x & \left(z_0^1 - \frac{4z_0^3}{3h^2}\right)d_x & 0 & 0 & -z_0^1 d_{xx} \\ 0 & 0 & d_y & \left(z_0^1 - \frac{4z_0^3}{3h^2}\right)d_y & -z_0^1 d_{yy} \\ 0 & 0 & 0 & \left(1 - \frac{4z_0^2}{h^2}\right) & 0 \\ 0 & 0 & 0 & 0 & 0 \\ 0 & \left(1 - \frac{4z_0^2}{h^2}\right) & 0 & 0 & 0 \\ d_y & \left(z_0^1 - \frac{4z_0^3}{3h^2}\right)d_y & d_x & \left(z_0^1 - \frac{4z_0^3}{3h^2}\right)d_x & -2z_0^1 d_{xy} \end{bmatrix} \tag{3.4.9}$$

$$\mathbf{u} = \begin{bmatrix} u & \phi_x & v & \phi_y & w \end{bmatrix}^T \tag{3.4.10}$$

and

$$z_0^1 = \frac{1}{2}\left(z_{k-1} + z_k\right) \tag{3.4.11}$$

$$z_0^2 = \frac{1}{2}\left(z_{k-1}{}^2 + z_k{}^2\right) \tag{3.4.12}$$

$$z_0^3 = \frac{1}{2}\left(z_{k-1}{}^3 + z_k{}^3\right) \tag{3.4.13}$$

$$d_x = \frac{\partial}{\partial x}, \quad d_y = \frac{\partial}{\partial y}, \quad d_{xy} = \frac{\partial^2}{\partial x \partial y} \tag{3.4.14}$$

The charge due to mechanical deformation at any given moment is related to a voltage which can be measured as follows.

$$V_k(t) = \frac{q_k(t)}{C_k} \tag{3.4.15}$$

where C_k is the capacitance of the piezoelectric layer (Fig. 3.8). This measured voltage is proportional to the strain in the sensor at any given time. The current produced is obtained by differentiating the charge with respect to time as follows.

$$i_k(t) = \frac{dq_k(t)}{dt} \tag{3.4.16}$$

The current is proportional to the strain rate.

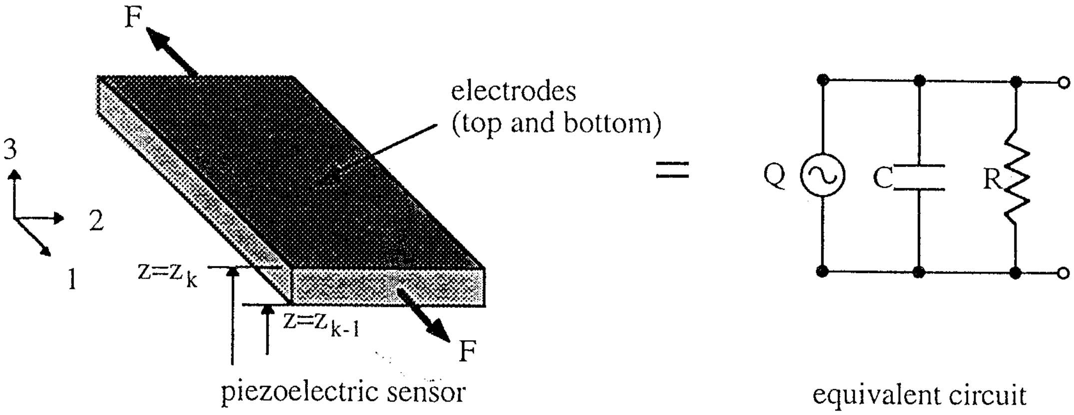

Fig. 3.8 Equivalent circuit for piezoelectric sensor in k-th layer.

Sensor circuits: The ultimate goal of implementing piezoelectric sensors is to obtain a signal, in the form of a voltage, which is proportional to either the strain or strain rate present in the structure. This is accomplished by connecting the piezoelectric sensors to op-amp circuits which can then be coupled to either a data acquisition system or a feedback control loop. Strain measurements are accomplished through the use of a charge amplifier shown in Fig. 3.9. The output voltage, v_0 is calculated as follows.

$$v_o(t) = -\frac{q(t)}{C_f} \tag{3.4.17}$$

The circuit must be designed around the lower and upper cutoff frequencies given as follows.

$$f_{cp}^1 = \frac{1}{2\pi R_f C_f} \tag{3.4.18}$$

$$f_{cp}^2 = \frac{1}{2\pi R_1 C} \tag{3.4.19}$$

where f^1_{cp} and f^2_{cp} are the lower and upper cutoff frequencies, respectively. The feedback capacitor, C_f, is chosen to match the capacitance of the piezoelectric sensor, C. Once the cutoff frequencies are determined, R_1 and R_f are obtained from Eqns 3.4.18 and 3.4.19.

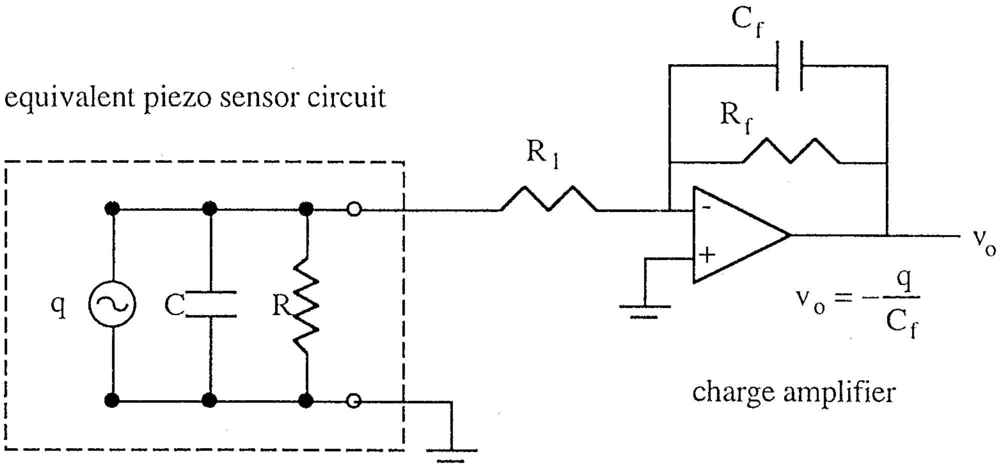

Fig. 3.9 Piezoelectric sensor circuit for strain measurement.

A transimpedance amplifier (Fig. 3.10) is used to convert the sensor current, which is proportional to the strain rate, to a voltage which can then be used by the measurement instrumentation. The output voltage, v_o, is proportional to the sensor current, i, as follows.

$$v_o(t) = -R_2 i(t) \tag{3.4.20}$$

$$v_o = -R_2 i \tag{3.4.21}$$

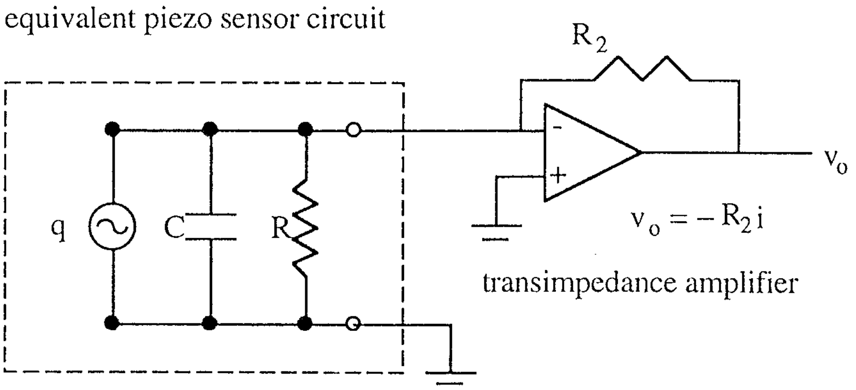

Fig. 3.10 Piezoelectric sensor circuit for strain rate measurement.

3.5 Equilibrium Equations and Boundary Conditions

A variational approach using Hamilton's principle is used to derive the equilibrium equations and boundary conditions for a nondebonded plate including piezoelectric actuation. The formulation can easily be extended to debonded plates by specializing the following analysis to each region $(\Omega^r, r = u, d1, d2)$. In the absence of any nonconservative forces, Hamilton's principle is stated as follows.

$$\delta \int_{t_1}^{t_2} [T - (V + U)] dt = 0 \tag{3.5.1}$$

where T is the kinetic energy, V is the potential energy due to external forces, U is the strain energy and t_1 and t_2 are the initial and final times, respectively The detailed derivation of these quantities are presented in the following sections.

<u>3.5.1 Potential energy formulation</u>: The elastic strain energy, U, is calculated by integrating the strain energy density, U_0, over the volume of the laminate as follows.

$$U = \frac{1}{2} \int_{-h/2}^{h/2} \int_A U_0 dAdz$$
$$= \frac{1}{2} \int_{-h/2}^{h/2} \int_A [\sigma_1 \varepsilon_1 + \sigma_2 \varepsilon_2 + \sigma_3 \varepsilon_3 + \sigma_4 \varepsilon_4 + \sigma_5 \varepsilon_5 + \sigma_6 \varepsilon_6] dAdz \tag{3.5.2}$$

The variation of the potential energy is obtained as follows

$$\delta U = \int_{-h/2}^{h/2} \int_A (\sigma_1 \delta\varepsilon_1 + \sigma_2 \delta\varepsilon_2 + \sigma_4 \delta\varepsilon_4 + \sigma_5 \delta\varepsilon_5 + \sigma_6 \delta\varepsilon_6) dAdz \tag{3.5.3}$$

It is noted that the transverse normal strain associated with the assumed displacement field (Eqn. 3.5.2) is zero. Hence, the admissible virtual strain is also zero, making the term $\sigma_3 \delta\varepsilon_3 = 0$ in Eqn. 3.5.3. On the other hand, σ_3 is assumed to be negligible by using the plane stress assumption. Integration through the thickness and substitution of the expressions for the variations in the strains, obtained from Eqn. 3.2.2, yields the following expression.

$$\begin{aligned}
\delta U = \int_A \Bigg[& N_1 \frac{\partial \delta u}{\partial x} + M_1 \left(\frac{\partial \delta\phi_x}{\partial x} - \frac{\partial^2 \delta w}{\partial x^2} \right) - P_1 \frac{4}{3h^2} \frac{\partial \delta\phi_y}{\partial x} \\
& + N_2 \frac{\partial \delta v}{\partial y} + M_2 \left(\frac{\partial \delta\phi_y}{\partial y} - \frac{\partial^2 \delta w}{\partial y^2} \right) - P_2 \frac{4}{3h^2} \frac{\partial \delta\phi_y}{\partial y} \\
& + Q_2 \delta\phi_y - R_2 \frac{4}{3h^2} \delta\phi_y + Q_1 \delta\phi_x - R_1 \frac{4}{3h^2} \delta\phi_x \\
& + N_6 \left(\frac{\partial \delta u}{\partial y} + \frac{\partial \delta v}{\partial x} \right) + M_6 \left(\frac{\partial \delta\phi_x}{\partial y} + \frac{\partial \delta\phi_y}{\partial x} - \frac{\partial^2 \delta w}{\partial x \partial y} \right) \\
& - P_6 \frac{4}{3h^2} \left(\frac{\partial \delta u}{\partial y} + \frac{\partial \delta v}{\partial x} \right) \Bigg] dA
\end{aligned} \tag{3.5.4}$$

where N_i, M_i and P_i (i=1,2,6) and Q_i and R_i (i=1,2) are the laminate stress resultants which are defined in Eqns. 3.3.3

The potential energy due to an applied distributed load is formulated as follows.

$$V = \int_A p(x,y)U_3 dA \tag{3.5.5}$$

where p(x,y) is the distributed load. Upon substituting the appropriate expression for U_3, taking the variation of V yields the following expression.

$$\delta V = \int_A p(x,y)\delta w dA \tag{3.5.6}$$

<u>3.5.2 Kinetic energy formulation</u>: The kinetic energy, T, is calculated by first considering the kinetic energy of a system of particles relative to an inertial frame of reference (Fig. 3.11)

$$T = \frac{1}{2}\sum_{i=1}^{n} m_i \overline{v}_i \bullet \overline{v}_i \tag{3.5.7}$$

where $\overline{v}_i$ is the absolute velocity of the i-th particle.

$$\overline{v}_i = v_i + (\Omega_i \times r_i) \tag{3.5.8}$$

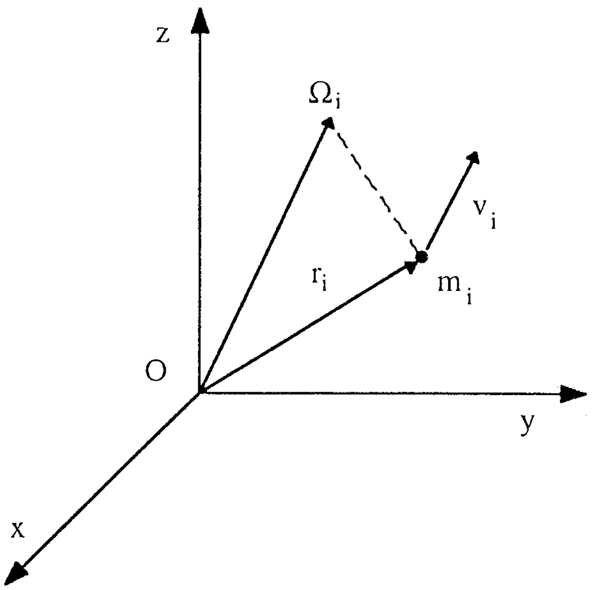

Fig. 3.11 Particle relative to inertial frame of reference.

In the context of laminate theory the rotational velocity term $(\Omega_i \times r_i)$ is much smaller than the transitional velocity term (v_i). Therefore, it is appropriate to retain only v_i.

$$T = \frac{1}{2}\sum_{i=1}^{n} m_i v_i \bullet v_i \tag{3.5.9}$$

Summation of all of the infinitesimally small particles throughout the laminate allows the sum to be represented as an integral over the volume of the laminate as follows.

$$T = \frac{1}{2}\int_V (\mathbf{v} \bullet \mathbf{v})dV \tag{3.5.10}$$

where the transitional velocity, **v**, is calculated by taking the time derivative of the refined displacement field. Carrying through the dot product in Eqn. 3.5.10 , substituting in terms from the displacement field and taking the variation of T yields the following expression.

$$\delta T = \frac{1}{2}\int_{-h/2}^{h/2}\int_A \{$$

$$+ \left[\dot{u} + z\left(\dot{\phi}_x - \frac{\partial \dot{w}}{\partial x}\right) - \frac{4}{3h^2} z^3 \dot{\phi}_x\right]\left[\delta\dot{u} + z\left(\delta\dot{\phi}_x - \frac{\partial \delta\dot{w}}{\partial x}\right) - \frac{4}{3h^2} z^3 \delta\dot{\phi}_x\right]$$

$$+ \left[\dot{v} + z\left(\dot{\phi}_y - \frac{\partial \dot{w}}{\partial y}\right) - \frac{4}{3h^2} z^3 \dot{\phi}_y\right]\left[\delta\dot{v} + z\left(\delta\dot{\phi}_y - \frac{\partial \delta\dot{w}}{\partial y}\right) - \frac{4}{3h^2} z^3 \delta\dot{\phi}_y\right] \qquad (3.5.11)$$

$$+ \ [\dot{w}][\delta\dot{w}] \ \Big\} dAdz$$

Integration with respect to z yields the following expression.

$$\delta T = \frac{1}{2}\int_A \Bigg\{ \quad \left[I_1\dot{u} + I_2\left(\dot{\phi}_x - \frac{\partial \dot{w}}{\partial x}\right) - \frac{4}{3h^2} I_4 \dot{\phi}_x\right]\delta\dot{u}$$

$$+ \left[I_1\dot{v} + I_2\left(\dot{\phi}_y - \frac{\partial \dot{w}}{\partial y}\right) - \frac{4}{3h^2} I_4 \dot{\phi}_y\right]\delta\dot{v}$$

$$+ \left[\left(I_2 - \frac{4}{3h^2} I_4\right)\dot{u} + \left(I_3 - \frac{4}{3h^2} I_5\right)\left(\dot{\phi}_x - \frac{\partial \dot{w}}{\partial x}\right) + \left(-\frac{4}{3h^2} I_5 + \frac{16}{9h^4} I_7\right)\dot{\phi}_x\right]\delta\dot{\phi}_x$$

$$+ \left[\left(I_2 - \frac{4}{3h^2} I_4\right)\dot{v} + \left(I_3 - \frac{4}{3h^2} I_5\right)\left(\dot{\phi}_y - \frac{\partial \dot{w}}{\partial y}\right) + \left(-\frac{4}{3h^2} I_5 + \frac{16}{9h^4} I_7\right)\dot{\phi}_y\right]\delta\dot{\phi}_y$$

$$+ \left[-I_2\dot{u} - I_3\left(\dot{\phi}_x - \frac{\partial \dot{u}_{30}}{\partial x}\right) + \frac{4}{3h^2} I_5 \dot{\phi}_x\right]\frac{\partial \delta\dot{w}}{\partial x}$$

$$+ \left[-I_2\dot{v} - I_3\left(\dot{\phi}_y - \frac{\partial \dot{u}_{30}}{\partial y}\right) + \frac{4}{3h^2} I_5 \dot{\phi}_y\right]\frac{\partial \delta\dot{w}}{\partial y}$$

$$+ \ [I_1\dot{w}]\delta\dot{w} \ \Big\} dA \qquad (3.5.12)$$

where

$$\left(I_1, I_2, I_3, I_4, I_5, I_7,\right) = \int_{-h/2}^{h/2} \rho\left(1, z, z^2, z^3, z^4, z^6\right) dz \qquad (3.5.13)$$

3.5.3 Hamilton's principle: The variation of the integral in Eqn 3.5.1 is performed as follows.

$$\int_{t_1}^{t_2}\left[\delta T-(\delta V+\delta U)\right]dt=0 \qquad (3.5.14)$$

The formulations for the variation of the kinetic energy (δT), the potential energy due to an applied load (δV) and the variation of the strain energy (δU) are now substituted into Eqn. 3.5.14. Further integration by parts using Green's theorem yields the following set of governing equations and boundary conditions.

$$\begin{aligned}
\delta u_{10}:&\quad \frac{\partial N_1}{\partial x}+\frac{\partial N_6}{\partial y}=I_1\ddot{u}+I_2\left(\ddot{\phi}_x-\frac{\partial \ddot{w}}{\partial x}\right)-\frac{4}{3h^2}I_4\ddot{\phi}_x\\
\delta u_{20}:&\quad \frac{\partial N_6}{\partial x}+\frac{\partial N_2}{\partial y}=I_1\ddot{v}+I_2\left(\ddot{\phi}_y-\frac{\partial \ddot{w}}{\partial y}\right)-\frac{4}{3h^2}I_4\ddot{\phi}_y\\
\delta u_{30}:&\quad \frac{\partial^2 M_1}{\partial x^2}+\frac{\partial^2 M_2}{\partial y^2}+2\frac{\partial^2 M_6}{\partial x\partial y}+p\\
&\quad =-I_2\ddot{u}-I_3\left(\ddot{\phi}_x-\frac{\partial \ddot{w}}{\partial x}\right)+\frac{4}{3h^2}I_5\ddot{\phi}_x\\
&\quad -I_2\ddot{v}-I_3\left(\ddot{\phi}_y-\frac{\partial \ddot{w}}{\partial y}\right)+\frac{4}{3h^2}I_5\ddot{\phi}_y\\
&\quad +I_1\ddot{w}\\
\delta u_{11}:&\quad \frac{\partial M_1}{\partial x}+\frac{\partial M_6}{\partial y}-\frac{4}{3h^2}\left(\frac{\partial P_1}{\partial x}+\frac{\partial P_6}{\partial y}\right)-Q_1+R_1\frac{4}{h^2}\\
&\quad =\left(I_2-\frac{4}{3h^2}I_4\right)\ddot{u}+\left(I_3-\frac{4}{3h^2}I_5\right)\left(\ddot{\phi}_x-\frac{\partial \ddot{w}}{\partial x}\right)+\left(-\frac{4}{3h^2}I_5+\frac{16}{9h^4}I_7\right)\ddot{\phi}_x\\
\delta u_{21}:&\quad \frac{\partial M_6}{\partial x}+\frac{\partial M_2}{\partial y}-\frac{4}{3h^2}\left(\frac{\partial P_6}{\partial x}+\frac{\partial P_2}{\partial y}\right)-Q_2+R_2\frac{4}{h^2}\\
&\quad =\left(I_2-\frac{4}{3h^2}I_4\right)\ddot{v}+\left(I_3-\frac{4}{3h^2}I_5\right)\left(\ddot{\phi}_y-\frac{\partial \ddot{w}}{\partial y}\right)+\left(-\frac{4}{3h^2}I_5+\frac{16}{9h^4}I_7\right)\ddot{\phi}_y
\end{aligned} \qquad (3.5.15a\text{-}e)$$

The boundary conditions are as follows.

specify:

Natural	Essential
$N_1 n_x + N_6 n_y$	u_{10}
$N_6 n_x + N_2 n_y$	u_{20}
$\left(\frac{\partial M_1}{\partial x} + \frac{\partial M_6}{\partial y}\right) n_x + \left(\frac{\partial M_2}{\partial y} + \frac{\partial M_6}{\partial x}\right) n_y$	u_{30}
$M_1 n_x + M_6 n_y$	$\frac{\partial u_{30}}{\partial x}$
$M_1 n_x + M_6 n_y$	$\frac{\partial u_{30}}{\partial y}$
$\left(M_1 - \frac{4}{3h^2} P_1\right) n_x + \left(M_6 - \frac{4}{3h^2} P_6\right) n_y$	u_{11}
$\left(M_6 - \frac{4}{3h^2} P_6\right) n_x + \left(M_2 - \frac{4}{3h^2} P_2\right) n_y$	u_{21}

where $n_x = \cos(\phi)$, $n_y = \sin(\phi)$ and ϕ represents the angle tangent to the boundary. Although the relevant equilibrium equations and boundary conditions are quite lengthy, important physical interpretation of the contribution of the higher order terms can be gained. As a check, when the higher order terms are set to zero, the above equations reduce exactly to those obtained using the classical theory. It must be noted that in the derivation of the equations of motion, the influence of the electric potential is assumed to be small and is therefore neglected. In the literature, the treatment of the piezoelectric effects in this manner is referred to as an induced strain formulation (Mitchell and Reddy; 1995).

3.6 Finite Element Implementation

Application of the higher order theory, including piezoelectric sensing and actuation, to realistic problems requires that complex geometries and boundaries be incorporated into the analysis. The logical choice for the solution technique is the finite element method which easily accommodates material discontinuities and is well suited for numerical implementation and solution. The following sections contain details of the finite element formulation.

3.6.1 Equations of motion: The displacements in matrix form are presented as follows.

$$\mathbf{U} = \begin{bmatrix} U^r & V^r & W^r \end{bmatrix}^T \tag{3.6.1}$$

where the subscript "r" corresponds to the nondebonded and debonded regions $(r = u, d1, d2, \ldots)$. In the following development, it is assumed that specialization to each region is performed when necessary. Therefore, the subscript "r" is dropped. The global displacements are represented in matrix form as follows.

$$\mathbf{U} = \mathbf{G}\mathbf{L}_G\mathbf{u} \tag{3.6.2}$$

where $\mathbf{u}$ is a vector of the five unknown displacement functions.

$$\mathbf{u} = \begin{bmatrix} u & \phi_x & v & \phi_y & w \end{bmatrix}^T \tag{3.6.3}$$

The quantity $\mathbf{L}_G$ is a derivative operator matrix and $\mathbf{G}$ contains the z dependence of the displacement field. These matrices are defined as follows.

$$\mathbf{L}_G = \begin{bmatrix} 1 & 0 & 0 & 0 & 0 \\ 0 & 1 & 0 & 0 & 0 \\ 0 & 0 & 1 & 0 & 0 \\ 0 & 0 & 0 & 1 & 0 \\ 0 & 0 & 0 & 0 & 1 \\ 0 & 0 & 0 & 0 & d_x \\ 0 & 0 & 0 & 0 & d_y \end{bmatrix} \tag{3.6.4}$$

$$\mathbf{G}=\begin{bmatrix} 1 & \bar{z}-\bar{z}^3\frac{4}{3d^2} & 0 & 0 & 0 & -\bar{z} & 0 \\ 0 & 0 & 1 & \bar{z}-\bar{z}^3\frac{4}{3d^2} & 0 & 0 & -\bar{z} \\ 0 & 0 & 0 & 0 & 1 & 0 & 0 \end{bmatrix} \tag{3.6.5}$$

and

$$d_x=\frac{\partial}{\partial x},\quad d_y=\frac{\partial}{\partial y},\quad d_{xx}=\frac{\partial^2}{\partial x^2},\quad d_{yy}=\frac{\partial^2}{\partial y^2},\quad d_{xy}=\frac{\partial^2}{\partial x \partial y} \tag{3.6.6}$$

$$\bar{z}=z-c \tag{3.6.7}$$

where c is the local midplane and d is the local thickness. Theses quantities vary from region to region. The generalized in-plane and transverse strains (Eqns. 3.3.6 and 3.3.17) are written in matrix form as follows

$$\varepsilon_B=\mathbf{L}_B\mathbf{u} \tag{3.6.8}$$

$$\varepsilon_T=\mathbf{L}_T\mathbf{u} \tag{3.6.9}$$

where $\mathbf{L}_B$ and $\mathbf{L}_T$ are derivative operator matrices. The derivative operator matrices are defined as follows.

$$\mathbf{L}_B=\begin{bmatrix} d_x & 0 & 0 & 0 & 0 \\ 0 & 0 & d_y & 0 & 0 \\ d_y & 0 & d_x & 0 & 0 \\ 0 & d_x & 0 & 0 & -d_{xx} \\ 0 & 0 & 0 & d_y & -d_{xy} \\ 0 & d_y & 0 & d_x & -2d_{xy} \\ 0 & -\frac{4}{3d^2}d_x & 0 & 0 & 0 \\ 0 & 0 & 0 & -\frac{4}{3d^2}d_y & 0 \\ 0 & \frac{4}{3d^2}d_y & 0 & \frac{4}{3d^2}d_x & 0 \end{bmatrix} \tag{3.6.10}$$

$$\mathbf{L}_T = \begin{bmatrix} 0 & 0 & 0 & 1 & 0 \\ 0 & 1 & 0 & 0 & 0 \\ 0 & 0 & 0 & -\frac{4}{d^2} & 0 \\ 0 & -\frac{4}{d^2} & 0 & 0 & 0 \end{bmatrix} \tag{3.6.11}$$

The kinetic energy is presented in matrix form using Eqn. 3.5.10 as follows.

$$T = \frac{1}{2}\int_V \rho \mathbf{U}^T \mathbf{U} dV \tag{3.6.12}$$

$$= \frac{1}{2}\int_A \rho \dot{\mathbf{u}}^T \mathbf{L}_G^T \tilde{\mathbf{G}} \mathbf{L}_G \dot{\mathbf{u}} dA \tag{3.6.13}$$

where

$$\tilde{\mathbf{G}} = \int_z \mathbf{G}^T \mathbf{G} dz \tag{3.6.14}$$

Using Eqns. 3.6.8 and 3.6.9, the strain energy is written as follows

$$U = \frac{1}{2}\left\{\int_A \varepsilon_B^T \mathbf{N}_B dA + \int_A \varepsilon_T^T \mathbf{N}_T dA\right\} \tag{3.6.15}$$

$$= \frac{1}{2}\left\{\int_A \varepsilon_B^T \mathbf{A}_B \varepsilon_B dA - \int_A \varepsilon_B^T \mathbf{N}^P dA + \int_A \varepsilon_T^T \mathbf{A}_T \varepsilon_T dA\right\} \tag{3.6.16}$$

Also, the potential energy due to an applied transverse load, p(x,y), is as follows.

$$V = \int_A \mathbf{U}^T \overline{\mathbf{F}} dA \tag{3.6.17}$$

where

$$\overline{\mathbf{F}} = \begin{bmatrix} 0 & 0 & p(x,y) \end{bmatrix} \tag{3.6.18}$$

Each of the five unknown functions are represented by their corresponding elemental functions $u^e(x,y)$ which are interpolated as follows.

$$u^e(x,y) = \sum_{i=1}^{N_n} N_i^e(x,y) w_i^e \tag{3.6.19}$$

where N_n is the number of nodes, N_i^e are the interpolation functions and the superscript e denotes the corresponding parameter at the element level. The quantities w_i^e are the nodal degrees of freedom defined as follows.

$$w_i^e = \left[u_i \quad \phi_{xi} \quad v_i \quad \phi_{yi} \quad w_i \quad \frac{\partial w_i}{\partial x} \quad \frac{\partial w_i}{\partial y} \right]^T \tag{3.6.20}$$

Bilinear shape functions are used for the first four unknowns while 12 term cubic polynomials are used for the transverse displacements (w). The derivative terms are included as degrees of freedom since C^1 continuity is required for the transverse displacement field . The resulting four noded rectangular elements are nonconforming for computational efficiency and contain 28 degrees of freedom each.

The elemental ($\mathbf{U}^e$) displacements are now represented as follows

$$\mathbf{U}^e = \mathbf{G}\mathbf{B}_G^e \mathbf{w}^e \tag{3.6.21}$$

where

$$\mathbf{B}_G^e = \mathbf{L}_G \mathbf{N}^e \tag{3.6.22}$$

The elemental generalized in-plane and transverse strains are represented as follows

$$\varepsilon_B^e = \mathbf{B}_B^e \mathbf{w}^e \tag{3.6.23}$$

$$\varepsilon_T^e = \mathbf{B}_T^e \mathbf{w}^e \tag{3.6.24}$$

where

$$\mathbf{B}_B^e = \mathbf{L}_B \mathbf{N}^e \tag{3.6.25}$$

$$\mathbf{B}_T^e = \mathbf{L}_T\mathbf{N}^e \tag{3.6.26}$$

The elemental expressions for the displacements and strains are now substituted into the formulation for the kinetic, strain and potential energies. (Eqns. 3.6.12,15,17) Taking the variation of each quantity yields the following expressions.

$$\delta T = \delta\dot{\mathbf{w}}^{eT}\mathbf{M}^e\dot{\mathbf{w}}^e \tag{3.6.27}$$

$$\delta K = \delta\mathbf{w}^{eT}\mathbf{K}^e\mathbf{w}^e - \delta\mathbf{F}_p^{eT} \tag{3.6.28}$$

$$\delta V = \delta\mathbf{w}^{eT}\mathbf{F}^e \tag{3.6.29}$$

where

$$\mathbf{M}^e = \int_{A_e}\mathbf{B}_G^{eT}\tilde{\mathbf{G}}\mathbf{B}_G^e dA^e \tag{3.6.30}$$

$$\mathbf{K}^e = \int_{A_e}\mathbf{B}_B^{eT}\mathbf{A}_B\mathbf{B}_B^e dA^e + \int_{A_e}\mathbf{B}_T^{eT}\mathbf{A}_T\mathbf{B}_T^e dA^e \tag{3.6.31}$$

$$\mathbf{F}^e = \int_{A_e}\mathbf{N}^{eT}p^e(x,y)dA^e \tag{3.6.32}$$

$$\mathbf{F}_P^e = \int_{A_e}\mathbf{N}^{eT}\mathbf{N}^P dA^e \tag{3.6.33}$$

The quantities $\mathbf{M}^e$, $\mathbf{K}^e$ and $\mathbf{F}^e$ represent the elemental mass and stiffness matrix and force vector due to a distributed load, respectively. The quantity $\mathbf{F}_P^e$ is the force vector due to the piezoelectric actuation. The laminate stiffness matrices ($\mathbf{A}_B$, $\mathbf{A}_T$) are integrated analytically through the thickness of the laminate, ply by ply and the finite element matrices are assembled using exact or full numerical integration. It must be noted that reduced integration and shear correction factors are not needed in the current analysis. According to the discretized form of Hamilton's principle where the above quantities are summed over all of the elements, the following must be true

$$\delta\Pi = \int_{t_1}^{t_2} \sum_{e=1}^{N_e} \left[\delta T^e - \delta U^e + \delta V^e\right] dt = 0 \tag{3.6.34}$$

where t_1 and t_2 are the initial and final times, respectively and N^c is the number of elements. Integration by parts and consideration of the arbitrary nature of the variation $\delta \mathbf{w}^e$ leads to a linear set of equations which are solved for the nodal displacements $\mathbf{w}$.

$$\mathbf{M}\ddot{\mathbf{w}} + \mathbf{K}\mathbf{w} = \mathbf{F} + \mathbf{F}_P \tag{3.6.35}$$

where the quantities $\mathbf{M}$, $\mathbf{K}$, $\mathbf{F}$ and $\mathbf{w}$ denote the global mass and stiffness matrices, the force vector due to a distributed load and the nodal displacement vector, respectively. The quantity $\mathbf{F}_P$ is the force vector due to the piezoelectric actuation.

3.6.2 Sensor equations: The charge from the piezoelectric sensors is determined independent of the finite element equations in post computation calculations since the electric displacements are not considered as additional degrees of freedom. This leads to a significant amount of computational savings and is consistent with the current approach which is an induced strain formulation. The short circuit voltage in the k-th layer is related to the charge and the displacements as follows.

$$V_k = \frac{q_k}{C_k} = \frac{1}{C_k} \mathbf{d}_k^T \mathbf{Q}_k \int_A \mathbf{H}_k \mathbf{u} \, dA \tag{3.6.36}$$

where V_k is the voltage, q_k is the charge and C_k is the capacitance of the k-th layer. The displacement vector $\mathbf{u}$ is represented in terms of the shape functions $\mathbf{N}^e$ and nodal displacements, $\mathbf{w}^e$, as before. Summing over all elements and plies leads to the following expression.

$$V=\sum_{e=1}^{N_e}\sum_{k=1}^{N}\frac{1}{C_k}\mathbf{d}_k^T\mathbf{Q}_k\overline{\mathbf{H}}^e\mathbf{w}^e \tag{3.6.37}$$

where

$$\overline{\mathbf{H}}^e=\int_{A^e}\mathbf{H}\mathrm{N}^e dA^e \tag{3.6.38}$$

It is important to note that only the piezoelectric plies which are used in a sensor mode are to be included in the above sum. The current is determined as follows.

$$i(t)=\frac{dq}{dt} \tag{3.6.39}$$

Summing over all plies and differentiating yields the following expression.

$$i(t)=\sum_{e=1}^{N_e}\sum_{k=1}^{N}\mathbf{d}_k^T\mathbf{Q}_k\overline{\mathbf{H}}^e\dot{\mathbf{w}}^e \tag{3.6.40}$$

3.7 Implementation of Continuity Conditions

One the finite element model has been constructed, it is necessary to implement the continuity conditions to ensure continuity of displacements at the interface of the nondebonded and debonded regions (S). For simplicity, consider the simple case where the displacements in a nondebonded region, $\left(\Omega^u\right)$, must be identical to the displacements in the debonded region, $\left(\Omega^d\right)$ at the interface between these two regions, (S) (Fig. 3.12). Since the displacements are represented in terms of the nodal quantities in the finite element implementation, this is accomplished by applying the continuity conditions developed in Section 3.2.3 on the unknown displacement quantities associated with the nodes contained in S. These constraints could be applied directly using the Lagrange multiplier technique. However, this leads to a nonsymmetric set of equations which has very undesirable consequences in the solution sequence of the finite element model. A more efficient approach which retains symmetry of the equations of motion needs to be developed. This is outlined below.

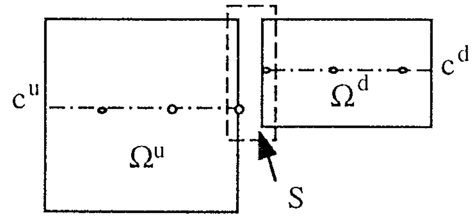

Fig. 3.12 Finite element discretization of debonding.

The continuity conditions presented in Eqns. 3.2.13 a-g, between the nondebonded $\left(\Omega^u\right)$ and debonded $\left(\Omega^d\right)$ regions, are applied to the finite element degrees of freedom at the interface of the nondebonded and debonded regions (S) by first presenting these discretized conditions in matrix form as follows.

$$\tilde{\mathbf{R}}\tilde{\mathbf{w}} = \mathbf{0} \tag{3.7.1}$$

where

$$\tilde{\mathbf{R}} = \begin{bmatrix} 1 & \alpha^r & 0 & 0 & 0 & c' & 0 & -1 & 0 & 0 & 0 & 0 & 0 & 0 \\ 0 & d^r\gamma^r & 0 & 0 & 0 & 0 & 0 & 0 & -d^r & 0 & 0 & 0 & 0 & 0 \\ 0 & 0 & 1 & \alpha^r & 0 & 0 & c' & 0 & 0 & -1 & 0 & 0 & 0 & 0 \\ 0 & 0 & 0 & d^r\gamma^r & 0 & 0 & 0 & 0 & 0 & 0 & -d^r & 0 & 0 & 0 \\ 0 & 0 & 0 & 0 & 1 & 0 & 0 & 0 & 0 & 0 & 0 & -1 & 0 & 0 \\ 0 & d^r\beta^r & 0 & 0 & 0 & d^r & 0 & 0 & 0 & 0 & 0 & 0 & -d^r & 0 \\ 0 & 0 & 0 & d^r\beta^r & 0 & 0 & d^r & 0 & 0 & 0 & 0 & 0 & 0 & -d^r \end{bmatrix} \tag{3.7.2}$$

$$\tilde{\mathbf{w}} = \left[\mathbf{u}^u \quad \mathbf{u}^d\right]^T \tag{3.7.3}$$

$$\mathbf{u}^u = \left[u^u \quad \phi_x^u \quad v^u \quad \phi_y^u \quad w^u \quad \frac{\partial w^u}{\partial x} \quad \frac{\partial w^u}{\partial y}\right]^T \tag{3.7.4}$$

$$\mathbf{u}^d = \left[u^d \quad \phi_x^d \quad v^d \quad \phi_y^d \quad w^d \quad \frac{\partial w^d}{\partial x} \quad \frac{\partial w^d}{\partial y}\right]^T \tag{3.7.5}$$

$$c' = c^u - c^d \tag{3.7.6}$$

Quantities with superscripts u and d refer to the corresponding quantities contained in S as well as the nondebonded $\left(\Omega^u\right)$ and debonded $\left(\Omega^d\right)$, regions, respectively. The formulation for α^r β^r and γ^r are presented in Eqns. 3.2.14 a-c. It must be noted that to obtain Eqn. 3.7.1, Eqns. 3.2.13 (d-g) have been multiplied by the thickness of the debonded layer, d^r, for consistency of units. Continuity of velocities must also be maintained. Therefore, Eqn. 3.7.2 is differentiated with respect to time to yield the following expression

$$\tilde{\mathbf{R}}\dot{\tilde{\mathbf{w}}} = \mathbf{0} \tag{3.7.7}$$

Next, the discretized potential energy is reformulated as follows.

$$V = \frac{1}{2}\left(-\mathbf{w}^T\mathbf{K}\mathbf{w} + \mathbf{w}^T\mathbf{F} + \mathbf{w}^T\mathbf{F}_p\right) - \frac{1}{2}\rho_1\tilde{\mathbf{w}}^T\mathbf{R}^T\mathbf{R}\tilde{\mathbf{w}} \tag{3.7.8}$$

where the first term in parentheses on the right hand side of Eqn. 3.7.8 corresponds to the actual potential energy while the last term corresponds to the penalty term related to the continuity constraints which has been introduced. Minimization of this penalty term leads to satisfaction of the continuity conditions. Similarly, the kinetic energy is reformulated as follows.

$$T = \frac{1}{2}\dot{\mathbf{w}}^T\mathbf{M}\dot{\mathbf{w}} + \frac{1}{2}\rho_2\dot{\tilde{\mathbf{w}}}^T\mathbf{R}^T\mathbf{R}\dot{\tilde{\mathbf{w}}} \tag{3.7.9}$$

where the first term on the right hand side represents the actual kinetic energy while the second term is the penalty term related to the continuity constraints. Again, minimization of this penalty term requires that the continuity conditions be satisfied. The scalar penalty factors, ρ_1 and ρ_2, are chosen to be on the order of the 1-norm of the stiffness and mass matrices, respectively. According to Lagrange's method for a discrete system,

$$\frac{\partial}{\partial t}\left(\frac{\partial T}{\partial \dot{q}_k}\right) - \frac{\partial T}{\partial q_k} + \frac{\partial L}{\partial q_k} = Q_k^{nc} \tag{3.7.10}$$

where q_k are the generalized coordinates and Q_k^{nc} are the generalized forces. The following symmetric set of augmented equations of motion is obtained $\left(\text{with} \quad Q_k^{nc} = 0\right)$

$$[\mathbf{M} + \rho_2 \mathbf{P}]\ddot{\mathbf{w}} + [\mathbf{K} + \rho_1 \mathbf{P}]\mathbf{w} = \mathbf{F} + \mathbf{F}_P \tag{3.7.11}$$

where **P** is the penalty matrix corresponding to the continuity constraints be satisfied. It is obtained first in terms of the nodes contained in (S) as follows.

$$\tilde{\mathbf{P}} = \tilde{\mathbf{R}}^T \tilde{\mathbf{R}} \tag{3.7.12}$$

The penalty matrix $\tilde{\mathbf{P}}$ is then expanded to correspond to the global degrees of freedom (**u**) and has the following form.

$$\mathbf{P} = \begin{bmatrix} \ddots & & & & \\ & \mathbf{R}^{uu} & \cdots & \mathbf{R}^{ud} & \\ & \vdots & & \vdots & \\ & \mathbf{R}^{du} & \cdots & \mathbf{R}^{dd} & \\ & & & & \ddots \end{bmatrix} \tag{3.7.13}$$

where

$$\mathbf{R}^{uu} = \begin{bmatrix} 1 & \alpha^r & 0 & 0 & 0 & c' & 0 \\ & \bar{\alpha}^r & 0 & 0 & 0 & \alpha^r c' + \beta^r \left(d^r\right)^2 & 0 \\ & & 1 & \alpha_j & 0 & 0 & c' \\ & & & \bar{\alpha}^r & 0 & 0 & \alpha^r c' + \beta^r \left(d^r\right)^2 \\ & & & & 1 & 0 & 0 \\ & \text{sym.} & & & & c'^2 + \left(d^r\right)^2 & 0 \\ & & & & & & c'^2 + \left(d^r\right)^2 \end{bmatrix} \tag{3.7.14a-b}$$

$$\bar{\alpha}^r = \alpha^{r^2} + \left(d^r\right)^2 \left(\beta^{r^2} + \gamma^{r^2}\right)$$

$$\mathbf{R}^{dd} = \begin{bmatrix} 1 & 0 & 0 & 0 & 0 & 0 & 0 \\ & \left(d^r\right)^2 & 0 & 0 & 0 & 0 & 0 \\ & & 1 & 0 & 0 & 0 & 0 \\ & & & \left(d^r\right)^2 & 0 & 0 & 0 \\ & & & & 1 & 0 & 0 \\ & \text{sym.} & & & & \left(d^r\right)^2 & 0 \\ & & & & & & \left(d^r\right)^2 \end{bmatrix} \qquad (3.7.15)$$

$$\mathbf{R}^{ud} = \begin{bmatrix} -1 & 0 & 0 & 0 & 0 & 0 & 0 \\ -\alpha^r & -\gamma^r d^{r^2} & 0 & 0 & 0 & -\beta^r d^{r^2} & 0 \\ 0 & 0 & -1 & 0 & 0 & 0 & 0 \\ 0 & 0 & -\alpha^r & -\gamma^r d^{r^2} & 0 & 0 & -\beta^r d^{r^2} \\ 0 & 0 & 0 & 0 & -1 & 0 & 0 \\ -c' & 0 & 0 & 0 & 0 & -d^{r^2} & 0 \\ 0 & 0 & -c' & 0 & 0 & 0 & -d^{r^2} \end{bmatrix} \qquad (3.7.16)$$

$$\mathbf{R}_{ji} = \mathbf{R}_{ij}^{T} \qquad (3.7.17)$$

3.8 State Space Controls Analysis:

The discretized linear equations of motion to model piezoelectric sensing and actuation of composite laminates, including debonded, are stated as follows.

$$\mathbf{M} * \ddot{\mathbf{w}} + \mathbf{C}\dot{\mathbf{w}} + \mathbf{K} * \mathbf{w} = \mathbf{F} + \mathbf{F}_P \qquad (3.8.1)$$

where

$$\mathbf{M}* = \left[\mathbf{M} + \rho_1 \mathbf{P}\right] \qquad (3.8.2)$$

$$\mathbf{K}* = \left[\mathbf{K} + \rho_2 \mathbf{P}\right] \qquad (3.8.3)$$

The above matrices are determined from the finite element implementation of the higher order theory. It must be noted that the viscous damping matrix **C** has also been introduced. This damping term arises due to internal friction. A simple damping model is used for computational efficiency. The static displacements, $\mathbf{w}$, are obtained by solving the following set of linear equations.

$$\mathbf{K}^{*}\mathbf{w} = \mathbf{F} + \mathbf{F}_{P} \tag{3.8.4}$$

The undamped open loop frequencies and mode shapes are calculated by solving the following eigenvalue problem.

$$\left(-\omega_i^2\mathbf{M}^{*} + \mathbf{K}^{*}\right)\phi_i = 0 \tag{3.8.5}$$

where ω_i are the undamped natural frequencies and ϕ_i are the undamped mode shapes for the i-th mode. The eigenvectors (mode shapes) are combined into a single modal matrix as follows.

$$\Phi = \begin{bmatrix}\phi_1 & \phi_2 & \cdots & \phi_N\end{bmatrix} \tag{3.8.6}$$

where N ≤ NDOF, the total number of degrees of freedom contained in Eqn. 3.8.1. The mode shapes are orthogonal and are mass orthonormalized as follows.

$$\phi_i^T\mathbf{M}^{*}\phi_i = 1 \tag{3.8.7}$$

Classical damping, also known modal damping, is assumed (Meirovitch; 1990). Using this approach, the undamped and damped mode shapes are identical and remain orthogonal. The damping matrix also has the following property

$$\Phi^T\mathbf{C}\Phi = \mathbf{Z} \tag{3.8.8}$$

where

$$\mathbf{Z} = \begin{bmatrix} 2\zeta_1\omega_1 & & & \\ & 2\zeta_2\omega_2 & & \\ & & \ddots & \\ & & & 2\zeta_N\omega_N \end{bmatrix} \tag{3.8.9}$$

and ζ_i are the damping ratios for the i-th mode. The original discretized degrees of freedom, **w**, are represented in term of the mode shapes and modal participation factors as follows

$$\mathbf{w} = \Phi\mathbf{q} \tag{3.8.10}$$

where **q** is a vector of the modal participation factors.

$$\mathbf{q} = \begin{bmatrix} q_1 \\ q_2 \\ \vdots \\ q_N \end{bmatrix} \tag{3.8.11}$$

By pre multiplying the original equations of motion by Φ^T, the modal equations of motion are written as follows.

$$\ddot{\mathbf{q}} + \mathrm{Z}\dot{\mathbf{q}} + \Lambda\mathbf{q} = \Phi^T\left[\mathbf{F} + \mathbf{F}_p\right] \tag{3.8.12}$$

where

$$\Lambda = \Phi^T\mathbf{K}\Phi = \begin{bmatrix} \omega_1^2 & & & \\ & \omega_2^2 & & \\ & & \ddots & \\ & & & \omega_N^2 \end{bmatrix} \tag{3.8.13}$$

In practice, potentially thousands of degrees of freedom contained in Eqn. 3.8.1 are accurately represented using just a few modes in Eqn. 3.8.12. The response of the piezoelectric sensors is now represented as follows.

$$\mathbf{v} = \mathbf{H}_v\Phi\mathbf{q} \tag{3.8.14}$$

$$\mathbf{i} = \mathbf{H}_c\Phi\dot{\mathbf{q}} \tag{3.8.15}$$

where **v** is the vector of one or more sensor voltages and $\mathbf{H}_v$ is the global sensor matrix which relates the sensor voltages to the displacements. Similarly, **i** contains the sensor currents which are obtained using the global matrix $\mathbf{H}_c$ which relates the sensor currents to the velocities.

In state space, the above equations are represented in standard form as follows.

$$\frac{d}{dt}\begin{bmatrix} q \\ \dot{q} \end{bmatrix} = \mathbf{A}\begin{bmatrix} q \\ \dot{q} \end{bmatrix} + \mathbf{B}\mathbf{u} \tag{3.8.16}$$

$$y = \mathbf{C}\begin{bmatrix} q \\ \dot{q} \end{bmatrix} \tag{3.8.17}$$

where $\mathbf{A}$ is the plant matrix, $\mathbf{B}$ is the control matrix and $\mathbf{C}$ is the observer matrix. The quantity $\mathbf{q}$ contains the modal participation factors, $\mathbf{u}$ contains the control inputs and y contains the sensor outputs.

These quantities are expressed as follows.

$$\mathbf{A} = \begin{bmatrix} \mathbf{0} & \mathbf{I} \\ -\Lambda & -\mathbf{Z} \end{bmatrix} \tag{3.8.18}$$

$$\mathbf{B} = \begin{bmatrix} \mathbf{0} & \mathbf{0} \\ \Phi^T\mathbf{F} & \Phi^T\mathbf{F}_p' \end{bmatrix} \tag{3.8.19}$$

$$\mathbf{C} = \begin{bmatrix} \mathbf{H}_v\Phi & \mathbf{H}_c\Phi \end{bmatrix} \tag{3.8.20}$$

$$y = \begin{bmatrix} \mathbf{v}^T & \mathbf{i}^T \end{bmatrix} \tag{3.8.21}$$

$$\mathbf{u} = \begin{bmatrix} 1 \\ v_1^a \\ v_2^a \\ \vdots \end{bmatrix} \tag{3.8.22}$$

The first element of the control vector, $\mathbf{u}$, is simply the number one which corresponds to the external disturbance force vector, $\mathbf{F}$, contained in the control matrix ($\mathbf{B}$). It must be noted that the quantity $\mathbf{F}_p'$ contained in $\mathbf{B}$ are the control forces per unit volt due to each piezoelectric actuator. The input voltages to the actuators are contained in $\mathbf{u}$ (v_1^a, v_2^a, etc.)

The voltage inputs are related to the sensor voltage and current outputs for feedback control through a gain matrix **G**.

$$\mathbf{u} = \mathbf{G}\mathbf{y} \tag{3.8.23}$$

The standard state space notation used here to represent the equations of motion and the feedback control allows the effects of piezoelectric sensing and actuation to be used in the design of a multi input multi output (MIMO) control system

3.9 Implementation of the Finite Element Model:

3.9.1 Laminate discretization: A few words regarding the discretization of the composite laminate incorporating piezoelectric sensors and actuators for use with the finite element model are in order. First, boundaries of the piezoelectric sensors and actuators must correspond to element boundaries as shown in Fig. 3.13. Although the piezoelectric sensors and actuators may occupy one or more elements, a single element either does or does not contain one ore more piezoelectric layers.

Although small meshes can be formulated by hand, the generation of large meshes with multiple sensors and actuators quickly becomes a daunting task. An automatic mesh generation procedure to incorporate piezoelectric transducers is essential, although it has never been discussed in the literature. Therefore, a new mesh generation procedure is developed which is described in Appendix C.

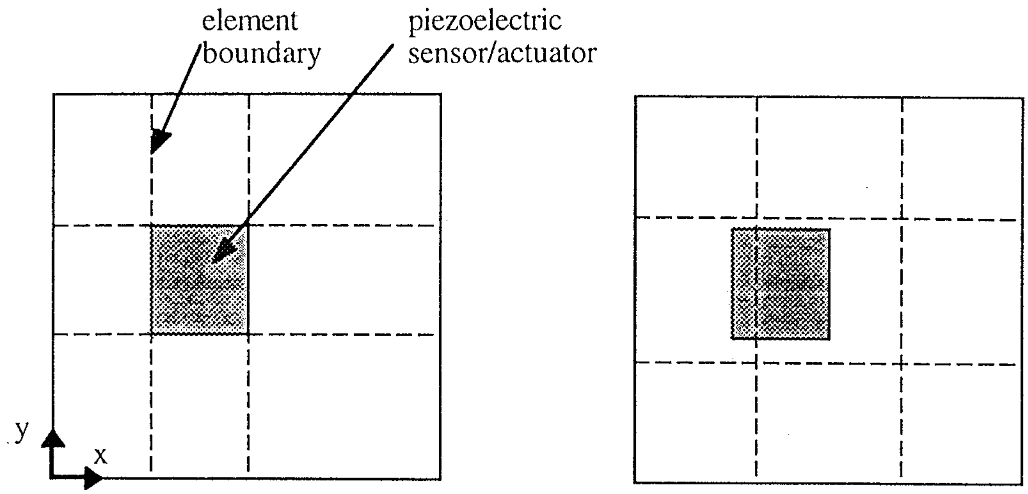

(a) valid discretization (b) invalid discretization

Fig 3.13 Finite element discretization of piezoelectric sensor/actuator.

The next issue involves the modeling of debonding. The higher order theory and corresponding finite element implementation are essentially two dimensional in nature. Nodes are defined at the laminate midplane. All of the unknown quantities are calculated in terms of these in-plane nodal values from the finite element solution. However, a debonding is assumed to occur between two plies at an arbitrary location through the thickness as well as the in-plane directions. Therefore, it is necessary to define the nodal points in terms of the thickness (z) direction as well. The regions both above and below the debonding are also discretized at their corresponding midplanes as shown in Fig. 3.14. The continuity conditions, as described above, are imposed on the nodes at the interface between the nondebonded and debonded region (S).

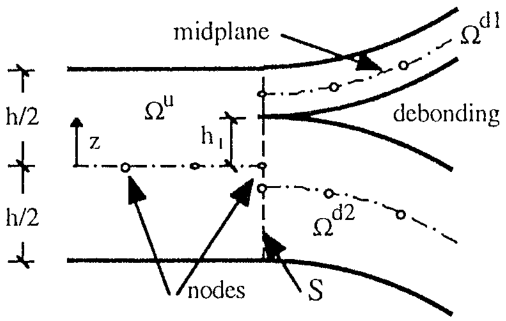

Fig 3.14 Finite element discretization of debonding

3.9.2 Computational considerations: The mass and stiffness matrices which are used in the finite element solution (FEM) of the static and dynamic equations of motion (**M*** and **K***) are potentially quite large. Therefore, solution of the equations of motion may become computationally prohibitive. Some consideration of the form of these matrices leads to a considerable savings in computational effort. These matrices are in general both symmetric and sparse. Storage requirements of the entire matrices (dense storage) increases as N^2, where N is the size of **M*** and **K***. Storage of only the symmetric terms gives some degree of savings. However, storage requirements of only the nonzero symmetric terms (sparse storage) increases at a much more manageable linear rate as shown in Fig. 3.15 and gives a significant savings over other types of storage schemes.

The displacement vector is the unknown quantity in the static equations of motion (Eqn. 3.8.4). The solution to these linear equations is obtained using any one of several standard iterative technique for solving large sparse symmetric linear systems. The Jacobi Conjugate Gradient method is selected for this research (Kincaid et al.; 1996). The generalized eigenvalue problem found in Eqn. 3.8.5 is solved using the Lanczos method which is most effective for finding a few eigenvalues and eigenvectors of the large sparse symmetric generalized eigenproblem (Jones and Patrick; 1996).

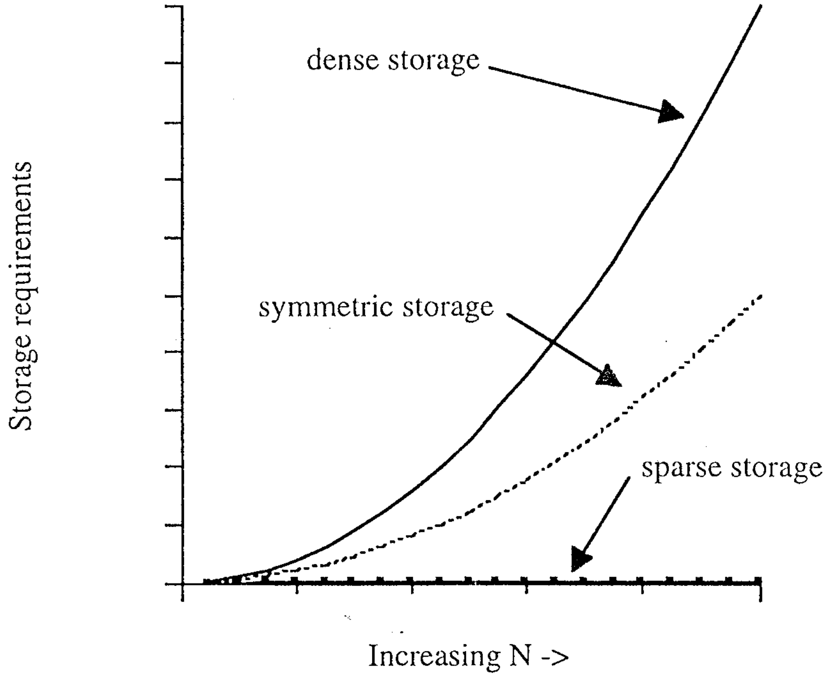

Fig 3.15 Storage requirements of FEM matrices.

4. Verification Studies

The higher order theory, as implemented using the finite element method in this research, must be correlated with other approaches to ensure its accuracy. Therefore, the purpose of this chapter is to provide validation studies to access the validity of the higher order theory for modeling piezoelectric actuation of composite laminates with debonding. Verification is established for the fundamental cases of plates with no debonding or piezoelectric actuation before additional complexity is added. Then, major features of the new theory, such as piezoelectric actuation and debonding, are introduced. Exact approaches provide excellent benchmarks to access the validity of the higher order theory when available. Experimental data is also very useful for comparison. Other approaches, such as the Ritz method and commercial finite element codes, such as NASTRAN, provide useful verification tools as well. Standard isotropic plate problems are used in the first part of the validation. Material orthotropy is then introduced. Further comparisons are then presented which include piezoelectric actuation and finally debonding. Comparison of the current higher order theory with other models is also discussed.

4.1 Fundamental Correlation of Isotropic Plates

4.1.1 Simply supported isotropic plates: In this section, the developed higher order theory (HOT), implemented with the finite element method, is compared with exact solutions for the classical laminate theory (CLT), first order shear deformation theory (FSDT) and exact elasticity solutions. The exact solutions for the CLT and FSDT are obtained according to standard techniques (Reddy, 1984). A 4x4 quarter plate finite element mesh is used to generate the static HOT solution while and 8x8 mesh for the full plate is used to obtain the plate natural frequencies so that anti symmetric modes will not be missed. The test article is an isotropic, simply supported plate with material properties $E = 74.5\ GPa$ and $\upsilon = 0.3$ and an applied uniform distributed load shown in Fig 4.1. The plate is analyzed for several different widths and thicknesses using CLT, FSDT and HOT. The static results are recorded in Table 4.1 where the nondimensional displacement (w*) is presented at the middle of the plate and is formulated as follows.

$$w^* = \frac{w(a/2, b/2)h^3 E}{q_0 a^4} \tag{4.1.1}$$

where $q=q_0$ is the uniform distributed load. Natural frequencies are presented in Table 4.2 where the first 10 nonrepeated frequencies are presented. The frequencies are normalized as follows.

$$\omega_i{}^* = \omega_i \frac{a^2}{h}\sqrt{\frac{\rho}{G}} \qquad i = 1,2,3,\ldots \tag{4.1.2}$$

All theories agree quite well for the static results for thin plates as expected (a/h=100). However, significant deviations between CLT and the other theories occur for thicker plates at lower a/h ratios, even for this simple isotropic example. This is because classical theory does not take into account transverse shear deformation and is therefore not valid for thick plates. The FSDT is able to account for a constant transverse shear stress through the thickness. The HOT, which has the same number of unknowns as the FSDT, allows for a quadratic variation in transverse shear deformation and predicts a significantly larger displacement compared to CLT, but agrees with FSDT. The HOT consistently gives a slightly higher deflection, but never deviates more than 2% from the FSDT. The HOT is also most accurate for a/b=1 since the elements are square. At other a/b ratios, the aspect ratio of each element is no longer equal to one and the solution is slightly less accurate. These results indicate that the HOT agrees with exact solutions for CLT and FSDT for thin plates as it should, but deviates from the CLT while still agreeing with the FSDT for thick plates.

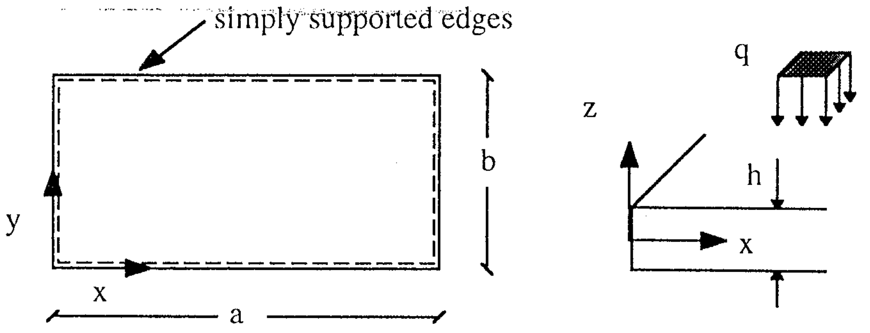

Fig. 4.1 Simply supported isotropic plate with distributed load.

Table 4.1 Comparison of normalized center deflections (w*) of simply supported isotropic plates under uniform distributed load.

b/a	a/h	w* CLT	w* FSDT	w* HOT
	100	0.0444	0.0444	0.0448
1	10	0.0444	0.0467	0.0471
	5	0.0444	0.0536	0.0541
	100	0.1106	0.1106	0.1119
2	10	0.1106	0.1142	0.1155
	5	0.1106	0.1248	0.1262

The normalized natural frequencies are presented in Table 4.2. for the CLT, FSDT, the exact elasticity solution and the current HOT using an 8x8 mesh. The exact elasticity solution is obtained by formulating the equilibrium equations, where no assumptions are made for the displacements, and solving using Fourier series (Srinivas et al.: 1970). The CLT consistently over predicts the frequencies for this moderately thick plate (L/h=10) since it neglects transverse shear deformation. The HOT agrees well with both the FSDT and the exact elasticity solution. The deviation increases with mode number since the mesh for representing the higher modes is somewhat crude. Errors are within acceptable limits and never exceed 5% for the modes presented.

Table 4.2 Comparison of normalized natural frequencies of simply supported isotropic plates (a/h=10, b/a=1)

m	n	CLT	FSDT	Exact[a]	HOT (8x8)
1	1	0.0963	0.0930	0.0932	0.0922
2	1	0.2408	0.2219	0.2260	0.2192
2	2	0.3853	0.3406	0.3421	0.3304
1	3	0.4816	0.4149	0.4171	0.4100
2	3	0.6261	0.5206	0.5239	0.5004
1	4	0.8187	0.6520	-	0.6469
3	3	0.8669	0.6834	0.6889	0.7169
2	4	0.9632	0.7446	0.7511	0.7375
3	4	1.2040	0.8896	-	0.8611
1	5	1.2521	0.9174	0.9268	0.9207

a) From Srinivas et al. (1970)

4.1.2 Static and dynamic convergence evaluation: In this section, convergence of the finite element model developed for the higher order theory (HOT) is investigated for both static and dynamic analyses. The test article is a simply supported isotropic plate with a constant distributed load identical to the one used in the previous section. For both static and dynamic cases, the HOT is compared to the corresponding exact solution for first order shear deformation theory (FSDT).

Convergence for the static case is investigated by examining a quarter plate model where the aspect ratio b/a corresponds to the full plate. In Fig. 4.2, the HOT normalized displacement results are presented for six meshes ranging from 1x1 to 6x6 for several different thicknesses with b/a=1. The displacement is normalized in the same manner as the previous section. These results are compared to the corresponding exact solutions using FSDT. In all cases, convergence is very rapid. The 4x4 mesh yields acceptable results with very little CPU time required. The 6x6 mesh is slightly more expensive, but yields displacements which are within 1% of the exact solution. The HOT also converges very rapidly for b/a=2 (Fig. 4.3). The error is slightly higher since the finite elements are no longer square, but it does not appear to be significant.

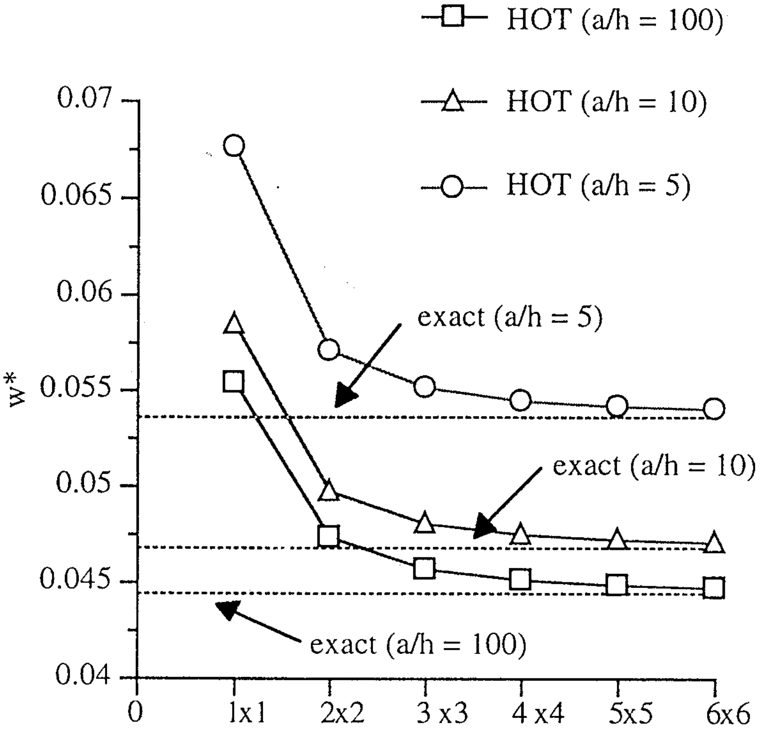

Fig. 4.2 Static convergence for simply supported plate (b/a=1).

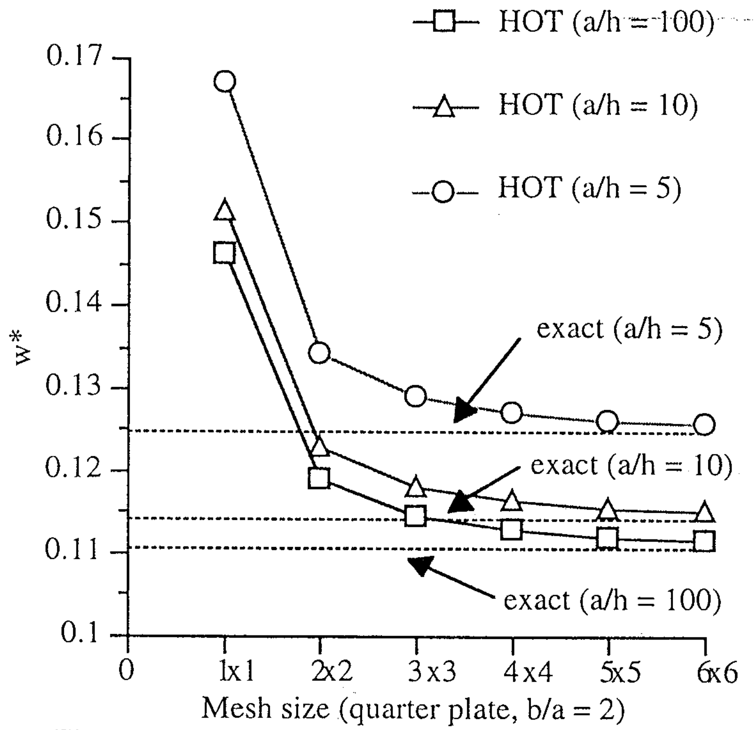

Fig. 4.3 Static convergence for simply supported plate (b/a=2).

Next, convergence of the plate natural frequencies is investigated as shown in Fig. 4.4 for a moderately thick plate (a/h=10). In this study, a full plate model is used so that both symmetric and anti symmetric modes are captured. The first five natural frequencies for the HOT, which are normalized as indicated in the previous section, are presented for mesh sizes ranging from 4x4 to 12x12. These results are compared to the exact values of the natural frequencies obtained using FSDT (Reddy, 1984). The 8x8 mesh provides very good results and the 12x12 mesh results agree with the exact solutions within 1%.

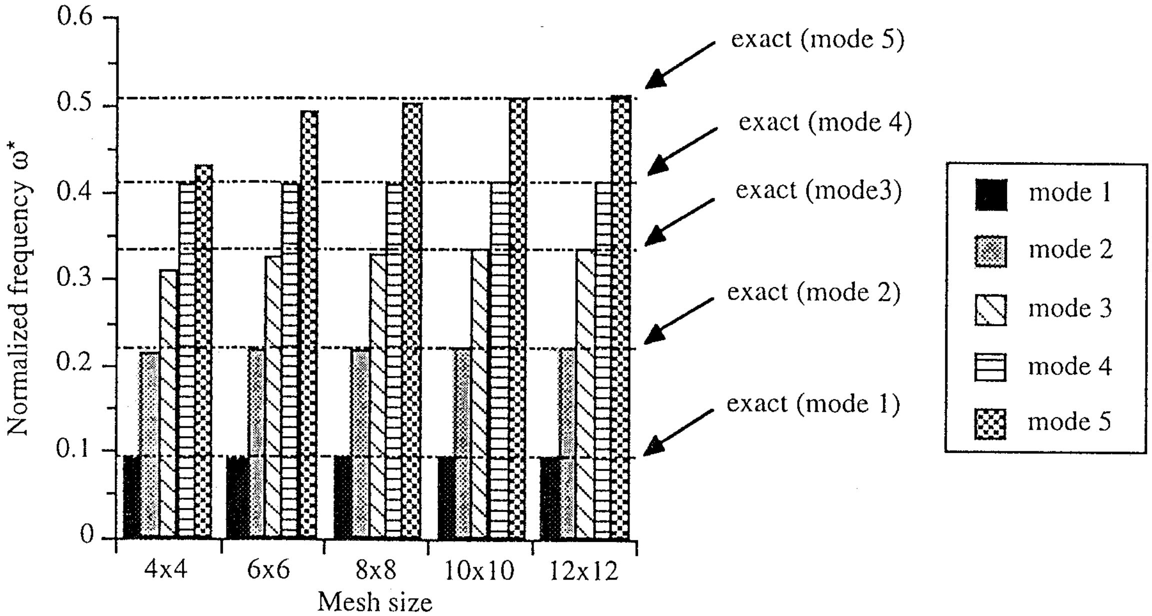

Fig. 4.4 Convergence of natural frequencies using HOT for a simply supported plate (b/a=1, a/h=10).

4.1.3 Thick isotropic cantilever plates: The higher order theory is now applied to the problem of determining natural frequency parameters for moderately thick and thick cantilever plates to determine its accuracy. Dimensions of the cantilever plate are presented in Fig 4.5 and the material properties are identical to those used in Section 4.1. The frequencies are normalized as follows for comparison with published results.

$$\omega^* = \omega a^2 \sqrt{\frac{\rho h}{D}} \tag{4.1.3}$$

where

$$D = \frac{Eh^3}{12\left(1-\upsilon^2\right)} \tag{4.1.4}$$

First, the higher order theory (HOT) is compared to published results for a moderately thick plate (b/h=20). Results using the HOT are presented in Table 4.3 using an 8x8 mesh. Results obtained using a Ritz solution with polynomial shape functions and also NASTRAN results using a standard triangular element are also presented. Aspect ratios of both a/b=1 and a/b=3 are shown for the first eight modes of plate vibration. Agreement between the HOT and both the Ritz and NASTRAN results is very good. The largest deviation between the HOT and the other approaches occurs for the sixth mode for a/b=1. However, the Ritz and NASTRAN results do not agree in this case either so that no conclusion can be drawn to the accuracy of any of the methods presented for this mode. NASTRAN appears to over predict the frequency for the eighth mode since both the HOT and the Ritz approaches agree for this mode. The HOT agrees well with the first seven frequencies for the plate with an aspect ratio of a/b=3. This is true even for frequencies 4-6 which are closely spaced. The last frequency presented (mode eight) deviates slightly from the Ritz and NASTRAN solution. Again, the Ritz and NASTRAN results do not agree either, so no special significance is placed on this small difference.

Next, natural frequencies obtained using the HOT (8x8 mesh) for very thick cantilever plates are compared to published values for aspect ratios of a/b=1 and a/b=2 (Table 4.4). These published values are obtained using a three dimensional Ritz approach, again with polynomial shape functions, and NASTRAN results using a standard three dimensional elements. It must be noted that it can be difficult to choose shape functions for the Ritz approach for unusual geometries and the three dimensional NASTRAN results are very expensive to obtain due to the large number of degrees of freedom required. The HOT can be easily used with complicated geometries with far fewer degrees of freedom since it is a two dimensional model. The HOT agrees very well with the Ritz and NASTRAN results for both aspect ratios. The largest deviation occurs in the seventh and eighth modes of the plate with an aspect ratio of a/b=2. These frequencies are slightly over predicted by the HOT.

The results presented in this section correlate cantilever isotropic plate natural frequencies obtained using the HOT and published values. These frequencies agree very well in most cases. Small deviations occur in a few cases, but often the published values disagree as well. Therefore, confidence is obtained that the HOT correctly predicts frequencies for cantilever plates, including very thick plates where shear deformation is significant.

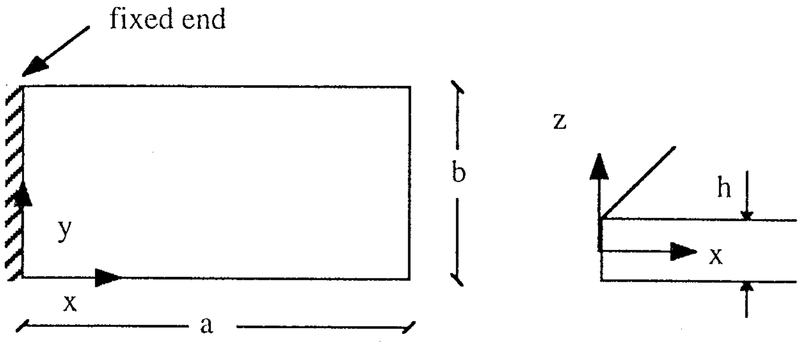

Fig. 4.5 Isotropic cantilever plate.

Table 4.3 Normalized natural frequency parameters (ω^*) for moderately thick isotropic cantilever plates (b/h=20)

a/b	Mode no.	HOT[a]	Ritz[b]	NASTRAN[c]
1	1	3.465	3.452	3.475
	2	8.417	8.504	8.547
	3	21.06	21.09	21.42
	4	26.73	27.34	27.27
	5	30.32	30.07	31.24
	6	43.93	46.59	44.42
	7	52.17	53.52	-
	8	59.59	59.01	64.66
3	1	3.233	3.420	3.419
	2	20.95	21.25	21.12
	3	21.33	22.09	21.38
	4	59.99	60.37	60.19
	5	64.11	65.40	63.47
	6	65.87	67.40	66.42
	7	118.01	122.00	120.40

(a) 8x8 mesh using current HOT
(b) Ritz solution using polynomial shape functions (Zienkiewicz, 1977)
(c) NASTRAN using CTRIA2 elements (Ramamurti and Kielb, 1984)

Table 4.4 Normalized natural frequency parameters (ω^*) for thick cantilever plates (b/h=5)

a/b	Mode no.	HOT[a]	Ritz[b]	NASTRAN[c]
1	1	3.3565	3.3687	3.3624
	2	7.4805	7.3397	7.3941
	3	10.985	10.984	10.943
	4	17.890	17.694	17.672
	5	22.644	23.688	22.148
	6	24.47	24.999	23.950
	7	26.185	26.234	26.227
	8	29.733	29.388	29.187
2	1	3.384	3.3397	3.411
	2	13.493	12.459	13.283
	3	14.602	14.390	14.452
	4	20.375	19.596	20.364
	5	42.735	38.771	41.908
	6	52.295	52.282	52.334
	7	53.937	52.469	53.483
	8	56.527	54.814	54.737

(a) 8x8 mesh using current higher order theory
(b) Ritz solution using polynomial shape functions (McGee and Leissa; 1991)
(c) 14x14x3 mesh using MSC/NASTRAN CHEXA elements (McGee and Leissa; 1991)

4.2 Fundamental Correlation of Orthotropic Laminates

In this section, the higher order theory (HOT) is compared to several existing theories to determine the accuracy of displacements, stresses and natural frequencies. Static displacements and stresses are correlated first. Next, the accuracy of natural frequencies predicted by the HOT are investigated and mode shapes are discussed.

4.2.1 Static evaluation: The test article for static evaluation is a simply supported plate with dimensions shown in Fig. 4.1. However, now a sinusoidal distributed load is applied and the plate is constructed of a three ply [0°/90°/0°] orthotropic laminate with ply thickness t = h/3. The aspect ratio of the laminate is a/b=3 and material properties are as follows.

$$E_1 = 25\ GPa,\ E_2 = 1\ GPa,\ \upsilon_{12} = 0.25,\ G_{23} = 0.2\ GPa,\ G_{13} = 0.5\ GPa,\ G_{12} = 0.5\ GPa,$$

The static results due to an applied sinusoidal load using the HOT are compared to four existing theories for analyzing composite laminates. The first of these theories is an exact elasticity solution for cross ply laminates formulated by Pagano (1970) (Exact). The second theory is an exact solution to an alternative form of the higher order theory (Reddy, 1984) (HSDT) . The last two theories are the first order shear deformation theory (FSDT) and classical laminate theory (CLT). The transverse displacement predicted by each theory is evaluated at the center of the plate and is normalized as follows

$$w^* = w(a/2, b/2, h/2)\frac{h^3 E_2}{q_0 a^4} \times 100 \tag{4.2.1}$$

The stresses are evaluated and normalized as follows.

$$\sigma_1{}^* = \sigma_1(a/2, b/2, h/2)\frac{h^2}{q_0 a^2}$$

$$\sigma_2{}^* = \sigma_2(a/2, b/2, h/6)\frac{h^2}{q_0 a^2}$$

$$\sigma_6{}^* = \sigma_6(0, 0, h/2)\frac{h^2}{q_0 a^2} \qquad (4.2.2\ \text{a-e})$$

$$\sigma_4{}^* = \sigma_4(a/2, 0, 0)\frac{h}{q_0 a^2}$$

$$\sigma_5{}^* = \sigma_5(0, b/2, 0)\frac{h^2}{q_0 a^2}$$

Results are presented in Figs 4.6 (a-f) for the current approach as well as four existing theories. The normalized displacements for all theories agree very well for a thin laminate (a/h=100) as shown in Fig 4.6 (a). However, the displacements predicted by the CLT depart radically from the true displacement as indicated by the Exact solution for very thick laminates (a/h=4). This is due to transverse shear deformation which is ignored in the CLT, but is important to consider in thicker laminates. The HOT agrees very closely with the HSDT for all thicknesses and differs by a maximum of only 6% from the Exact solution for the very thick laminate while the CLT solution under predicts the displacement by 82% in this case. The HOT provides good estimates for the inplane stresses, σ_1, σ_2, and σ_6 as shown in Figs. 4.6 (b-d). Again, all approaches agree well for the thin laminate (a/h=100) although significant differences are observed for the thicker laminates. Surprisingly, the well known FSDT noticeably under predicts these stresses for all thicknesses other than a/h=100, 44% in the worse case. The HOT agrees very well with the exact solution for the alternate form of the higher order theory (HSDT) and is much closer to the Exact solution than both the FSDT and the CLT for all inplane stresses. Results for the transverse shear stresses are presented in Figs 4.6 (e-f) for the HOT, Exact and FSDT solutions. These stresses are assumed to be zero for CLT and are not presented. All solutions presented for σ_4 in Fig. 4.6 (e) predict similar values at the location where this stress is evaluated. However, it must be noted that the FSDT predicts a constant value of this stress through the thickness and does not satisfy the requirement that this stress vanish on the free surfaces. In Fig 4.6 (f), the HOT under predicts σ_5 compared to the elasticity solution. It agrees very well with the HSDT and errors compared to the Exact solution are approximately one half of those using the FSDT. The deviation in this case is possibly due to the fact that the HOT is a two dimensional theory which is used to represent a three dimensional state of stress while the Exact approach is a pure three dimensional approach. Over all, the HOT predicts stresses much more accurately than the FSDT or CLT approaches compared to the Exact approaches. Very close agreement with HSDT is also observed from which it can be concluded that the HOT can be used to accurately predict displacements and stresses in more complex laminates where exact solutions are not practical.

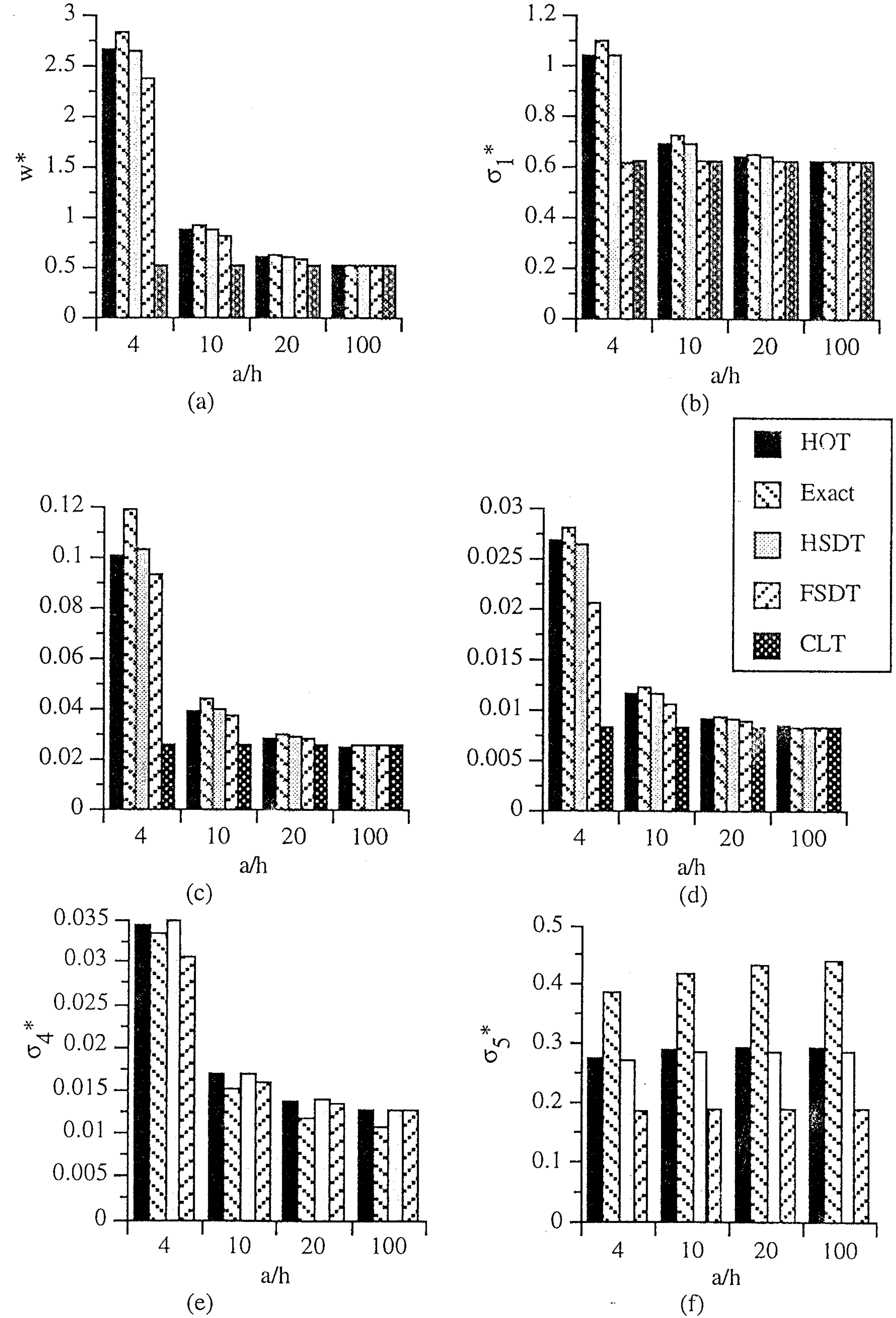

Fig. 4.6 (a-f) Normalized displacements and stresses in orthotropic laminate.

4.2.2 Dynamic evaluation: Natural frequencies predicted by the higher order theory (HOT) of an orthotropic composite laminate are investigated for a variety of geometries and stacking sequences. The test article consists of a four ply orthotropic laminate with identical material properties as those used in the previous example. The geometry of this laminate is shown in Fig. 4.5 with one end fixed. The stacking sequence of the four ply laminate is $[\pm\theta]_s$ which is defined by a singe variable θ. Each ply is assumed to have thickness t=h/4. Normalized frequencies using the HOT are compared to frequencies predicted by NASTRAN using two dimensional, shear deformable CQUAD4 elements which are based on first order shear deformation theory. Results are also obtained for classical laminate theory (CLT) which is obtained by setting the higher order terms in the HOT to zero. All of the results in this section, including CLT, HOT and CQUAD4 were obtained by the author.

Results to assess the accuracy of natural frequencies for orthotropic laminates using the HOT are presented in Tables 4.5 - 4.8. Frequency parameters for two different aspect ratios (a/b=1,2) are presented for several different stacking sequences (θ=0°, 15°, 30°, 45°, 60°) and four different laminate thicknesses ranging from thin to very thick (a/h=100,25,10,5). Five modes are obtained in each case where the frequencies are normalized as follows

$$\omega_i{}^* = \omega_i a^2 \sqrt{\frac{\rho h}{D}} \times 10 \qquad i = 1,2,3,4,5 \tag{4.2.3}$$

where

$$D = \frac{E_1 h^3}{12(1 - \upsilon_{12}\upsilon_{21})} \tag{4.2.4}$$

Correlation between the HOT and the NASTRAN (CQUAD4) results is very good. In general, the HOT predicts slightly higher frequencies compared to CQUAD4. The formulation of the CQUAD4 elements requires shear correction factors and reduced integration techniques which are tricks needed to avoid shear locking behavior for thin elements. These tricks could result in an overly "soft" element for highly orthotropic materials, such as used in this example. The mode shapes for θ=0° and a/b=1 indicate that the first five frequencies correspond to the first bending, first torsion, first camber, second camber and second bending modes, respectively. Increasing θ from θ=0° to θ=30° results in a decreased bending stiffness and an increased torsional stiffness. Both the HOT and the CQUAD4 results display this trend for the bending and torsional frequencies as shown in Tables 4.5 - 4.8. Increasing θ also results in a more pronounced coupling between the bending and torsional behavior of the laminate. This is especially evident in the higher modes. Beyond θ=30°, the bending stiffness continues to decrease while the torsional stiffness also decreases as indicated by a reduction in the second frequency. Although in the static case the maximum torsional stiffness occurs at θ=45°, this is not exactly true in the dynamic case since the mode shapes exhibit bending-twist coupling. Although in the static case the laminate becomes more stiff in torsion, the influence of the softer bending behavior reduces, rather than increases the natural frequencies for these modes. These features are even more evident for the case of a/b = 2. Here, the first five frequencies correspond to the first bending, first torsion, first camber, second bending and second torsional mode shapes, respectively. Again, the distinction between the bending and torsional mode shapes becomes blurred for the higher modes as θ is increased due to the coupling of these features. In this case, the frequency corresponding to the second bending mode decreases as θ is increased as expected while the frequency corresponding to the second torsional mode increases up to θ=30°, then decreases. According to the classical laminate theory (CLT), the normalized natural frequency parameters remain constant for increasing laminate thickness since transverse shear deformation is neglected. This leads to serious errors for thicker laminates, especially for highly orthotropic materials, as observed in Tables 4.7 and 4.8. In the worst case, the CLT over predicts the natural frequency by as much as a factor of four (Table 4.8) for a/b=2, a/h=5 and θ=45°. It can therefore be concluded that the CLT is unacceptable for prediction of natural frequencies in thicker orthotropic laminates. However, the HOT agrees well with the NASTRAN results and is considered effective for dynamic analysis of composites, even thick and highly orthotropic laminates.

Table 4.5 Normalized frequency parameters (ω*) for cantilever orthotropic plates, a/h=100

a/b	θ	Solution	mode 1	mode 2	mode 3	mode 4	mode 5
1	0	HOT	5.580	6.119	10.300	21.567	34.578
		CQUAD4	5.544	5.994	9.758	19.799	33.731
		CLT	5.590	6.132	10.318	21.605	34.995
	15	HOT	4.725	7.030	12.992	24.528	30.072
		CQUAD4	4.660	6.917	12.341	22.388	28.228
		CLT	4.734	7.050	13.045	24.631	30.426
	30	HOT	3.537	8.214	16.427	22.825	28.327
		CQUAD4	3.500	8.041	15.323	21.544	26.118
		CLT	3.546	8.254	16.568	23.043	28.612
	45	HOT	2.281	8.296	12.959	20.964	27.222
		CQUAD4	2.261	8.061	12.169	20.030	25.718
		CLT	2.289	8.346	13.068	21.120	27.495
	60	HOT	1.404	6.763	8.387	19.655	23.176
		CQUAD4	1.400	6.501	8.118	18.642	22.098
		CLT	1.407	6.796	8.411	19.767	23.299
2	0	HOT	5.579	7.492	30.459	34.662	37.047
		CQUAD4	5.543	7.324	28.929	33.786	35.575
		CLT	5.589	7.514	30.519	35.079	37.494
	15	HOT	4.537	10.848	29.256	33.452	41.438
		CQUAD4	4.489	10.628	28.033	31.873	39.805
		CLT	4.549	10.925	29.612	33.658	41.984
	30	HOT	3.201	13.993	19.961	40.237	46.442
		CQUAD4	3.148	13.614	18.956	38.408	44.085
		CLT	3.221	14.163	20.257	40.746	47.269
	45	HOT	1.982	11.585	14.790	34.888	43.521
		CQUAD4	1.910	11.173	14.002	33.485	40.696
		CLT	2.003	11.715	15.055	35.450	44.341
	60	HOT	1.115	7.845	12.136	23.140	36.887
		CQUAD4	1.260	7.657	11.383	22.322	34.104
		CLT	1.123	7.884	12.299	23.326	37.427

Table 4.6 Normalized frequency parameters (ω^*) for cantilever orthotropic plates, a/h=25

a/b	θ	Solution	mode 1	mode 2	mode 3	mode 4	mode 5
1	0	HOT	5.437	5.937	10.027	20.899	22.926
		CQUAD4	5.391	5.805	9.512	19.295	22.849
		CLT	5.590	6.132	10.318	21.605	34.995
	15	HOT	4.595	6.755	12.304	23.126	26.003
		CQUAD4	4.519	6.630	11.658	21.143	24.188
		CLT	4.734	7.050	13.045	24.631	30.426
	30	HOT	3.433	7.751	14.913	20.345	25.236
		CQUAD4	3.375	7.551	13.810	19.096	23.363
		CLT	3.546	8.254	16.568	23.043	28.612
	45	HOT	2.206	7.773	11.862	19.228	24.352
		CQUAD4	2.163	7.500	11.099	18.336	22.981
		CLT	2.289	8.346	13.068	21.120	27.495
	60	HOT	1.380	6.411	8.102	18.345	21.689
		CQUAD4	1.360	6.115	7.837	17.360	20.635
		CLT	1.407	6.796	8.411	19.767	23.299
2	0	HOT	5.434	7.170	21.766	29.223	29.884
		CQUAD4	5.390	7.010	21.686	28.073	28.790
		CLT	5.589	7.514	30.519	35.079	37.494
	15	HOT	4.392	10.051	25.348	30.881	35.741
		CQUAD4	4.342	9.844	24.068	29.691	34.151
		CLT	4.549	10.925	29.612	33.658	41.984
	30	HOT	3.049	12.629	17.577	33.532	35.432
		CQUAD4	2.985	12.272	16.651	32.207	34.027
		CLT	3.221	14.163	20.257	40.746	47.269
	45	HOT	1.861	10.681	13.024	19.827	30.453
		CQUAD4	1.772	10.314	12.388	17.344	29.082
		CLT	2.003	11.715	15.055	35.450	44.341
	60	HOT	1.159	7.544	10.982	15.378	21.530
		CQUAD4	1.211	7.359	10.287	13.337	20.817
		CLT	1.123	7.884	12.299	23.326	37.427

Table 4.7 Normalized frequency parameters (ω^*) for cantilever orthotropic plates, a/h=10

a/b	θ	Solution	mode 1	mode 2	mode 3	mode 4	mode 5
1	0	HOT	4.783	5.148	8.962	9.171	19.567
		CQUAD4	4.709	5.010	8.609	9.140	17.326
		CLT	5.590	6.132	10.318	21.605	34.995
	15	HOT	4.067	5.769	10.279	17.495	18.764
		CQUAD4	3.980	5.650	9.829	16.280	17.577
		CLT	4.734	7.050	13.045	24.631	30.426
	30	HOT	3.069	6.437	11.552	14.830	18.316
		CQUAD4	3.014	6.284	10.850	14.129	17.283
		CLT	3.546	8.254	16.568	23.043	28.612
	45	HOT	1.990	6.445	9.443	13.553	14.939
		CQUAD4	1.959	6.243	8.977	12.680	14.418
		CLT	2.289	8.346	13.068	21.120	27.495
	60	HOT	1.293	5.506	7.217	10.001	14.791
		CQUAD4	1.287	5.304	7.037	9.474	14.266
		CLT	1.407	6.796	8.411	19.767	23.299
2	0	HOT	4.782	5.962	8.706	19.586	21.075
		CQUAD4	4.708	5.849	8.674	18.173	19.667
		CLT	5.589	7.514	30.519	35.079	37.494
	15	HOT	3.889	7.958	16.524	17.223	22.878
		CQUAD4	3.824	7.836	16.187	16.408	21.939
		CLT	4.549	10.925	29.612	33.658	41.984
	30	HOT	2.720	9.644	13.021	13.412	25.144
		CQUAD4	2.672	9.480	12.416	12.883	24.347
		CLT	3.221	14.163	20.257	40.746	47.269
	45	HOT	1.595	7.933	8.804	9.735	21.952
		CQUAD4	1.598	6.938	8.568	9.532	21.056
		CLT	2.003	11.715	15.055	35.450	44.341
	60	HOT	0.976	6.154	6.736	8.540	17.189
		CQUAD4	1.156	5.335	6.665	8.312	16.995
		CLT	1.123	7.884	12.299	23.326	37.427

Table 4.8 Normalized frequency parameters (ω*) for cantilever orthotropic plates, a/h=5

a/b	θ	Solution	mode 1	mode 2	mode 3	mode 4	mode 5
1	0	HOT	3.617	3.818	4.585	7.284	12.393
		CQUAD4	3.442	3.637	4.570	7.203	10.893
		CLT	5.590	6.132	10.318	21.605	34.995
	15	HOT	3.113	4.271	7.863	10.149	11.174
		CQUAD4	3.010	4.136	7.722	10.095	10.235
		CLT	4.734	7.050	13.045	24.631	30.426
	30	HOT	2.484	4.758	8.205	10.008	11.000
		CQUAD4	2.423	4.636	7.850	9.579	10.688
		CLT	3.546	8.254	16.568	23.043	28.612
	45	HOT	1.704	4.807	6.776	6.777	11.731
		CQUAD4	1.685	4.694	6.340	6.536	10.189
		CLT	2.289	8.346	13.068	21.120	27.495
	60	HOT	1.210	4.285	5.001	5.742	8.994
		CQUAD4	1.190	4.194	4.737	5.640	8.857
		CLT	1.407	6.796	8.411	19.767	23.299
2	0	HOT	3.619	4.195	4.353	12.406	13.355
		CQUAD4	3.441	4.186	4.337	10.892	12.432
		CLT	5.589	7.514	30.519	35.079	37.494
	15	HOT	3.012	5.476	8.262	11.087	14.882
		CQUAD4	2.936	5.510	8.204	10.178	14.175
		CLT	4.549	10.925	29.612	33.658	41.984
	30	HOT	2.246	6.442	6.706	8.887	16.098
		CQUAD4	2.239	6.441	6.526	8.411	15.451
		CLT	3.221	14.163	20.257	40.746	47.269
	45	HOT	1.462	3.966	6.373	6.549	10.976
		CQUAD4	1.435	3.469	6.390	6.518	10.668
		CLT	2.003	11.715	15.055	35.450	44.341
	60	HOT	1.057	3.075	5.469	5.748	8.594
		CQUAD4	1.097	2.667	5.458	5.911	8.497
		CLT	1.123	7.884	12.299	23.326	37.427

4.3 Correlation of Piezoelectric Actuation of Beams and Plates

4.3.1 Correlation with isotropic piezoelectric beam: The higher order theory is applied to the problem of determining static displacements of a beam constructed entirely of piezoelectric material. The beam is constructed from two plies of PVDF polymeric piezoelectric material. Beam dimensions and poling directions of the piezoelectric plies are shown in Fig 4.7. Note that the top layer is polarized in the direction of the applied voltage and the bottom layer is polarized in the direction opposite the applied voltage. An electric field due to the voltage source is applied across the beam such that the top layer expands while the bottom layer contracts causing bending moment and a transverse deflection. The material properties for this beam-like piezoelectric structure can be assumed to be isotropic with values given as follows

$E=2.0\ GPa,\ \nu=0.30,\ d_{31}=23pm/V$

The transverse tip deflection (w) for the piezoelectric cantilever beam is calculated over a wide range of applied electric fields which corresponds to a range of applied voltage $0 \leq V \leq 500$ Volts. Results using the HOT are compared with experimental results obtained by Lee and Moon (1989) as shown in Fig 4.8. The tip deflections predicted using the HOT are in excellent agreement with the experimental results. It must be noted that PVDF has the advantage over piezoceramic materials, such as PZT, that significantly higher electric fields can be applied without damage to the piezoelectric properties. The results is that larger deflections are possible compared to PZT. However, PVDF is much more compliant than stiff PZTs. Therefore, the force developed using PVDF materials is significantly lower than that possible using piezoceramics.

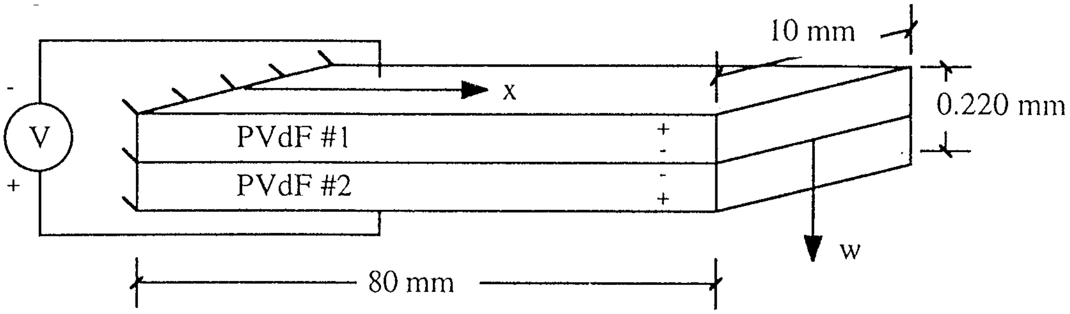

Fig. 4.7 Two layer piezoelectric cantilever beam.

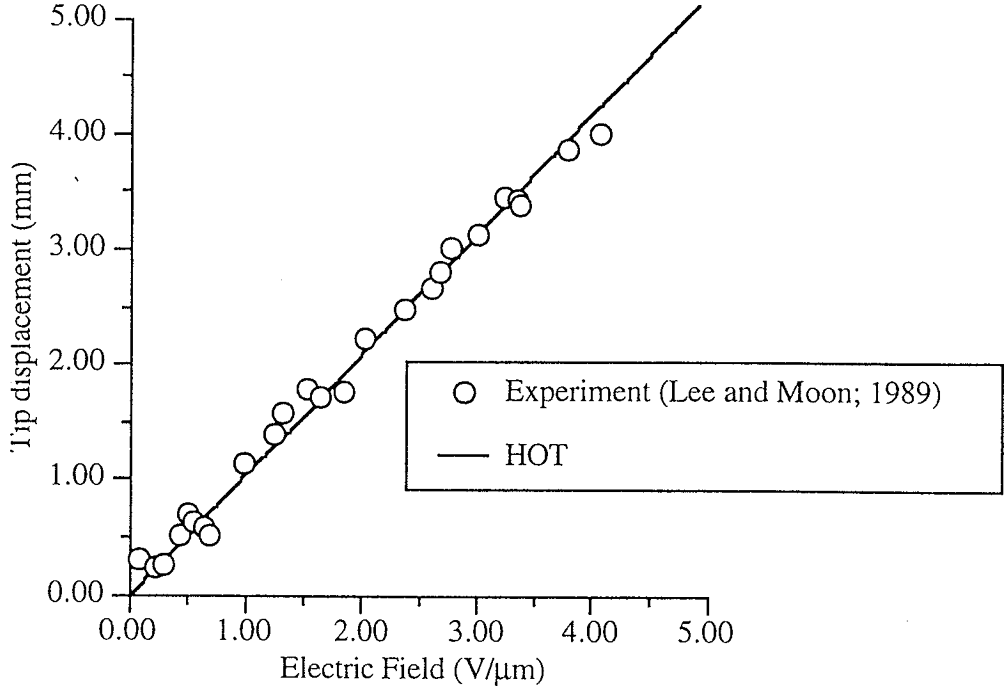

Fig. 4.8 Tip deflection piezoelectric cantilever beam.

4.3.2 Correlation of piezoelectric actuation of isotropic and orthotropic plates: The higher order theory (HOT) is now used to predict displacements and rotations of isotropic and orthotropic laminates which are deformed by energizing surface bonded piezoelectric actuators. The results using the HOT are compared to experimental results obtained by Crawley and Lazarus (1991). The test case consists of a cantilever laminate with dimensions shown in Fig. 4.9. Fifteen pairs of piezoceramic PZT actuators are surface bonded to either an aluminum plate or a graphite/epoxy plate of the same dimensions with stacking sequences $[0°/45°/-45°]_s$ and $[30°/30°/0°]_s$. The thicknesses of the composite laminate and the surface bonded piezoelectric actuators are 0.83 mm and 0.25 mm, respectively. The bimorph piezoelectric actuator pairs are energized with opposite electric fields to produce plate bending. Material properties are presented in Table 4.9 and will be discussed in further detail in a moment.

The HOT finite element model comprises 77 elements and a total of 616 degrees of freedom. Overall, good agreement is observed between the HOT and the experimental results for both the aluminum and Gr/Ep plates as shown in Figs. 4.10 - 4.12. The nondimensional quantities shown include the plate bending (w_1), twist (w_2) and camber or transverse bending (w_3) which are defined as follows.

$$w_1 = M_2 / W \tag{4.3.1}$$

$$w_2 = (M_3 - M_1) / W \tag{4.3.2}$$

$$w_3 = \frac{M_2 - (M_3 + M_1)/2}{W} \tag{4.3.3}$$

where M_1 and M_3 are transverse displacements measured at the outer transverse edges, M_2 is the transverse displacement measured at the center of the plate and W is the width of the plate (Fig 4.9).

As indicated previously, the material properties for the composite laminate and the piezoelectric actuators is presented in Table 4.9. The properties used are identical to those used by Seeley and Chattopadhyay (1996) indicated as [1] in Table 4.9. It must be noted that the composite substructure is an orthotropic material (Gr/Ep T300/976) while the piezoelectric material (PZT G-1195) is considered an isotropic material in the context of two dimensional laminate theories. The values used in this work are either taken directly from the original research paper by Crawley and Lazarus (1991), or a reasonable estimate is made for properties not listed in the original study. For instance, the piezoelectric coupling can be represented by either a single constant (d_{31}), or two experimentally determined parameters as described by Crawley and Lazarus (1991). Neither of these values used in their study are listed in their paper for the cases presented. Therefore, a reasonable guess must be made. However, other authors have taken unusual liberties with the values for the material parameters in an effort to obtain experimental verification. The values used by several different authors for verification studies are presented in Table 4.9 when available. Relevant data which is not given in these references is also indicated. As an example, both Chandrashekhara and Agarwal (1993) and Ha et al. (1992) use significantly different values of the shear moduli (G_{23}, G_{13}, and G_{12}) for their research. Only G_{12} is given in the original work which is different from both of the values used by these authors. Detwiler (1995) does not specify the material properties used, but the applied electric fields (E_3) for the two cases indicated as specified in their work are completely different from the original work of Crawley and Lazarus (1991). All of the authors indicated in Table 4.9 present results which correlate with the experimental data. However, deviations are also apparent. From this discussion, it can be concluded that the HOT agrees with the published experimental data as well as can be expected. Deviations are the result of imprecise knowledge of the experimental parameters.

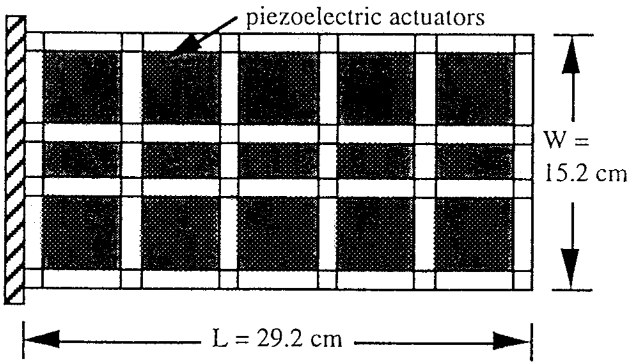

Fig. 4.9 Cantilever plate with piezoelectric actuators.

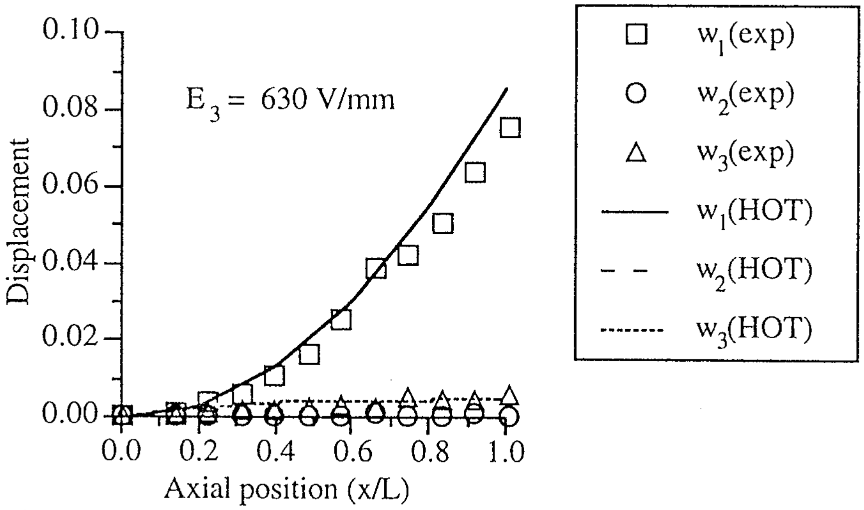

Fig. 4.10 Nondimensional static mode shapes for aluminum plate.

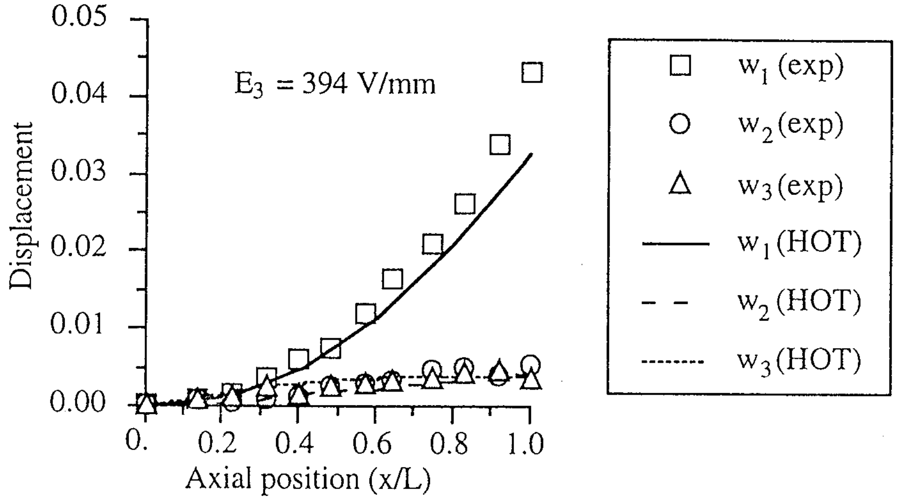

Fig. 4.11 Nondimensional static mode shapes for Gr/Ep [0°/45°/-45°]$_s$ plate.

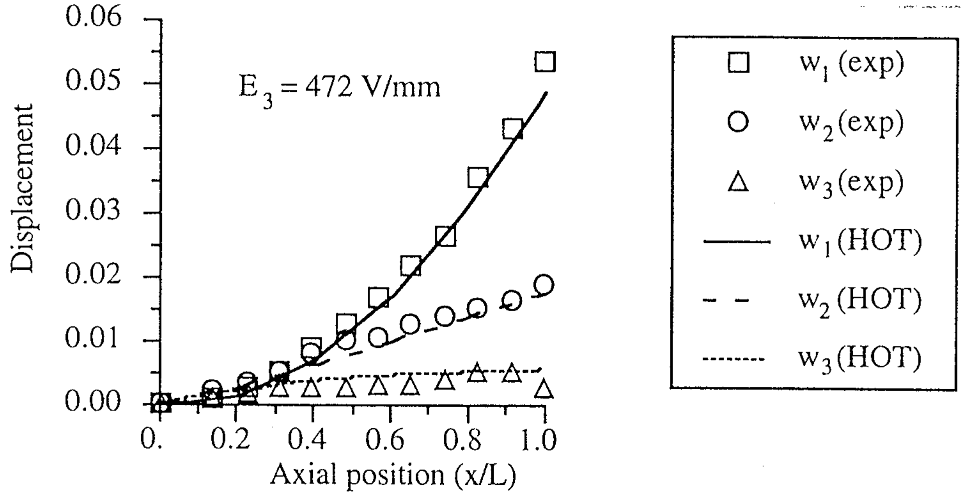

Fig. 4.12 Nondimensional static mode shapes for Gr/Ep [30°/30°/0°]$_s$ plate.

Table 4.9 Material properties for cantilever plate experimental validation.

Material	Authors					
	[1]	[2]	[3]	[4]	[5]	[6]
<u>T300/976 Gr/Ep</u>						
E_1 (GPa)	143	143	144.23	150	*	150
E_2 (GPa)	9.7	9.7	9.65	9	*	9
ν_{12}	0.3	0.3	0.3	0.3	*	0.3
$G_{12}=G_{13}$ (GPa)	6.0	6.0	4.14	7.10	*	7.10
G_{23} (GPa)	2.5	-	3.45	2.50	*	*
<u>PZT G-1195</u>						
E (GPa)	63.0	63.0	63.0	63.0	*	63.0
ν	0.3	0.3	0.28	0.3	*	0.3
d_{31} (pm/V)	253	*	254	254	*	264
E_3 (Al) (V/mm)	630	630	-	-	-	-
E_3 ([0°/±45°]$_s$) (V/mm)	394	394	394	394	630	400
E_3 ([0°/30°$_2$]$_s$) (V/mm)	472	472	-	-	755	480

[1] Seeley and Chattopadhyay (1996)
[2] Crawley and Lazarus (1991)
[3] Chandrashekhara and Agarwal (1993)
[4] Ha et al. (1992)
[5] Detwiler et al. (1995)
[6] Koconis et al. (1994)
(-) nonessential parameter absent
(*) essential parameter absent

4.3.3 Correlation of composite beam natural frequencies: The current higher order theory (HOT) is now applied to the problem of determining the natural frequencies of beam with bonded piezoelectric actuators. Two examples are presented to correlate the HOT with both experimental data and other analytical techniques. The dimensions of the two beams used in this study which have varying boundary conditions are shown in Figs 13 (a and b) along with the actuator locations. The material properties for the aluminum beam sub structure and the PZT piezoelectric actuators used for both examples are assumed to be isotropic and are given as follows

Al: $E=70$ GPa $\nu=0.3$ $\rho=2700$ kg/m^3 PZT: $E=63$ GPa $\nu=0.3$ $\rho=7600$ kg/m^3 $d_{31}=254$pm/V

In the first example the first five natural frequencies of a simply supported aluminum beam with dimensions shown in Fig 4.13 (a) are determined using the HOT and compared to experimental results obtained by Richard and Cudney (1993). A piezoelectric patch of dimensions 38x38mm and thickness 0.3 mm is bonded to one surface of the beam at the location indicated in Fig 4.13 (a). Although the stiffness of the piezoelectric patch is similar to that of aluminum, it is almost three times as dense. Therefore, the natural frequencies of the beam with the piezoelectric patch are different from those of a similar beam with no piezoelectric patch. Results obtained using the HOT and from the experiments are presented in Fig. 4.14 where it is observed that the first five natural frequencies of the beam agree fairly well with the experimental results. In general, the frequencies are over predicted by the HOT indicating that the structure is slightly softer than indicated by the material and geometric properties alone. This is most likely due to nonideal boundary conditions which allow small displacements that cause the experimental frequencies to be lower than if perfect boundary conditions were possible. The largest deviation occurs for the fifth mode and is less than 10%. Therefore, correlation between the HOT and these experimental results is satisfied.

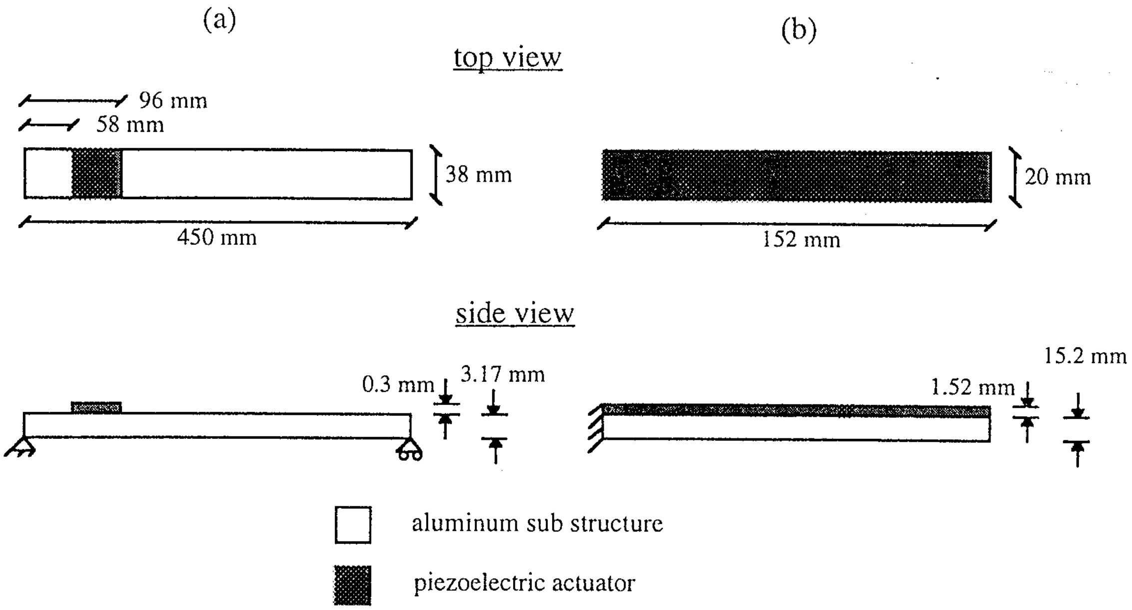

Fig. 4.13 Beams with piezoelectric actuators (a) simply supported (b) cantilever.

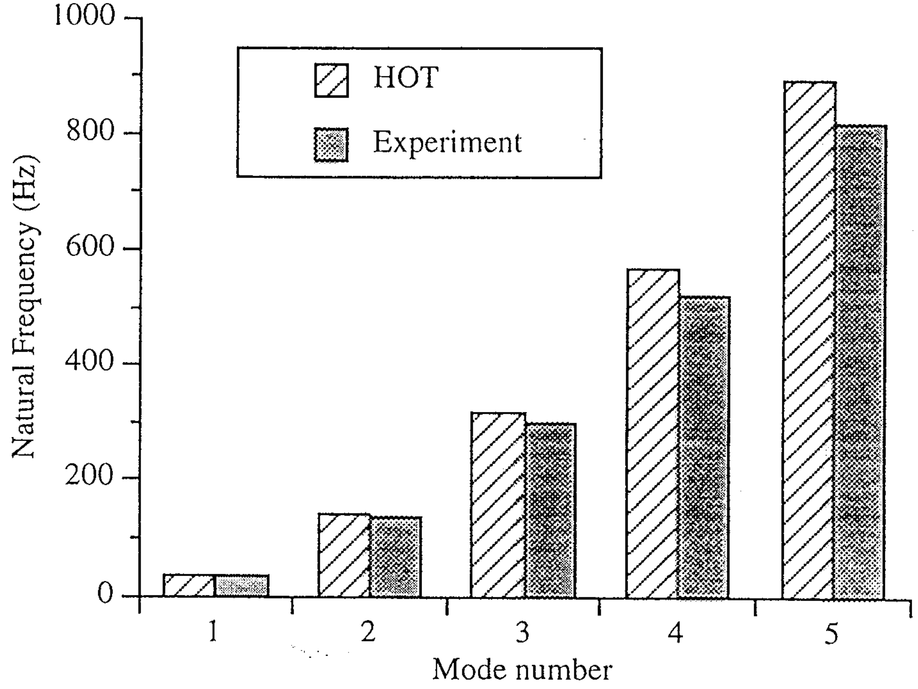

Fig. 4.14 Correlation of HOT with experimentally determined natural frequencies

The next example is studied to determine how well the HOT predicts the natural frequencies of a cantilever beam with a bonded piezoelectric actuator compared to other analytical approaches. The test article is again an aluminum beam with a PZT actuator, only now cantilever boundary conditions are used. Dimensions of this beam are shown in Fig. 4.13 (b) where it is shown that the PZT actuator covers the entire top surface of the beam. The first ten natural frequencies are computed using the HOT. These results are compared to the same frequencies determined using the first order shear deformation theory (FSDT) and the layerwise theory of Reddy (1991) (LT). It must be noted that implementation of the layerwise theory requires discretization through the thickness direction as well as the inplane directions which improves the accuracy of the theory, but significantly increases the computational effort as well. Results obtained using the FSDT, HOT and LT approaches are presented in Table 4.10. In general, frequencies predicted using the HOT lie between the values predicted by the FSDT and the LT. The FSDT is generally slightly stiffer than either the HOT or the LT due to its crude approximation for the transverse shear stress. The LT can be considered the most accurate of the three approaches, but is also the most expensive by a significant margin. The frequency for the lowest mode is approximately 2% higher than either the FSDT or the LT. For this study, both the FSDT and the LT are implemented using 30 lengthwise elements while only 15 lengthwise elements are used for the HOT. Further mesh refinement for the HOT would most likely reduce this effect. Overall, the trends in the frequencies predicted by the HOT correlate well with the FSDT and the LT.

Table 4.10 Correlation of natural frequencies (Hz) for cantilever beam.

Mode Number	FSDT	HOT	LT
1	537.6	548.4	538.4
2	3193.0	3189.1	3180.7
3	7576.6	7583.7	7565.6
4	8324.0	8331.3	8200.9
5	14970.1	15005.4	14434.2
6	22428.1	21982.5	21371.3
7	22984.4	22480.6	22709.0
8	31056.9	30761.5	28886.5
9	37901.0	36169.6	33985.3
19	39994.7	38001.4	37947.8

4.4 Correlation of Debonded Orthotropic Laminates

In this section, the higher order theory (HOT) is used to predict displacements and natural frequencies of a debonded composite laminate. The geometry of the test structure is shown in Fig 4.15. This laminate consists of four plies, each with thickness t=h/4, and the stacking sequence is $[0°/90°]_s$. Debonding is introduced at the tip of the laminate between the third and fourth plies shown in the side view of Fig. 4.15. The length of the debonding (L_d) is described by the nondimensional debonding parameter β ($\beta=L_d/a$). The static displacements are caused by a transversely applied tip load which is uniformly distributed across the width of the laminate, but is applied directly to the fourth ply which becomes separated from the rest of the laminate due to debonding. The material properties of the laminate are as follows

$E_1 = 60\ GPa,\ E_2 = 25\ GPa,\ \upsilon_{12} = 0.25,\ G_{23} = 4.8\ GPa,\ G_{13} = 12\ GPa,\ G_{12} = 12\ GPa,\ \rho = 1500\ kg/m^3.$

The static and dynamic results obtained using the HOT are compared with results acquired using NASTRAN. The HOT analysis, which is two dimensional in nature, consists of either a 10x10 or 12x12 mesh, depending on the length of the debonding. The nondebonded region requires only one element through the thickness while two elements through the thickness are used to model the debonded region. Three dimensional CHEXA elements in NASTRAN are used to correlated the HOT results. These elements contain eight nodes with three degrees of freedom at each node. A 20x20x4 mesh is used in this case. This is the smallest practical mesh for the example presented here due to limitations on the aspect ratios of the CHEXA elements. It must be noted that many more degrees of freedom are required for the NASTRAN results which results in significantly more computation time and memory requirements. To obtain correlation for displacements and natural frequencies, several different laminate thicknesses are studied ranging from thin to very thick (a/h=100, 25, 10) for different debonding lengths (β=0, 0.10, 0.25, 0.50). Both the HOT and NASTRAN results were obtained by the author.

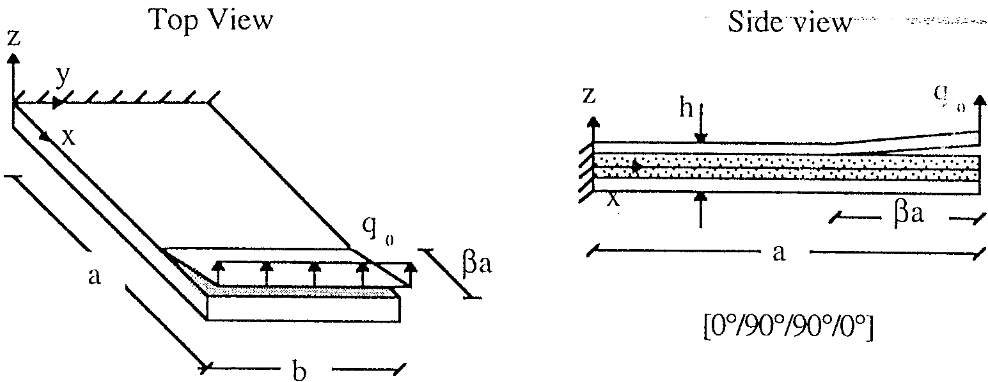

Fig. 4.15 Debonded cantilever composite laminate with tip load

4.4.1 Static correlation of debonded composite laminate: The static deflections of the debonded composite laminate due to an applied tip load are evaluated first to judge the accuracy of the HOT compared to a three dimensional NASTRAN analysis. The transverse deflections are normalized as follows

$$w^* = w\frac{h^3E_2}{q_0a^4} \tag{4.4.1}$$

In Figs 4.16 (a-d), w* is presented for the case of a moderately thick laminate (a/h=25) for varying debonding lengths (β=0, 0.10, 0.25, 0.50) for both the HOT and NASTRAN results. Obviously, the case of β=0 represents the limiting case for a composite laminate with no debonding. The nondimensionalized deflections are presented along the center of the laminated from the clamped end to the tip (w*(x,b/2)). Deflections both above and below the debonding are shown which occurs as the debonded section pulls away from the rest of the laminate. This is because the tip load is applied to debonded ply, which is the fourth and outermost ply. It can be seen that the deflections in the regions above and below the debonding become largely independent of one another as the debonding length increases. Increasing the debonding length also significantly increases the nondimensionalized deflections since the structure is weakened by the presence of debonding. It must be noted that the deflections of the debonded composite laminate compared to the geometric dimensions of the laminated appear greatly exaggerated in Figs 4.16 (a-d) to facilitate determining the accuracy of the HOT. Agreement between the HOT and NASTRAN is excellent, even for large debonding lengths (β=0.25, 0.50) . The HOT predicts deflections which are very similar to those predicted by NASTRAN for this moderately thick (a/h=25) laminate.

The HOT is used to predict deflections of debonded composite laminates for several different thicknesses ranging from thin to very thick (a/h=100,25,10). The tip deflections for these three cases are presented in Figs 4.17 (a-c) where the deflections are normalized as before. Both the deflection of the debonded ply above the debonding at the tip of the laminate and the other region below the debonding are shown for values of β=0, 0.10, 0.25, 0.50. Results are presented for these deflections using both the HOT and NASTRAN. As before, agreement between the HOT and NASTRAN is excellent. The tip deflection of the debonded region increases significantly as the debonding length is increased. Since this region is the most compliant region of the structure, is deflects the most. The deflection of the region below the debonded region actually decreases as the debonding length is increased since it is significantly stiffer than the debonded region and the force is applied only to the debonded region. The HOT under predicts the deflection of the debonded region by a small amount for large debonding lengths (β=0.50). This is possibly due to the following rational. The stress gradients near the interface of the debonded and nondebonded region are large. The fine mesh used for the three dimensional NASTRAN analysis, which includes discretization through the thickness direction, more accurately captures local stress concentrations in this area. The course mesh used by the two dimensional HOT produces a some what stiffer structure which results in slightly smaller displacements for this extreme case. The difference between the HOT and the NASTRAN deflections is about 6% in the worse case, but is generally much less. The HOT also uses significantly fewer degrees of freedom than the NASTRAN analysis.

Therefore, the HOT is a reliable, but much more efficient, method of studying the effects of debonding in composite laminates.

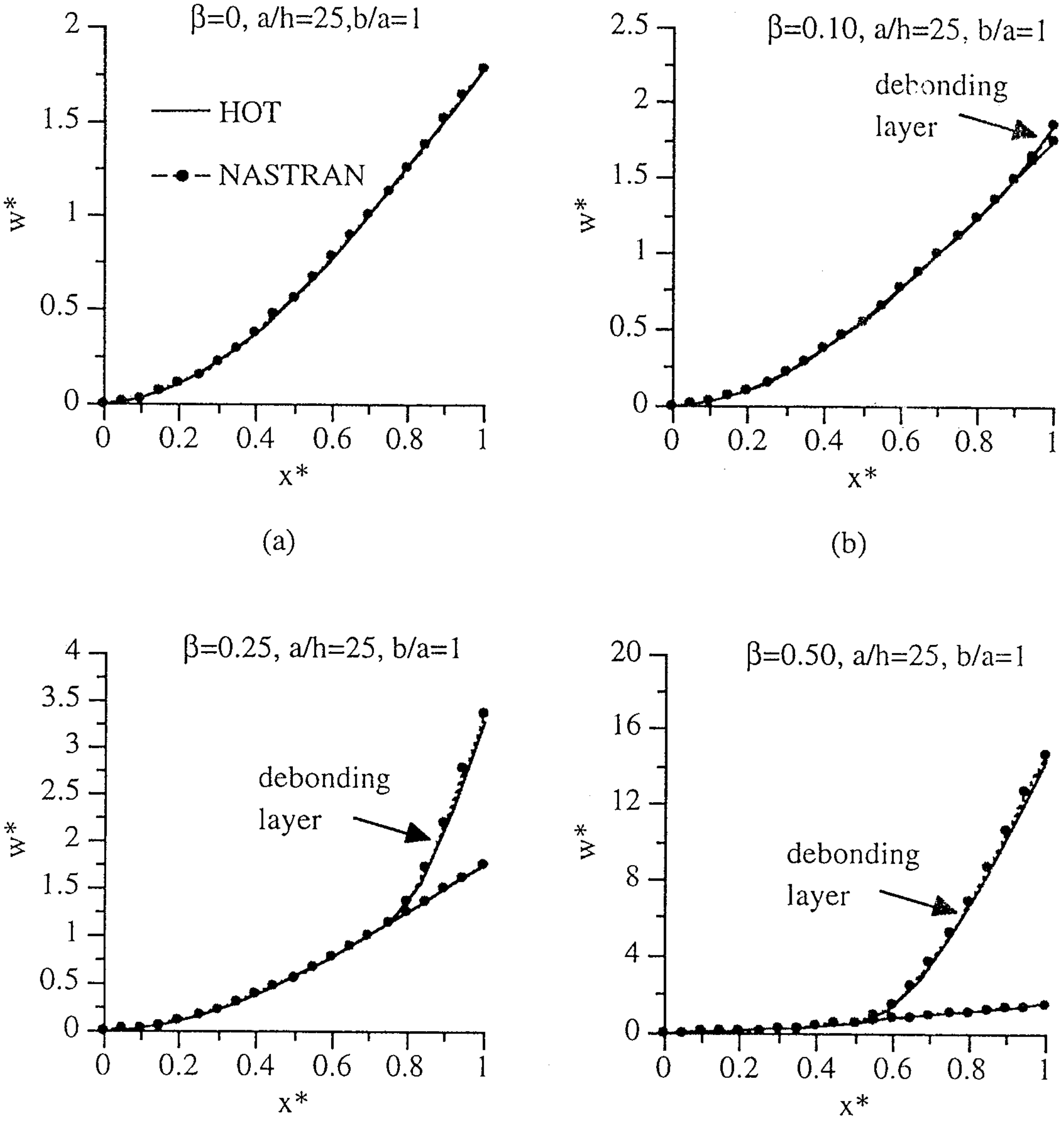

(a) (b)

(c) (d)

Fig. 4.16 Nondimensional displacements of debonded composite laminated.

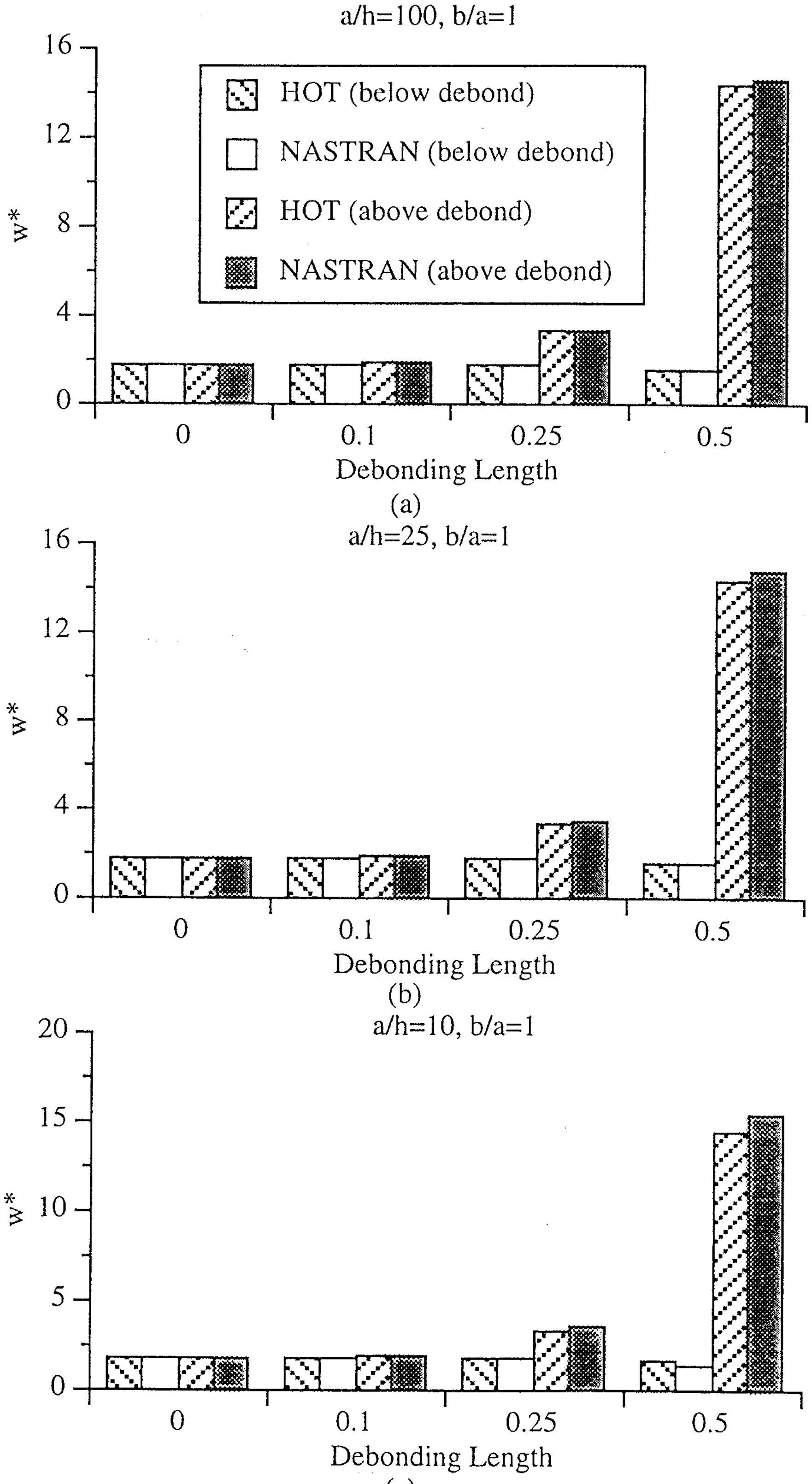

(c)

Fig. 4.17 Nondimensional displacements for debonded composite laminates with varying thickness.

4.4.2 Natural frequency determination of debonded composite laminate: The HOT is now used to predict the natural frequencies of the debonded composite laminate being studied shown in Fig 4.15. To obtain correlation for the natural frequencies, several different laminate thicknesses are again studied ranging from thin to very thick (a/h=100, 25, 10) for four different debonding lengths (β=0, 0.10, 0.25, 0.50). The HOT results are compared to NASTRAN results using three dimensional CHEXA elements as before. Again, all results were obtained by the author. The natural frequencies for the first ten modes are presented in Tables 4.11 - 4.13. The natural frequencies are normalized as follows.

$$\omega_i^* = \omega_i \frac{a^2}{h}\sqrt{\frac{\rho}{E_2}} \qquad i = 1,2,\ldots,10 \qquad (4.4.2)$$

Correlation between the HOT and the NASTRAN (CQUAD4) results is very good. In general, the frequencies are reduced for all modes as the debonding length increases. The only exceptions to this trend occurs for the first mode of each thickness case studied from β=0 to β=0.10. This is because a 12x12 mesh is used for β=0 and a 10x10 mesh is used for β=0.10. The courser mesh has a slight effect on the natural frequency determination, but is on the order of 1% and does not have a significant effect on any of the other modes. The lowest natural frequency is not significantly effected by the presence of the debonding until it becomes very large. This is because the fundamental mode for the nondebonded laminate is also the first bending mode which is relatively insensitive to localized changes, such as debonding, until it becomes very large. The second mode, which is a twisting mode, is also relatively insensitive to the debonding until it becomes very large. It does appear to be more sensitive than the first mode to changes in the debonding length, however. The third through sixth modes become increasingly more sensitive to the debonding length. A significant drop in these frequencies is observed from β=0.10 to β=0.25 whereas the first two modes remain mostly unchanged until the debonding length is increased from β=0.25 to β=0.50. This is because these modes, begin to be effected by localized changes in the stiffness properties of the structure due to debonding. The higher modes presented, seven through ten, contain many local inflection points and are significantly altered by the presence of even relatively small debondings. These mode shapes are altered significantly as β is increased and incorporate localized deflections due the debonding rather than the global deflections contained in the first few modes. Some of the frequencies for modes with large debonding are very closely spaced. It must be noted that the debonded structure is not symmetric. Therefore, these frequencies do not correspond to repeated symmetric modes, but rather distinct mode shapes due the presence of debonding. The closeness of their values is mere coincidence. The frequencies corresponding to all modes are also effected by the thickness to length ratio (a/h) of the laminates. Increasing the thickness of the laminate results in more deformation due to transverse shear effects. The effect is lower natural frequencies as observed in Tables 4.11 - 4.13. The HOT captures all of the features of the natural frequencies and mode shapes found in the more expensive three dimensional NASTRAN analysis. The results of these two approaches correlate very well. Therefore, the HOT can be used as a reliable technique to predict natural frequencies of debonded composite laminates.

Table 4.11 Natural frequency parameters for debonded composite laminate (a/h=100)

mode number	analysis type	debonding length β=0	β=0.10	β=0.25	β=0.50
1	HOT	0.2427	0.2465	0.2449	0.2068
	NASTRAN	0.2436	0.2436	0.2424	0.2057
2	HOT	0.4924	0.4897	0.4650	0.3118
	NASTRAN	0.4839	0.4771	0.4580	0.2995
3	HOT	1.3908	1.3687	1.0501	0.3120
	NASTRAN	1.3733	1.3560	1.0338	0.3100
4	HOT	1.5379	1.5363	1.1460	0.5009
	NASTRAN	1.5401	1.5352	1.1128	0.5107
5	HOT	1.9268	1.8736	1.1516	0.5545
	NASTRAN	1.9084	1.8665	1.1171	0.5208
6	HOT	3.0349	2.9024	1.5212	0.9745
	NASTRAN	2.9840	2.8782	1.4981	0.9285
7	HOT	3.3196	3.1790	1.5965	1.0725
	NASTRAN	3.2837	3.1869	1.5720	1.0694
8	HOT	4.2619	4.2021	1.7340	1.2858
	NASTRAN	4.2817	4.1994	1.6242	1.2905
9	HOT	4.6268	4.4877	1.8610	1.3950
	NASTRAN	4.6091	4.4590	1.8882	1.4244
10	HOT	4.9103	4.6435	2.3755	1.6188
	NASTRAN	4.8430	4.6071	2.2228	1.5634

Table 4.12 Natural frequency parameters for debonded composite laminate (a/h=25)

mode number	analysis type	debonding length β=0	β=0.10	β=0.25	β=0.50
1	HOT	0.2418	0.2424	0.2409	0.2053
	NASTRAN	0.2433	0.2433	0.2421	0.2047
2	HOT	0.4856	0.4770	0.4532	0.3101
	NASTRAN	0.4802	0.4739	0.4547	0.2962
3	HOT	1.3693	1.3410	1.0450	0.3102
	NASTRAN	1.3599	1.3425	1.0073	0.3058
4	HOT	1.5063	1.4995	1.1360	0.4924
	NASTRAN	1.5281	1.5232	1.0851	0.5065
5	HOT	1.8767	1.8214	1.1389	0.5528
	NASTRAN	1.8833	1.8443	1.0973	0.5164
6	HOT	2.9297	2.8016	1.4892	0.9712
	NASTRAN	2.9239	2.8223	1.4756	0.9232
7	HOT	3.1598	3.1047	1.5704	1.0589
	NASTRAN	3.2216	3.1226	1.5501	1.0581
8	HOT	3.2483	3.1379	1.7190	1.2648
	NASTRAN	3.4287	3.4284	1.5937	1.2794
9	HOT	4.0596	3.9949	1.8071	1.3733
	NASTRAN	4.2060	4.1202	1.8580	1.3990
10	HOT	4.3959	4.2628	2.3523	1.6112
	NASTRAN	4.5061	4.3500	2.1889	1.5545

Table 4.13 Natural frequency parameters for debonded composite laminate (a/h=10)

mode number	analysis type	debonding length β=0	β=0.10	β=0.25	β=0.50
1	HOT	0.2375	0.2378	0.2365	0.2033
	NASTRAN	0.2417	0.2417	0.2405	0.2020
2	HOT	0.4578	0.4516	0.4304	0.3054
	NASTRAN	0.4659	0.4608	0.4420	0.2880
3	HOT	1.2640	1.2549	1.0177	0.3056
	NASTRAN	1.2992	1.2828	0.9399	0.2956
4	HOT	1.2778	1.2580	1.0896	0.4700
	NASTRAN	1.3715	1.3714	1.0151	0.4918
5	HOT	1.3658	1.3544	1.1042	0.5448
	NASTRAN	1.4675	1.4629	1.0403	0.5044
6	HOT	1.6681	1.6248	1.2079	0.9541
	NASTRAN	1.7779	1.7471	1.3694	0.9055
7	HOT	2.5372	2.4515	1.3471	0.9946
	NASTRAN	2.6814	2.5983	1.4012	1.0188
8	HOT	2.9460	2.8346	1.4861	1.0483
	NASTRAN	2.9444	2.8533	1.4737	1.2307
9	HOT	3.2713	3.1140	1.6013	1.2013
	NASTRAN	3.2741	3.2734	1.5107	1.2985
10	HOT	3.3203	3.2350	1.6485	1.2773
	NASTRAN	3.6858	3.6845	1.7465	1.3863

4.5 Determination of Penalty Factors

The determination of the numerical values of the penalty factors, ρ_1 and ρ_2, which are used in conjunction with implementation of the continuity conditions, is an important issue which needs to be addressed (Section 3.7). The augmented equations of motion (Eqn. 3.7.11) are found by minimizing the potential and kinetic energies which include the penalty terms to satisfy the continuity conditions (Eqns. 3.7.8 and 3.7.9). Minimizing the augmented potential and kinetic energies represents minimizing the actual potential and kinetic energy functions while satisfying the constraints introduced by the penalty terms. To be effective, magnitude of the penalty terms must be comparable to the magnitude of the potential and kinetic energies. This is achieved by setting the penalty terms, ρ_1 and ρ_2, to the 1-norms of the stiffness and mass matrices, respectively. In practice, the natural frequencies predicted using this penalty approach are relatively insensitive to the actual values of ρ_1 and ρ_2 as demonstrated through the example presented next.

Consider the case for the four ply cantilever composite laminate used in the previous section where b/a=1, a/h=25, β=0.50. Debonding is introduced at the tip of the laminate between the third and fourth plies as shown in Fig. 4.15. The 1-norm of the finite element stiffness and mass matrices for this case, as predicted by the higher order theory, are on the order of 10^8 and 10^{-1}, respectively. Selecting $\rho_1=10^8$ and $\rho_2=10^{-1}$ yields very good correlation with NASTRAN results as indicated in the previous section. The sensitivity of the natural frequencies to changes in the values of these penalty factors is determined by varying the values of ρ_1 and ρ_2 over a wide range.

Results for this investigation are presented in Table 4.14. Here, the natural frequency parameters, which are normalized according to Eqn. 4.4.2, are presented for the first mode of vibration where the values of ρ_1 and ρ_2 are varied over nine orders of magnitude. In Table 4.14, values for the first natural frequency for varying ρ_1 are presented by column while values for varying ρ_2 are presented by row. It is observed that the normalized frequency parameter for the first mode changes less than 3.5% over five orders of magnitude for $10^6 \leq \rho_1 \leq 10^{10}$. This frequency parameter remains essentially unchanged over seven orders of magnitude for $10^{-5} \leq \rho_2 \leq 10^2$. Similar trends are observed for frequencies corresponding to the higher modes. Numerical ill-conditioning of the system matrices is present for values of ρ_1 and ρ_2 larger than those presented in Table 4.14 relative to the 1-norms of the mass and stiffness matrices. Clearly, this study indicates that the accuracy of the results is relatively insensitive to a reasonable selection of the penalty terms ρ_1 and ρ_2.

Table 4.14 First natural frequencies parameters for Gr/Ep $[0^\circ/90^\circ]_S$ beam, $\beta=0.50$.

ρ_1	10^3	10^4	10^5	10^6	10^7	10^8	10^9	10^{10}	10^{11}
ρ_2									
10^{-5}	0.001	0.040	0.133	0.199	0.205	0.205	0.206	0.204	0.187
10^{-4}	0.001	0.040	0.133	0.199	0.205	0.205	0.206	0.204	0.187
10^{-3}	0.001	0.040	0.133	0.199	0.205	0.205	0.206	0.204	0.187
10^{-2}	0.001	0.040	0.133	0.199	0.205	0.205	0.206	0.204	0.187
10^{-1}	0.001	0.040	0.132	0.199	0.205	0.205	0.206	0.204	0.187
10^{0}	0.001	0.037	0.122	0.199	0.205	0.205	0.206	0.204	0.187
10^{1}	0.001	0.024	0.078	0.195	0.205	0.205	0.206	0.204	0.187
10^{2}	0.000	0.009	0.000	0.000	0.204	0.205	0.206	0.204	0.187
10^{3}	0.000	0.003	0.010	0.031	0.000	0.205	0.206	0.204	0.187

5. Results for the Higher Order Theory

The developed refined higher order theory provides a framework for the analysis of composite laminates of arbitrary thickness with surface bonded/embedded actuators and is computationally efficient. Numerical results are presented first to investigate strain and stress distributions resulting from piezoelectric actuation which are presented for a cantilever composite plate with varying thicknesses. Differences between the developed higher order theory and the classical laminate theory are discussed. Static results are presented for a composite laminate including debonding. The effect of debonding on the open loop mode shape of the composite beams used in the experimental investigation are examined. Closed loop mode shapes are also presented.

5.1 Analysis of Stresses and Strains

In this section, a detailed investigation of the stresses and strains throughout a composite laminate is considered. The test article is a cantilever $[0°/0°/45°/-45°]_s$ Gr/Ep laminate with embedded PZT actuators with material properties listed in Table 5.1. The laminate is 25.0 cm in length and 12.5 cm in width (Fig. 5.1). The outermost plies have thicknesses 0.050h, the adjacent plies are 0.200h thick, and the remaining plies are 0.125h thick where h is the total laminate thickness indicated in Fig. 5.1. The piezoelectric actuators are embedded such that they replace the outermost plies in sections of the laminate where they are located. Equal but opposite electric fields of magnitude 500 V/mm are applied through the thicknesses of each actuator pair to produce bending which results in a tip displacement in the positive z direction (Fig. 5.1). All other loads are assumed to be zero. The actuators are located centrally on the laminate and the actuator length and width are 15 cm and 5.25 cm, respectively. The finite element model comprises 80 equal-sized elements with 630 total degrees of freedom. For comparison, the equivalent model using the classical laminate theory consists of 450 degrees of freedom.

Table 5.1. Material properties.

	Gr/Ep	PZT
E_1 (GPa)	143	63.0
E_2 (GPa)	9.70	63.0
ν_{12}	0.300	0.300
G_{12}, G_{13} (GPa)	6.00	24.2
G_{23} (GPa)	2.50	24.2
ρ ($\times 10^3$ Kg/m^3)	1.39	7.60
d_{31} ($\times 10^{-12}$ m/V)	-	253

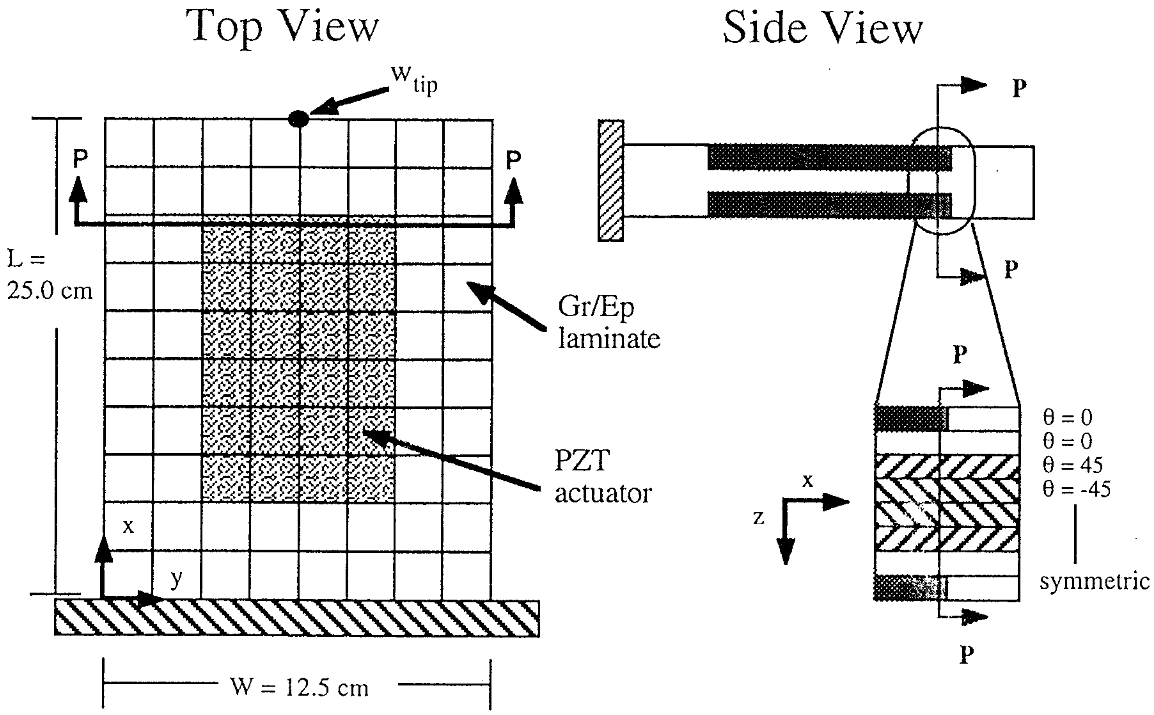

Fig. 5.1 Cantilever Gr/Ep [0°/0°/45°/-45°]$_s$ laminate with piezoelectric actuators ; top and side views.

Strains and stresses are calculated throughout the laminate at the elemental gauss points used in the stiffness matrix assembly (4x4 integration). In Figs. 5.2 - 5.3, the axial strain and stress distributions are presented, through the thickness, close to the center of section P-P as indicated in Fig 5.1. This section is chosen to study the effects of induced strain actuation where local stresses are expected to be large without the influence of global boundary conditions such as the fixed end. The transverse shear strain distribution (ε_{13}) is presented in Fig. 5.4 at this same location. Results are presented for laminates of length to thickness ratio L/h = 10 and 4 which are considered moderately thick and very thick, respectively, using both the classical laminate theory (CLT) and the higher order theory (HOT).

Figures 5.2 (a-b) present the strain distribution through the thickness for the moderately thick and very thick laminates, respectively. Although the strain distribution is slightly nonlinear for the moderately thick laminate (Fig. 5.2 (a)), the refined theory shows that it is significantly nonlinear for the very thick laminate (Fig. 5.2 (a)). The CLT does not accurately capture this complexity. The strain is larger near the free edge of the laminate due to local deformation from the piezoelectric actuation in the outermost plies, but drops off more rapidly away from the actuator near the neutral axis as compared to the CLT.

The stresses due to the piezoelectric actuation are presented in Figs. 5.3 (a-b) for four plies (one half of the laminate thickness). The stresses in the other half of the laminate are equal, but opposite, due to the symmetry of the laminate and the actuation mode. In these figures, the stresses are normalized, ply by ply, to the largest value predicted by CLT. The deviation in the stresses predicted by the HOT and the CLT are small in the outermost ply, which is the piezoelectric layer. This is because the effect of the additional strain predicted by the HOT is offset by the induced strain due to piezoelectric actuation. In the adjoining substrate ply, where the induced strain is zero, the stress is significantly larger than that predicted by the CLT. However, the stresses in the plies away from the actuator and near the midplane are less than those predicted by the CLT due to the localized nature of the stresses resulting from piezoelectric actuation. These results indicate that the contribution of the higher order terms from the refined displacement field is significant and is important in the prediction of the strains and stresses through the thickness of composite laminates, particularly near the source of the induced strain actuation.

The distribution of the transverse shear strain (ε_{13}) through the thickness of the laminate is presented in Fig. 5.4 for both L/h values and shows significant variation through the thickness. The maximum value occurs at the midplane of the plate. As expected, the strain increases as the thickness of the plate is increased. It must be noted that the transverse strains are assumed to be zero in the classical theory.

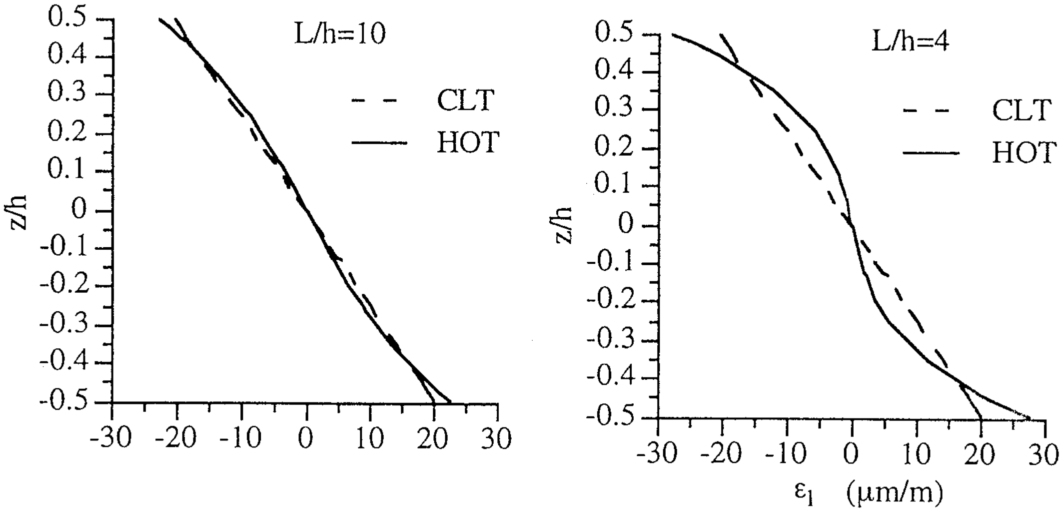

(a) (b)

Fig. 5.2 Axial strain (a) L/h=10; (b) L/h=4.

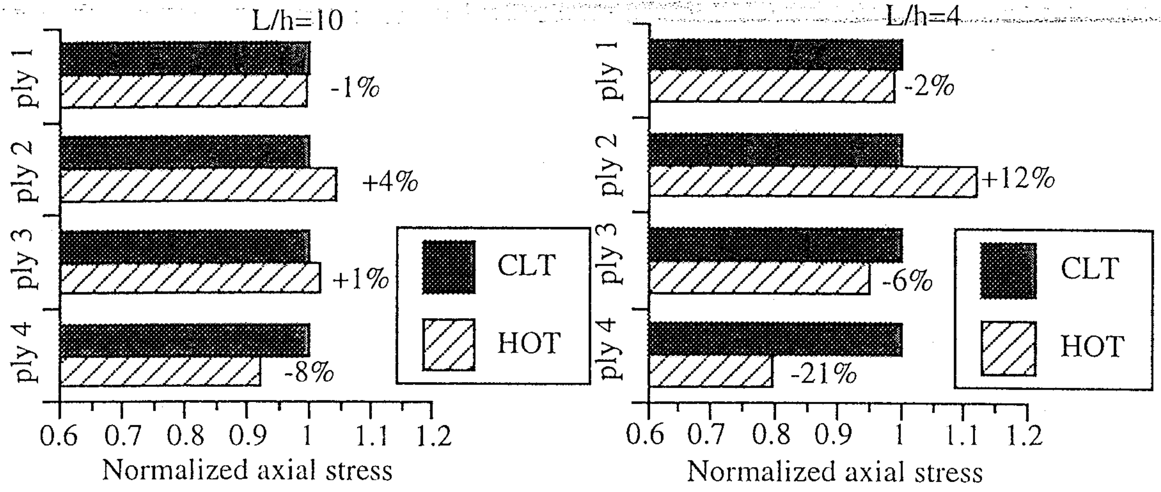

(a) (b)

Fig. 5.3 Normalized Axial stress (a) L/h=10; (b) L/h=4.

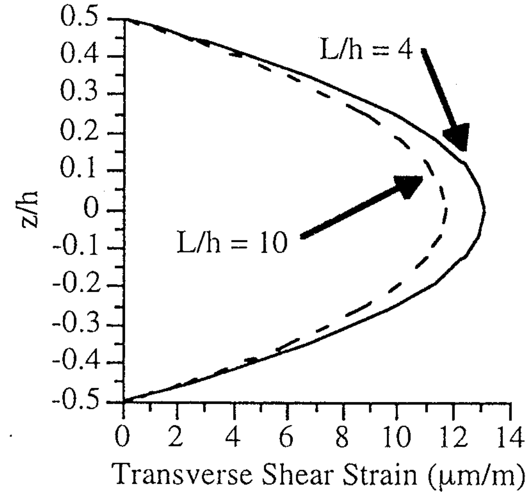

Fig. 5.4 Transverse Shear Strain (ε_{13}).

5.2 Static displacements including debonding

Numerical results are presented for a cantilever Gr/Ep composite plate with embedded piezoelectric actuators and a stacking sequence of $[0°/90°/0°]_6$ and dimensions L = 25cm, W = 10cm, and h = 2.286mm. The ply thickness is 0.127mm. Plies numbered 13-16 are replaced with a single PZT piezoelectric layer of thickness 0.381mm which represents a commercially available piezoelectric material thickness. Material properties are those of

Gr/Ep and PZT shown in Table 5.1. A mesh size of 25x10 elements, resulting in 2002 degrees of freedom, is used for the nondebonded finite element model. The piezoelectric layer is energized with a constant voltage of 150 volts.

Both longitudinal bending and camber deflections result from the piezoelectric actuation for the case with no debonding shown in Fig. 5.5. This type of deformation is produced because the piezoelectric layer is offset from the neutral axis of the plate which produces bending moments about the X and Y axes. Next, a debonding is introduced at the interface between the composite substructure and the piezoelectric layer (plies 12 and 13), located at the free end of the plate, through the entire width (20 cm < x < 25 cm, 0 cm < y < 10 cm). The mesh for the composite substructure, located at the midplane of the nondebonded portion of the plate, comprises 20x10 elements. Two additional 5x10 meshes are generated above and below the debonding at the midplanes of each region. These meshes are offset from the midplane of the nondebonded portion of the plate as shown in Fig. 5.6. It is important to note that Figs. 5.5 and 5.6 are not to scale so that the different meshes may be easily identified. The piezoelectric layer is again energized with a constant voltage of 150 volts. The static deflection in this case (Fig. 5.6) is significantly different from the first case (Fig. 5.5) where actuation produces bending which results in negative transverse displacements. The nondebonded portion of the plate bends downward as before, as does the region below the debonding. However, the region above the debonding bends in a positive transverse direction. This is because the offset of the piezoelectric layer from the local midplane in the debonded region is opposite the offset in the nondebonded region. This results in a reversal of the bending moment due to piezoelectric actuation and a positive transverse displacement. Therefore, the presence of debonding causes the actuator to peel away from the substructure. These results indicate that a thorough understanding of the effects due to debonding is critical to designing structures with smart composite materials.

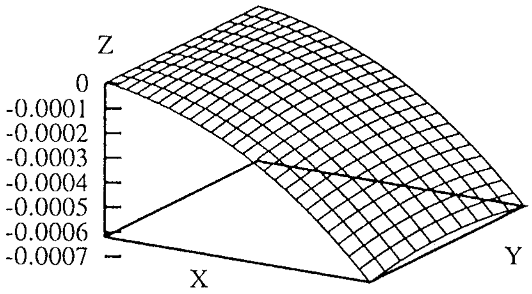

Fig. 5.5 Static deflection due to piezoelectric actuation.

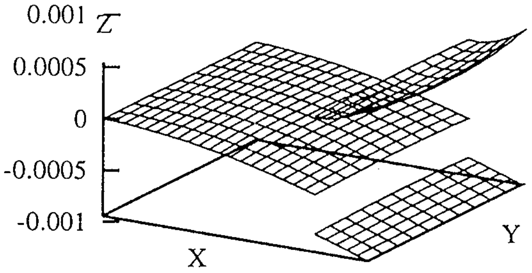

Fig. 5.6 Static deflection due to piezoelectric actuation including debonding.

5.3 Open loop frequencies and mode shapes including debonding

The effect of debonded piezoelectric transducers on the open loop frequencies and mode shape of the composite substructure is investigated in this section. The test specimens are identical to those utilized in the experimental investigation corresponding to beams 1-4 used in the Chapter 6.. These beams have dimensions 30 x 5.3 x 0.194 cm with a stacking sequence of $[0°/90°]_{3S}$. Piezoelectric transducers with thickness 0.76 mm are bonded near the root of the beam for vibration control. Debonding is introduced at the interface of piezoelectric transducer #2 (top surface) and the Gr/Ep substructure at the edge of the transducers nearest the root and extends through the width of the beam. As before, the parameter β represents the length of the debonding. Values of β = 0.0, 0.06, 0.12, 0.18 are investigated for several different modes. The results obtained using the higher order theory (HOT) for the nondebonded cases comprise a 17x3 finite element mesh and additional elements are added as needed to account for varying lengths of debonding.

The open loop mode shapes with and without debonding of piezoelectric transducer #2, obtained using the present approach, are presented in Figs. 5.7 and 5.8 and the frequencies are shown in Table 5.2. The first five mode shapes in the absence of debonding are shown in Fig. 5.7. These mode shapes are typical of the structure being analyzed. The first two modes represent bending modes, the third and the fourth modes are twist modes and the fifth mode represents the third bending mode as indicated in the first column. The frequencies corresponding to these nondebonded (β=0) modes are presented in Table 2. The sequential mode number of each of the frequencies is shown in parenthesis. As the debonding length is increased to $\beta = 0.06$, the magnitudes of the frequencies decrease slightly. This is due to a small reduction in the structural stiffness due to debonding. However, no significant changes are observed in the mode shapes.

Further increase in the debonding length produces significant changes in the mode shapes. The first several open loop mode shapes for $\beta = 0.18$ are shown in Fig. 5.8. It must be noted that in Fig. 5.8, the wire frame elements used to represent the mode shapes are plotted at the midplane of each element. The midplane corresponding to the debonded portions of the structure is different from the midplane corresponding to the nondebonded structure. Therefore, the elements in the debonded regions appear to be disconnected from the rest of the structure. This presentation of the mode shapes is chosen for clarity. Some of these modes, such as the first bending mode (Fig. 5.8 (a)) exhibit global deformation of the substructure. Other modes, such as the second bending mode (Fig. 5.8 (c), clearly indicates local deformation caused by the debonding of the actuators. Therefore, it is necessary to study the modes with debonding in greater detail. In Table 2, frequencies corresponding to modes which exhibit bending or twisting are indicated using B or T, respectively. The letters G and L are used to indicate global or local behaviors, respectively and S and A refer to symmetric and antisymmetric modes, respectively. For instance, Figs. 5.8 (a) and (b) show mode shapes which have characteristics of the first bending mode (B1). In Fig. 5.8 (a), the deformation is primarily global in nature (G). However, Fig 5.8 (b) indicates that the deformation is predominately local (L) due to the debonding of the actuator. The mode shape presented in Fig. 5.8 (a) shows that both the deformation of the debonded region and the rest of the substructure are in phase indicating a symmetric (S) mode. This is in contrast to the mode shape presented in Fig. 5.8 (b) where the local and global deformation are out of phase indicating an antisymmetric (A) mode. Therefore, the mode shapes presented in Figs. 5.8 (a) and (b) are denoted GB1S and LB1A, respectively. The frequencies corresponding to these modes are sequential as indicated in Table 2, but their values differ significantly (24.208 Hz for LB2A and 55.911 Hz for GB2S for β=0.18).

The presence of debonding can have a significant and counter intuitive influence on the values of the frequencies corresponding to the global and local counterparts of modes displaying similar physical characteristics. It is observed that increase in the debonding length introduces local modes. For example, LB1S (β=0.12) and LB1A (β=0.18) correspond to local bending modes which are absent for smaller values of β (Table 2). Similar observations are made for the higher modes as well. It is also interesting to note that although there is a general decrease in the values of the natural frequencies as the debonding length is increased, the value of the frequency corresponding to the second global bending mode increases (from 114.85 Hz to 118.12 Hz) as β is increased. Another point is that for β=0.12, although the local twist modes are present (LT1A, LT2S), the second local bending mode is absent. When the second local bending mode (LB2S) does appear at β=0.18, it is at a significantly higher frequency that either of the twist modes as indicated by the magnitude of the frequency and the sequential mode number of the frequency in parenthesis The global and local counterparts of the first twist modes for β=0.12 and β=0.18 display symmetric/antisymmetric behavior while both the global and local counterparts of the second twist modes are symmetric. These observations indicate that the dynamic characteristics of the composite laminate can be greatly altered by the presence of debonding of the piezoelectric transducers. Therefore, careful attention must be paid to the existence of such imperfections in predicting the dynamic response of such smart structures.

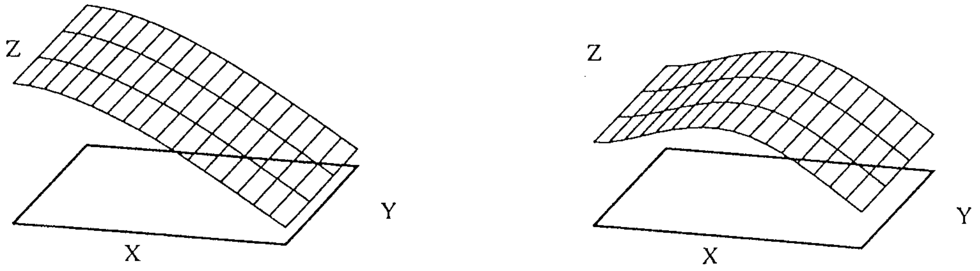

(a) GB1 (b) GB2

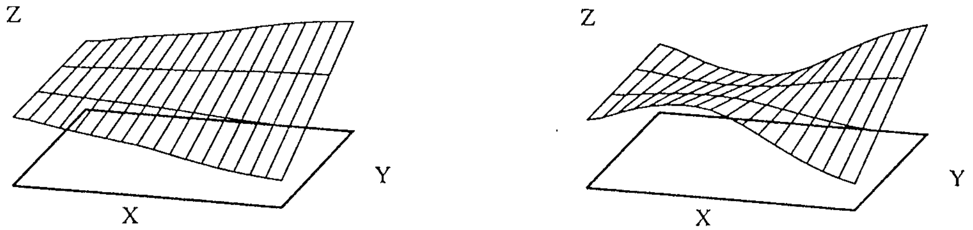

(c) GT1 (d) GT2

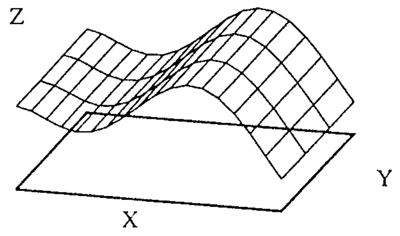

(e) GB3

Fig. 5.7 (a-e) Mode shapes with no debonding obtained using HOT.

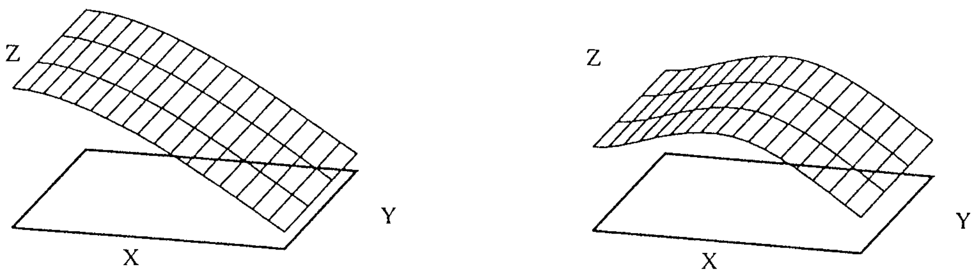

(a) GB1 (b) GB2

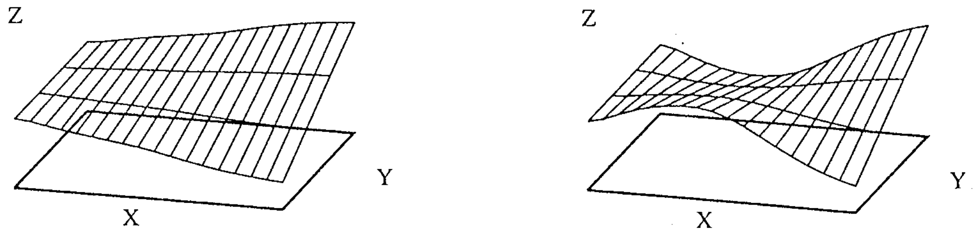

(c) GT1 (d) GT2

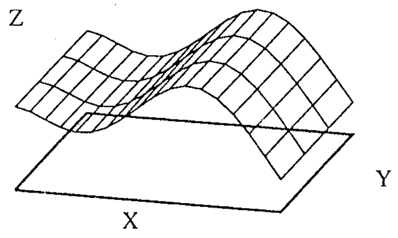

(e) GB3

Fig. 5.8 (a-e) Open loop mode shapes with including debonding obtained using HOT.

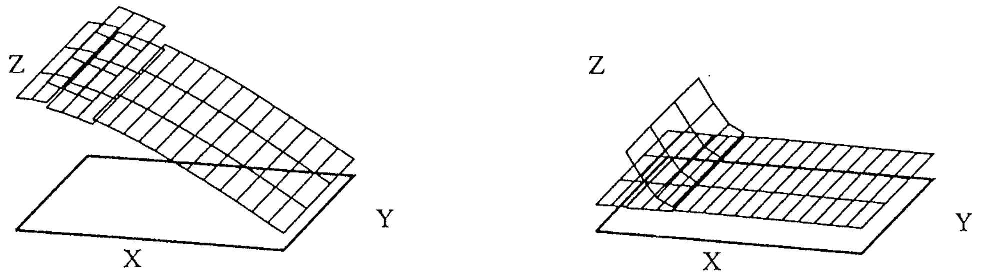

(a) GB1S (b) LB1A

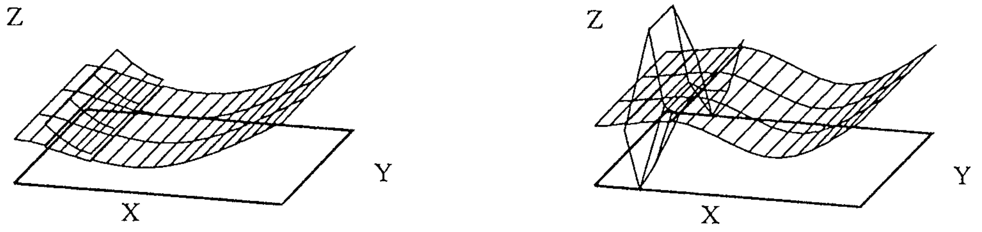

(c) GB2S (d) LB2A

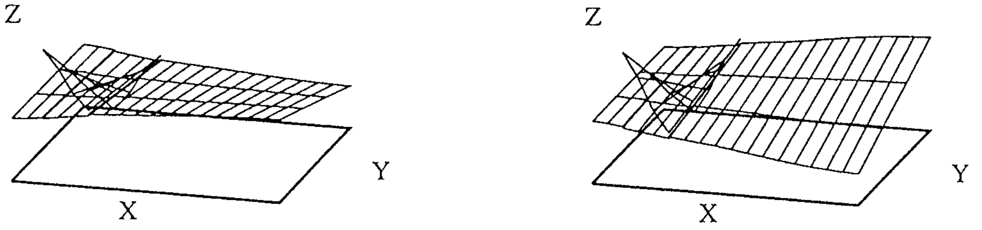

(e) LT1S (f) GT1A

Fig. 5.8 (f-i) Open loop mode shapes with including debonding obtained using HOT.

Table 5.2 Change in open loop frequencies due to debonding (Hz)*.

type	β = 0.0			β = 0.06			β = 0.12			β = 0.18		
1st bending	25.749	(1)	GB1	24.958	(1)	GB1	24.555	(1)	GB1S	24.208	(1)	GB1S
							128.70	(3)	LB1S	55.911	(2)	LB1A
2nd bending	118.07	(2)	GB2	117.01	(2)	GB2	114.85	(2)	GB2	118.12	(3)	GB2S
										382.29	(9)	LB2A
1st twist	153.28	(3)	GT1	146.26	(3)	GT1	139.42	(4)	GT1S	122.55	(4)	LT1S
							222.56	(5)	LT1A	146.66	(5)	GT1A
2nd twist	311.47	(4)	GT2	299.02	(4)	GT2	266.19	(6)	LT2S	275.84	(6)	LT2S
							302.81	(7)	GT2S	297.55	(7)	GT2S
3rd bending	345.54	(5)	GB3	341.98	(5)	GB3	347.48	(8)	GB3	327.82	(8)	GB3

* (G) global, (L) local, (B) bending, (T) twist, (S) symmetric, (A) antisymmetric

5.4 Closed loop mode shapes.

In this section, the effect of the closed loop control due to piezoelectric actuation is investigated. The test articles are identical to the nondebonded $[0°/90°]_{3s}$ and $[45°/-45°]_{3s}$ composite beams with bonded piezoelectric transducers (β=0). The closed loop control consists of an accelerometer located at the tip of the cantilever beams and piezoelectric transducer #2 (top) is again used as an actuator. The first mode shape for the open and closed loop cases of each beam are presented in Figs 5.9 (a-b). In each case, the modes are normalized to unity for comparison. The gain for the closed loop case is 8700 which was the largest gain considered in the experimental investigation. It is observed from Figs 5.9 (a) and 5.9 (b) that the closed loop mode shapes are nearly the same as the open loop mode shapes. The control forces act to stiffen the beams near the piezoelectric transducers. However, the transducers already add stiffness to the beams in the same locations from their material properties and the additional thickness which they provide. Therefore, the additional stiffness provided by the closed loop control does not significantly change the mode shapes. The higher mode shapes exhibit more localized deformation, such as that caused by the piezoelectric actuation. However, the feedback control is most responsive to the first mode due to the presence of the low pass filter and less responsive to the higher modes. Therefore, the higher closed loop mode shapes do not differ by a significant amount either from their open loop counterparts.

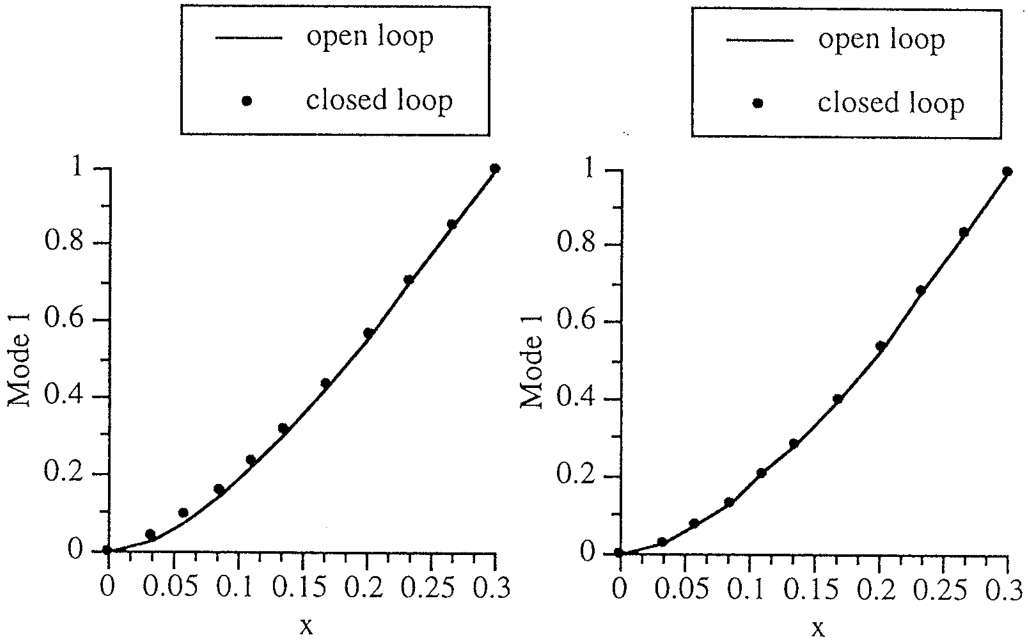

(a) (b)

Fig. 5.9 First open and closed loop mode shapes for (a) $[0°/90°]_{3s}$ and (b) $[45°/-45°]_{3s}$ beams.

6. Experimental Investigation

The principal objective of the current research is to develop practical analysis tools for studying composite structures incorporating piezoelectric sensors and actuators. However, it is necessary to validate these tools through experimental correlations. Furthermore, no published experimental results have been presented to date which address the issue of partially debonded piezoelectric actuators. Many practical issues, which are not obvious in the development of the mathematical model, must also be addressed. Therefore, an experimental investigation was performed as part of the research for this dissertation. The goals of this investigation are twofold:

1. Assess the accuracy of the higher order theory to model composite structures incorporating piezoelectric actuators including the effects of partially debonded actuators
2. Address practical challenges related to the implementation of smart structures.

In the following sections, details are presented to describe the construction and testing of composite structures incorporating piezoelectric sensors and partially debonded actuators to reduce vibration.

6.1 Test Specimen Construction

The test specimens were constructed to represent variations in: (a) composite ply stacking sequence and (b) amount of piezoelectric actuator debonding. Construction occurred in two phases. The first phase consisted of the layup and curing of the composite specimens. In the second phase, the piezoelectric transducers and accelerometers were bonded to the composite substructures. These two phases of construction are described next.

<u>6.1.1 Composite substructure construction</u>: The material selected for the composite substructure was HYE-3574 OH Graphite/Epoxy fabric. Two different ply stacking

sequences were studied, $[0°/90°]_{3s}$ and $[45°/-45°]_{3s}$. These ply layups represent commonly used laminates in the industry. Two large flat plates (122 x 30 cm), one for each stacking sequence, were constructed from the prepreg fabric. The three stage curing cycle was standard for this type and geometry of specimen and was specified as follows.

Stage 1: Heat to 126° C, pressurize to 690 kPa

Stage 2: Maintain 126° C, 690 kPa for 120 min.

Stage 3: Cool to 60° C, 690 kPa for 60 min.

Once the plates were removed from the autoclave, they were cut into strips approximately 56.26 x 5.34 cm. These strips were of the exact width as the final specimens, but were longer than the test articles to allow for clamping at one end. The average thickness of the specimens was 1.94 mm. Therefore, the ply thickness was approximately 0.161 mm. The average density was calculated by dividing the average mass of each test specimen by its volume and was found to be 1507 kg/m^3.

6.1.2 Incorporation of piezoelectric transducers.: The second phase of construction consisted of attaching the piezoelectric transducers to the composite samples. In this phase, it was first necessary to locate practical piezoelectric transducers to be used as sensors and actuators. Lead zirconate titanate (PZT) piezoceramic transducers were found to be the most useful for the current application of vibration control since they exhibit a relatively high elastic modulus and piezoelectric coupling coefficients. Although wafers of raw PZT can be purchased, it was impractical to use these in the current investigation for two reasons. First, electrodes must be soldered to the material without destroying the piezoelectric properties. Second, the bare electrodes would be exposed to the conductive Graphite/Epoxy substructure necessitating an insulating layer and thereby complicating fabrication. However, PZT transducers were available in a prepackaged format with pre-attached leads and electrodes encased in an insulating Kapton package. ACX QP40N piezoceramic transducers were selected with dimensions 10.16 x 2.54 x 0.0762 cm. These transducers contained two stacks of two PZT wafers shown in Fig. 6.1 and were used as both sensors and actuators.

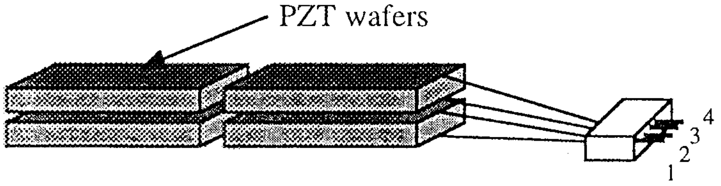

Fig. 6.1 ACX QP40N piezoceramic transducer.

Once practical transducers were obtained, it was then necessary to bond them to the composite specimens. Reliable bonding was essential to ensure the most efficient transfer of strain from the actuator to the composite substructure and vice versa. Creating a bonding layer which was stiff, thin, and free of air pockets was critical to maximize the effectiveness of the actuators. The adhesive material was chosen to be Ecobond 45 clear epoxy adhesive. It was a stiff, room temperature cure epoxy which had a working life of at least an hour and was recommended by the manufacturer of the piezoelectric transducers (ACX).

Several prototypes were constructed to debug the process of bonding the actuators to the composite substructure. The composite specimens and piezoelectric transducers were quite expensive. Therefore, the prototypes were constructed from plexiglass, which was used to represent the composite specimens, and aluminum strips, which represented the piezoelectric transducers. Since the plexiglass was clear, the additional benefit of visual inspection of the bonding layer from the bottom was possible. The manufacturer of the piezoelectric actuators recommended vacuum bagging their products to the host structure while the adhesive layer cures. After several attempts, this procedure was determined to be impractical since the epoxy was consistently drawn out from the interface of the transducer and substructure. A more practical procedure was found to be simply placing weights on top of the transducers while the epoxy cured. However, this approach lead to the problem of minuscule air pockets contaminating the bonding layer. Placing the epoxy in a vacuum chamber for several minutes before applying it to the bonding surfaces, which allowed the air pockets to expand and burst, produced favorable results. Teflon tape was placed on the composite substructure around the area to be bonded to prevent excessive flow of epoxy. Release paper was placed in between the test specimen and the weights to prevent bonding of the weights to the test specimens. Teflon tape, with thickness 5.08 μm, was placed underneath portions of the piezoelectric actuators to create pre-existing debonding of the actuators. The tape was coated with a thin layer of petroleum jelly to ensure that no adhesion between the actuator and composite substructure occurred. After allowing 24 hours for the epoxy to cure, the specimens were released and the excess epoxy trimmed. The entire configuration is presented in Fig. 6.2. Additionally, a single Endevco 2250A Micro miniature accelerometer was bonded to the tip of each of the test specimens using a cyanoacrylate adhesive.

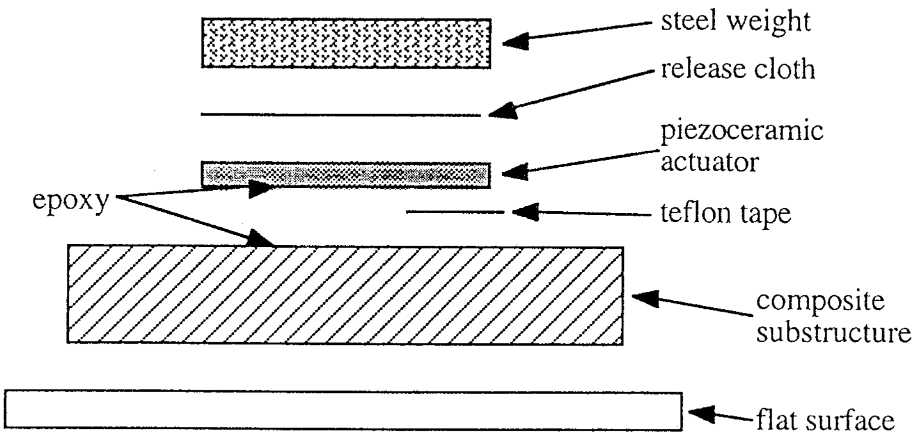

Fig. 6.2 Bonding configuration for the test specimens.

<u>6.1.3 Test specimen configuration</u>: Eight composite test specimens were constructed with varying stacking sequences and debonding lengths. Piezoelectric transducers were bonded to the top and bottom surfaces of the composite substructure as indicated in Fig. 6.3 along with a single accelerometer at the tip. Wooden blocks were clamped at one end to provide

fixed boundary conditions. The test specimens were clamped sideways in a vise during testing to further ensure satisfaction of the fixed boundary conditions and minimize extraneous vibration from corrupting the data. Debonding was introduced between the top piezoelectric transducer and the composite substructure through the width of the transducer near the clamped end as shown in Fig. 6.3 (a) The nondimensional debonding length, β, is defined as follows.

$$\beta = \frac{L_D}{L} \tag{6.1.1}$$

where L_D is the actual debonding length and L is the length of the test specimen. The physical dimensions of the test specimens are presented in Table 6.1 and the exact configuration of each beam is presented in Table 6.2. Material properties are presented in Table 6.3. It must be noted that the d_{31} value listed for the PZT transducers is that of the piezoelectric material only. The transducers are really composite structures containing several different materials, such as the electrodes and the Kapton casing. Therefore, it is more useful to express the piezoelectric coupling in terms of micro-strain per volt for the entire composite transducer. This quantity also has a small but noticeable dependency on the applied electric field. The value for the transducers used for beams 1-4 ($[0°/90°]_{3s}$) was $0.81\frac{\mu m / m}{V}$ while the value for beams 5-8 ($[45°/-45°]_{3s}$)was $0.73\frac{\mu m / m}{V}$ due to the lower fields used during testing.

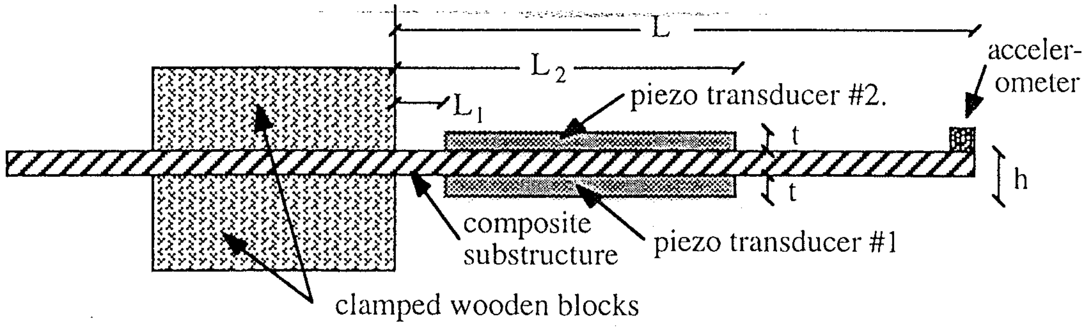

Side View (a)

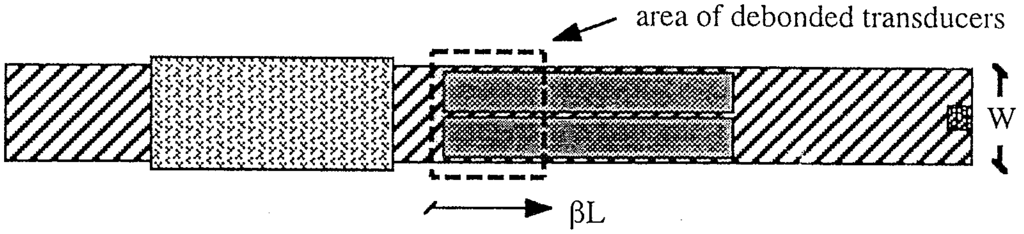

Top View (b)

Fig. 6.3 Test specimen configuration.

Table 6.1 Test specimen dimensions (cm.).

L	L_1	L_2	W	t	h
30 cm	3.4 cm	13.7 cm	5.3 cm	0.76 mm	1.94 mm

Table 6.2 Test specimen configuration.

beam	stacking sequence	β
1	$[0°/90°]_{3s}$	0
2	$[0°/90°]_{3s}$	0.06
3	$[0°/90°]_{3s}$	0.12
4	$[0°/90°]_{3s}$	0.18
5	$[45°/-45°]_{3s}$	0
6	$[45°/-45°]_{3s}$	0.06
7	$[45°/-45°]_{3s}$	0.12
8	$[45°/-45°]_{3s}$	0.18

Table 6.3 Test specimen material properties.

	HYE-3574 OH Gr/Ep	PZT
E_1 (GPa)	114	6.9
E_2 (GPa)	9.5	6.9
$G_{12}=G_{13}$ (GPa)	4.7	2.6
G_{23} (GPa)	2.1	2.6
υ_{12}	0.30	0.31
ρ (kg/m^3)	1507	5000
d_{31} (pm/V)	-	-179
k_3	-	1800

Wires had to be attached to the piezoelectric transducers and the accelerometer on each specimen. This was accomplished via two channels in the clamped wooden blocks (Fig. 6.4). Digi-Key flex cables plug into the piezoelectric transducers and run through the channels in the wooden blocks. The same was true for the wires which were connected to the accelerometers. The flex cable was then attached to AWG 22 stranded core wire which lead to a terminal bus with screw connectors. This intricate wiring scheme was necessary for two reasons. First, it allowed for the least possible interference with the clamped boundary conditions. Second, the four pin connectors mounted on the piezoelectric transducers were extremely fragile. The extension to the terminal bus provided a rugged and convenient connection for practical test conditions.

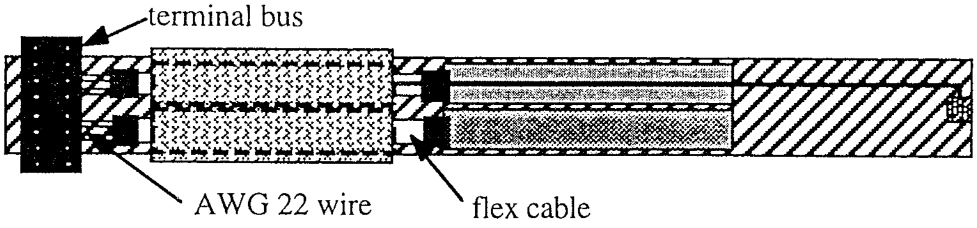

Fig. 6.4 Test specimen wire configuration.

6.2 System Identification

The main goal of the experimental investigation is to correlate the developed mathematical model with the composite beams which were constructed. This requires experimental determination of the frequencies and damping ratios for each test specimen. These quantities are extracted from the raw experimental data using a stochastic method known as the Auto Regressive Moving Average with eXogenious input model (ARMAX) (Lee and Fassois; 1990: Mignolet et al.; 1993: Mignolet and Red-Horse; 1994). Using this method, the system is assumed to be linear and represented in the continuous domain by the following standard set of second order ordinary differential equations.

$$\mathbf{M}\ddot{\mathbf{x}} + \mathbf{C}\dot{\mathbf{x}} + \mathbf{K}\mathbf{x} = \mathbf{f}(t) \tag{6.2.1}$$

where **M**, **C** and **K** are the standard mass, damping and stiffness matrices, respectively, **x** is the displacement vector and **f**(t) is the time varying force vector. This system is parameterized in the discrete domain as follows

$$\tilde{\mathbf{A}}(z)\mathbf{x}(z) = \tilde{\mathbf{B}}(z)\mathbf{f}(z) + \tilde{\mathbf{C}}(z)\mathbf{e}(z) \tag{6.2.2}$$

where the term on the left hand side represents the output, the first term on the right hand side represents the input while the second term represents the noise. The parameters contained in $\tilde{\mathbf{A}}$, $\tilde{\mathbf{B}}$ and $\tilde{\mathbf{C}}$ are determined using the ARMAX system identification technique and z is the unit lag operator. The system poles, z_i, are determined from the solution of the following characteristic equation.

$$\det\left(\tilde{\mathbf{A}}(z_i)\right) = 0 \tag{6.2.3}$$

The natural frequencies and damping ratios of the structure are obtained by mapping the system poles from the discrete to the continuous domain as follows.

$$\omega_i = \frac{1}{\tau}\left(\ln(r_i)^2 + \theta_i^2\right)^{\frac{1}{2}} \tag{6.2.4}$$

$$\zeta_i = -\ln(r_i)\left(\ln(r_i)^2 + \theta_i^2\right)^{-\frac{1}{2}} \tag{6.2.5}$$

where

$$r_i = |z_i|, \qquad \theta_i = \tan^{-1}\left(\frac{\mathrm{Im}(z_i)}{\mathrm{Re}(z_i)}\right) \tag{6.2.6}$$

6.3 Open Loop Structural Response

6.3.1 Open loop transient response: The open loop natural frequencies and damping ratios of the test specimens are experimentally determined in this section The ARMAX system identification technique was used on the transient response records of each of the eight test specimens. The natural frequencies and damping ratios corresponding to first two modes of vibration, which were the first two bending modes, were then compared with those predicted by the developed finite element model implementation of the higher order theory. The next two modes, which were twisting modes, were neither observable or controllable using the current sensor/actuator configuration. Therefore, they were not considered. The third bending mode occurred at a frequency nearly three times higher than the second bending mode and was not considered either.

The test setup consisted of clamping each specimen in a vise which provided fixed boundary conditions. The tip of each beam was lightly tapped and the charge output of piezoelectric transducer #1 (bottom) was converted to a voltage and recorded using the data acquisition system. The entire configuration is shown in Fig. 6.5

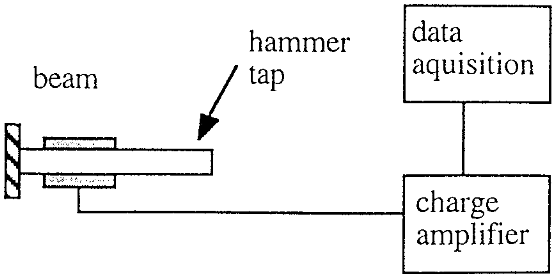

Fig. 6.5 Open loop transient response configuration:

The response was measured in terms of a voltage which is directly proportional to the charge generated by piezoelectric transducer. This charge is proportional to the strain in the piezoelectric transducer and therefore represents the displacement of the beam at a given time. The voltage history for beams 1 and 5 ([0°/90°]$_{3s}$ and [45°/-45°]$_{3s}$, β=0) is presented in Figs 6.6 and 6.7.

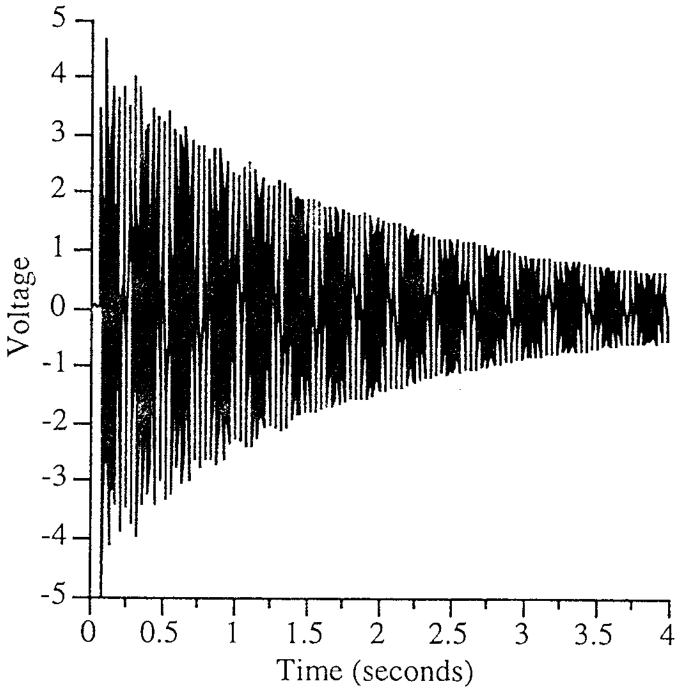

Fig. 6.6 Open loop transient response beam 1 ([0°/90°]$_{3s}$, β=0).

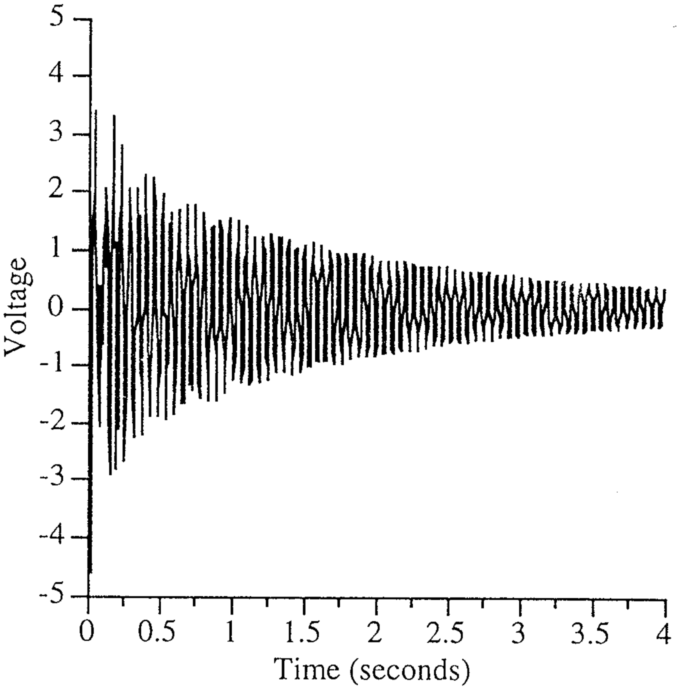

Fig. 6.7 Open loop transient response beam 5 ($[-45°/45°]_{3s}$, $\beta=0$).

A fast Fourier transform on the voltage response records of beams 1 and 5 reveals the frequency content. These transforms are presented in Figs. 6.8 (a-b)

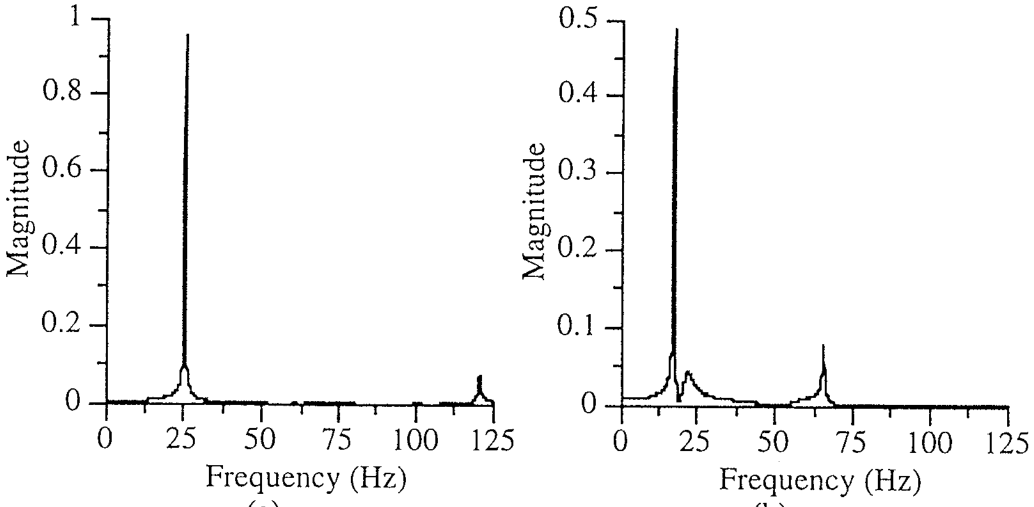

(a) (b)

Fig. 6.8 FFT of open loop transient response (a) beam 1 (b) beam 5

The first peak in Figs 6.8 (a-b) represents the frequency of the first mode while the second peak represents the second mode. From Fig. 6.8 (a), the frequencies of the first two modes for beam 1 were approximately 25 Hz and 120 Hz while the first two frequencies of beam 5 were approximately 18 and 65 (Fig. 6.8 (b)). The open loop natural frequencies of beams 1-4 were expected to be similar since all of these beams have the same stacking sequence. The same was true for beams 5-8. Some small variation was expected due to the debonding, though. Once the frequencies had been approximately determined, damping in each of the beams was estimated using the logarithmic decrement approach as follows.

$$\delta = \frac{1}{n}\ln\left(\frac{x_0}{x_n}\right) \tag{6.3.1}$$

where δ is the logarithmic decrement and x_n is the amplitude after n cycles. The damping ratio, ζ, is approximated as follows

$$\zeta \approx \frac{\delta}{2\pi} \tag{6.3.2}$$

Using this approach, the damping ratio for the first mode in each beam, which is the dominate mode in the transient response, was found to be quite small (ζ=0.0025). In general, the decay envelope of the structure is expressed as follows

$$x(t) = e^{-\omega\zeta t} \tag{6.3.3}$$

Starting from the initial time t_0, the fraction of amplitude Δ which remains after some time t is as follows.

$$\Delta = \frac{Ae^{-\omega\zeta(t_0+t)}}{Ae^{-\omega\zeta t_0}} = e^{-\omega\zeta t} \tag{6.3.4}$$

In order to accurately measure the damping ratios of the test specimens, a significant decay in the vibrational amplitude had to be obtained. The amount of time required to allow for the structure to decay to a certain level was found by rearranging the above equation as follows.

$$t = -\frac{\ln(\Delta)}{\omega\zeta} \tag{6.3.5}$$

Engineering judgment suggested that the vibrational amplitude should be reduced to less than 10% of its original value to allow for accurate determination of the damping ratio. Using the above equation, along the lowest expect natural frequency (18Hz) and damping ratio (0.0025), the time required was approximately eight seconds. Therefore, eight seconds of data were recorded to determine the open loop transient response of each beam.

Once the transient voltage histories of each beam were obtained, the ARMAX technique was applied to the voltage records to more accurately determine the open loop natural frequencies and damping ratios for the first two modes of each test specimen. Model orders ranged from five to twenty five. Lower model orders were consistently inaccurate while higher model orders resulted in numerical problems due to over determination. Frequency estimates were consistent over the range of model orders considered. However, the damping ratio estimates varied somewhat due to the presence of nonlinear damping. Therefore, several different models, using different model orders, of each voltage history were generated. Then, the average damping ratios were calculated. The sampling rate used was 250 Hz. This is more that two times the highest expected frequency to be determined for accuracy, but is not so high as to degrade the signal to noise ratio of the data.

The experimentally determined frequencies (EXP) for the first two modes are presented in Table 6.4 and are compared to the same frequencies predicted using the higher order theory (HOT). In general, the agreement is very good. Although the mass of the accelerometers is very small (0.4 g), it is included in the mathematical model. The frequencies were expected to decrease slightly with increasing debonding length which was observed as a general trend. Since the change is relatively small, it is not clearly observed in the experimental results of the first mode of the $[0°/90°]_{3s}$ beams due to experimental uncertainty, but it is observed in the $[45°/-45°]_{3s}$ beams. However, this trend is always observed in the HOT results. An unexpected change occurred in the frequency of the second mode as the debonding length increases from $\beta=0.12$ to $\beta=0.18$. Although the structure became less stiff due to the increased debonding length, which would indicate a reduction in the frequencies, the experimental value of the frequency of the second mode actually increased. This increase is also observed in the HOT results for both beams and in the experimental results for the $[0°/90°]_{3s}$ beams as well. The reason for this anomaly is that a new localized mode was introduced between the first and second bending modes due to the flapping motion of the debonded actuator. This new mode alters the dynamic response of the beam which results in a slightly higher frequency for the second bending mode.

Table 6.4 Open loop natural frequency estimates (Hz)

	mode 1			mode 2		
beam	EXP	HOT	% error	EXP	HOT	% error
1	25.1	25.4	1.0	120.6	116.3	3.6
2	24.5	24.6	0.3	118.7	115.3	2.9
3	24.6	24.2	1.7	119.4	113.1	5.3
4	24.5	23.8	2.7	120.3	116.3	3.3
5	17.3	16.4	5.3	65.5	68.0	3.9
6	16.3	15.6	4.1	66.3	67.3	1.5
7	15.5	15.2	2.1	66.6	67.2	0.9
8	15.4	14.8	4.1	65.9	68.4	3.8

The experimentally determined open loop damping ratios are presented in Table 6.5 The damping in all cases was found to be less than 1% which was quite small. The damping increases from the first to the second mode for beams 1-4 ($[0°/90°]_{3s}$) while it decreases for beams 5-8 ($[45°/45°]_{3s}$). The damping was generally higher for the $[45°/45°]_{3s}$ beams compared to the $[0°/90°]_{3s}$ beams. This was because the epoxy matrix, which has inherently higher damping characteristics than the graphite fibers, had a more significant effect on the structural response of the $[45°/45°]_{3s}$ beams.

Table 6.5 Open loop damping ratio estimates

beam	EXP- mode 1	EXP - mode 2
1	0.0030	0.0039
2	0.0023	0.0060
3	0.0035	0.0038
4	0.0036	0.0040
5	0.0054	0.0049
6	0.0053	0.0046
7	0.0068	0.0046
8	0.0085	0.0052

6.3.2 Open loop frequency response: The open loop frequency response of the test specimens is determined next. A sinusoidal voltage with varying frequency is applied to piezoelectric transducer #1 and the voltage response of piezoelectric transducer #2 was recorded. The experimental setup is presented in Fig. 6.9. A voltage controlled oscillator circuit, which was designed, tested, and built, was coupled with the data acquisition system and provided the frequency sweep. Acquiring the frequency response data was very difficult due to the range of amplitudes at different frequencies. The response of the specimens near their respective natural frequencies was very large since the structural damping was very small. Therefore, the input voltage, V, was required to be very small to keep the structural response within reasonable limits at the resonant frequencies. However, the response of the structure at other frequencies was extremely small at the same voltage and often difficult to distinguish from ambient noise in the structure and the charge amplifier.

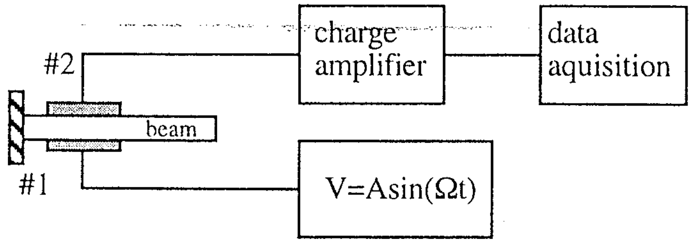

Fig. 6.9 Open loop frequency response experimental setup.

The frequency response of test specimens 1 ($[0°/90°]_{3s}$) and beam 5 ($[45°/-45°]_{3s}$), which have different stacking sequences but no debonding, are presented in Figs 6.10 (a-b). The magnitudes in these plots are relative and are only relevant for comparing the higher order theory (HOT) to the experimental data (EXP). The frequency response of test specimens 2-4 and 6-8 were similar to test specimens 1 and 5, respectively and were largely unaffected by the presence of debonded transducers, except for a small shift in the resonant frequencies. Therefore, only the response of test specimens 1 and 5 are presented.

The location of the peaks in the structural response observed by piezoelectric transducer #2 correlated very well with the peaks which were observed experimentally for all of the test specimens. This was expected since the natural frequencies predicted by the higher order theory correlated well with the experimental results as indicated in the previous section. The first two modes were bending modes and were observable by the sensor. The next two modes were twist modes and were not observable or controllable using the current sensor and actuator configuration. The next observable mode, which was the third bending mode, has a frequency much higher than the first two modes and was not present in the frequency range of interest. Due to the close proximity of transducers #1 (actuator) and #2 (sensor), the deformation seen by transducer #2 included both the global response of the structure as well as the local deformation produced by transducer #1. The phase of each these components below resonance was 0° and they became additive. However, each these components above resonance was 180° out of phase and they had a canceling effect on each other. This explains the nonsymmetric shape of the peaks at each of the resonant frequencies which was predicted by the higher order theory and verified experimentally. (Figs. 6.10 (a-b)). Since a significant portion of the deformation observed by piezoelectric transducer #2 was local deformation caused by the actuation of transducer #1, stability problems were encountered for the closed loop control which required information about the global response of the structure. Therefore, the accelerometer at the tip was used as a sensor instead for the closed loop feedback control presented next.

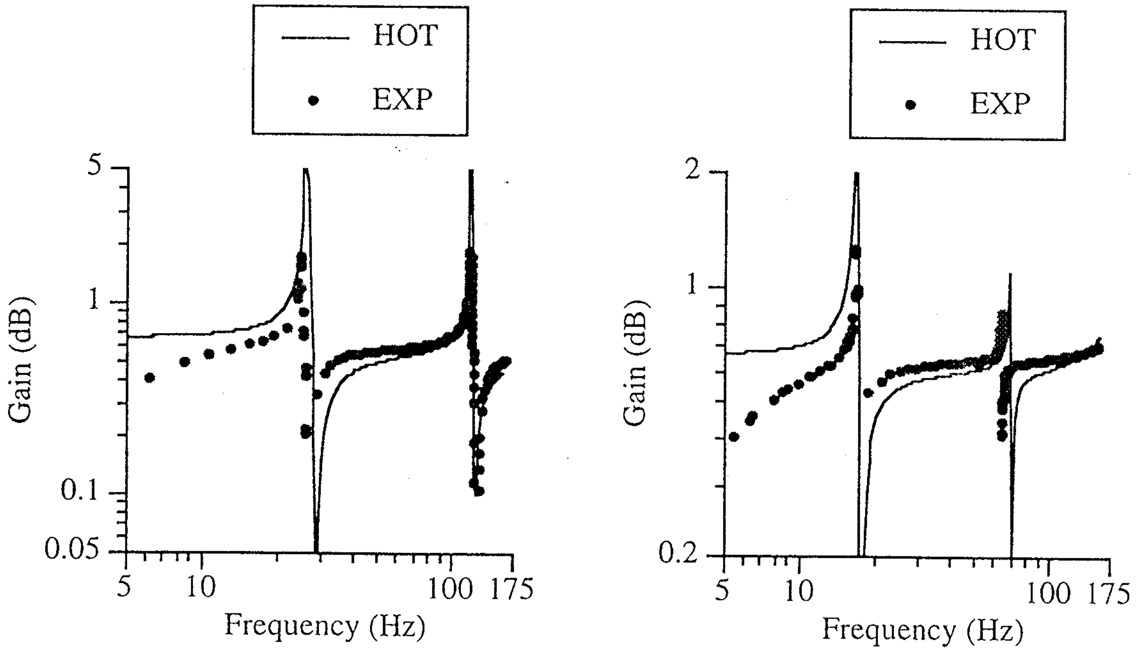

Fig. 6.10 Open loop frequency response (a) beam 1 ($[0°/90°]_{3s}$) (b) beam 5 ($[45°/-45°]_{3s}$).

6.4 Control Design

In this section, topics relating to design and implementation of the feedback control system are discussed. A simple analysis based on classical control theory is developed to understand basic concepts relating to the control system. The full state space equations are then introduced and the corresponding circuit design for implementation of the controls is presented.

6.4.1 Classical approach to control design: Consider a cantilever beam with a piezoelectric transducer used as an actuator and an accelerometer used as a sensor. The equation of motion for the first bending mode of the beam, which is assumed to be the most important mode, is given as follows.

$$\ddot{q} + 2\zeta_b\omega_b\dot{q} + \omega_b^2 q = \phi^T\left(F + F_p\right) \qquad (6.4.1)$$

where q, ϕ, ζ_b and ω_b are the modal participation factor, mode shape, damping ratio and frequency of the first mode of vibration, respectively, and F and F_p are the external and piezoelectric forces, respectively. The signal obtained from the accelerometer v_i, is proportional to the acceleration of the beam.

$$v_i = a\ddot{q} \qquad (6.4.2)$$

where a is the proportionality constant. A second order low pass filter is employed in the feedback loop which serves two purposes. First, high frequency noise, which could lead to unexpected results, is filtered out. Second, the low pass filter provides a 90° phase shift at its resonance, or cutoff frequency, so that the piezoelectric actuation forces are 180° out of phase with the displacement of the beam. Therefore, the control forces act as viscous dampers to reduce vibrational amplitudes in the beam. The governing equation for the second order low pass filter is as follows (Stout; 1976).

$$\ddot{v}_o + 2\zeta_f\omega_f\dot{v}_o + \omega_f^2 v_o = bv_i \qquad (6.4.3)$$

where v_0, ζ_f and ω_f are output voltage, damping ratio, and cutoff frequency of the filter and b is a constant of proportionality. The piezoelectric control forces are set to be proportional to the filter output voltage which is fed back into the control loop.

$$F_p = cv_o \qquad (6.4.4)$$

The block diagram for this system using the Laplace-transformed transfer functions for the above governing equations, assuming a=b=c=1, is presented in Fig. 6.11 The closed loop transfer function for this system is as follows.

$$\frac{C(s)}{R(s)} = \frac{s^2 + 2\zeta_f\omega_f s + \omega_f{}^2}{\left(s^2 + 2\zeta_f\omega_f s + \omega_f{}^2\right)\left(s^2 + 2\zeta_b\omega_b s + \omega_b^2\right) + s^2} \qquad (6.4.5)$$

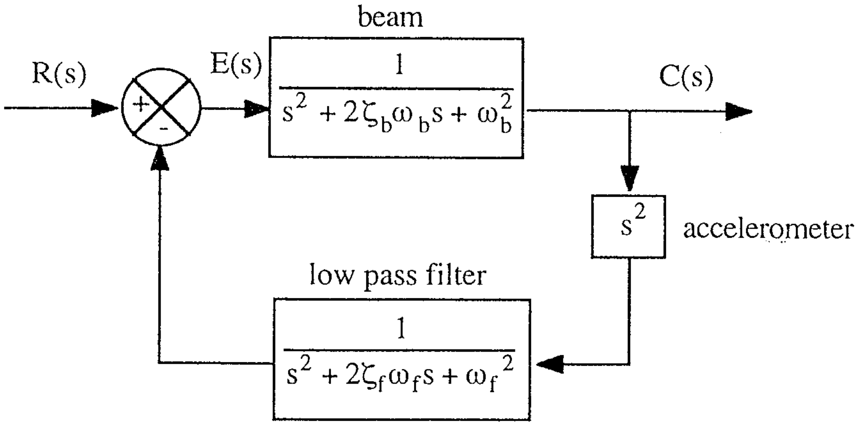

Fig. 6.11 Feedback control loop

The control system is most effective when the cutoff frequency of the low pass filter is tuned to the natural frequency of the beam.

$$\omega_f = \omega_b \qquad (6.4.5)$$

A high filter damping ratio is also desirable to minimize the phase shift near the cutoff frequency. The damping ratio of the filter is selected to be that of a Butterworth second order low pass filter (ζ_f=0.7072) (Stout; 1976). The frequency response of the filter is presented in Fig 6.12 where the amplitude predicted by the transfer function is compared to experimental results with ω_f = (25 Hz). The correlation of the filter response is excellent. The phase is also verified to be -90° at ω_f.

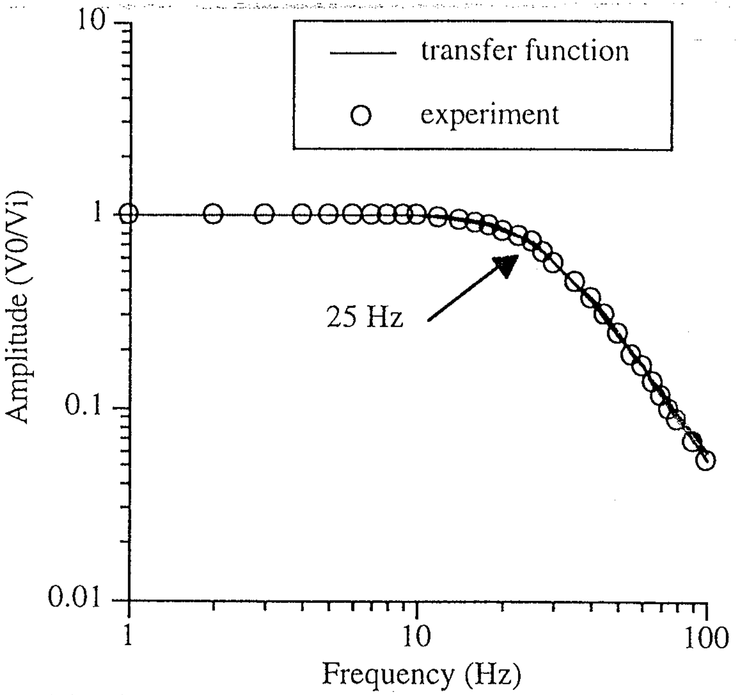

Fig. 6.12 Low pass filter frequency response

Stability of the control system needs to be studied. This is especially true since the damping ratio corresponding to the structural damping in the beam for the first mode was found to be quite small (ζ_f=0.003). A root locus of the control system is constructed to examine its stability characteristics with $\omega_f = \omega_b = 157$ rad/sec (25 Hz) (Fig. 6.13). This corresponds to parameters similar to beams 1-4. A similar analysis was also performed for beams 5-8. The two poles nearest the vertical axis correspond to the beam. They are very close the real axis due to the low damping in the beam. The other two poles correspond to the low pass filter. All values remain on the left hand side of the root locus plot indicating stability at any gain. This is a desirable feature of the control system selected to provide for increased damping. However, it is important to keep in mind that only a single bending mode has been used for the control design. It is possible that under certain circumstances, higher modes become excited at large gains which may threaten the stability of the control system. It is assumed for the current investigation that the influence of the higher modes is reduced by the low pass filter and do not present any stability problems.

In practice, the natural frequency of the beam may not correspond exactly to the cutoff frequency of the filter. It is important to determine the effect of imprecise parameters on the control system. The root locus is presented in Figs 6.14 and 6.15 for beams frequencies which are 5% higher and 5% lower than the low pass filter cutoff frequency, respectively. If the open loop beam frequency is reduced by a small amount (Fig. 6.14), the poles corresponding to the beam are more strongly attracted to the single zero. The closed loop frequencies are calculated by finding the square root of the sum of the squares of the real and imaginary parts of the roots which are shown on the root locus. In this case, the root locus indicates that the closed loop frequency of the beam decreases as the gain is increased. Further analysis reveals that the closed loop damping increases to a value of approximately 0.3 until it starts to decrease at very high gains. When the beam natural frequency is slightly higher than that of the filter (Fig. 6.15), the root locus changes significantly. As before, the poles corresponding to the beam are nearest the vertical axis since the damping in the beam is small compared to the filter. However, these poles are no longer attracted to the single zero. Instead, they increase in magnitude until out of range of the figure. This indicates that the closed loop frequency of the beam increases, rather than decreases, as the gain is increased. As before, further analysis indicates that the closed loop damping increases to a value of approximately 0.3 until it starts to decrease at very high gains.

Next, the frequency response of the control system is analyzed by constructing Bode plots of both the open and closed loop systems for the parameters considered above. (Figs. 6.16 and 6.17). The open loop frequency response is presented in Fig. 6.16. A sharp peak exists in the amplitude response near the frequency of the beam. This is due to the low structural damping in the beam and was observed in the experimental open loop frequency response in the previous section. Only a single peak is observed here since only one mode is used in the control design. The phase shift near the natural frequency is very abrupt, again due to the low damping. The closed loop frequency response is presented in

Fig. 6.17. The amplitude peak near the natural frequency is not nearly as sharp as the one in the open loop Bode plot indicating increased damping. The magnitude of this peak is also reduced substantially. The phase shift near the natural frequency is much more gradual compared to the open loop response which also indicates increased damping due to the feedback control.

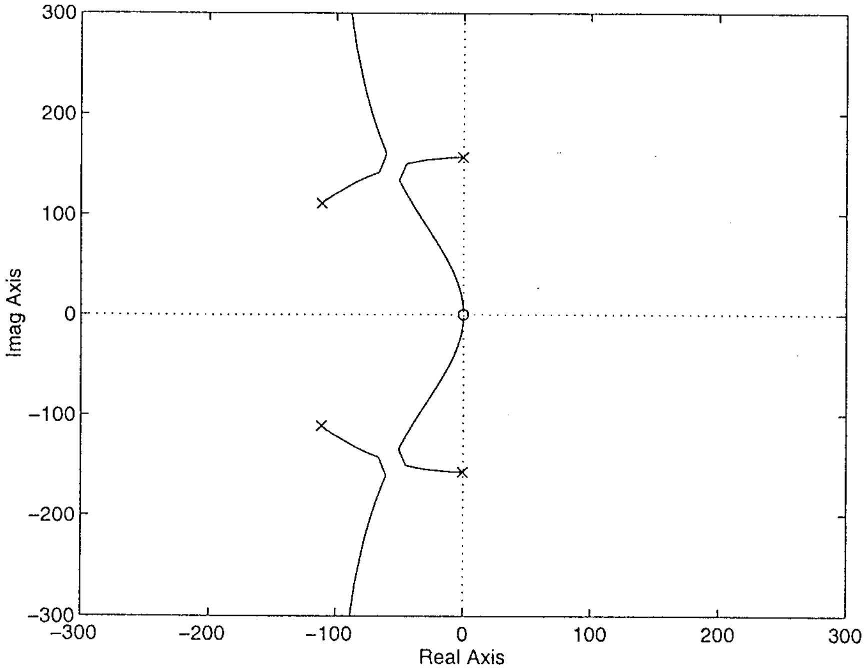

Fig. 6.13 Feedback control loop root locus

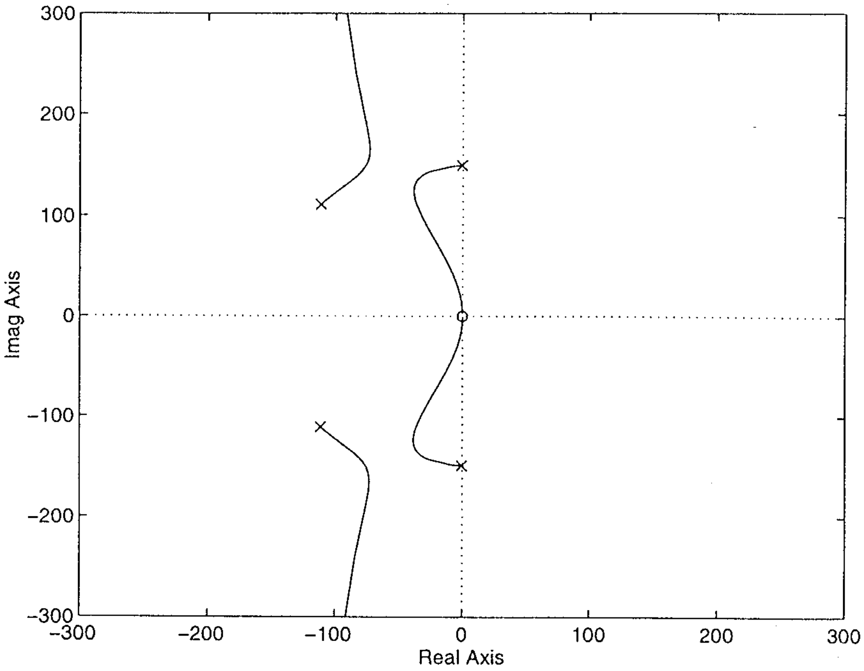

Fig. 6.14 Feedback control loop root locus; $\omega_b < \omega_f$

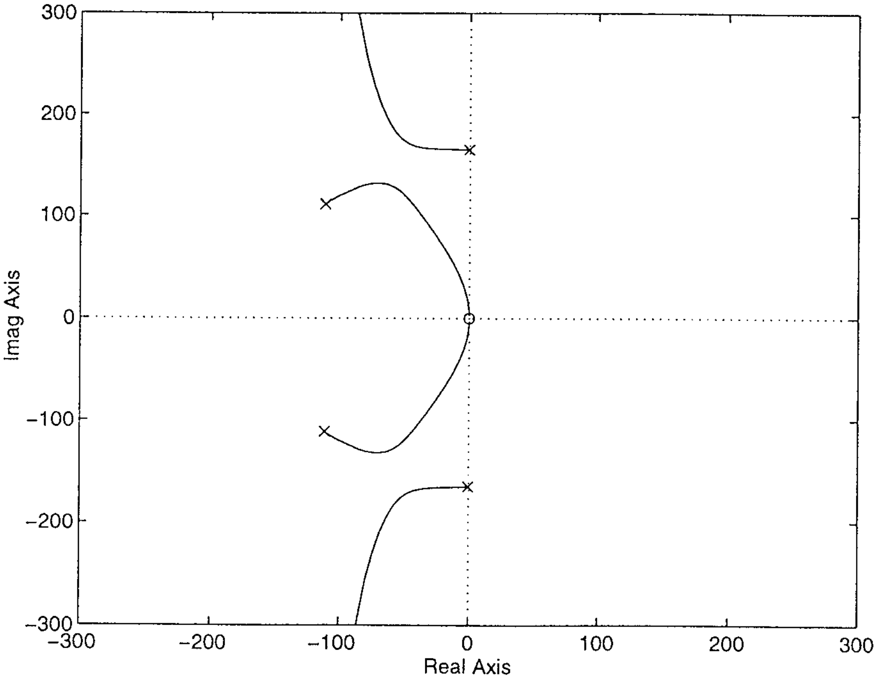

Fig. 6.15 Feedback control loop root locus; $\omega_b > \omega_f$

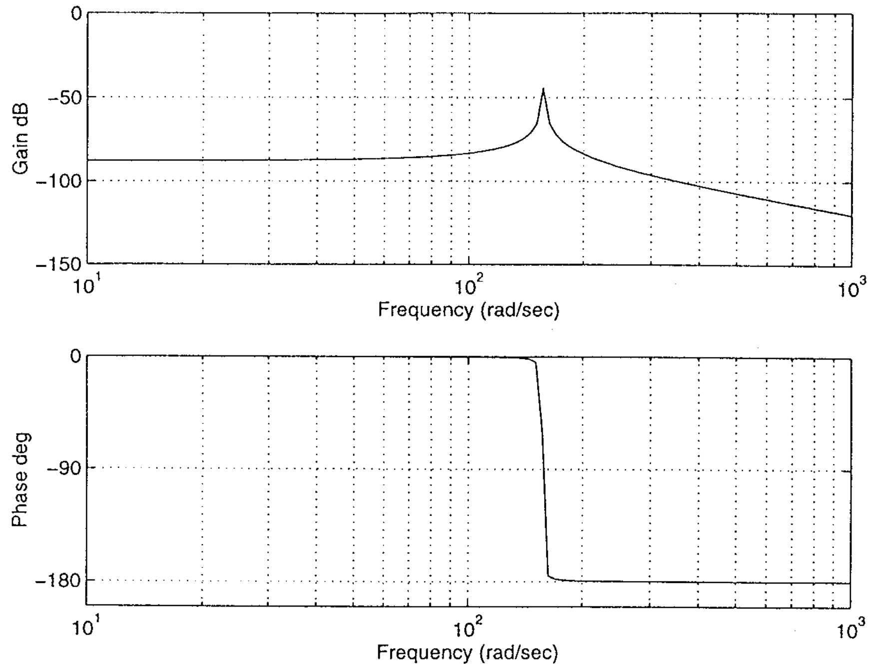

Fig. 6.16 Open loop frequency response.

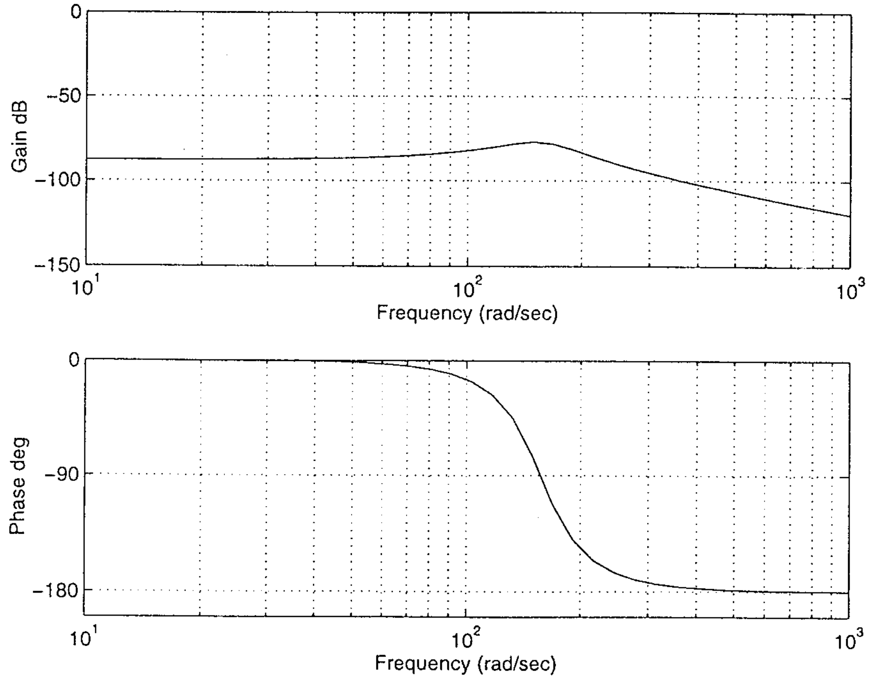

Fig. 6.17 Closed loop frequency response.

6.4.2 State space approach: Several modes must be included in the control analysis used for the experimental tests to more accurately determine the response of the coupled controls/structures system. A state space representation of the system is more convenient to work with than the classical approach and is developed in this section. However, the conventional notation of state space controls analysis used in Section 3.8 is not practical due to the presence of second derivative terms from the accelerometer output. Therefore, an alternative approach is used. The equations of motion of the structure are now given as follows.

$$\ddot{\mathbf{q}} + \mathbf{Z}_b\dot{\mathbf{q}} + \Lambda_b\mathbf{q} = \Phi^T\left(\mathbf{F} + \mathbf{F}_p\right) \tag{6.4.6}$$

where

$$\Lambda_b = \begin{bmatrix} \ddots & & \mathbf{0} \\ & \omega_{b_i}^2 & \\ \mathbf{0} & & \ddots \end{bmatrix} \tag{6.4.7}$$

$$\mathbf{Z}_b = \begin{bmatrix} \ddots & & \mathbf{0} \\ & 2\zeta_{b_i}\omega_{b_i} & \\ \mathbf{0} & & \ddots \end{bmatrix} \tag{6.4.8}$$

$$\Phi = \begin{bmatrix} \vdots & \vdots & \\ \phi_1 & \phi_2 & \cdots \\ \vdots & \vdots & \end{bmatrix} \tag{6.4.9}$$

The matrix Λ_b contains the square of the natural frequencies, $\mathbf{Z}_b$ contains the structural damping terms, Φ is the modal matrix containing the normalized eigenvectors and $\mathbf{q}$ is a vector of the modal participation factors. The quantity $\mathbf{F}$ contains the applied forces and $\mathbf{F}_p$ are the piezoelectric forces determined as follows.

$$\mathbf{F}_p = \mathbf{G}\mathbf{F}_p'\mathbf{v}_0 \tag{6.4.10}$$

where $\mathbf{F}_p'$ contains the piezoelectric forces per volt for one or more actuators with v_0 as the vector containing the applied voltages to the piezoelectric actuators and **G** contains the gains of each actuator. The signal obtained from the accelerometer v_i, is proportional to the acceleration of the beam as before. The signals from several accelerometers are related to the accelerations at different points as follows.

$$\mathbf{v}_i = \mathbf{S}\Phi\ddot{\mathbf{q}} \tag{6.4.11}$$

where **S** contains the sensitivities of the accelerometers. The Endevco 2250A Micro miniature accelerometers used in this study have a sensitivity of 0.012 V/(m/s^2). The governing equation for a single second order low pass filter is also the same as before (Eqn. 6.4.3). Although only one filter is used in the current study, several filters can be used in a MIMO type control system with governing equations as follows.

$$\ddot{\mathbf{v}}_o + \mathbf{Z}_f\dot{\mathbf{v}}_o + \Lambda_f\mathbf{v}_o = \mathbf{b}\mathbf{v}_i \tag{6.4.12}$$

where the matrices $\mathbf{Z}_f$ and Λ_f are analogous to the matrices $\mathbf{Z}_b$ and Λ_b, respectively. The coupled controls/structures equations of motion are represented in state space as follows .

$$\begin{bmatrix} \mathbf{I} & \mathbf{0} & \mathbf{0} & \mathbf{0} \\ \mathbf{0} & \mathbf{I} & \mathbf{0} & \mathbf{0} \\ \mathbf{0} & \mathbf{0} & \mathbf{I} & \mathbf{0} \\ \mathbf{0} & -\mathbf{S}\Phi & \mathbf{0} & \mathbf{I} \end{bmatrix} \frac{d}{dt} \begin{bmatrix} \mathbf{q} \\ \dot{\mathbf{q}} \\ \mathbf{v}_o \\ \dot{\mathbf{v}}_o \end{bmatrix} = \begin{bmatrix} \mathbf{0} & \mathbf{I} & \mathbf{0} & \mathbf{0} \\ -\Lambda_b & -\mathbf{Z}_b & \Phi^T\mathbf{F}_p'\mathbf{G} & \mathbf{0} \\ \mathbf{0} & \mathbf{0} & \mathbf{0} & \mathbf{I} \\ \mathbf{0} & \mathbf{0} & -\Lambda_f & -\mathbf{Z}_f \end{bmatrix} \begin{bmatrix} \mathbf{q} \\ \dot{\mathbf{q}} \\ \mathbf{v}_o \\ \dot{\mathbf{v}}_o \end{bmatrix} + \begin{bmatrix} \mathbf{0} \\ \Phi^T\mathbf{F} \\ \mathbf{0} \\ \mathbf{0} \end{bmatrix} \tag{6.4.13}$$

The complex eigenvalues and eigenvectors of the above state space representation of the control system are determined from the following equation.

$$(\mathbf{A} - \lambda\mathbf{B})\mathrm{x} = \mathbf{0} \tag{6.4.14}$$

where

$$\mathbf{A} = \begin{bmatrix} \mathbf{0} & \mathbf{I} & \mathbf{0} & \mathbf{0} \\ -\Lambda_b & -\mathbf{Z}_b & \Phi^T\mathbf{F}_p'\mathbf{G} & \mathbf{0} \\ \mathbf{0} & \mathbf{0} & \mathbf{0} & \mathbf{I} \\ \mathbf{0} & \mathbf{0} & -\Lambda_f & -\mathbf{Z}_f \end{bmatrix} \tag{6.4.15}$$

$$\mathbf{B} = \begin{bmatrix} I & 0 & 0 & 0 \\ 0 & I & 0 & 0 \\ 0 & 0 & I & 0 \\ 0 & -S\Phi & 0 & I \end{bmatrix} \tag{6.4.16}$$

Thus the state space representation used here reduces to an eigenvalue problem which is solved using standard techniques in a computationally efficient manner since no matrix inversions are necessary (Mignolet; 1995). Frequencies and damping ratios for the closed loop system are determined from the complex conjugate eigenvalue pairs as follows.

$$\omega_{n_j} = \sqrt{\mathrm{Re}(\lambda_j)^2 + \mathrm{Im}(\lambda_j)^2} \tag{6.4.17}$$

$$\zeta_{n_j} = \frac{\mathrm{Re}(\lambda_j)}{\sqrt{\mathrm{Re}(\lambda_j)^2 + \mathrm{Im}(\lambda_j)^2}} \tag{6.4.18}$$

It is important to note that the above matrices, **A** and **B**, do not correspond to the **A** and **B** matrices often used in the state space approach for MIMO control systems.

6.5 Closed Loop Structural Response

In this section, the closed loop structural response is investigated. First, the experimental procedure is described and the design of the analog circuit to implement the control law are discussed. Results are then presented to correlate the predicted closed loop response using the higher order theory with experimental data.

6.5.1 Experimental procedure: The goal of the closed loop structural response investigation is to correlate the closed loop frequencies and damping ratios predicted by the HOT with experimental results. This was accomplished by recording the transient response of the beam due to an initial excitation. The hammer hit used in the open loop response to provide the initial excitation was not appropriate in the closed loop tests because this resulted in a large voltage spike at t = 0 which could have damaged the feedback control electronics and the data acquisition system. Instead, a random noise was used to excite the structure which was produced by applying a random voltage signal to piezoelectric transducer #2 for several seconds before the control loop was turned on (t < 0). At t = 0, the random noise was turned off and the feedback control loop was turned on. For t > 0, the output of the accelerometer was recorded for an appropriate length of time (two seconds) while the response of the system decayed. This procedure is illustrated in Fig. 6.18. The operation was repeated for all the test specimens for two different stacking sequences, four debonding lengths and seven different gains. Several tests were performed at different times to ensure consistency of the data. Several ARMAX models were generated for each test record to determine the frequencies and damping ratios. Engineering judgment was used to discard defective data. The remaining results for each test were then averaged.

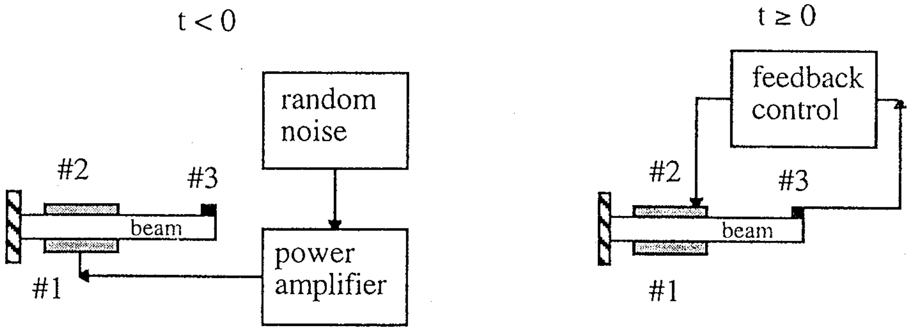

Fig. 6.18 Test procedure.

6.5.2 Analog circuit design: Implementation of the control law was a non-trivial procedure. The control loop needed to respond in real time to the motion of the structure while data was being taken at the same time Ambient noise was a factor and voltage and current limits of the actuators, data acquisition and control loop had to be considered. This lead to the implementation of the feedback control loop and test procedure via a nonlinear analog circuit which is shown in Fig. 6.19 (Durney et al; 1982). Not shown are the power supplies for the operational amplifiers and ground connections. Only the connections to the data acquisition system are shown for simplicity although the data acquisition software (Labview 3.0), hardware (Macintosh 7200/90) and I/O card (Labview PCI 1200) played an integral role to the test procedure. The accelerometer also required a signal conditioner which is not shown. The entire circuit was designed, tested, and implemented in-house using commercially available electronic parts. The operation of the circuit is described next.

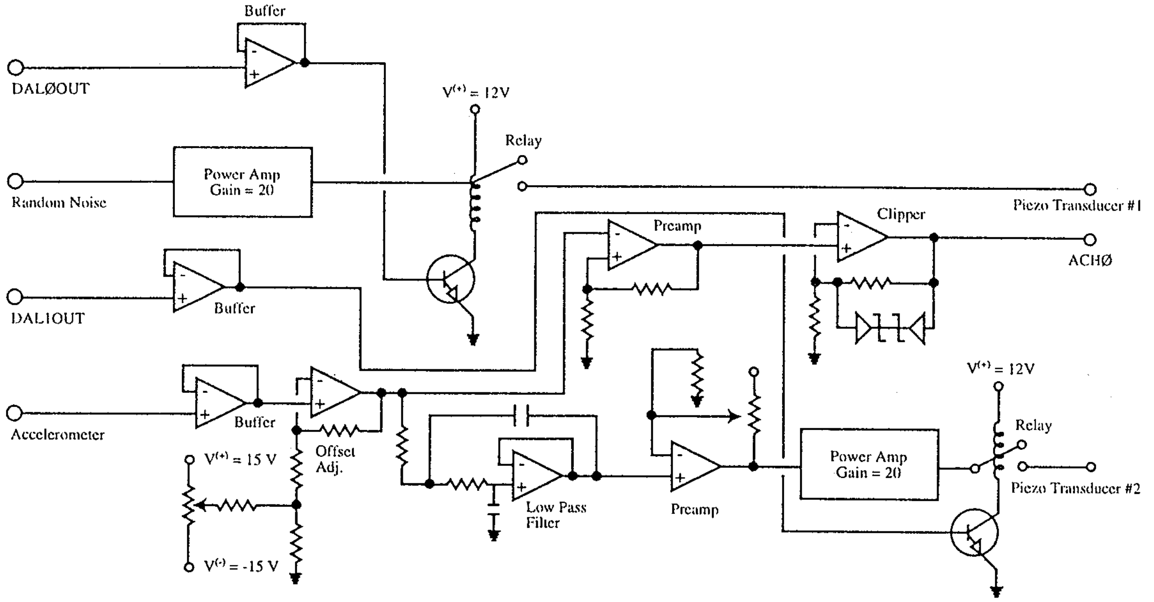

Fig. 6.19 Closed loop feedback circuit.

At time $t < 0$, the data acquisition system outputs were as follows.

DAC0OUT = 1 volt, DAC1OUT = 0 volt, $(t < 0)$

These values positioned the relays in the circuit such that the random signal was connected to piezoelectric transducer #1 while the control loop remained disconnected. This provided the initial excitation to the structure and avoided a potentially dangerous voltage spike from the accelerometer. At time $t = 0$, these values swapped as follows.

DAC0OUT = 0 volt, DAC1OUT = 1 volt $(0 \leq t \leq t_1)$

This disconnected the random excitation and connected the feedback control loop. Data acquisition from the accelerometer output began immediately through ACH0 and transpired for the required length of time (t_1) to observe sufficient decay in the response of the structure due to the feedback control. Once data acquisition was complete, these values returned to their original values, thus disconnecting the closed loop control, for safety.

DAC0OUT = 1 volt, DAC1OUT = 0 volt ($0 \leq t \leq t_1$)

The relays required 12 volts @ 11 ma to be triggered. However, the data acquisition outputs could only supply ± 5 volts @ 2 ma. Therefore, a separate power supply was used for the relay coils which are switched on and off using 2N2222A transistors The transistor bases were connected to both DAC0OUT or DAC1OUT through buffers to retain high impedance for protection. The relays were placed after the power amplifiers rather than before since the power amplifiers could potentially saturate from a floating input.

The feedback control loop consisted of the accelerometer input, preamp, lowpass filter and power amplifier. The cutoff frequency of the low pass filter was adjusted for different test specimens by selecting appropriate values for the resistors and capacitors. It also provided the required phase shift at the resonant frequency of the beam. The gain of the preamp was selected by changing values of its feedback resistor. It provided a relatively high gain since the accelerometer signal level is so low (~10 ma). This high gain resulted in an annoying DC offset drift which was compensated for somewhat using another unity gain amplifier with an offset adjustment.

The accelerometer output was also sent to the A/D converter in the data acquisition system (ACH0). It was amplified using a separate preamp from the feedback control loop. It was taken before the low pass filter since filtered data may have corrupt the system identification technique in post computation (Lyon; 1996). It was passed through a voltage clipper (± 5 volts) which utilized zener diodes to protect the data acquisition system.

6.5.3 Transient response: Representative transient responses of beam 1 ($[0°/90°]_{3s}, \beta = 0$) are presented in Figs 6.20 (a-g) for increasing gains obtained from the experimental data. The quantity shown is the unfiltered output of the accelerometer which is in the millivolt range. Clearly, as the gain increases, the decay of the structure also increases. A smooth exponential decay is observed for gains 0-2000 and the corresponding frequencies and damping ratios calculated by the ARMAX procedure were very consistent. At higher gains, the decay is not quite as smooth. Although the ARMAX frequencies were consistent, there was some variation in the damping ratios. This is due to the presence of nonlinear damping. The response of the analog circuit feedback control at higher gains may be partially responsible. The effect of higher modes may be enhanced at higher gains and also contribute to the appearance of the transient response at higher gains. It must be noted that the twist modes are neither controllable or observable in the current configuration and are assumed to have little effect on the transient response tests.

The transient response decay envelopes for the first mode of vibration are presented in Figs. 6.21 (a-d) and 6.22 (a-d) for both $[0°/90°]_{3s}$ and $[45°/-45°]_{3s}$ beams. Debonding lengths of $\beta = 0.0, 0.06, 0.12$ and 0.18 for gains of 0, 200, 400, 1000, 2000, 4000 and 8700 are shown. The response of each case is normalized to unity at $t = 0$ for comparison of the experimentally determined values using ARMAX (EXP) and the higher order theory (HOT). In general, agreement is very good. Increasing the gain significantly reduces the settling time for all cases. However, the presence of debonding tends to reduce the authority of the actuators and increases the settling time.

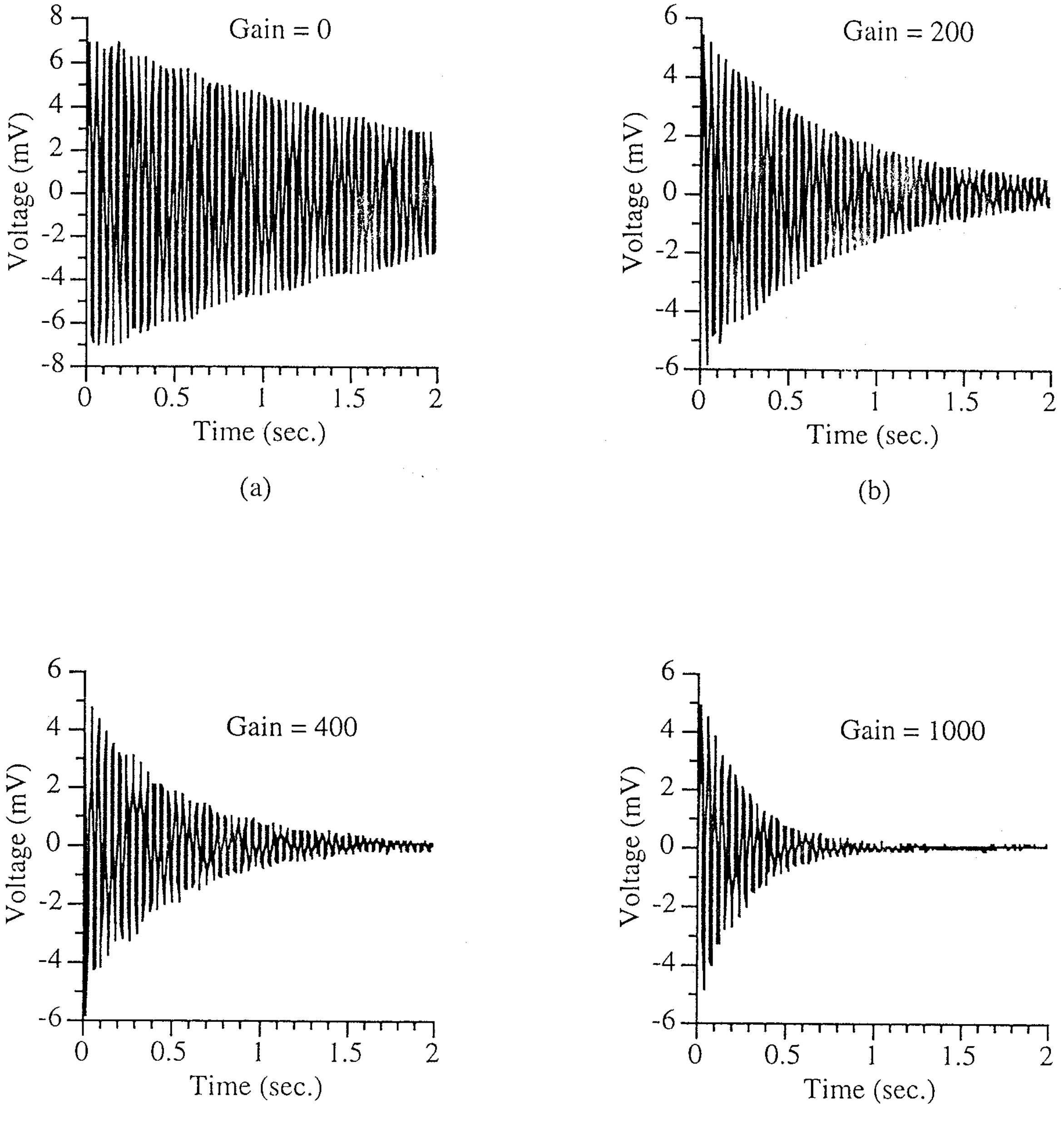

(a) (b)

(c) (d)

Fig.6.20 (a-d) Transient response of $[0°/90°]_{3s}$ beam with increasing gain ($\beta = 0$).

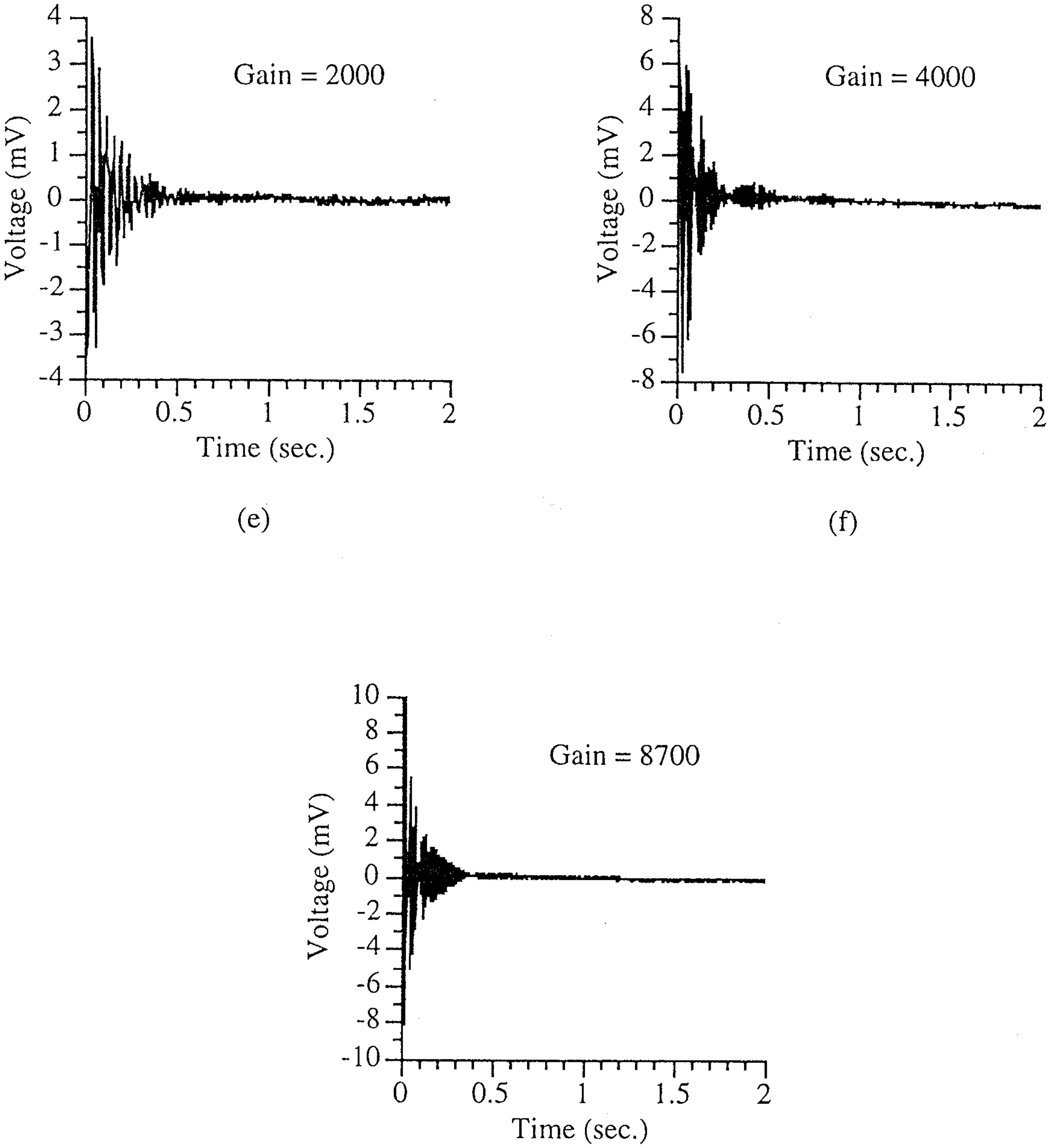

(e)

(f)

(g)

Fig. 6.20 (e-g) Transient response of $[0°/90°]_{3s}$ beam with increasing gain ($\beta = 0$).

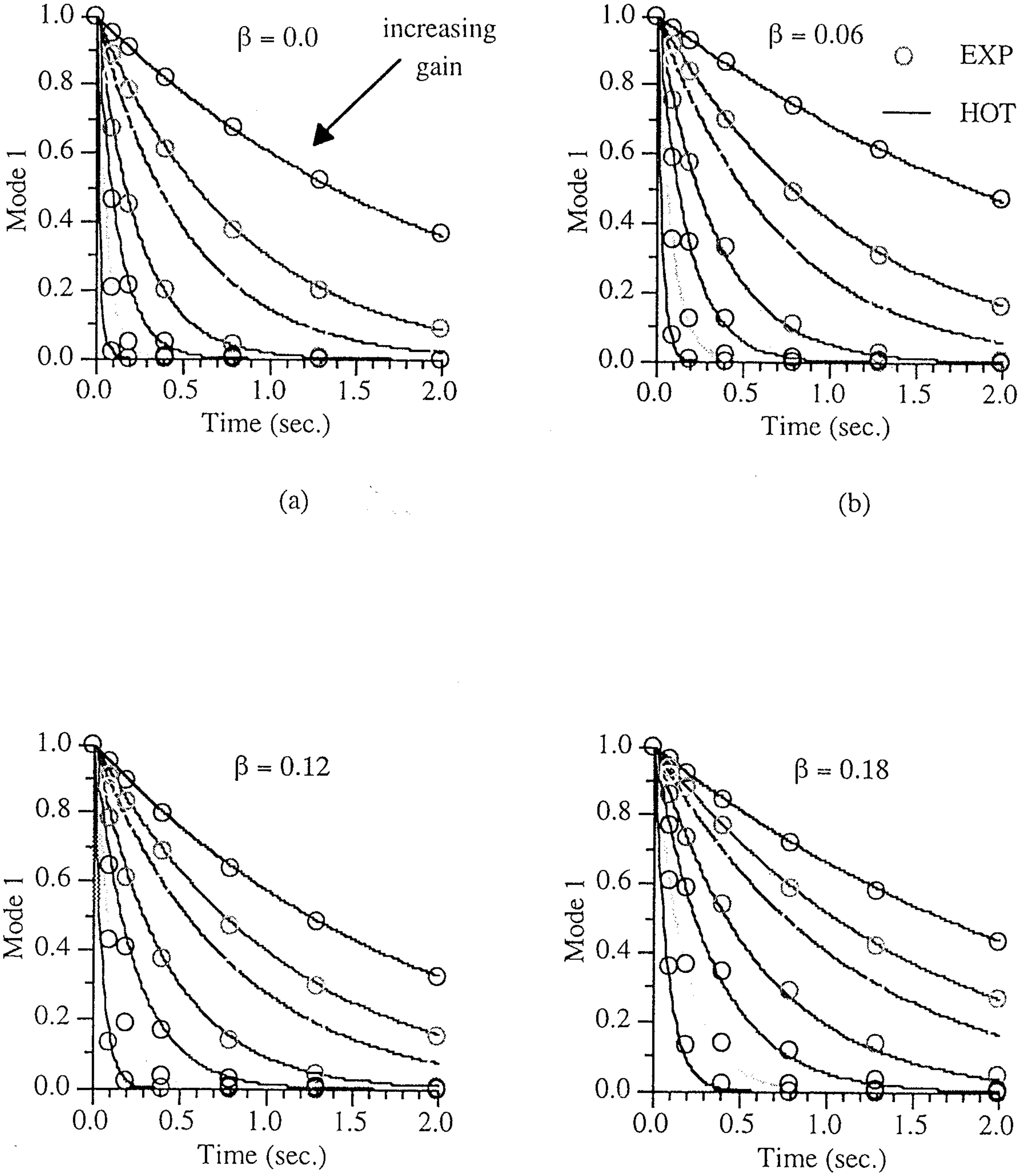

(a) (b)

(c) (d)

Fig. 6.21 (a-d) Decay envelopes for Mode 1 of $[0°/90°]_{3s}$ beams with debonding.

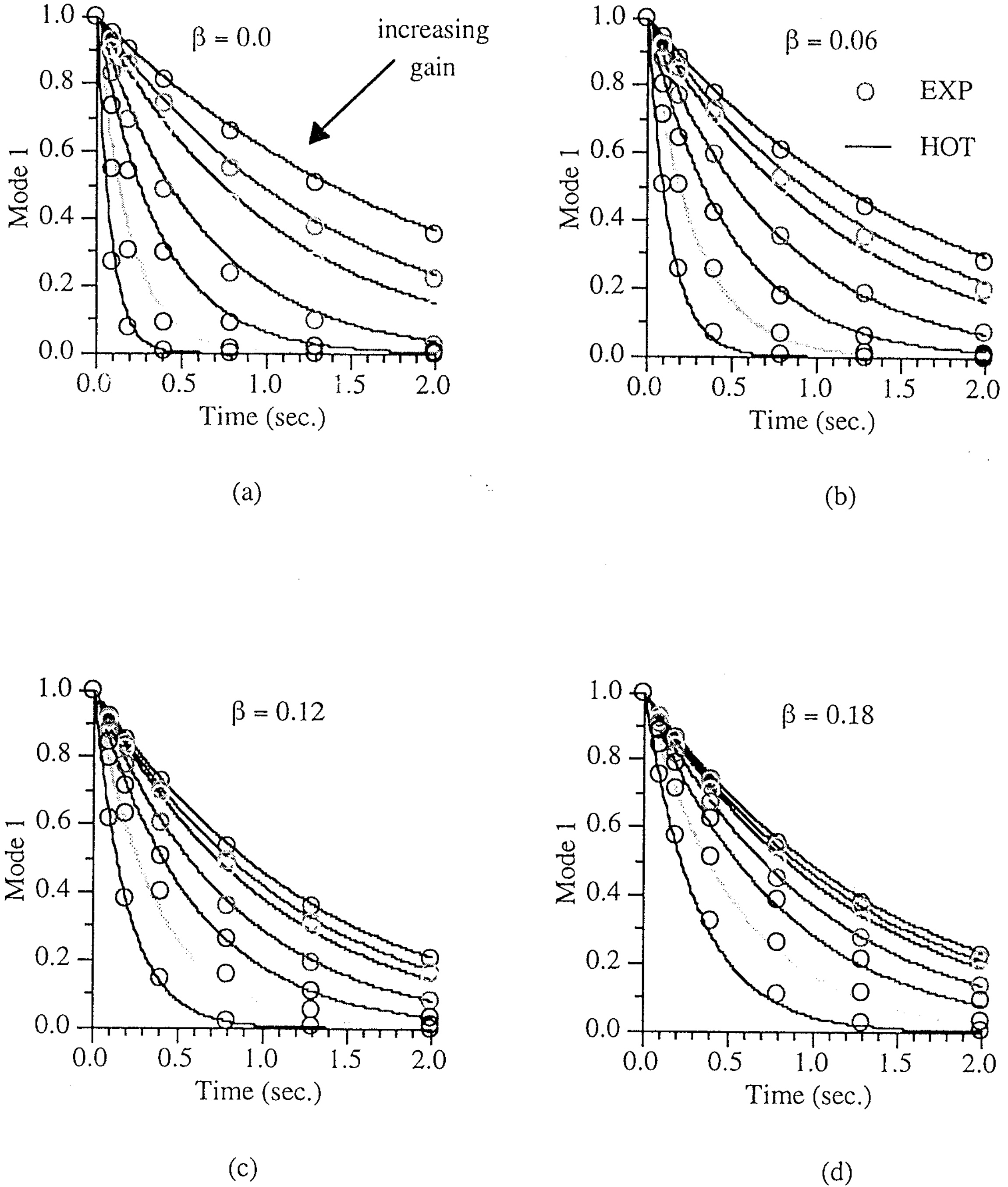

(a) (b)

(c) (d)

Fig. 6.22 (a-d) Decay envelopes for Mode 1 of $[45°/-45°]_{3s}$ beams with debonding.

6.5.4 Correlation of frequencies and damping ratios: In this section, the experimentally determined closed loop frequencies and damping ratios (EXP) are compared to the values of these quantities predicted by the higher order theory (HOT). Correlation is presented for both $[0°/90°]_{3s}$ and $[45°/-45°]_{3s}$ beams with debonding lengths of $\beta = 0.0$, 0.06, 0.12 and 0.18 for gains of 0, 200, 400, 1000, 2000, 4000 and 8700. The results are shown in Tables 6.6 and 6.7 and Figs 6.23 - 6.28. It must be noted that the mass of the accelerometer is included in the analysis using the HOT each case.

Correlation between the closed loop frequencies for the EXP and HOT determined cases is very good in general as shown in Tables 6.6 and 6.7. Overall, increasing debonding length decreases the frequencies for both $[0°/90°]_{3s}$ and $[45°/-45°]_{3s}$ beams. This is because the debonded portion of the actuators does not contribute any stiffness to the overall structure while the mass is still present. Decreasing stiffness with constant mass results in reduced frequencies. This is also true since the debonded actuators have less control authority over the structure resulting in less influence of the control system on the structural response. The effects of increasing gain are observed most predominately in the nondebonded beams. The natural frequency of the $[0°/90°]_{3s}$ beam ($\beta = 0.0$) increases 11.1% from 25.2 to 28.0 Hz while the $[45°/-45°]_{3s}$ ($\beta = 0.0$) beam increases 2.3% from 17.3 to 17.7 Hz for the EXP case as the gains are increased from 0 to 8700. The HOT predicts similar increases in the natural frequency of 13.6% and 1.9%, respectively. The open loop frequencies of all of the $[0°/90°]_{3s}$ test specimens are larger than the cutoff frequency of the low pass filter. Therefore, the closed loop frequencies of these beams are expected to increase with increasing gain as indicated by the root loci for the closed loop system presented earlier (Fig. 6.15). This trend is observed in both the EXP and HOT results. Although the open loop frequency of the nondebonded $[45°/-45°]_{3s}$ beam is larger than the cutoff frequency of the low pass filter, the open loop beam frequency decreases significantly (~ 10%) for increasing debonding length. In fact, the open loop frequencies of the debonded $[45°/-45°]_{3S}$ beams ($\beta>0$) are less than the cutoff frequency of the filter. Therefore, the closed loop frequencies are expected to decrease, rather than increase, according to the root loci presented earlier (Fig. 6.14). Although this effect is less noticeable for these beams since it is within the range of experimental accuracy, it is observed in the HOT results.

The results for the closed loop damping ratios are presented in Figs. 6.23 and 6.24 for the $[0°/90°]_{3S}$ beams and Figs. 6.25 and 6.26 for the $[45°/-45°]_{3S}$ beams with debonding lengths ranging from $\beta = 0.0$, 0.06, 0.12 and 0.18 and gains of 0, 200, 400, 1000, 2000, 4000 and 8700 as before. Increases in closed loop damping ratios up to $\zeta = 0.25$ due to piezoelectric actuation are obtained. Agreement between the EXP and HOT results is excellent. The closed loop damping ratios include contributions from both the passive structural damping and the active control. The damping ratios corresponding to the passive structural damping using the HOT are set equal to the experimentally determined damping ratios at zero gain in each case These structural damping ratios are included in the calculation of the closed loop damping ratios. In general, debonding decreases the closed loop damping ratios, especially at high gain (Figs. 6.24 and 6.26). The presence of debonded actuators has the effect of increasing the open loop damping ratios (gain = 0) and low gain (gain = 200, 400) in some cases. This is due to friction between the interfaces of the debonded actuator and the substructure. The open loop damping ratios represent the passive structural damping present in the system. The structural damping dominates the closed loop response at low gain and explains why the damping may actually increase as the debonding length increases (Figs. 6.23 and 6.25). However, once the closed loop damping is above 0.01, the effect of the control system dominates the response and debonding consistently reduces the actuator authority in all cases. In the worst case, debonding reduces the closed loop damping ratio of the $[0°/90°]_{3S}$ beam 68% from 0.023 to 0.073 at a gain of 8700 as the debonding length is increased from $\beta = 0.0$ to $\beta = 0.18$. Debonding clearly has a detrimental effect on the closed loop damping ratios. This detrimental effect on the control authority is especially clear on the settling time of the coupled controls/structures system as shown in Figs 6.27 and 6.28. The 2% settling time for the first mode is calculated as the time it takes for the control system to reduce the vibrational amplitude of the first mode to 2% of its initial value as follows.

$$t = -\frac{\ln(0.02)}{\zeta_b \omega_b} \tag{6.5.1}$$

where ζ_b and ω_b are the closed loop frequencies corresponding to the first mode of the beam. It is presented in Figs. 6.27 and 6.28 for values of high gain at various debonding lengths for the $[0°/90°]_{3s}$ and the $[45°/-45°]_{3s}$ beams, respectively. Clearly, increasing debonding significantly increases the settling time for both beams at relatively high gains. The settling time increases approximately 230% in the worse case for the $[0°/90°]_{3s}$ beam as the debonding length increases from $\beta = 0.0$ to $\beta = 0.18$ at a gain of 8700.

It must be noted that, in general, the piezoelectric actuators have more control over a relatively soft structure compared to a relatively stiff one. The $[45°/-45°]_{3s}$ beams are relatively softer than the $[0°/90°]_{3s}$ beams in bending types of deformation. Therefore, the piezoelectric actuators should demonstrate greater control authority. However, the closed frequency is significantly less which reduces the output of the accelerometer. Therefore, in the current study, the feedback control demonstrates relatively less authority over the $[45°/-45°]_{3s}$ beams.

Table 6.6 First closed loop natural frequency of $[0°/90°]_{3S}$ beams with debonding.

Debonding length (β)	Gain	EXP	HOT	% error
0.0	0	25.2	25.4	0.7
	200	25.1	25.4	1.0
	400	25.1	25.4	1.1
	1000	25.2	25.4	0.9
	2000	25.3	25.6	0.9
	4000	25.7	25.9	0.9
	8700	28.0	28.8	2.7
0.06	0	24.6	24.6	0.1
	200	24.6	24.6	0.1
	400	24.6	24.6	0.0
	1000	24.6	24.6	0.1
	2000	24.7	24.7	0.1
	4000	24.8	24.8	0.0
	8700	26.1	26.0	0.4
0.12	0	24.7	24.2	1.9
	200	24.7	24.2	1.9
	400	24.7	24.2	1.9
	1000	24.7	24.2	1.9
	2000	24.7	24.2	1.9
	4000	24.8	24.3	1.8
	8700	25.3	24.7	2.2
0.18	0	24.5	23.8	2.9
	200	24.6	23.8	2.9
	400	24.6	23.8	2.9
	1000	24.6	23.9	3.0
	2000	24.6	23.9	2.9
	4000	24.7	23.9	3.1
	8700	24.8	24.1	2.8

Table 6.7 First closed loop natural frequency of $[45°/-45°]_{3s}$ beams with debonding.

Debonding length (β)	Gain	EXP	HOT	% error
0.0	0	17.3	16.4	5.1
	200	17.3	16.4	5.1
	400	17.3	16.4	5.2
	1000	17.3	16.4	5.4
	2000	17.3	16.4	5.3
	4000	17.4	16.4	5.6
	8700	17.7	16.5	6.8
0.06	0	16.4	15.6	4.5
	200	16.4	15.6	4.4
	400	16.4	15.6	4.4
	1000	16.4	15.6	4.6
	2000	16.4	15.6	4.8
	4000	16.4	15.6	4.7
	8700	16.4	15.6	5.2
0.12	0	15.6	15.2	2.4
	200	15.6	15.2	2.7
	400	15.6	15.2	2.6
	1000	15.6	15.2	2.8
	2000	15.6	15.2	2.6
	4000	15.6	15.1	2.6
	8700	15.6	15.1	3.1
0.18	0	15.4	14.8	4.2
	200	15.4	14.8	4.1
	400	15.5	14.8	4.4
	1000	15.4	14.8	4.3
	2000	15.4	14.8	4.2
	4000	15.4	14.8	4.4
	8700	15.4	14.7	4.4

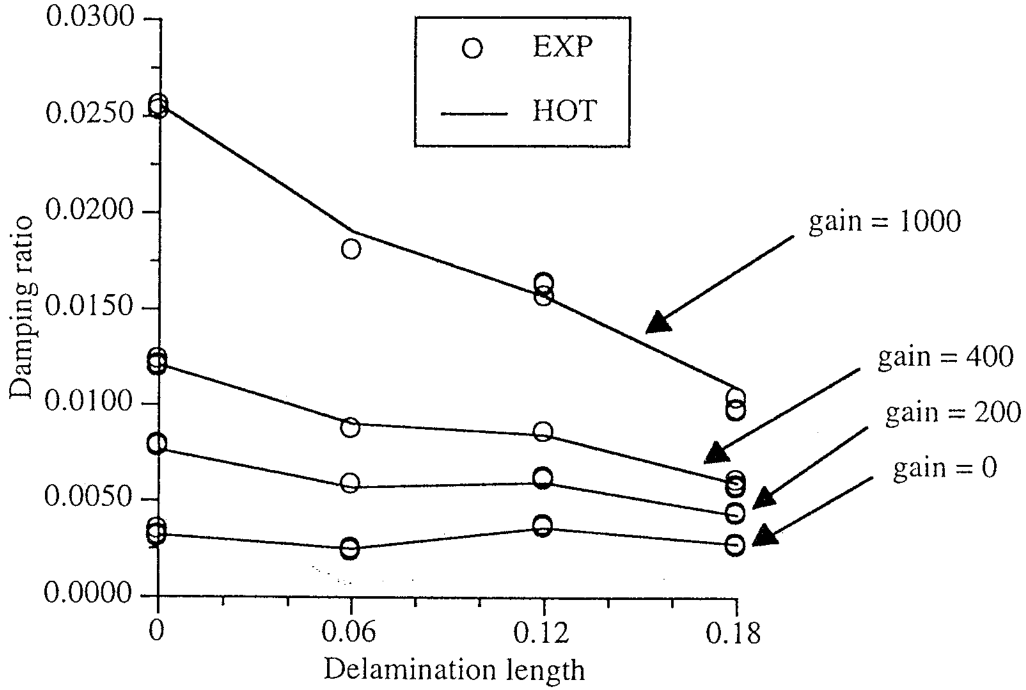

Fig. 6.23 Closed loop damping ratios for Mode 1 of $[0°/90°]_{3s}$ beams with debonding - low gain.

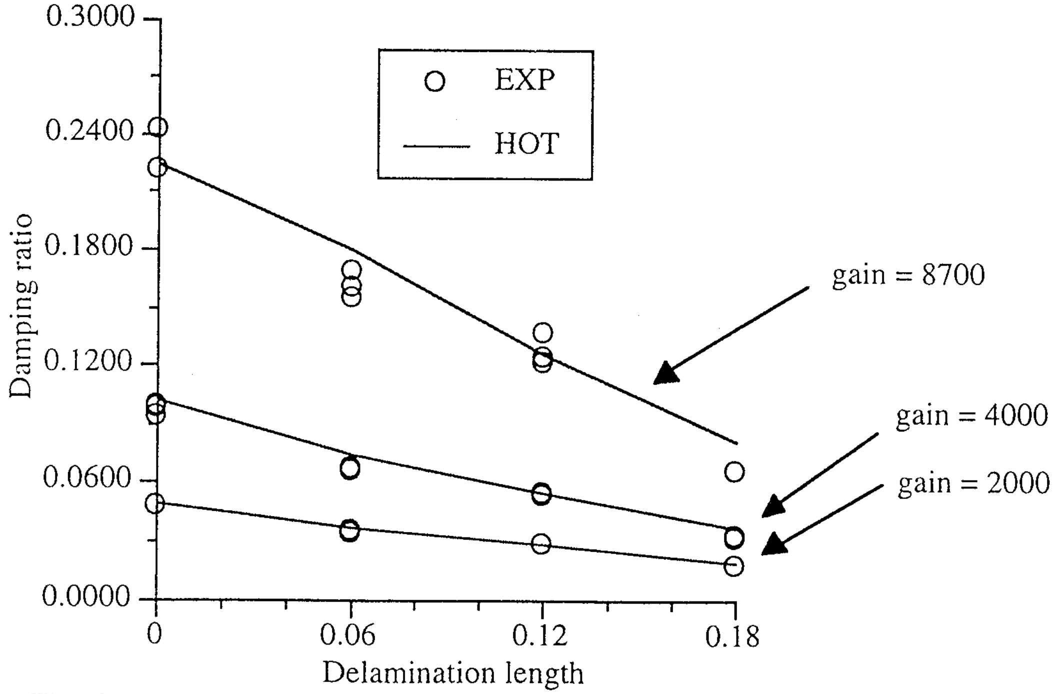

Fig. 6.24 Closed loop damping ratios for Mode 1 of $[0°/90°]_{3s}$ beams with debonding - high gain.

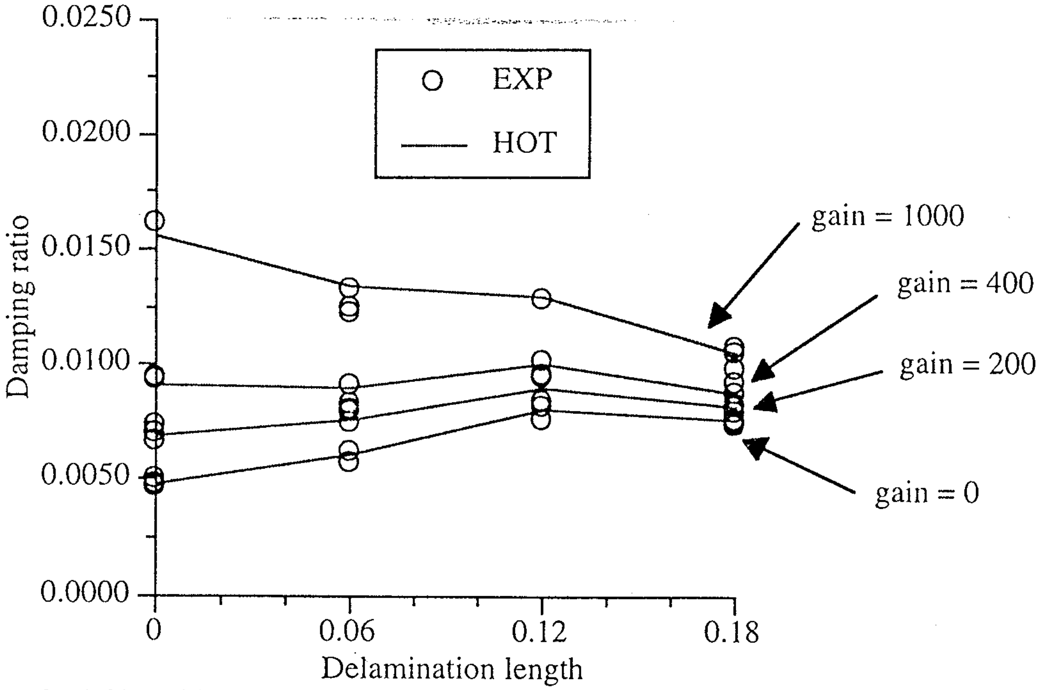

Fig. 6.25 Closed loop damping ratios for Mode 1 of [45°/-45°]$_{3S}$ beams with debonding - low gain.

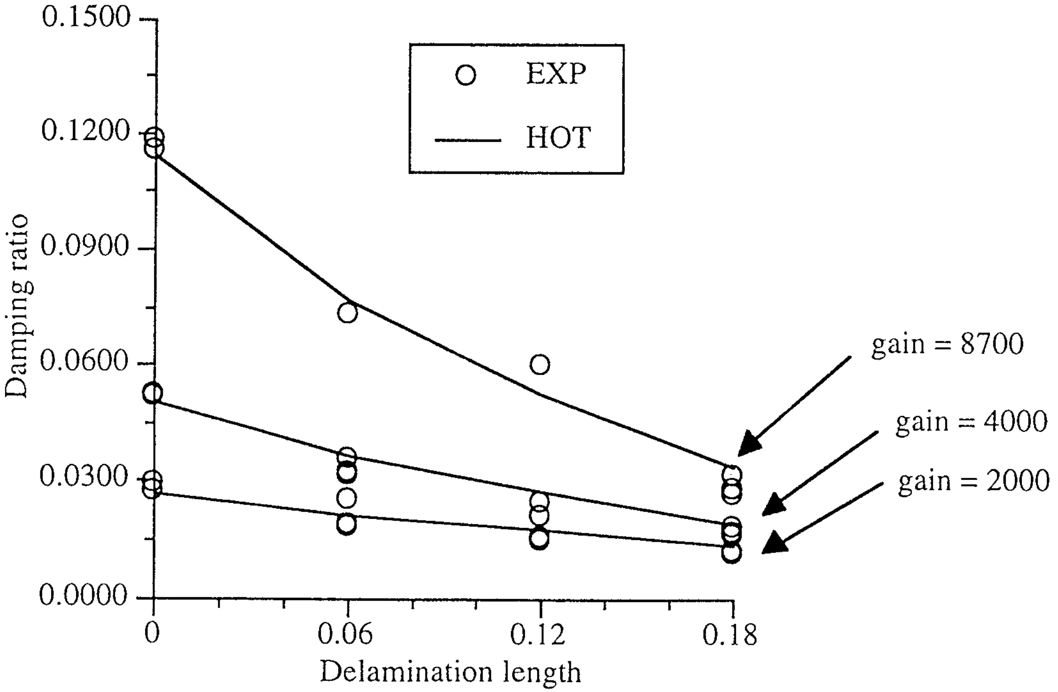

Fig. 6.26 Closed loop damping ratios for Mode 1 of [45°/-45°]$_{3S}$ beams with debonding - high gain.

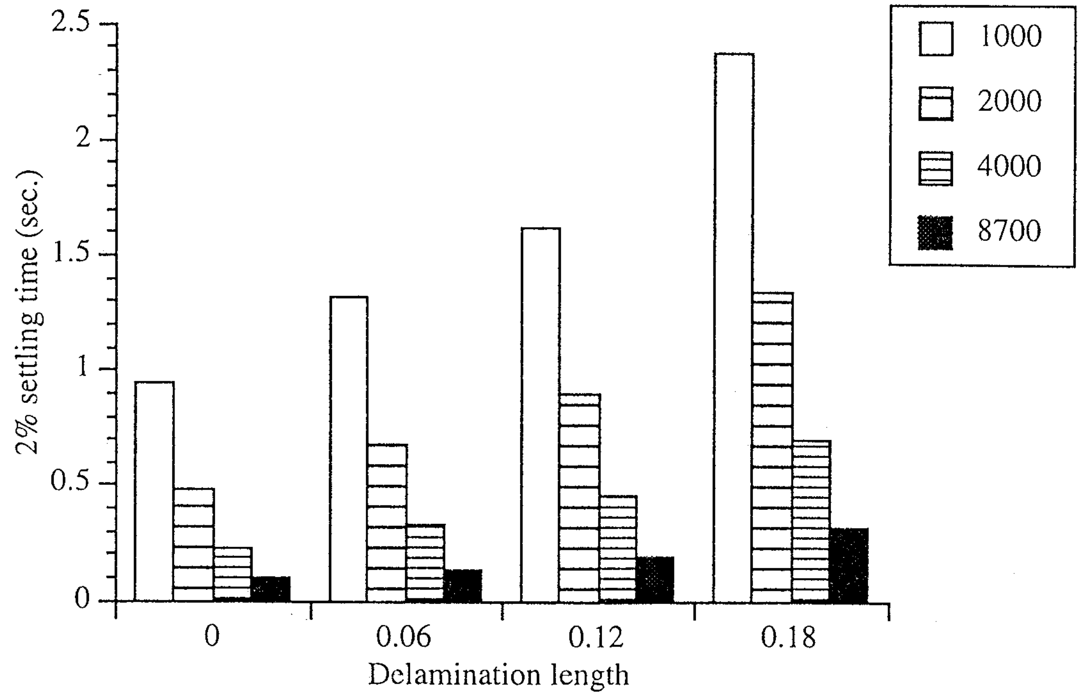

Fig.6.27 Settling time for Mode 1 of $[0°/90°]_{3s}$ beams with debonding - high gain.

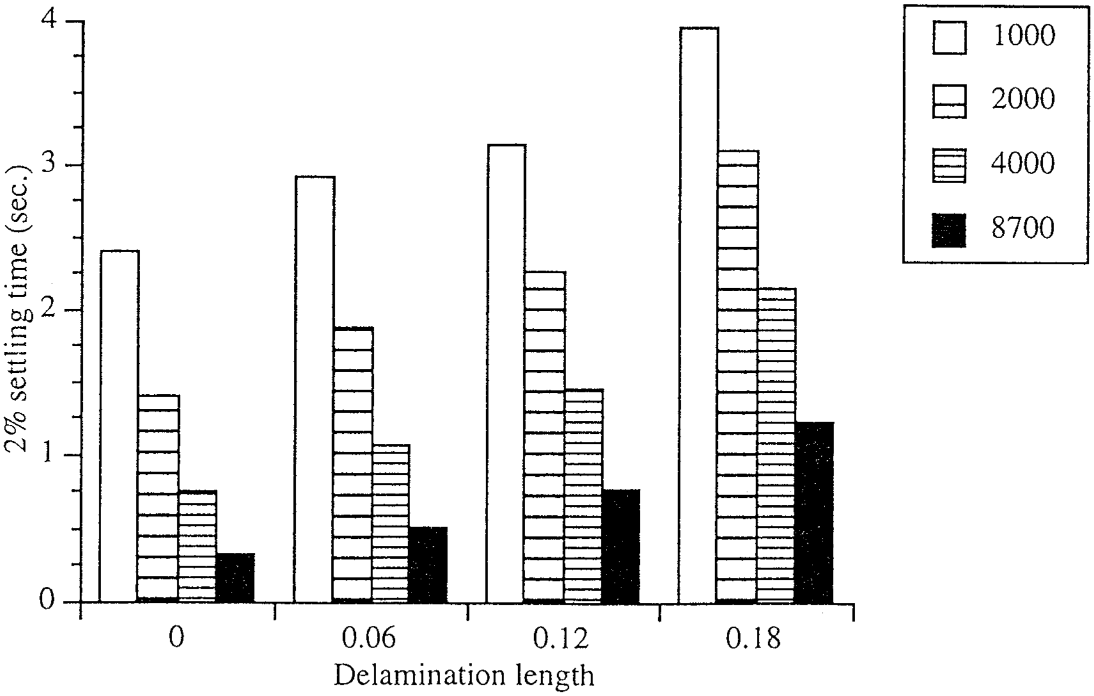

Fig.6.28 Settling time for Mode 1 of $[45°/-45°]_{3s}$ beams with debonding - high gain.

6.5.5 Laboratory setup: A visual record of the laboratory setup was obtained and is presented in this section. A test specimen is shown clamped in the vise ready to be tested in Fig. 6.29. Steel weights held the vise to a large concrete mass to minimize mechanical noise. The test specimen was mounted sideways to further reduce unwanted noise. The piezoelectric transducers are visible near the clamped end and the accelerometer can be seen near the tip of the beam. Some of the electronic devices used in the experiments are shown in Fig. 6.30. The two power amplifiers for the piezoelectric transducers are seen in the middle of the figure. On top of the power amplifiers are located the power supplies for the feedback control circuit. The feedback control circuit was constructed on two breadboards which are shown lying on the table. Connections between the power amplifiers, circuits, data acquisition system and test specimens were made via RG-58 cable with BNC connectors which comprise the "nest" of wires near the breadboards.

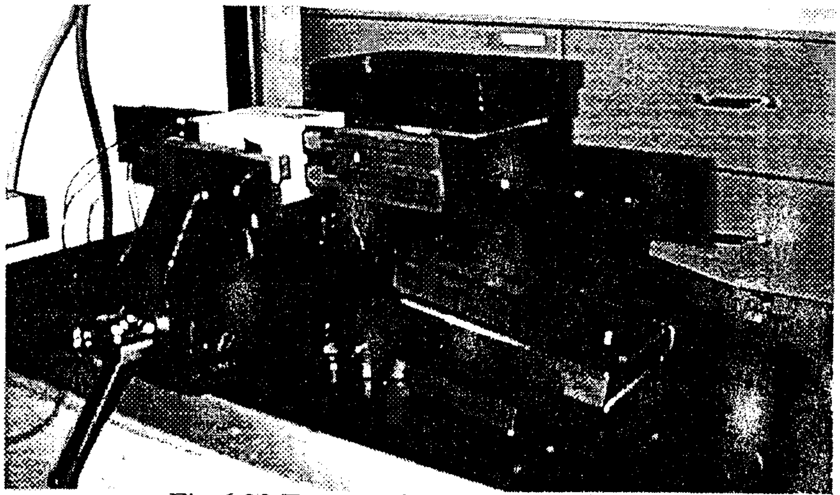

Fig.6.29 Test specimen clamped in vice

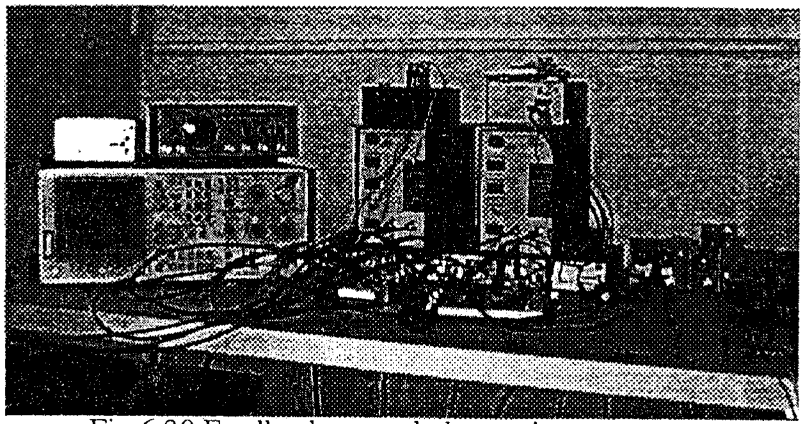

Fig.6.30 Feedback control electronic components

7. Concluding Remarks

A new theory has been developed to model composite laminates with surface bonded or embedded piezoelectric sensors and actuators. The theory is extended to incorporate the presence of pre-existing debonding in the composite laminate at the interface between the piezoelectric actuators and the underlying substructure. A refined higher order displacement field accurately captures the transverse shear deformation through the thickness of the smart composite laminate while satisfying the stress free boundary conditions on the free surfaces, including the debonded region. The higher order theory is implemented using the finite element method. The state space equations of motion utilizes the developed theory to account for piezoelectric sensing and actuation for closed loop control. Correlation of the higher order theory with analytical, numerical and experimental data is performed. Comparisons are also made with a commercial finite element code. An experimental investigation is conducted to further understand issues related to control of structures using piezoelectric actuation. Results are presented to demonstrate the analysis capability of the new theory. Additional studies are presented on the development of the constitutive equations for piezoelectric materials, justification of the higher order displacement field, and mesh generation which accounts for discrete piezoelectric layers. The following important observations are made.

1) The developed higher order theory provides an accurate, computationally efficient analysis tool for the study of composite laminates with piezoelectric sensing and actuation.

2) The theory is extended to incorporate debonded actuators.

3) The theory is implemented using the finite element method to allow incorporation of practical geometries, boundary conditions and discrete piezoelectric transducer locations.

4) Correlation with analytical, numerical and experimental data is established for isotropic and orthotropic plates, piezoelectric actuation and debonding. Both static and dynamic results agree very well.

5) The experimental investigation addressed practical issues, such as the design, construction, and testing of composite laminates and feedback control circuits. Consideration of these practical issues, coupled with the developed mathematical theory, provide an understanding and appreciation of the difficulty involved in implementation of smart structures as well as the potential benefit.

6) The agreement between the higher order theory and the experiments is very good. Subtle trends in the natural frequencies with increasing gain and debonding length are experimentally correlated with the higher order theory. Closed loop damping ratios on the order of more than 20% of critical are obtained and agree with the developed theory. Debonding of the piezoelectric actuators results in a reduction of the control authority which is also correlated with the higher order theory.

7) Significant deviations are observed between the higher order theory and the classical laminate theory in the strain and stress distributions through the thickness which indicates the importance of the higher order terms in the refined displacement field.

8) Debonding of the piezoelectric layer, which is modeled using the higher order theory, is shown to cause peeling of the actuator away from the substructure. This has important implications for failure analysis.

9) Local and global changes in the mode shapes also result due to debonding.

8. References

Aarts, Emile and Korst, Jan (1989) Simulated Annealing and Boltzmann Machines John Wiley and Sons, N.Y..

Abbott, I. H and Von Doenhoff, A. E. (1959) Theory of Wing Sections Dover Publications, Inc., N.Y..

Agarwal, B. D. and Broutman, L.J. (1990) Analysis and Performance of Fiber Composites John Wiley and Sons Inc., N.Y..

Andre, B., Clot, J. Partouche, E. and Simonne, J. J. (1992) "Thin Film PVDF Sensors Applied to High Acceleration Measurements" *Sensors and Actuators* pt. A, Vol. 33, pp. 111-114.

Anonymous (1994) "Smart Hush Helicopters" Machine Design, Aug., pp. 36-38.

Bailey, Thomas and Hubbard, James E. Jr. (1985) "Distributed Piezo-Polymer Active Vibration Control of a Cantilever Beam" *Journal of Guidance and Control,* Vol. 8, No. 5, Sep.-Oct., pp. 605-611.

Barbero, E. J. and Reddy, J. N. (1991) "Modeling of Delamination in Composite Laminates Using a Layer-wise Plate Theory" *International Journal of Solids and Structures*, Vol. 28, No. 3, pp. 373-388.

Ben-Zeev, O. and Chopra, I. (1995) "Continued Development of a Helicopter Rotor Model Employing Smart Trailing-Edge Flaps for Vibration Suppression" *Proc.* SPIE's 1995 Conference on Smart Structures and Materials, San Diego, CA, Feb. 27 - Mar. 3, pp. 2-19.

Bhimaraddi, A. and Stevens, L. K. (1984) "A Higher Order Theory for Free Vibration of Orthotropic, Homogeneous, and Laminated Rectangular Plates" *Journal of Applied Mechanics*, No. 51, Mar., pp. 195-198.

Brei, D. (1994) "Design and Development of a New Class of Piezoelectric Actuators for Force Improvement" *Proc.* Society of Engineering Science 31st Annual Technical Meeting, College Station TX, Oct. 10-12.

Cady, W. G. (1964) Piezoelectricity Vol. 1 Dover Publications Inc., N.Y..

Card, Michael F. (1992) A State of the Art Assessment of Active Structures, NASA TM #107681, Sep..

Carlson et al. (1990) Electrorheological Fluid Composite Structures, U.S. patent # 4923057, May 8.

Cerny, V. (1982) A Thermodynamical Approach to the Travelling Salesman Problem: An Efficient Simulation Algorithm, Report, Comenius University.

Chandra, R. (1993) "Active Strain Energy Tuning of Composite Beams Using Shape Memory Alloy Actuators" *Proc.* SPIE's 1993 North American Conference on Smart Materials and Structures, Albuquerque, NM, Feb. 1-4, pp. 1-18.

Chandrashekhara, K. and Agarwal, A. N. (1993) "Active Vibration Control of Laminated Composite Plates Using Piezoelectric Devices: A Finite Element Approach" *Journal of Intelligent Material Systems and Structures*, Vol. 4, Oct., pp. 496-508.

Chandrashekhara, K. and Donthireddy, P. (1996) "Modeling and Shape Control of Composite Beams with Embedded Piezoelectric Actuators" *Composite Structures*, Vol. 35, pp. 237-244.

Chattopadhyay, A. And Gu, H (1996) "An Experimental Investigation of Delamination Buckling and Postbuckling of Composite Laminates" *Proc.* ASME International Mechanical Engineering Congress and Exposition, Atlanta, GA, Nov. 17-22.

Chattopadhyay, A. and Gu, H. (1994) "A New Higher-Order Plate Theory in Modeling Delamination Buckling of Composite Laminates" *AIAA Journal*, Vol. 32, No. 8, Aug., pp. 1709-1718.

Chattopadhyay, A. and Gu, H. (1996) "Exact Elasticity Solution for Buckling of Composite Laminates" *Composite Structures*, Vol. 34, No. 3, pp. 291-299.

Chattopadhyay, A. and Jha, R. (1996) "Application of Hybrid Optimization Technique for Improved Aeroelastic Performance of Composite Wings" *Proc.* 6th AIAA/USAF/NASA/ISSMO Symposium on Multidisciplinary Analysis and Optimization, Bellevue, WA, Sep. 4-6.

Chattopadhyay, A. and Jha, R. (1996) "Application of Hybrid Optimization Technique for Improved Aeroelastic Performance of Composite Wings" Proc. 6th AIAA/USAF/NASA/ISSMO Symposium on Multidisciplinary Analysis and Optimization, Bellevue, WA, Sep. 4-6.

Chattopadhyay, A. and McCarthy, T. (1991) Multiobjective Design Optimization of Helicopter Rotor Blades with Multidisciplinary Couplings Structural Systems and Industrial Applications, pp. 451-461, Ed. S. Hernandez and C. A. Brebbia.

Chattopadhyay, A. and Seeley, C. E. (1994) "A Simulated Annealing Technique for Multiobjective Optimization of Intelligent Structures" *Smart Materials and Structures,* Vol. 3, pp. 98-106.

Chattopadhyay, A. and Seeley, C. E. (1995) "A Coupled Controls/Structures Optimization Procedure for the Design of Rotating Composite Box Beams with Piezoelectric Actuators" *Smart Materials and Structures*, Vol. 4, pp. 170-178.

Chattopadhyay, A. and Seeley, C. E. (1995) "Development of a Hybrid Optimization Technique with Application to Buckling of Cylindrical Shells" *Proc.* WCSMO-1, The First World Congress of Structural and Multidisciplinary Optimization, Goslar, Lower Saxony, Germany, May 28-June 2.

Chattopadhyay, A. and Seeley, C. E. (1996) "A Higher Order Theory for Modeling Composite Laminates with Induced Strain Actuators" *Composites Part B: Engineering*, Feb., accepted for publication.

Chaudhry, Z. and Rogers, C. A. (1993) "Performance and Optimization of Induced Strain Actuated Structures Under the Action of External Loads" *Proc.* 33rd AIAA/ASME/ASCE/AHS/ASC Structures, Structural Dynamics and Materials Conference, Dallas, TX, Apr 13-15, pp. 3475-3484.

Chopra, I. (1993) "Development of a Smart Rotor" *Proc.* 19th European Rotorcraft Forum, Cernobbio (Como) - Italy, Sep. 14-16.

Chopra, I. (1996) "Overview on Smart Structures and Integrated Systems" *Proc.* SPIE's 1996 Conference on Smart Structures and Materials, San Diego, CA, Feb. 26-29.

Chandra, R. and Chropra, I. (1993) "Structural Modeling of Composite Beams with Induced-Strain Actuators" AIAA Journal, Vol. 31, No. 9, Sep., pp. 1692-1701.

Cook, R. D. and Young, W. C. (1985) Advanced Mechanics of Materials Macmillan Publishing Company, N.Y..

Crawley, E. F. and Anderson, E. H. (1989) "Detailed Models of Piezoelectric Actuation of Beams" *Proc.* 30th AIAA/ASME/ASCE/AHS/ASC Structures, Structural Dynamics and Materials Conference, Mobile, AL, Apr., pp. 2000-2010.

Crawley, E. F. and de Luis, J. (1987) "Use of Piezoelectric Actuators as Elements of Intelligent Structures" *AIAA Journal*, Vol. 25, No. 10, pp. 1373-1385.

Crawley, E. F. and Lazarus, K. B. (1991) "Induced Strain Actuation of Isotropic and Anisotropic Plates" *AIAA Journal,* Vol. 29, No. 5, June, pp. 944-951.

Detwiler, D. T., Shen, M.-H.H. and Venkayya, V. B. (1995) "Finite Element Analysis of Laminated Composite Structures Containing Distributed Piezoelectric Actuators and Sensors" *Finite Elements in Analysis and Design*, Vol. 20, pp. 87-100.

Dowell, E. H. (ed.), Crawley, E. F., Curtiss, H. C. Jr., Peters, D. A., Scanlan, R. H., and Sisto, F. (1995) A Modern Course in Aeroelasticity Kluwer Academic Publishers, Boston.

Durney, C.H., Harris, L.D. and Alley, C.L. (1982) Electric Circuits: Theory and Engineering Applications Holt, Rinehart and Winston, N.Y..

Encyclopedia Britannica (1994) Piezoelectricity Encyclopedia Britannica Inc., Chicago.

Fadel, G. M., Riley, M. F. and Barthelemy, J. F. (1990) "Two Point Exponential Approximation Method for Structural Optimization" *Structural Optimization*, Vol. 2, pp. 117-124.

Fletcher, R. (1970) "A New Approach to Variable Metric Algorithms" *Computer Journal,* Vol. 13, No. 13, pp. 317-322.

Freidmann, P. P., Carman, G. and Millott, T. A. (1995) "Magnetostrictively Actuated Control Flaps for Vibration Reduction in Helicopter Rotors" *Proc.* Second Workshop on Smart Structures and Materials, Sponsored by the U. S. Army Research Office, University of Maryland, College Park, MD, Sep. 5-7.

Funakubo, H. (1987) Shape Memory Alloys Gordon and Breach Science Publisher, N.Y..

Fung, Y.C. (1993) An Introduction to the Theory of Aeroelasticity Dover Publications, Inc, New York.

Garner, G. M. (1977) "A New Microphone for Telephone Handsets" Systems Technology, Vol. 27, Nov..

Geman, S. and Geman, D. (1984) "Stochastic Relaxatin, Gibbs Distributions, and the Bayesian Restoration of Images" *Proc.* IEEE Transactions on Pattern Analysis and Machine Intelligence, Vol. 6, No. 6, Nov..

Ghorayeb, S. R. and Straub, F. K. (1995) "Application of Magnetostrictive Smart Materials in Rotor Servoflap Control" *Proc.* SPIE's 1995 Conference on Smart Structures and Materials, San Diego, CA, Feb. 27 - Mar. 3, pp. 28-37.

Gummadi, L. N. B. and Hanagud, S. (1995) "Vibration Characteristics of Beams with Multiple Delaminations" *Proc.* 36th AIAA/ASME/ASCE/AHS/ASC Structures, Structural Dynamics and Materials Conference - Adaptive Structures Forum, New Orleans, LA, Apr. 10-14, pp. 140-150.

Guo, R. and Chattopadhyay, A. (1995) "Energy Absorption in Composite Plates Using Analytical Sensitivity Analysis and Hybrid Optimization" *Proc.* . AHS National Technical Specialists Meeting, Williamsburg, VA, Oct. 30-Nov. 2.

Ha, Sung Kyu, Keilers, Charles and Chang, Fu-Kuo (1992) "Finite Element Analysis of Composite Structures Containing Distributed Piezoceramic Sensors and Actuators" *AIAA Journal*, Vol. 30, No. 3, Mar., pp. 772-780.

Hanagud, S., Obal, M. W., Calise, A. J. (1992) "Optimal Vibration Control by the Use of Piezoceramic Sensors and Actuators" *Journal of Guidance, Control and Dynamics*, Vol. 15, No. 5, pp. 1199-1205.

Heeg, J. (1992) "An Analytical and Experimental Investigation of Flutter Suppression via Piezoelectric Actuation" *Proc.* AIAA 33rd Dynamics Specialists Meeting, Washington D.C., pp. 237-247.

Hwang, W. S., Park, H. C. and Hwang, W. (1993) "Vibration Control of a Laminated Plate with Piezoelectric Sensor/Actuator: Finite Element Formulation and Modal Analysis" *Journal of Intelligent Material Systems and Structures*, Vol. 4, July, pp. 317-329.

Ikuta, K. Tsukamoto, M. and Hirose, S. (1992) "A Tiny Silent Linear Cybernetic Actuator Driven by Piezoelectric Device with Electromagnetic Clamp" *Proc.* IEEE Robotics and Automation Society Conference on MicroElectroMechanical Systems, Travemunde, Germany, Feb. 4-7, pp. 232-237.

Ingber, L. (1993) "Simulated Annealing: Practice versus Theory" *Journal of Mathematical and Computational Modeling*, Vol. 18, No. 11, pp. 29-57.

Jones, M. T., Patrick, M. L. (1996) LANZ: Software for Solving the Large Sparse Symmetric Generalized Eigenproblem, Public Domain Software Documentation, Apr..

Kalman, R. E. (1963) The Calculus of Variations and Optimal Control Theory University of California Press, Berkeley, CA.

Kamath, G. M. and Wereley, N. M. (1995) "Development of ER-Fluid Based Actuators for Rotorcraft Flexbeam Applications" *Proc.* SPIEs 1995 North American Conference on Smart Materials and Structures, San Diego, CA, Feb. 27 - Mar. 3, pp. 120-133.

Kardomateas, G. A and Schmueser (1988) "Buckling and Postbuckling of Delaminated Composites Under Compressive Loads Including Transverse Shear Effects" *AIAA Journal*, Vol. 26, No. 3, pp. 337-343.

Kawai, H. (1969) "The Piezoelectricity of Poly Vinylidene Fluoride" *Japanese Journal of Applied Physics,* Vol. 8, pp. 975-976.

Kawai, H. (1969) "The Piezoelectricity of Poly Vinylidene Fluoride" *Japanese Journal of Applied Physics*, Vol. 8, pp. 975-976.

Kim, S. J. and Jones, J. D. (1990) "Optimal Design of Piezo-Actuators for Active Noise and Vibration Control" *Proc.* AIAA 13th Aeroacoustics Conference, Tallahasse, FL, Oct. 22-24, pp. 1-11.

Kincaid, D. R., Respess, J. R., Young, D. M., and Grimes, R. G. (1996) ITPACK 2C: A FORTRAN Package for Solving Large Sparse Linear Systems by Adaptive Accelerated Iterative Methods, Public Domain Software Documentation, Apr..

Koconis, D. B., Kollar, L. P. and Springer, G. S. (1994) "Shape Control of Composite Plates and Shells with Embedded Actuators. I. Voltages Specified" Journal of Composite Materials, pp. 415-456.

Lee C. K. (1990) "Theory of Laminated Piezoelectric Plates for the Design of *Distributed Sensors/Actuators. Part 1: Governing Equations and Reciprocal Relationships" Journal of the Acoustical Society of America*, Vol. 87, No. 3, Mar., pp. 1144-1158.

Lee, C. K. and Moon, F. C. (1989) "Laminated Piezopolymer Plates for Torsion and Bending Sensors and Actuators" *Journal of the Acoustical Society of America*, Vol. 85, No. 6, June, pp. 2432-2439.

Lee, H. J. and Saravanos, D. A. (1995) "Coupled Layerwise Analysis of Thermopiezoelectric Smart Composte Beams" *AIAA Journal*, Aug, submitted for possible publication.

Lee, J. E. and Fassois, S. D. (1990) "A Stochastic Suboptimum Maximum Likelihood Approach to Structural Dynamics Identification" *Proc.* of the 8th International Model Analysis Conference, Kissimmee, FL, Jan. 29-Feb. 1, pp. 1424-1433.

Leeks, T. J. and Weisshaar, T. A. (1995) "Optimization of Unsymmetric Actuators for Maximum Panel Deflection Control" *Proc.* SPIE's 1995 Conference on Smart Structures and Materials, San Diego, CA, Feb. 27 - Mar. 3, pp. 40-51.

Lin, C. Y. and Crawley, E. F. (1995) "Aeroelastic Actuation Using Elastic and Induced Strain Anisotropy" *Journal of Aircraft*, Vol. 32, No. 5, Sep.-Oct., pp. 1130-1137.

Lin, M. W. and Rogers, C. A. (1993) "Modeling of the Actuation Mechanism in a Beam Structure with Induced Strain Actuators" *Proc.* 34th AIAA/ASME/ASCE/AHS/ASC Structures, Structural Dynamics and Materials Conference, LaJolla, CA, Apr. 19-22, pp. 3608-3617.

Lobitz, D. W., Grossman, J. W., Allen, J. J. and Rice, T. M. (1995) "Shape Control of Solar Collectors Using Shape Memory Alloy Actuators" *Proc.* 36th AIAA/ASME/ASCE/AHS/ASC Structures, Structural Dynamics and Materials Conference - Adaptive Structures Forum, New Orleans, LA, Apr. 10-13, pp. 3357-3369.

Luenberger, D. G. (1989) Linear and Nonlinear Programming Addison-Wesley Publishing Company, Reading, MA.

Lyon, J. (1996) "Development and Validation of a Linearized ARMAX System Identification Algorithm" Masters Thesis, Arizona State University.

Makris, N., Hill, D. Burton, S. and Jordan, M. (1995) "Electrorheological Fluid Damper for Seismic Protection of Structures" *Proc.* SPIEs 1995 North American Conference on Smart Materials and Structures, San Diego, CA, Feb. 27 - Mar. 3, pp.184-194.

Mason. W. (1950) Piezoelectric Crystals and Their Application to Ultrasonics D. Van Nostrand Co. , N.Y..

McGee, O. G. and Leissa, A. W. (1991) "Three-Dimensional Free Vibrations of Thick Skewed Cantilevered Plates" *Journal of Sound and Vibration*, Vol. 144, No. 2, pp. 305-322.

Meirovitch, L. (1990) Dynamics and Control of Structures John Wiley and Sons, N.Y..

Metropolis, N., Rosenbluth, A., Rosenbulth, M, Teller, A. H. and Teller, E. (1953) "Equation of State Calculations by Fast Computing Machines" *Journal of Chemical Physics*, Vol. 21, pp. 1087-1092.

Mignolet, M. P., Red-Horse, J. R and Lin, C-C (1993) “A Multistage ARMAX Identification of Structures” *Proc.* 34th AIAA/ASME/ASCE/AHS/ASC Structures, Structural Dynamics and Materials Conference, LaJolla, CA, Apr. 19-22, pp. 3366-3374.

Mignolet, M. P. and Red-Horse, J. R. (1994)“ARMAX Identification of Vibrating Structures: Model and Model Order Estimation” *Proc.* 35th AIAA/ASME/ASCE/AHS/ASC Structures, Structural Dynamics and Materials Conference - Adaptive Structures Forum, Hilton Head, SC, Apr. 21-22. pp. 1628-1637.

Mignolet, M. (1995) MAE 515: Structural Dynamics (class notes), Jan. - May.

Mitchell, J. A. and Reddy, J. N. (1995) "A Refined Hybrid Plate Theory for Composite Laminates with Piezoelectric Laminae" *International Journal of Solids and Structures*, Vol. 32, No. 16, pp. 2345-2367.

Mitchell, J. A. and Reddy, J. N. (1995) "A Study of Embedded Piezoelectric Layers in Composite Cylinders" *Journal of Applied Mechanics*, Vol. 62, Mar., pp. 166-173.

Mollenhauer, D. H. and Griffen, O. H. Jr. (1994,) "Induced Strain of Actuation of Surface Bonded Piezoceramic Patches: A Numerical and Experimental Study" Journal of Intelligent Material Systems and Structures, Vol. 5, pp. 335-362.

Newnham, R. E. and Ruschau, G. R. (1991) "Smart Electroceramics" *Journal of the American Ceramic Society*, Vol. 74, No. 3, Mar., pp. 463-480.

Pagaldipti, N., Narayan, J. R. and Chattopadhyay, A. (1996) "Multidisciplinary Optimization Procedure for High Speed Aircraft Using a Semi-Analytical Sensitivity Analysis Procedure and Multilevel Decomposition" *Proc.* 37th AIAA/ASME/ASCE/AHS/ASC Structures, Structural Dynamics and Materials Conference, Salt Lake City, UT, Apr. 15-18.

Pagano, N. J, (1970) "Exact Solutions for Rectangular Bidirectional Composites and Sandwich Plates" *Journal of Composite Materials*, Vol. 4, pp. 20-34.

Paige, D. A., Scott, R. C. and Weisshaar, T. A. “Active Control of Composite Panel Flutter Using Piezoelectric Materials” *Proc.* SPIE’s 1993 North American Conference on Smart Materials and Structures, Albuquerque, NM, Feb. 1-4.

Pavier, M. J. and Clarke, M. P. (1996) "A Specialized Composite Plate Element for Problems of Delamination Buckling and Growth" *Composite Structures,* Vol. 35, pp. 45-53.

Pinkerton, J. L., McGowan, A. R., Moses, R. W., Scott, R. C. and Heeg, J. (1996) "Controlled Aeroelastic Response and Airfoil Shaping Using Adaptive Materials and Integrated Systems" *Proc.* SPIEs 1996 Conference on Smart Structures and Materials, San Diego, CA, Feb. 26-29.

Ramamurti, V. and Kielb, R. (1984) "Natural Frequencies of Twisted Rotating Plates" *Journal of Sound and Vibration*, Vol. 97, No. 3, pp. 429-449.

Ray, M. C., Bhattacharya, R. and Samanta, B. (1993) "Exact Solutions for Static Analysis of Intelligent Structures" *AIAA Journal*, Vol. 31, No. 9, Sep., pp. 1684-1691.

Reddy, J. N. (1984) Energy and Variational Methods in Applied Mechanics John Wiley and Sons, N.Y..

Reddy, J. N. (1990) "A General Non-Linear Third-Order Theory of Plates with Moderate Thickenss" *Internation Journal of Non-Linear Mechanics*, Vol. 25, No. 6, pp. 677-686.

Ren, J. G. and Hinton, E. (1986) "The Finite Element Analysis of Homogeneous and Laminated Composite Paltes Using a Simple Higher Order Theory" *Communications in Applied Numerical Methods*, Vol. 2, pp. 217-228.

Richard, J. S. and Cudney, H. H. (1993) "Modeling Multiple Layer Piezoelectric Actuators in Active Structural Control" *Proc.* SPIE’s 1993 North American Conference on Smart Materials and Structures, Albuquerque, NM, Feb. 1-4.

Robbins, D. H. and Reddy, J, N. (1993) "Modeling of Actuators in Laminated Composite Structures" *Proc.* SPIE's 1993 North American Confernece on Smart Structures and Materials, Albuquerque, NM, Feb 1-4, pp. 485-495.

Robbins, D. H. and Reddy, J. N. (1991) "Analysis of Piezoelectrically Actuated Beams Using a Layerwise Displacement Theory" *Computers and Structures*, Vol. 41, No. 2, pp. 265-279.

Rodden, W. P. and Albano, E. (1969) "A Doublet-Lattice Method for Calculating Lift Distributions on Oscillating Surfaces in Subsonic Flows" *AIAA Journal*, Vol. 7, No. 2, Feb., pp. 279-285.

Rogers, C. A, Barker, D. K. and Jaeger, C. A. (1989) "Introduction to Smart Materials and Structures" Proc. U. S. Army Workshop on Smart Materials, Structures and Mathematical Issues, Virginia Polytechnic Institute, Sep. 15-16.

Schetky, L. (1979) "Shape Memory Alloys" *Scientific American*, Vol. 241, pp. 74-82.

Seeley, C. E. and Chattopadhyay, A. (1996) "Modeling Delaminations in Smart Composite Laminates" Proc. 37th AIAA/ASME/ASCE/AHS/ASC Structures, Structural Dynamics and Materials Conference and Adaptive Structures Forum, Salt Lake City, UT, Apr. 15-19.

Seeley, C. E., Chattopadhyay, A. and Brei, D. (1996) "Development of a Polymeric Piezoelectric C-Block Actuator Using a Hybrid Optimization Procedure" *AIAA Journal*, Vol. 34, No. 1, Jan., pp. 123-128.

Seeley, C. E., Chattopadhyay, A. and Mitchell, L. (1996) "Design of a Smart Flap Using C-Block Actuators and a Hybrid Optimization Technique" *Proc.* SPIEs 1996 North American Conference on Smart Materials and Structures, San Diego, CA, Feb. 26-29.

Seeley, C. E., Chattopadhyay, A. and Mitchell, L. (1997) "Design of a Smart Flap Using C-Block Actuators and a Hybrid Optimization Technique" *Smart Materials and Structures*, Jan., accepted for publication.

Shah, D. K., Joshi, S, P, and Chan, W. S. (1993) "Structural Response of Plates with Piezoceramic Layers" *Proc.* SPIE's 1993 North American Conference on Smart Materials and Structures, Albuquerque, NM, Feb. 1-4, pp. 428-439.

Shieh, R. C. (1993) "Finite Element Formulation for Dynamic Response Analysis of Multiaxially Active 3-D Piezoelectric Beam Element Structures" *Proc.* 34th AIAA/ASME/ASCE/AHS/ASC Structures, Structural Dynamics and Materials Conference, LaJolla, CA, Apr. 19-22, pp. 3250-3260.

Sirkis, J. S. (1996) "What Does it Take to be Smart ?" *Proc.* SPIE's 1996 Conference on Smart Structures and Materials, San Diego, CA, Feb. 26-29, invited technical talk.

Song, O., Ligrescu, L. and Rogers, C. A. (1992) "Application of Adaptive Technology to Static Aeroelestic Control of Wing Structures" *AIAA Journal*, Vol. 30, No. 12, Dec., pp. 2882-2889.

Sprangler, R. L. Jr. and Hall, S. R. (1990) "Piezoelectric Actuators for Helicopter Rotor Control" *Proc.* 31st AIAA/ASME/ASCE/AHS/ACE Structures, Structural Dynamics and Materials Conference, Long Beach, CA, Apr. 2-4, pp. 1589-1599.

Srinivas, S., Joga Rao, C. V. and Rao, A. K. (1970) "An Exact Analysis for Vibration of Simply Supported homogeneoys and Laminated Thick Rectangular Plates" *Journal of Sound and Vibration*, Vol. 12, pp. 187-199.

Stevens, T. (1991) "Structures Get Smart" *Materials Engineering*, Oct., pp. 18-20.

Stout, D. F. (1976) Handbook of Operational Amplifier Circuit Design, NY, McGraw Hill.

Sullivan, T. D. and Powers, J. M. (1978) "Piezoelectric Polymer Flexural Disk Hydrophone" *Journal of the Acoustical Society of America*, Vol. 63, No. 5, May.

Szu, Harold and Hartley, Ralph (1987) "Fast Simulated Annealing" *Physical Letters A*, Vol. 122, No. 3, June, pp. 157-162.

Taguchi, M. (1987) "Applications of High Technology Ceramics in Japanese Automobiles" *Advances in Ceramic Materials*, Vol. 2, pp. 754-762.

Thirupathi, S. R. and Naganathan, G. G. (1992) "Use of Piezoceramic Actuator For Automotive Active Suspension Mechanisms: A Feasibility Study" *Proc.* 22nd Biennial Mechanism Conference, Scottsdale AZ, Sep. 23-26, pp. 233-241.

Tiersten, H. F. (1969) Linear Piezoelectric Plate Vibrations Plenum Press, New York.

Tsai, S. W. and Wu, E. M. (1971) "A General Theory of Strength for Anisotropic Materials" *Journal of Composite Materials*, Vol. 5, pp. 58-80.

Tsuka, H. and Nakomo, J. (1990) "A New Electronic Controlled Suspension Using Piezoelectric Ceramics" *Proc.* IEEE Workshop on Electronic Applications in Transportation.

Tzou, H. S. and Zhong, J. P. (1993) "Electromechanics and Vibrations of Piezoelectric Shell Distributed Systems" *Journal of Dynamic Systems Measurement, and Control,* Vol. 115, Sep., pp. 506-517.

Vanderplaats, G. N. (1984) Numerical Optimization Techniques for Engineering Design with Applications McGraw-Hill Publishing Company, N.Y..

Vinson, J. R. and Sierakowski, R. L. (1987) The Behavior of Structures Composed of Composite Materials Martinus Nijhoff, Dordrecht, The Netherlands.

Voigt, W. (1928) Lehrbuch der Kristallphysik, 2nd ed. B. G. Teubner, Leipzig.

Walz, C. and Chopra, I. (1994) "Design and Testing of a Helicopter Rotor Model with Smart Trailng Edge Flaps" *Proc.* 35th AIAA/ASME/ASCE/AHS/ASC Structures, Structural Dynamics and Materials Conference - Adaptive Structures Forum, Hilton Head, SC, Apr. 21-22.

Wang, Bor-Tsuen and Rogers, Craig A. (1991) "Laminate Plate Theory for Spatially Distributed Induced Strain Actuators" *Journal of Composite Materials*, Vol. 25, Apr., pp. 433-452.

Whitcomb, J. D. (1981) "Finite Element Analysis of Instability Related Delamination Growth" *Journal of Composite Materials,* Vol. 15, pp. 403-426.

Whitcomb, J. D. (1989) "Three Dimensional Analysis of a Postbuckled Embedded Delamination" *Journal of Composite Materials*, Vol. 23, pp. 862-889.

Winslow, W. M. (1949) "Induced Fibration of Suspensions" *Journal of Applied Physics,* Vol. 20, Dec., pp. 1137-1140.

Xu, Q. C., Newnham, R. E., Blaskiewicz, Fang, T. T., Srinivasan, T. T. and Yoshikawa, S. (1990) "Nonlinear Multilayer Composite Transducers" *Proc.* IEEE 7th International Symposium on Applications for Ferroelectrics, Urbana, Il, June 6-8.

Yang, H. T. Y. and He, C. C. (1994) "Three-Dimensional Finite Element Analysis of Gree Edge Stresses and Delamination of Composite Laminates" *Journal of Composite Materials*, Vol. 28, No. 15, pp. 1394-1412.

Zienkiewicz, O. C. (1977) The Finite Element Method, New York, McGraw Hill.

Appendix A

Piezoelectric Constitutive Relations

A.1 General formulation

Voigt (1928) formalized the equations for the free energy of a piezoelectric material which he called the "thermodynamic potential". When the free energy is expressed in terms of strains, it is known as the first thermodynamic potential and is denoted by H(ε,E). In tensor notation, it is formulated as follows (Tiersten; 1969).

$$H(\varepsilon,E) = \frac{1}{2}c^{E}_{ijkl}\varepsilon_{ij}\varepsilon_{kl} - e_{ijk}E_i\varepsilon_{jk} - \frac{1}{2}\eta^{\varepsilon}_{ij}E_iE_j \tag{A.1}$$

where c^{E}_{ijkl}, e_{ijk} and η^{ε}_{ij} are the coefficients of the elastic stiffness at constant electric field, piezoelectric stress and dielectric permittivity at constant strain, respectively. The quantities ε_{ij} and E_i are the components of strain and electric field, respectively. The first term on the right hand side of Eqn. A.1 represent the elastic strain energy. The second term represents the electro-mechanical coupling while the third term is the electric energy. The differential coefficients of the first thermodynamic potential with respect to the components of elastic strain are the components of stress and the differential coefficients with respect to the components of electric field are the components of charge. These are the fundamental piezoelectric equations in terms of the strains and are given as follows

$$\frac{\partial H(\varepsilon,E)}{\partial \varepsilon_{ij}} = \sigma_{ij} = c^{E}_{ijkl}\varepsilon_{kl} - e_{kij}E_k \quad \text{(converse effect)} \tag{A.2}$$

$$\frac{\partial H(\varepsilon,E)}{\partial E_i} = D_i = e_{ikl}\varepsilon_{kl} + \eta^{\varepsilon}_{ik}E_k \quad \text{(direct effect)} \tag{A.3}$$

The free energy can also be expressed in terms of stresses. It is then called the second thermodynamic potential, denoted by H(σ,E) and is expressed as follows.

$$H(\sigma,E) = -\frac{1}{2}s^{E}_{ijkl}\sigma_{ij}\sigma_{kl} + d_{ijk}E_i\sigma_{jk} + \frac{1}{2}\eta^{\sigma}_{ij}E_iE_j \tag{A.4}$$

where s^{E}_{hi}, d_{ijk} and η^{σ}_{ij} are the coefficients of the elastic compliance at constant electric field, piezoelectric strain and dielectric permittivity at constant stress, respectively and σ_{ij} are the components of stress. The differential coefficients of the second thermodynamic potential with respect to the components of elastic stress are the components of strain and the differential coefficients with respect to the components of electric field are the components of charge These are the alternative form of the fundamental piezoelectric equations in terms of the stresses.

$$\frac{\partial H(\sigma,E)}{\partial \sigma_{ij}} = \varepsilon_{ij} = s^{E}_{ijkl}\sigma_{kl} + d_{kij}E_k \quad \text{(converse effect)} \tag{A.5}$$

$$\frac{\partial H(\sigma,E)}{\partial E_i} = D_i = d_{ikl}\sigma_{kl} + \eta^{\sigma}_{ik}E_k \quad \text{(direct effect)} \tag{A.6}$$

The constitutive relations based on the first thermodynamic potential are used most often since they are a function of the components of strain rather than stress. However, the piezoelectric strain coefficients (d_{ikl}) are more commonly used than the stress coefficients (e_{ikl}). A relationship between the piezoelectric strain and stress coefficients allows the constitutive relations based on the first thermodynamic potential to be expressed using the piezoelectric strain coefficients. It is known that dielectric terms η^{ε}_{ij} and η^{σ}_{ij} are largely independent of stress and strain. Therefore, the following relationship using Eqns. A.3 and A.6 can be obtained.

$$e_{ikl}\varepsilon_{kl} = d_{ikl}\sigma_{kl} \tag{A.7}$$

The stress is related to the strain through Hooke's law

$$\sigma_{ij} = c_{ijkl}\varepsilon_{kl} \tag{A.8}$$

Substituting Hooke's law into Eqn. A.7, the piezoelectric strain coefficients are now expressed as follows.

$$e_{ikl} = d_{ikl}c_{klmn} \tag{A.9}$$

Substituting the above equation into Eqns. A.2 and A.3 yields the following constitutive relations expressed in terms of the components of strain and piezoelectric strain coefficients.

$$\sigma_{ij} = c^{E}_{ijkl}\varepsilon_{kl} - d_{kij}c^{E}_{ijmn}E_k \quad \text{(converse effect)} \tag{A.10}$$

$$D_i = d_{ikl}c_{klmn}\varepsilon_{mn} + \eta^{\varepsilon}_{ik}E_k \quad \text{(direct effect)} \tag{A.11}$$

Rearranging and using matrix notation produces the constitutive equations for piezoelectric materials.

$$\sigma = \mathbf{Q}\left(\varepsilon - \mathbf{d}^{T}\mathbf{E}\right) \text{ (converse effect)} \tag{A.12}$$

$$\mathbf{D} = \Psi\mathbf{E} + \mathbf{dQ}\varepsilon \text{ (direct effect)} \tag{A.13}$$

where **Q** is the elastic stiffness matrix, **d** is the piezoelectric strain coefficient matrix, Ψ is the dielectric constant matrix, σ and ε are the stress and strain vectors, respectively and **D** and **E** are the electric charge and the electric field vectors, respectively.

A.2 Theoretical background

The focus of this dissertation is to utilize the macroscopic properties of piezoelectric materials and integrate them as elements of smart composite structures as both sensors and actuators. To achieve this goal, it is necessary to understand the electromechanical constitutive relationships which govern these materials . As mentioned previously, Jacques and Pierre Curie discovered the direct piezoelectric effect in 1880 when they observed that an electric charge developed on certain materials in response to a mechanical stress. Soon thereafter, Gabriel Lippman predicted the converse piezoelectric effect which occurs when a mechanical strain develops in response to an applied electric charge. His rational was as follows. Consider the following thermodynamic potential function formulated in terms of a single scalar stress and electric field (Cady; 1964).

$$\zeta = \frac{1}{2}c\sigma^2 + \frac{1}{2}\eta' E^2 + d'\sigma E \tag{A.14}$$

where c is the elastic compliance, η' is the permittivity, σ is the stress, E is the electric field and d' is the piezoelectric strain coefficient. The change in ζ due to a small variation in E and σ is as follows.

$$d\zeta = D dE + \varepsilon d\sigma \tag{A.15}$$

where D is the electric charge and ε is the strain which are found as follows.

$$D = \left.\frac{\partial \zeta}{\partial E}\right|_{\sigma} \tag{A.16}$$

$$\varepsilon = \left.\frac{\partial \zeta}{\partial \sigma}\right|_{E} \tag{A.17}$$

Since the order in which differentiation occurs, it follows that

$$\left.\frac{\partial D}{\partial \sigma}\right|_{E} = \left.\frac{\partial \varepsilon}{\partial E}\right|_{\sigma} \tag{A.18}$$

Since it is known that the relationship between an applied stress and an electric charge is linear over a wide range of pressure for most crystals, the following is true.

$$\left.\frac{\partial D}{\partial \sigma}\right|_{E} = \delta \tag{A.19}$$

where δ is a constant. This was verified by the Currie brothers to be true for piezoelectric crystals as well. Lippman showed that not only must converse relationship exist between the strain and an applied electric field, it must be equal to the same constant previously found for the direct relationship.

$$\left.\frac{\partial \varepsilon}{\partial E}\right|_{\sigma} = \left.\frac{\partial D}{\partial \sigma}\right|_{E} = \delta \tag{A.20}$$

His theoretical prediction was soon found to be true through further experiments by the Curries. It must be noted that Eqn. A.15 is analogous to the enthalpy of a reversible system where the quantities D, E, ε and σ are analogous to absolute temperature, entropy, volume and pressure in ordinary thermodynamics. The electric charge, D, is also analogous to the strain, ε, and is often termed the electric displacement. Similarly, the electric field, E, is analogous to the stress, σ, and is often termed the electric force. The above analysis can easily be expanded to incorporate a multi dimensional state of stress and electric field.

A.3 Physical interpretation of piezoelectric constants

Several coefficients are defined to characterize the properties of a piezoelectric material. Three axes are used to identify directions in a piezoelectric material which are necessary to define these coefficients. These axes, termed 1, 2 and 3, are analogous the X, Y and Z of the classical three dimensional orthogonal set of axes and are indicated in Fig. A.1 (a). The polar, or 3, axis is taken parallel to the direction of polarization within the ceramic. This direction is established during manufacturing by a high DC voltage that is applied between a pair of electroded faces to activate the material. The polarization vector "P" is represented by an arrow pointing from the positive to the negative poling electrode. Piezoelectric coefficients with double subscripts link electrical and mechanical quantities. The first subscript gives the direction of the electrical field associated with the voltage applied or the charge produced. The second subscript gives the direction of the mechanical stress or strain. For the current research, the most important coefficients are the piezoelectric strain coefficients (d_{ij}) which relate the mechanical strain developed in a piezoelectric material to the applied electric field.

$$d = \frac{\text{strain developed}}{\text{applied electric field}} \tag{A.21}$$

Conversely, the d_{ij} coefficients also relate the charge collected due to an applied mechanical stress. These are contained in the piezoelectric strain coefficient matrix, **d**, which has the following form for piezoelectric material having orthorhombic *mm2* symmetry such as PVDF (polyvinylidene fluoride) and PZT (lead zirconate titanate).

$$\mathbf{d} = \begin{bmatrix} 0 & 0 & d_{31} \\ 0 & 0 & d_{32} \\ 0 & 0 & d_{33} \\ 0 & d_{24} & 0 \\ d_{15} & 0 & 0 \\ 0 & 0 & d_{36} \end{bmatrix} \qquad (A.22)$$

The dimensions are expressed as length per length, per volts per length (length per volt). For instance, the d_{31} coefficient relates the coupling between an applied electric field (voltage) in the 3 direction to the strain in the 1 direction as shown in Fig. A.1 (b).

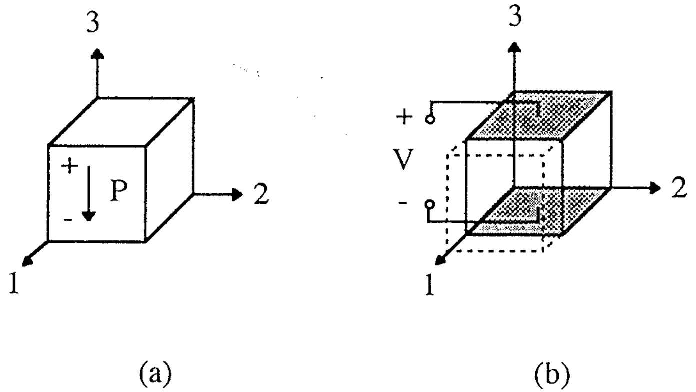

Fig. A1. Piezoelectric material: (a) coordinate system (b) effect of d_{31} coefficient.

The piezoelectric stress coefficients, g_{ij}, relate the open circuit electric field to the applied mechanical stress as follows.

$$g = \frac{\text{open circuit electric field}}{\text{applied mechanical stress}} \qquad (A.23)$$

The dimensions for g_{ij} are expressed as volts per length, per force per length squared. These coefficients are used less often then the d_{ij} coefficients since normally the electric field is taken as the independent variable. However, their is a direct correspondence of nonzero values of d_{ij} to nonzero values of g_{ij}. The relative dielectric constant K is the dimensionless ratio of the permittivity of the material, $\in$, to the permittivity of free space, $\in_o$.

$$K = \frac{\in}{\in_o} \tag{A.24}$$

The piezoelectric strain and stress coefficients are related through the dielectric properties as follows.

$$d_{ij} = K \in_o g_{ij} \tag{A.25}$$

Appendix B

Displacement Field Justification

The formulation of the higher order displacement field is based on both physical relevance and considerations for the finite element implementation in order to solve useful problems. A great deal of intuition is gained by solving a simple beam problem, using the Ritz method, which is used to illustrate concepts which can be applied to the advanced formulation of the smart composite laminate. The beam has length L, height h, distributed load q and elastic and shear moduli E and G, respectively. One end is fixed as indicated in Fig. B.1.

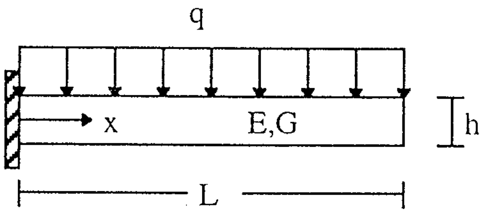

Fig. B1 Cantilever beam with distributed load.

The general higher order displacement field for the beam is given as a cubic expansion of the inplane displacements (u) and a single function for the transverse displacement (w) as follows.

$$\begin{aligned} u &= \phi_{10}(x) + z\phi_{11}(x) + z^2\phi_{12}(x) + z^3\phi_{13}(x) \\ w &= \phi_{30}(x) \end{aligned} \tag{B.1}$$

The in plane term $\phi_{10}(x,y)$ is ignored for this simple investigation. The relevant normal and shear strain are given as follows.

$$\varepsilon = \frac{\partial u}{\partial x} \tag{B.2}$$

$$\tau = \frac{\partial u}{\partial z} + \frac{\partial w}{\partial x} \tag{B.3}$$

where ε is the normal strain and τ is the transverse strain. The total potential energy is given as follows.

$$\Pi = \frac{1}{2}\int_0^L\int_0^b\int_{-h/2}^{h/2}\left(E\varepsilon^2 + G\tau^2\right)dzdydx - qw \tag{B.4}$$

The principle of minimum total potential energy states that the equilibrium position is found which minimizes the potential functional Π. This is achieved by applying standard procedures in variational calculus which are used to find a stationary point of Π and derive the Euler-Lagrange equations which constitute the equilibrium equations and boundary conditions. The results are well known and not presented here for the sake of brevity. Instead, approximate solutions are found using the Ritz approach to determine values for the coefficients of interpolating polynomials. These approximate solutions represent properties of the finite element solution which is used for implementation of the higher order theory (Chapter 3). This is achieved by finding a stationary point to Π with respect to the unknown coefficients of the approximation polynomials (a_i) as follows.

$$\frac{\partial\Pi}{\partial a_i} = 0 \tag{B.5}$$

Using this approach , the coefficients can be determined by solving the set of resulting equations from Eqn. B.5.

Classical theory

First, consider the case of classical theory which can be obtained by setting $\phi_{12}(x) = \phi_{13}(x) = 0$. The quantity $\phi_{12}(x,y)$ is determined by using the Kirchcoff condition that states planes normal to the neutral axis remain plane after bending for sufficiently thin beams and the shear stress vanishes as follows.

$$\tau = \phi_{11} + \frac{\partial\phi_{31}}{\partial x} = 0 \quad \rightarrow \quad \phi_{11} = -\frac{\partial\phi_{31}}{\partial x} \tag{B.6}$$

Setting $\phi_{31} = w_0$ yields the following displacement field for classical beam theory.

$$u = -z\frac{\partial w_0}{\partial x} \qquad \text{(B.7)}$$
$$w = w_0$$

Selecting a two term Ritz solution which satisfies the geometric boundary conditions at the fixed end, $w_0 = b_2x^2 + b_3x^3$, results in the following values for the unknown interpolation polynomial.

$$w_0 = \frac{5}{2}\frac{qL^2}{Eh^2}x^2 - \frac{qL}{Eh^2}x^3 \qquad \text{(B.8)}$$

A three term Ritz solution, $w_0 = b_2x^2 + b_3x^3 + b_4x^4$, yields the exact solution. That is,

$$w_0 = 3\frac{qL^2}{Eh^2}x^2 - 2\frac{qL}{Eh^2}x^3 + \frac{1}{2}\frac{q}{Eh^2}x^4 \qquad \text{(B.9)}$$

Upon closer examination, the two term solution is a least squares fit to the exact solution. It gives the exact solution at the points where the second order Legendre polynomial vanishes. It is important to note that the shear stiffness, G, does not enter here since the shear strain is assumed to be zero. The theory is valid for thin beams where the shear strain is not important. However, significant errors are obtained for thicker beams where the shear strain becomes important.

First order theory

The first order theory, which is identical to the Timeshenko beam theory, accounts for additional deformation of the cross section. It recognizes that the action of the shear force causes a shear strain which in turn causes a warping of planes normal to the neutral axis. The theory in effect averages the effect of shear strain over the entire cross section. This theory utilizes two functions, ϕ_{11} and ϕ_{31}. Setting $\phi_{11} = u_1$ and $\phi_{30} = w_0$ yields the following displacement field for first order theory.

$$u = zu_1 \qquad \text{(B.10)}$$
$$w = w_0$$

Selecting a two term Ritz solution which satisfies the geometric boundary conditions at the fixed end, $u_1 = a_1 x$ and $w_0 = b_1 x$, now results in the following values for the unknown interpolation polynomial.

$$u_0 = -3\frac{qL^2}{GL^2 + Eh^2}x \tag{B.11}$$

$$w_0 = \frac{1}{2}\frac{qL\left(4GL^2 + Eh^2\right)}{G\left(GL^2 + Eh^2\right)}x \tag{B.12}$$

A thin beam in which the shear strain is not important can be represented by an infinite shear stiffness ($G \rightarrow \infty$). It is clear that as $G \rightarrow \infty$, both a_1 and $b_1 \rightarrow 0$. This serious deficiency in the solution and a clear case of a shear "locking" since a large load q produces practically no displacements for thin beams. The principle of minimum potential energy can be viewed as a minimization process of the strain energy potential. The shear term in the energy functional, $G\tau^2$, represents a constraint, τ, with a penalty term, G. As the limit of this penalty term approaches infinity, a penalty condition is introduced on the shear strain which requires that the shear strain $\tau = a_1 x + b_1$ must vanish in the Ritz approximation which is the case for thin beams. This penalty term requires that both a_1 and $b_1 \rightarrow 0$ which also forces the bending strain to zero and does not accurately represent the physical situation. A meaningful solution can not be obtained in this case which results from the inconsistent interpolation of the shear strain. A three term Ritz solution with $u_1 = a_1 x$ and $w_0 = b_1 x + b_2 x^2$, gives the following approximate solution.

$$u_0 = -2\frac{qL^2}{Eh^2}x \tag{B.13}$$

$$w_0 = \frac{qL}{G}x - \frac{1}{2}\frac{q\left(-2GL^2 + Eh^2\right)}{EGh^2}x^2 \tag{B.14}$$

The shear strain is now given as

$$\tau = b_1 + \left(a_1 + 2b_2\right)x \tag{B.15}$$

Now, as $G \to \infty$, the shear strain penalty term governed by G also $\to 0$ since $b_1 \to 0$ and $(a_1 + 2b_2) \to 0$ as well. Therefore, the shear strain is now effectively approximated, even for a thin beam with a rigid shear stiffness. This is because the shear strain does not introduce a spurious constraint so that the bending strain, although constant, is not reduced to zero and the physical aspect of the problem is accurately modeled. The reason this interpolation is effective is because the constraint $(a_1 + 2b_2)$ is consistently balanced. That is, both u_0 and $\frac{\partial w_0}{\partial x}$ are of the same order. A finite element model based on this interpolation scheme is completely free from locking. However, a finite element model which uses quadratic interpolation is quite cumbersome to implement since it requires that extra nodes be defined which are not required using either linear or cubic interpolations. Another drawback is the representation of the shear strain as a linear function. Shear correction factors are required to obtain an accurate solution since the shear is a linear approximation of a quadratic function. The shear strain distribution also violates the stress free boundary conditions on the free surfaces which require the shear strain to vanish on the top and bottom surfaces of the beam.

Higher order theory

The conditions that the shear strains vanish are used by the higher order theory to satisfy this requirement. Consider the following displacement field.

$$\begin{aligned} u &= z\phi_{11}(x) + z^2\phi_{12}(x) + z^3\phi_{13}(x) \\ w &= \phi_{30}(x) \end{aligned} \tag{B.16}$$

In this general form, this higher order displacement field does not satisfy the requirement that the shear stresses vanish on the free surfaces. Imposing this requirement is equivalent to setting the shear strain equal to zero at ± h/2.

$$\varepsilon|_{h/2} = \varepsilon|_{-h/2} = 0 \tag{B.17}$$

This results in the following equations

$$\tau(h/2) = 0 = \phi_{11}(x) + h\phi_{12}(x) + \frac{3}{4}h^2\phi_{13}(x) + \frac{\partial\phi_{30}(x)}{\partial x} \tag{B.18}$$

$$\tau(-h/2) = 0 = \phi_{11}(x) - h\phi_{12}(x) + \frac{3}{4}h^2\phi_{13}(x) + \frac{\partial\phi_{30}(x)}{\partial x} \tag{B.19}$$

Clearly, $\phi_{12}(x)$ must be zero to satisfy both equalities. In addition, the higher order function $\phi_{13}(x)$ can be solved for in terms of the lower order functions. This leads to the following refined displacement field.

$$\begin{aligned} u &= z\phi_{11}(x) - \frac{4z^3}{3h^2}\left(\phi_{11}(x) + \frac{\partial\phi_{30}(x)}{\partial x}\right) \\ w &= \phi_{30}(x) \end{aligned} \tag{B.20}$$

The shear stress is then a quadratic function of z given by the following

$$\tau = \left(1 - 4\frac{z^2}{h^2}\right)\left(\phi_{11}(x) + \frac{\partial\phi_{30}(x)}{\partial x}\right) \tag{B.21}$$

which vanishes at ±h/2 as required. The refined theory, which contains the same number of unknown functions as first order theory, is finally obtained by setting $\phi_{11} = u_1$ and $\phi_{30} = w_0$ as follows.

$$\begin{aligned} u &= zu_1(x) - \frac{4z^3}{3h^2}\left(u_1(x) + \frac{\partial w_0(x)}{\partial x}\right) \\ w &= w_0(x) \end{aligned} \tag{B.22}$$

However, the appearance of the derivative term in u requires a higher order interpolation of w_0. Choosing a three term Ritz solution, $u_1 = a_1 x$ and $w_0 = b_2 x^2 + b_3 x^3$, yields the following approximate solution.

$$u = \frac{10qL^2}{Eh^2}\frac{\left(-7056G^2L^4 - 2261GEL^2h^2 + 100E^2h^4\right)}{\left(35280G^2L^4 + 7336GEL^2h^2 + 25E^2h^4\right)}x \tag{B.23}$$

$$w = \frac{5qL^2}{2Eh^2}\frac{\left(14112G^2L^4 + 49504GEL^2h^2 + 1165E^2h^4\right)}{\left(35280G^2L^4 + 7336GEL^2h^2 + 25E^2h^4\right)}x^2 - 525qL\frac{\left(168GL^2 + Eh^2\right)}{\left(35280G^2L^4 + 7336GEL^2h^2 + 25E^2h^4\right)}x^3 \tag{B.24}$$

Taking the limit $G \to \infty$ to represent a thin beam which has rigid shear stiffness of the Ritz solution yields the following displacement field.

$$u = -2\frac{qL^2}{Eh^2}x \tag{B.25}$$

$$w = \frac{qL^2}{Eh^2}x^2 \tag{B.26}$$

Despite the additional complexity of the refined displacement field, this approach reduces to the three term Ritz solution for first order theory. It is also no better than a two term solution for the refined displacement field using only the quadratic term for w since $b_2 \to 0$ for thin beams. In the finite element implementation of the refined displacement field, the quadratic interpolation of w is cumbersome to implement. A cubic interpolation that introduces additional degrees of freedom is not justified either since no improvement is observed in the solution over the simpler first order theory for thin plates. A better approach is needed.

Modified higher order theory

Considering the physical nature of the problem, it is expected that the bending strain result from the rotation of the beam $\left(-\frac{\partial w_0}{\partial x}\right)$, plus a distortion effect due to shear u_1, plus some higher order terms which can be solved in terms of lower order terms by using the stress free boundary conditions. This situation can be modeled mathematically by setting $\phi_{11} = u_1 - \frac{\partial w_0}{\partial x}$ and $\phi_{30} = w_0$. Substituting into the refined displacement field (Eqn. B.22) yields the following modified refined displacement field

$$u = z\left(u_1 - \frac{\partial w_0(x)}{\partial x}\right) - \frac{4z^3}{3h^2} u_1(x) \qquad \text{(B.27)}$$
$$w = w_0(x)$$

Using the same three term approximation to the unknown functions, $u_1 = a_1 x$ and $w_0 = b_2 x^2 + b_3 x^3$, yields the following approximate solution for the modified refined approach.

$$u = \frac{210qL^2}{\left(280GL^2 + Eh^2\right)} x \qquad \text{(B.28)}$$

$$w = \frac{qL^2\left(1400GL^2 + 173Eh^2\right)}{2Eh^2\left(280GL^2 + Eh^2\right)} x^2 - \frac{qL}{Eh^2} x^3 \qquad \text{(B.29)}$$

Again, taking the limit $G \rightarrow \infty$ to represent a thin beam and reduce the shear constraint to zero yields the following

$$u = 0 \qquad \text{(B.30)}$$

$$w_0 = \frac{5}{2}\frac{qL^2}{Eh^2} x^2 - \frac{qL}{Eh^2} x^3 \qquad \text{(B.31)}$$

These equations are exactly the same as the three term Ritz solution using the classical theory where the shear stress is assumed to be zero which is true for a beam with infinite shear stiffness. Therefore, the modified displacement field yields the correct trend for thin beams by reducing the shear constrain to zero. The higher order interpolation polynomials, which require additional degrees of freedom in the finite element interpolation, are now justified since the bending rotation is now a linear function rather than a constant as in the first order theory. The shear strain is given as follows

$$\tau = u_1 - \frac{\partial w_0}{\partial x} + \frac{\partial w_0}{\partial x} \qquad \text{(B.32)}$$

which, when calculated in terms of the Ritz coefficients, $\tau = a_1$, vanishes for thin plates as expected. For thicker plates, the shear strain is accurately accounted for as a quadratic function which vanishes on the free surfaces. Consistent interpolation for the shear strain is automatically satisfied while avoiding quadratic interpolation schemes which are difficult to implement. Understanding the physical nature of the problem and viewing the principle of minimum potential energy as a minimization process which includes the shear as a constraint allows a modified refined displacement field to be formulated. This displacement field accurately accounts for the shear strain and produces no spurious constraint which frees the solution from any form of locking.

Appendix C

Mesh Generation

Each element in the finite element model for the current study is formulated assuming that the piezoelectric layers are either present throughout the entire element, or are completely absent. While it is possible to formulate elements which only partially contain piezoelectric layers, it is quite laborious and computationally inefficient. Since the finite elements either contain, or do not contain, piezoelectric layers, the boundaries of piezoelectric layers must coincide with the element nodes. Therefore, a change in the shape of a piezoelectric layer must be reflected by a change in the finite element mesh. This task is non trivial and impractical to accomplish by hand for realistic mesh sizes or at each iteration of a closed loop optimization procedure. Therefore, an efficient strategy must be devised to generate a finite element mesh to accommodate arbitrary piezoelectric layer geometries.

The first step in accomplishing the mesh generation is to choose a proper mesh for the composite laminate with no piezoelectric layers. Ideally, this mesh should have equally sized elements for simplicity. The aspect ratio of the k-th element is defined as follows.

$$\alpha_k = \frac{l^e_{x_k}}{l^e_{y_k}} \tag{C.1}$$

where $l^e_{x_k}$ and $l^e_{y_k}$ are the length of the k-th element in the x and y direction, respectively. These geometric parameters are calculated from the nodal coordinates of each element as follows (Fig. C.1).

$$l^e_{x_k} = x_{i+1} - x_i \tag{C.2}$$

$$l^c_{y_i} = y_{j+1} - y_j \tag{C.3}$$

The element aspect ratio should be as close to one as possible since the accuracy of the finite element solution degrades as the aspect ratio differs from one. However, this equally sized mesh does not necessarily coincide with the boundaries of an arbitrary piezoelectric layer. Consider the introduction of a piezoelectric layer on a square laminate as shown in

Fig. C.1 (a). The original mesh of square elements is shown in Fig. C.1 (b) along with the modified mesh to incorporate the piezoelectric layer. In this case, it is clear that node points of the original mesh corresponding to x_3 and y_2 must be changed to accommodate the piezoelectric layer. In meshes with a practical number of elements, the process of determining nodal coordinates to incorporate the piezoelectric layer while retaining an aspect ratio as near to one as possible is a non trivial task.

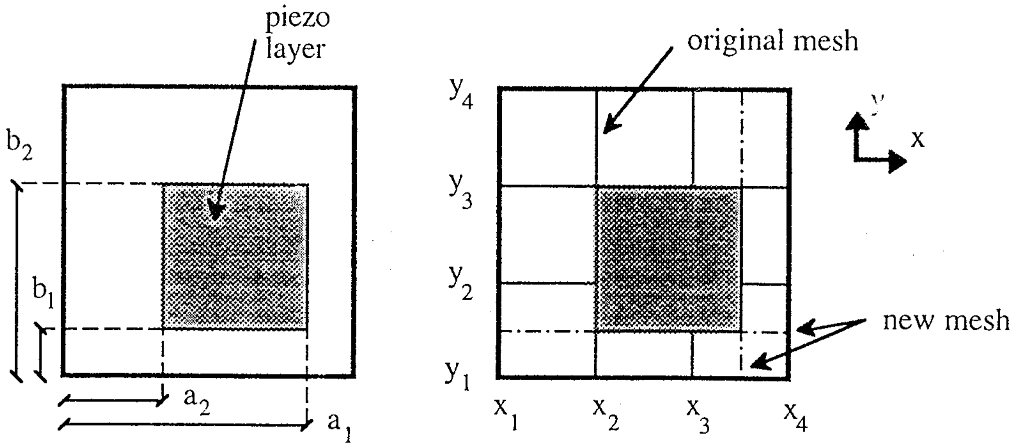

Fig. C1 Finite element mesh incorporating piezoelectric layers.

The process of determining the best possible mesh for a given actuator size and location is an optimization problem within itself. The objective is to retain the original element aspect ratios as closely as possible of the original mesh while incorporating the piezoelectric layer (an aspect ratio of one is best). A quadratic penalty function is defined which the sum of the squares of the difference between the element dimensions of the old and new mesh as follows.

$$F = \frac{1}{2} \sum_{k=1}^{NELEM} \left(\left(l_{x_k}^{e'} - l_{x_k}^{e} \right)^2 + \left(l_{y_k}^{e'} - l_{y_k}^{e} \right)^2 \right) \qquad \text{(C.4)}$$

The quantities $l_x^{e'}$ and $l_{y_i}^{e'}$ are the element aspect ratios for the new mesh which are calculated as follows.

$$l_{x_k}^{e'} = x'_{i+1} - x'_i \qquad \text{(C.5)}$$

$$l_{y_k}^{e'} = y'_{j+1} - y'_j \tag{C.6}$$

The quantities x'_{i+1}, x'_i, y'_{j+1} and y'_j are the nodal coordinates for the new mesh. Minimizing this penalty function corresponds to retaining the original aspect ratios as closely as possible. Of course, constraints need to be imposed to ensure that the original geometry of the laminate is retained and that the proper nodal values correspond to the edges of the piezoelectric layer. These constraints will be discussed shortly. The minimum value of F is found by setting the derivatives with respect to the new nodal coordinates to zero. First, F is rewritten in terms of the nodal coordinates for the original and new mesh.

$$F = \frac{1}{2}\sum_{i=1}^{M-1}\sum_{j=1}^{N-1}\left[\left(\{x'_{i+1} - x'_i\} - \{x_{i+1} - x_i\}\right)^2 + \left(\{y'_{j+1} - y'_j\} - \{y_{j+1} - y_j\}\right)^2\right] \tag{C.7}$$

where M and N are the number of nodes in the x and y directions, respectively. Next, derivatives of F are calculated with respect to the new nodal coordinates and are set to zero as follows.

$$\frac{\partial F}{\partial x'_i} = -x'_{i+1} + 2x'_i - x'_{i-1} = 0 \quad i = 2,3,\cdots,M-1 \tag{C.8}$$

$$\frac{\partial F}{\partial y'_j} = -y'_{j+1} + 2y'_j - y'_{j-1} = 0 \quad j = 2,3,\cdots,N-1 \tag{C.9}$$

where it is assumed that all of the nodes in the original mesh are evenly spaced in the x and y directions. It must be noted that the coordinates of the edges of the laminate are considered fixed (i=1,M and j=1,N) to retain the original geometry of the laminate. Therefore, derivatives of the penalty function with respect to the nodal coordinates which correspond to these nodes are zero. Four additional constraint equations are required to ensure that this is true.

$$x'_1 = 0, \quad x'_M = L \tag{C.10}$$

$$y'_1 = 0, \quad y'_N = W \tag{C.11}$$

where L and W are the length and width of the laminate, respectively. Constraints are also imposed on the nodes nearest the edges of the piezoelectric layer to ensure that these nodes are aligned with the border of the piezoelectric layer. This is accomplished by setting to zero all coefficients of the relevant equation except for a single term corresponding to the constrained node. The term on the right hand side is then set to the value of the nodal coordinate corresponding to the constrained value of the nodal coordinate. The above linear equations are uncoupled in the sense that the nodal coordinates in the x direction do not depend on the nodal coordinates in the y direction and vice versa. The equations which corresponds to the nodal coordinates in the x direction are written in matrix form as follows

$$\begin{bmatrix} 1 & & & & & & \\ -1 & 2 & -1 & & & \text{0's} & \\ & & 1 & & & & \\ & & -1 & 2 & -1 & & \\ & & & & \ddots & & \\ & & & & 1 & & \\ & \text{0's} & & & -1 & 2 & -1 \\ & & & & & & 1 \end{bmatrix} \begin{Bmatrix} x'_1 \\ x'_2 \\ x'_3 \\ x'_4 \\ \vdots \\ x'_{M-2} \\ x'_{M-1} \\ x'_M \end{Bmatrix} = \begin{Bmatrix} 0 \\ 0 \\ a_1 \\ 0 \\ \vdots \\ a_2 \\ 0 \\ L \end{Bmatrix} \begin{matrix} * \\ \\ * \\ \\ \\ * \\ \\ * \end{matrix} \qquad \text{(C.12)}$$

where the constraint equations are flagged with an asterisk (*). Although the resulting set of equations are not symmetric, they can easily be transformed into a symmetric set of equations by performing a few elementary row operations. Solving this set of equations yields optimal values of the nodal coordinates in the x direction to retain element aspect ratios as near to the original values as possible while incorporating new coordinates due to the introduction a piezoelectric layer. The equations to determine the nodal coordinates in the y direction are similar.